Early Age Fracture Mechanics and Cracking of Concrete

Experiments and Modelling

Østergaard, Lennart

Publication date:
2003

Document Version
Publisher's PDF, also known as Version of record

Lennart Østergaard

Early-Age Fracture Mechanics And Cracking of Concrete

Experiments and Modelling

BYG·DTU

DANMARKS TEKNISKE UNIVERSITET

DTU

PhD Thesis
BYG·DTU
Report R-070
2003
ISSN 1601-2917
ISBN 87-7877-133-1

Early-Age Fracture Mechanics and Cracking of Concrete

Experiments and Modelling

Lennart Østergaard

Ph.D. Thesis

Department of Civil Engineering
Technical University of Denmark

2003

Early-Age Fracture Mechanics
and Cracking of Concrete
Experiments and Modelling

Printed by DTU-Tryk
Department of Civil Engineering
Technical University of Denmark
ISBN number: 87-7877-133-1

Preface

This thesis is handed in as a partially fulfillment of the requirements to obtain a Ph.D.-degree at the Technical University of Denmark.

The author gratefully acknowledges the support of his main supervisor, Assoc. Prof. Henrik Stang, Technical University of Denmark as well the co-supervisors Assoc. Prof. David A. Lange, University of Illinois at Urbana-Champaign and Prof. Lars Damkilde, University of Aalborg at Esbjerg.

A special acknowledgement is given to Assoc. Prof. John Forbes Olesen with whom I have enjoyed many fruitful discussions.

Abstract

Modern high performance concretes have low water cement ratios and do often include silica fume. Also early age high strength cements are often applied and when all these factors sum up, it turns out that the cracking sensibility is dramatically increased in comparison with ordinary concrete. The reasons are the increased autogenous deformation, the high rate of heat evolution and a higher brittleness of these concretes.

Due to these adverse mechanisms the interest in the full description of the behavior of early age concrete has increased dramatically in the last two or three decades. Almost all the governing material parameters have undergone intensive research and the body of knowledge provides today a basis for calculation of the stress evolution and thus, represents a tool for prediction of whether cracking will occur or not.

However, the experimental investigation and the modelling of the early age concrete after crack initiation has occurred, is scarce. What are the constitutive properties for the crack in early age and how can they be determined? This is the subject for the present thesis.

A detailed analysis of five important test methods and their application for early age concrete have been carried out and experimental results generated. These test methods comprise the uniaxial tension test, the three point bending test, the split cylinder test, the wedge splitting test and a method for determination of the bond properties in early age between reinforcement and concrete.

The analysis has been carried out utilizing the finite element method and through analytical modelling. The uniaxial tension test is not suited for early age concrete, but it serves as an essential tool for comparison. The most well suited method for determination of early age fracture properties of concrete is the wedge splitting test. For this method a fast and simple method for interpretation and inverse analysis has been developed and calibrated versus the finite element method and experimental results. The analysis of the split cylinder test has shown that this test method produces erroneous results if applied in early age. The results are only valid after 24 hours for fast and normal hardening cements and after 48 hours for slow hardening cements. This is confirmed in a finite element model.

The fracture properties of early age concrete have been determined. The framework of the investigations has been the fictitious crack model and the aim has been experimentally to determine the fracture mechanical properties related to this model. The results provide interesting and important insight into the development of the fracture properties in early

age. It is found that the characteristic length has moments of low values in early age, which means that the cracking sensibility is higher at those time points.

The possible influence of time-dependent effects in the fracture mechanical properties on the cracking behavior in early age has also been investigated. The reason for this has been the known fact that viscoelasticity of the bulk material is very important for the determination of the stress evolution in early age, and thus, this could also be the case for the crack. However, it has not been possible to determine any rate effects or viscoelastic effects of the crack in early age. The observed time dependent deformations can entirely be ascribed the bulk creep effects.

The work on the bond properties between concrete and reinforcement in early age has resulted in the development of a method for interpretation and inverse analysis and also in a experimental setup, which is suited for determination of the early age properties.

Resumé

Moderne højkvalitetsbetoner er ofte kendetegnede ved et lavt vand-cement forhold samt brugen af microsilica. Herudover anvendes der ofte hurtighærdende cement. Disse faktorer har imidlertid vist sig at resultere i en dramatisk forøgelse af risikoen for revnedannelse i betonen i tidlig alder. Dette forårsages dels af den forøgede autogene deformation, den hurtige varmeudvikling samt af det forhold at disse betoner bliver langt sprødere end normal konstruktionsbetoner.

Som følge heraf er interessen for at kunne beskrive højkvalitetsbetonernes forhold og udvikling af egenskaber i tidlig alder meget stor. Næsten samtlige betydende materialeparametres udvikling har været underkastet intensiv forskning og resultaterne heraf har givet grundlaget for de idag eksisterende beregningsmodeller. Disse beregningsmodeller giver redskaber som kan bruges til en forudsigelse af hvorvidt revnedannelse vil finde sted eller ej.

Imidlertid findes der i litteraturen ikke mange resultater der beskriver hvad der sker i beton i tidlig alder efter at revnedannelse har fundet sted. Hvorledes udvikler de konstitutive parametre for revnen sig i tidlig alder - og hvorledes kan de bestemmes? Dette er et af temaerne for nærværende afhandling.

I denne forbindelse er fem vigtige eksperimentelle metoder og deres anvendelighed på beton i tidlig alder afprøvet. Disse metoder omfatter det enaksede trækforsøg, trepunktsbøjebjælken, splitcylindertesten, wedge splitting testen samt en metode til bestemmelse af forbindelsesstyrken mellem beton og armering i tidlig alder.

Modelleringen er foretaget ved anvendelse af dels finite element metoden og dels gennem analytiske betragtninger. Det kan konkluderes at det enaksede trækforsøg ikke er velegnet for bestemmelse af brudmekaniske egenskaber for beton i tidlig alder, men forsøget er alligevel relevant idet det giver en uundværlig mulighed for sammenligning med de indirekte forsøg. Det mest velegnede forsøg til bestemmelse af de brudmekaniske egenskaber for beton i tidlig alder er wedge splitting testen. Til dette forsøg er udviklet en simpel og hurtig metode til fortolkning og invers analyse af forsøgsresultater. Metoden er valideret og kalibreret imod finite element resultater samt eksperimentelle resultater. Undersøgelserne af split cylinder testen har vist at denne testmetode er uegnet til bestemmelse af trækstyrken for beton i tidlig alder. Resultaterne fra splitcylinderforsøget er kun korrekte for beton der har opnået en modenhed på mindst 24 timer for normal og hurtighærdende beton og en modenhed på mindst 48 timer for langsomthærdende beton. Dette er bekræftet

gennem finite element analyser.

De eksperimentelle undersøgelser har resulteret i bestemmelsen af betons brudmekaniske egenskaber i tidlig alder. I denne forbindelse er den fiktive revnemodel anvendt som grundhypotese og målet har været at bestemme spændingsrevnevidderelationen som postuleres at være en materialeparameter i den fiktive revnemodel. Resultaterne har givet interessante og vigtige informationer om udviklingen af brudmekaniske egenskaber i tidlig alder. Det er således konstateret at den karakteristiske længde undervejs under hærdningen med mellemrum antager små værdier. Dette antyder at risikoen for kritisk revnedannelse er større på disse tidspunkter.

Den mulige indflydelsen af belastningshastighed eller revne-viskoelasticitet i forhold til udseendet af spændingsrevnevidderelationen i tidlig alder er også undersøgt. Dette begrundes med det velkendte faktum at viskoelasticitet i betonen i sig selv er en meget vigtig mekaniske for bestemmelsen af egenspændingsudviklingen for beton i tidlig alder, hvorfor lignende forhold kunne gøre sig gældende for revnen. Det har imidlertid ikke været muligt at afdække nogen effekt af belastningshastigheden eller eventuel revne-viskoelasticitet for revnen i tidlig alder. De observerede tidsafhængige deformationer har fuldstændigt kunnet forklares med krybning i betonen i sig selv.

Arbejdet med udviklingen af forbindelsesstyrken mellem beton og armering i tidlig alder har resulteret i udviklingen af metoder for fortolkning og invers analyse. Herudover er der udviklet et eksperimentelt setup som er velegnet for bestemmelse af forbindelsesstyrken i tidlig alder.

Table of Contents

Chapter 1

Introduction

Properties of concrete in early age have been a major research area in the past two decades, and a significant number of publications and international conferences have been dedicated to the subject, see e.g. the RILEM state-of-the-art report *Properties of Set Concrete at Early Ages*, (RILEM 1981) or the proceedings from e.g. *Thermal Cracking in Concrete at Early Ages*, (Springenschmid 1994), *Control of Cracking in Early Age Concrete*, (Mihashi & Wittmann 2002), *RILEM International Conference on Early-Age Cracking in Cementitious Systems (EAC'01)*, (Bentur & Kovler 2001) or *Shrinkage 2000*, (Baroghel-Bouny & Kheirbek 2000). The reasons for the focus on this area are arising from the fact that many problems with concrete cracking are originated in the early ages. This is due to the considerable volumetric changes in early age caused by autogenous and thermal deformations; in combination with external or internal restraints; and complicated by the rapid development of all important material properties. The problems are furthermore accentuated by the use of modern concrete mixes, which have low water-cement ratios and include microsilica, two factors, which both increase the autogenous shrinkage, (Baroghel-Bouny & Kheirbek 2000), and thus the stresses, which might be built up in the concrete during hardening. The use of high early age strength cement does also contribute to the risk of early age cracking since the heat of hydration for such cement is produced faster than for ordinary cements, thus increasing the temperature gradients in the concrete structure, (Hansen & Pedersen 1982).

1.1 Early Age Concrete

Concrete at early ages is characterized by the rapid development of its properties due to the chemical and physical processes that take place between Portland cement and water, i.e. the hydration, (Young 1997). The properties change, after an apparent initial inactive period, very fast in the first days, whereafter the changes slow down and reach a slow diffusion controlled steady state after three to seven days. The hydration continues in this final stage, if sufficient water is present, for years at an ever slower rate until eventually the degree of hydration of the clinker minerals has approached 100 %. Note that total hydration may only be approached asymptotically due to the diffusion control of the reactions, (Young 1997). Although concrete continues to mature for many years,

the early age is usually only considered to be the first few days or weeks, depending on the situation, (Byfors 1980, Hauggaard-Nielsen 1997). In this period, the majority of the hydration of the clinker minerals, except for the belite (C_2S), take place and thus also the majority of the properties are developed. This is illustrated in Figure 1.1 where the degree of hydration of the different clinker minerals is plotted as a function of time. At an age of only 3 days around 70 % of the C_3A and 50 % of the alite (C_3S) phases have hydrated, while 45 % of the ferrite phase and 20 % of the belite phase has hydrated. The diffusion controlled slow rate of hydration is seen to finally dominate the rate of hydration at around two to four weeks.

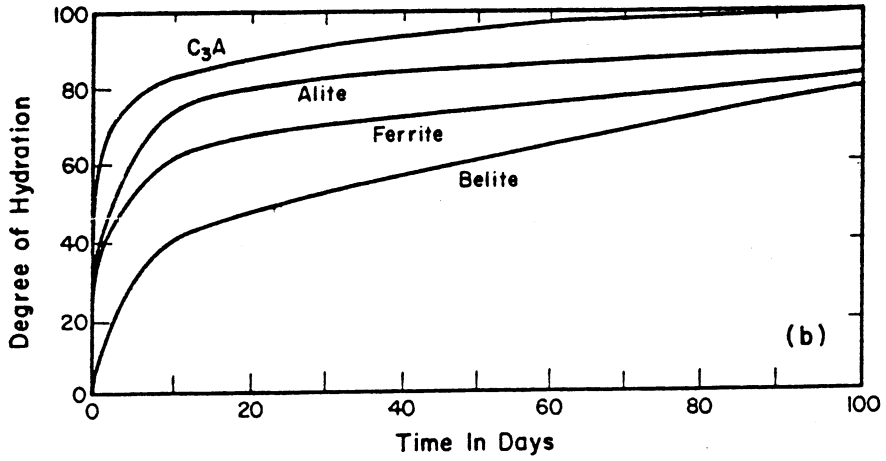

Figure 1.1 *Hydration of the clinker minerals in cement paste. (Young 1997)*

The hydration of the cement is highly exothermic and large amounts of heat is released during the process. This heat release is called the heat of hydration. The heat of hydration is dependent on the type of clinker mineral. Alite and C_3A releases high amounts of heat while hydrating as opposite to belite and C_4AF, which only release moderate to low amounts of heat, (Young 1997). One way temperature rises in concrete may be controlled is therefore by lowering the content of alite and C_3A since these compounds have the highest heats of hydration, and also the highest rate of heat evolution. On contrary, early age high strength, or rapid, cements usually have high amounts of alite compared with belite in combination with a finer grinding. The latter increases the surface area of the cement and gives therefore the water easier access to the cement, (Neville & Brooks 1990). These two measures increase the rate of hydration and thus the rate of development of properties.

The heat of hydration will lead to an increase of the concrete temperature. The rise in temperature can be large if adiabatic conditions exist. This may e.g. be the case in the central parts of mass concrete structures, where the concrete volume is large compared with the surface from which heat may be dissipated. The temperature rise under adiabatic conditions is shown in Figure 1.2 for different types of cement.

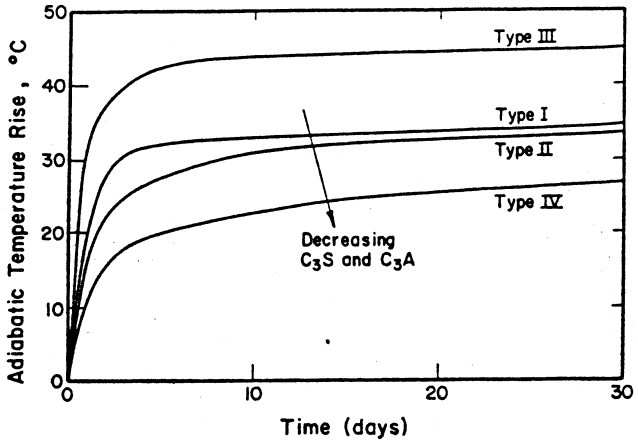

Figure 1.2 *Temperature rise in mass concrete under adiabatic conditions. (Young 1997)*

Early age high strength cement is denoted Type III in the figure. It is seen how both rate of temperature increase and the final level of temperature is highest for this type of cement. Type IV is a low heat cement and here both rate of increase and final temperature is significantly lower. The drawback for the latter type of cement is a slower development of the properties.

However, in most concreting situations, the conditions for the concrete will not be adiabatic - at least not throughout the structure. Instead, the temperature in the whole or some of the volume will be affected by the dissipation of heat from the surface. In this situation large temperature gradients may develop during hydration with peak temperature at the center of the volume and minimum temperature at the surface, see e.g. (Neville & Brooks 1990, Springenschmid 1994). The temperature rise and the gradients may lead to thermal cracking in early age concrete, as will be explained in the next section.

The hydration of the cement is also accompanied by volumetric changes due to volume differences between the reactants and the reaction products. The solid volume of the reaction products is lower than the initial volume of the reactants, (Powers & Brownyards 1948), see also Hansen (1986). Powers model can be applied to calculate the volume of a cement paste as function of the degree of hydration, and the result may be displayed graphically, see Figure 1.3. The figure shows how the volumetric phase composition changes as a function of the degree of hydration for two different cement pastes with water-cement ratios of 0.30 and 0.60. At the beginning only water and cement is present in the system. The water in this situation is termed the capillary water and represents the water, which is available for hydration. As hydration proceeds more and more of the cement reacts with the water and forms gel solid and gel water. Gel solid is cement, which has reacted with water to form hydration products, primarily calcium silicate hydrates, C-S-H, and calciumhydroxide, C-H. As the figure displays, also gel water is now present in the system. This is water, which is no longer available for hydration since it is bound so tight

to the hydration products that it cannot react with the cement. It is also seen that pores are formed. These represent the chemical shrinkage, which is a result of the fact that the hydration products have a lower volume than the reactants have. Hydration ceases when all the capillary water has been consumed, which is seen to occur in the low water-cement ratio paste. The systems shown in the figure are sealed, i.e. no external water is allowed access. If external water was present, the pores would have been water filled and the hydration of the low water-cement ratio paste could have continued a little further.

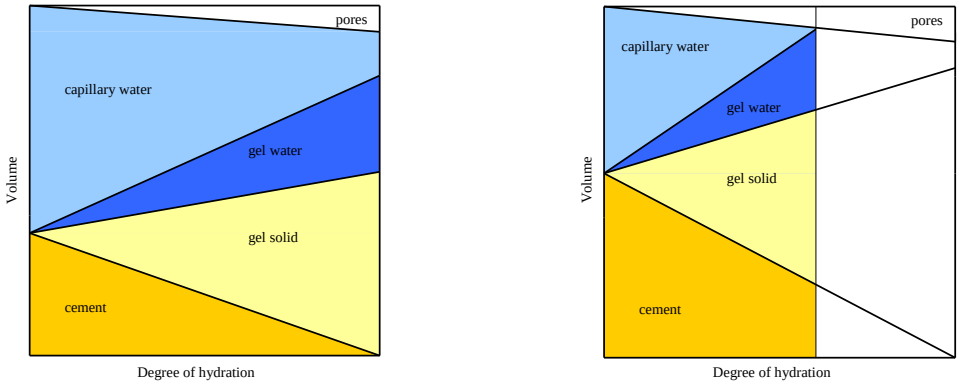

Figure 1.3 *Volumetric phase composition of cement paste as function of the degree of hydration with w/c=0.60 (a) and w/c=0.30 (b). Closed system. After (Jensen et al. 2001)*

The chemical shrinkage will result in not only the formation of pores, but will also cause external shrinkage, which is not shown in Figure 1.3 . This shrinkage is termed the autogenous shrinkage since it occurs without exchange of any matter with the surroundings, see e.g. (Davis 1940, Jensen & Hansen 2001*a*, Baroghel-Bouny & Aïtcin 2000). The relation between the chemical and the autogenous shrinkage is illustrated in Figure 1.4, see also Tazawa, Sato, Sakai & Miyazawa (2000). At first, before initial set of the concrete or paste under consideration has occurred, the autogenous shrinkage will equal the chemical shrinkage. Then, from initial set and onwards, a self supporting skeleton is formed by the hydration products and this structure restrains the material from having an outer shrinkage equalling the chemical shrinkage. Instead, voids will form as shown in the figure. The continued increase in autogenous shrinkage after the formation of a solid skeleton is caused by a number of reasons. The primary governing mechanism seems to be the self desiccation shrinkage, which is a result of the formation of partially saturated pores, which are formed as the water is consumed for hydration. The menisci formed in these pores will result in the development of capillary stresses leading to an outer shrinkage, (Bentur 2000, Jensen & Hansen 1996).

The picture is complicated by the fact that autogenous shrinkage is coupled with changes in the temperature. This was demonstrated in Jensen & Hansen (1999) and was explained

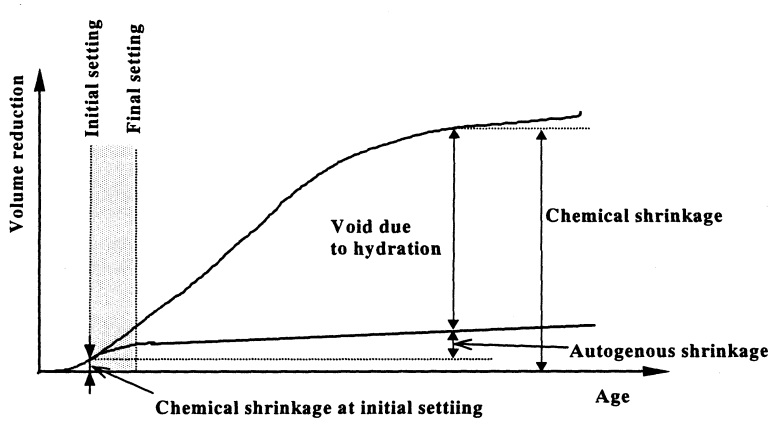

Figure 1.4 *Relation between chemical and autogenous shrinkage. (Tazawa et al. 2000)*

by changes in the surface tension. Other authors considered the redistribution of water within the hydrated material as a governing mechanism, (Bjøntegaard & Sellevold 1998).

Besides autogenous shrinkage also plastic shrinkage, see e.g. Neville & Brooks (1990), and drying shrinkage, see e.g. Altoubat (2000) may cause volumetric changes in early age concrete.

The evolution of properties in early age concrete is governed by the changes in the composition of the cement paste of the concrete. It is therefore interesting to focus on this phase of the concrete. This is often done by researchers and this fact is also reflected in the selection of references given in this section. However, concrete and pastes do of course behave differently. These differences are mostly expressed by the dilution of the paste in the concrete among sand and stones. Thus, e.g. the temperature evolution and the evolution of the autogenous dilation are dependent on the volume fraction of paste in the concrete. This is reflected in some of the papers published in the proceedings mentioned in the beginning of this chapter.

1.2 Cracking of Early Age Concrete

As shown in Chapter 1.1 sealed concrete exhibits dilation due to heat of hydration and autogenous shrinkage. It is clear that these volumetric expansions and contractions by themselves will not result in cracking. In order to build up stresses in the volume, some sort of restraint must be present. This criterium will in reality always be fulfilled to some extent, either externally or internally.

External restraints include structural restraints, e.g. when the volume is not free to dilate due to contact with a subbase or a previously cast structure or when the concrete is cast around rigid corners or around rigid inserts.

Internal restraints are caused by gradients in the dilation of the material or by rigid parts of the material itself, e.g. shrinkage cracking around aggregates. The latter mechanism was explored in Dela (2000), where also a device suited for measuring the shrinkage stress around aggregates was developed.

External restraints are often simulated using a cracking frame in which either the length of the specimen or the stress in the specimen is kept constant, see e.g. (Brameshuber & Hilsdorf 1987, Brameshuber 1988, Kovler 1994, Altoubat 2000) and a number of examples in Springenschmid (1994). A variation is the cracking frame where the temperature is controlled such that either isothermal conditions or certain temperature histories may be simulated, see e.g. Springenschmid (1994). An example of the cracking frame is shown in Figure 1.5. In this setup two specimens are tested. The left one in Figure 1.5a is free and may expand or shrink as a function of the thermal and autogenous dilations plus any extra dilations caused by exchange of matter with the surroundings. This specimen is a reference on which the free length change is measured. The right specimen is loaded with either a constant load, $P(t) = P_0$ or a time-dependent load, which suppresses the length change of this specimen, $P(t) = P(\varepsilon_s(t), \varepsilon_T(t))$ such that $\Delta L(t) \equiv 0$. The latter situation simulates a fully restrained situation and makes it possible to measure the self stresses, which are building up under such conditions - including the early age creep effects, which work as significant relaxation mechanisms.

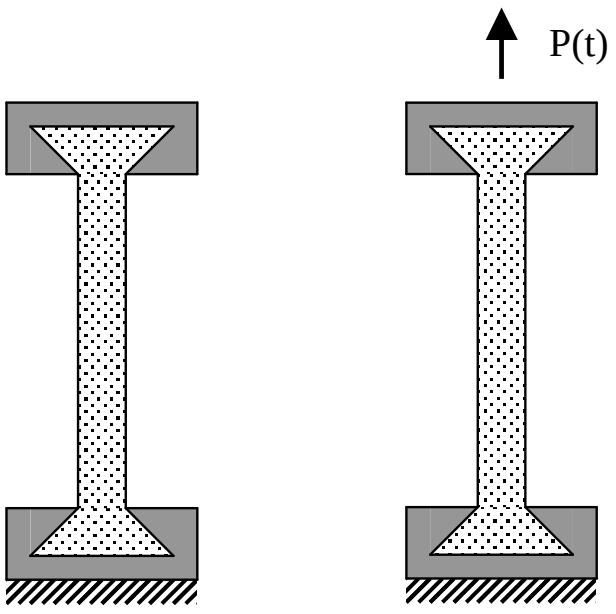

Figure 1.5 *Principle of the cracking frame, free specimen (a) and loaded specimen (b). After (Altoubat 2000)*

A setup similar to the one shown in Figure 1.5 was used by Brameshuber (1988) and a sample result is shown in Figure 1.6. In this particular experiment, the temperature was measured along with the force necessary to restrain the specimen. Due to the hydration a temperature rise is observed in the first 15 hours. Then, as the rate of heat evolution decreases, the specimen starts to cool off and ambient temperature, 20 ℃, is reached at 100 hours. As the lower part of the figure shows, initially this temperature rise results in compressive stresses in the specimen, peaking at 10 hours. Then, due to the early age relaxation of the stress and the decrease in rate of heat evolution, the compressive stress decrease and eventually, at 12 hours, the specimen experiences tensile stress. Now, the specimen contracts due to cooling and autogenous shrinkage, and these effects results in tensile stress. Also the tensile strength evolution is displayed on the lower part of the figure and, at approximately 70 hours, the tensile stress surpasses the tensile strength and cracking occurs.

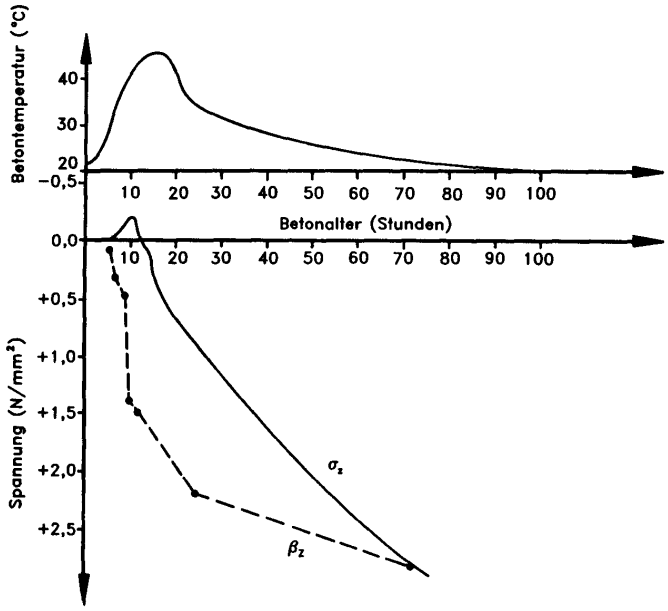

Figure 1.6 *Self stressing of a fully restrained specimen in a cracking frame. After (Brameshuber 1988)*

The problem illustrated with this example is often experienced in practice. Full or partial restraining of the early age dilations occur in numerous situations and they do result in cracking. A standard practical example is cracking of pavements since here not only a restrained situation is present due to the friction with the subbase, but also, often, large areas are cast in one operation.

The restraint could also be internal of nature caused by e.g. gradients in the concrete temperature, see (Hansen & Pedersen 1982, Neville & Brooks 1990). Temperature gradients will occur when heat is dissipated from the surface of the concrete volume. In the initial heating phase tensile stress may therefore occur at the surface and result in thermal cracks. Later, in the cooling phase, where the surface regions of the concrete has reached

ambient temperature, these regions will restrain the thermal contraction of the central parts and result in tensile stress here and possibly tensile cracking.

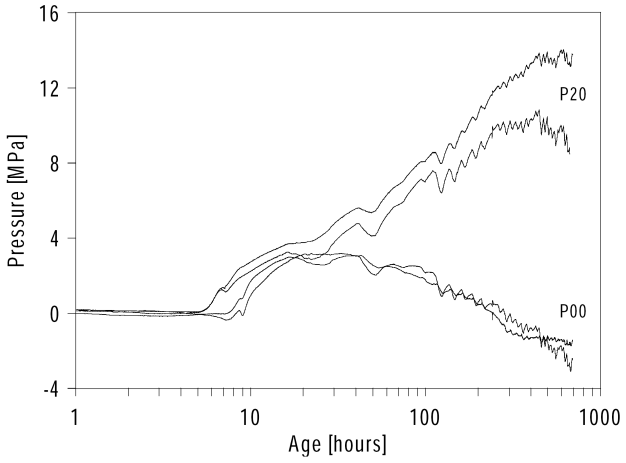

Figure 1.7 *Hydrostatic pressure exerted on stress sensor with time for two different cement pastes (P00 is without SF and P20 is with 20% SF.) After (Dela 2000)*

As mentioned, self stresses in the concrete will also occur due to the shrinkage of the cement paste. This was investigated in e.g. Stang (1996) where the shrinkage-induced clamping pressure on an inhomogeneity (in this case a thermometer) was measured experimentally. It is clear from these experiments that the clamping pressure is significant and strongly dependent of the amount of microsilica added to the paste. Shrinkage cracking around aggregates was investigated in Dela (2000) employing a stress sensor, which was developed for the purpose. Figure 1.7 shows the stresses, which are built up around the aggregate with time for two different cement pastes. It is seen that the hydrostatic pressure in the case of 20 % SF reaches high values and it was demonstrated that shrinkage-induced cracking around cylindrical aggregates did occur in the case of 20 % SF.

1.3 Coping with Early Age Cracking

So far, Chapter 1.1 and 1.2 have clarified that volumetric dilations occur in early age concrete and that cracking may occur if these deformations are restrained - which often is the case in practice. It is therefore not always possible or preferable to avoid early age cracking. Maintaining this ambition is merely a resemblance of the fact that knowledge concerning the cracked situation is lacking. If the cracked situation is well understood and can be modelled then cracking can be allowed. This can be acceptable if the crack widths are kept below certain values. It will certainly in many situations be economically desirable.

To model early age cracking in a methodic and knowledge based way detailed knowledge of the development of all the important material properties, and preferably their interactions, must be obtained. Important properties encompasses as a minimum the tensile

strength, modulus of elasticity, thermal dilation coefficient, Poisson's ratio, creep and relaxation properties and the development of these properties with time. However, also the fracture properties are of outmost importance in order to understand not only the crack initiation but also the crack propagation.

These properties may, once they are known, form the basis of detailed modelling from which a prediction of the possible cracks and their widths may be given. And based on such a model, the choice of material and structural design may be altered in a way such that the cracking is controlled.

Traditionally, the risk of cracking in early age concrete has been evaluated based on temperature criteria, see e.g. (Hansen & Pedersen 1982, Danish Standard, DS 411 1982). In its most simple form, a temperature criterion may be applied by limiting the maximum temperature in the concrete volume and the difference between parts of the concrete structure. This is done by requiring a maximum difference in temperature in the volume cast, and by requiring a maximum temperature gap between any existing structure or subbase and the concrete, which is being cast, see e.g. Hansen & Pedersen (1982). This simple temperature criterion is based on empiric experience from which it has been found that concrete can withstand the thermal dilations caused by a temperature difference of 15 ℃ - 20 ℃, (Hansen & Pedersen 1982). However, this method has clear limitations and may not be a safe criterion if applied to unusual situations, see e.g. Springenschmid (1994). First of all, the method does not regard the evolution of properties or the temperature history. Neither is the influence of any external restraint regarded - which, as seen in the previous section, may also cause thermal cracking. Depending on the temperature history, a temperature difference may be more or less detrimental. This was discussed in Mangold & Springenschmid (1995) who demonstrated that the internal restraint stresses depend on the temperature history and that they are not necessarily zero when the temperature gradient vanishes. In fact, only a certain temperature gradient, dependent on the temperature history, will produce zero stresses in the structure. In Eberhardt, Lokhorst & van Breugel (1995) it was found that if no external restraint is present, the simple temperature-differential method will be efficient, but also that any external restraint may cause thermal cracking for temperature differentials lower than 15 ℃. The method may also for massive structures yield unreliable results, see Emborg & Bernander (1995).

Furthermore, the differential temperature based criterion will not suffice for modern concrete mix designs, which show significant autogenous shrinkage, a dilation from which cracking may also occur if restrained, as demonstrated in the former section. Thus, autogenous dilation must also be modelled, (van Breugel 2000). Isothermal experiments on fully restrained reinforced concrete in early age was conducted by Sule & van Breugel (2001) and significant tensile stressed were observed during the testing period (144 hours). Although no cracking was observed during the experiments it was concluded that cracking was likely to occur at a later age since the rate of tensile stress increase was higher than the rate of tensile strength evolution.

The only way to cope with cracking occurring due to autogenous shrinkage is technologically to reduce the magnitude of these dilations. This was the subject of the work by Seigneur, Bonneau & Aïtcin (2000) who found that the use of shrinkage reducing admixtures (SRA) is a very efficient to reduce autogenous as well as drying shrinkage. This was also concluded by Holt & Leivo (2000). Another technique is being developed by Jensen & Hansen (2001*b*). Here, water filled super-absorbent polymers (SAP) are entrained in the cement paste and represent a water-supply, which suppresses the self-desiccation of the paste, thereby preventing the self-desiccation shrinkage and thus reducing the autogenous shrinkage. Also water filled lightweight aggregates have been employed for the same purpose, (Bentz & Snyder 1999).

However, it will never be possible to eliminate shrinkage due to autogenous dilation. Furthermore, it is important to view not only at the final magnitude of autogenous dilation, but also at the development since the history of dilation is very important for whether or not cracking will occur. Therefore, despite the technological measures, which may be taken in order to reduce the early age autogenous dilation, models must be able to include also the autogenous dilation evolution, (van Breugel 2000).

These considerations lead inevitably to the use of the finite element method if just slightly complicated problems are to be modelled. Modern finite element codes like e.g. DIANA, (DIANA 2000) are able to describe the evolution of properties in terms of strength, stiffness, creep/relaxation etc. and are also able to include the dilations due to heat of hydration and autogenous shrinkage. However, often the programs do not include the couplings between the different effects, see e.g. the review in Hauggaard-Nielsen (1997). One example is the lack of inclusion of the transitional thermal creep, an effect, which was modelled and seen to be significant in Hauggaard-Nielsen (1997).

The preceding sections give a sense of the mechanisms driving early age cracking and an idea of what methods, which must be considered in order to arrive at a prediction of the risk of early age cracking and how to control the crack widths. But none of the considerations have addressed what happens *if* cracking occurs. The goal of the analysis has been to predict the stress evolution and to see whether or not the tensile strength has been reached at any point of time during the hydration. A simple question is therefore: What happens beyond cracking? This is illustrated in Figure 1.8. This figure basically illustrates the same mechanism as shown in Figure 1.6. A fully restrained sample is allowed to hydrate, which results in a temperature rise followed by a cooling phase. Meanwhile, the properties develop and at a point of time, t_2, cracking occurs due to the stress buildup caused by the thermal contraction. Usually, this would pose the end of analysis. However, it is very interesting not only to understand the crack initiation situation, but also the crack propagation, as illustrated by the dotted line on the figure. How does the crack evolve - does it open up to unacceptable values or, does it close again after having experienced openings below any critical value with respect to durability, corrosion etc. And what is the influence of the fracture mechanical properties? This is an issue not well investigated and it is one of the central subjects for this thesis. Finite element codes like e.g. DIANA are able to, at least in a smeared crack implementation, include evolution of

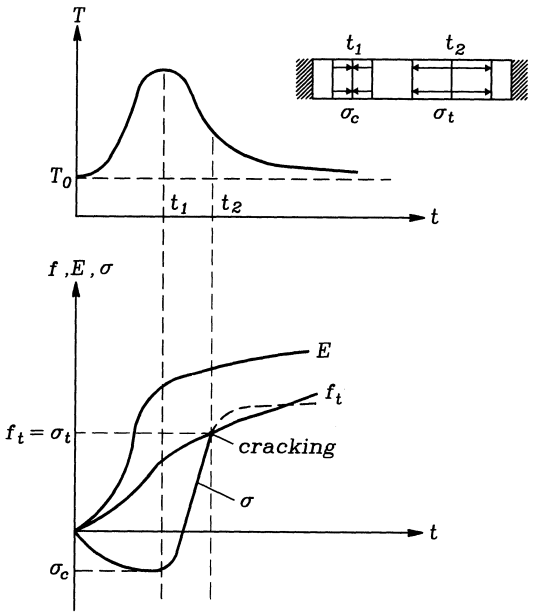

Figure 1.8 *What happens beyond cracking? After (Hauggaard-Nielsen 1997)*

many mechanical properties as a function of maturity, but the fracture mechanical properties may only be kept constant, and furthermore not very many experimental studies have been carried out in order to establish knowledge about this property in early age.

Furthermore, knowledge concerning the development of the properties of the bulk concrete is essential, but not enough. Also the development of the bond properties between reinforcement and concrete in early age is of keen importance. This arises from the fact that almost all concrete structures are reinforced. It is therefore important to obtain knowledge about at which point of time significant bond properties have developed. This important point of time marks the transition from unreinforced behavior to reinforced behavior for the concrete structure. Also the development of the properties with time is very important since it gives information about how a crack will evolve in the structure.

1.4 Identification of Important Problems

The previous sections lead to the central problems identified in this introduction and treated in this thesis:

1. Determination of the fracture mechanical properties for concrete in early age.

   Which experimental setup should be applied ?

   Which method of analysis will give useful results ?

2. Evolution of the fracture mechanical properties for concrete in early age.

3. Influence of rate-effects or viscoelasticity on the fracture mechanical properties.

4. Determination of the concrete-reinforcement bond properties in early age.

1.5 Aim of This Study

Section 1.3 leads to the main objectives of the present thesis. These include the mathematical modelling and experimental analysis of early age concrete with emphasis on the fracture mechanical properties.

The thesis will present a proposal for constitutive modelling of the fracture properties of early-age concrete. A review of fracture mechanical models for concrete will be conducted and an implementation will be preferred based on this discussion. This will include also consideration of the effects of long term loading on fracture properties.

Test methods suited for determination of the constitutive parameters in the chosen mathematical framework will be reviewed and analyzed. These include the uniaxial tension test, the three-point bending test, the Brazilian split cylinder and the wedge splitting test. The applicability of the different test methods will be discussed in terms of sensitivity to the minute properties of concrete in early age, maturity and maturity gradient problems, self-weight problems etc. A choice of most promising test method will be made while the other test methods will form a basis of mathematical and experimental comparison with the preferred method.

Besides the proposal of test methods for short-term determination of early-age properties, also a test method for determination of long-term effects on the fracture mechanical properties will be developed and described.

An experimental setup for determination of bond properties between concrete and reinforcement in early age will be developed and discussed. This setup will be designed to fit early age concrete and with the purpose of measuring the small values of slip, which are expected to occur in early age concrete due to the nature of the loading, see e.g. Sections 1.1-1.3.

For the preferred test methods an inverse analysis scheme will be developed. This scheme will be based on analytical methods in order to yield a short calculation time, while finite element calculations will form a basis for comparison and calibration.

Based on the preferred test methods and the methods for interpretation of the test results, experimental results will be analyzed and presented. These experiments will give a good sense of the development of fracture mechanical properties in early age using the applied constitutive modelling.

1.6 Organization of This Thesis

The thesis starts with a motivation for the work. Usually, engineers are able to conduct detailed analysis up to the point of crack initiation, then the investigations are stopped. This thesis aims at enlarging the knowledge of the fundamental properties which are needed if the analysis should be allowed to proceed beyond cracking.

The knowledge concerning the early development of the properties of concrete is summarized. This summary comprises the development of all important properties including thermal properties, autogenous dilations, mechanical properties and fracture mechanical properties. This part is important since early age concrete is a vast subject for which a solid connection with earlier work is imperative.

The next chapter introduces the reader to the fictitious crack model and the motivation of its use. Then a short introduction to viscoelasticity is carried out.

Chapter 5 goes through a detailed analysis of all usual mode I fracture mechanical testing methods for concrete. The importance of well defined crack boundary conditions for the uniaxial tension test is demonstrated. It is shown that the split cylinder test, often applied for the determination of tensile strength, may yield misleading results if applied to early age concrete. The three point bending test is demonstrated to yield a global load-deflection and load-CMOD curve, which is uniquely correlated with the fracture mechanical properties. However, the method is more cumbersome to use for early age concrete than the wedge splitting test. This test method is also demonstrated to be suited for an inverse analysis and it is furthermore ideal for early age concrete since the problems with self weight are small and the specimen dimensions such that only insignificant temperature gradients build up during hardening.

Chapter 6 summarizes the experimental results. First a specimen geometry comparative study is conducted. This study shows that the different test methods (uniaxial tension test, wedge splitting test and three point bending test) essentially lead to the same fracture mechanical properties. This is an important result, which means that it may not always be necessary to conduct the troublesome uniaxial tension test in order to arrive at a determination of the fracture mechanical properties. Then, the wedge splitting test is used to determine the development of the fracture mechanical properties and suitable functions able to fit the development are proposed. Finally, the viscoelastic properties for both the bulk concrete and for the crack are investigated. The viscoelasticity of the bulk concrete is determined, while it is not possible to observe a significant time-dependent deformation in the crack.

The next chapter deals with bond of reinforcement in concrete in early ages. First the known literature regarding this subject is summarized whereafter a model for the bond properties is derived. The validity of the model is investigated using the finite element method. Then, an inverse analysis method is proposed and finally, an experimental setup is developed and some preliminary results from this setup reported.

1.7 Major Achievements

This work has resulted in new insight into the behavior of early-age concrete and how to determine the fracture mechanical parameters of concrete.

The uniaxial tension test has been examined with regard to how to select the boundary conditions of the test. It has conclusively been demonstrated that the test method must be conducted such that the rotations of the crack boundary planes are sufficiently prevented.

The wedge splitting test has been studied and it has been revealed that the test method is very well suited for early-age testing of concrete. The test produces load-crack mouth opening displacement curves, which are uniquely correlated with the underlying fracture mechanical properties.

A new method for inverse analysis has proven to be able to yield the underlying fracture mechanical properties. This is demonstrated by comparison with the finite element method and by experiments, see below.

The three-point bending test has been studied for the purpose of comparison with the wedge splitting test. This comparison has also comprised the uniaxial tension test. The results of the comparisons are clearly that unique fracture mechanical properties may be derived for any concrete under consideration regardless of the testing method applied. Note that differences are present, but the overall values are unchanged.

The wedge splitting test has been applied for the determination of the development of the fracture mechanical properties for early age concrete. The results are the first of their kind and they form the basis for modelling of the cracked stages of concrete in early age.

The influence of the loading rate on the fracture mechanical properties in early age concrete has been investigated. It is hypothesized that the effect is unimportant, or at least outside what is measurable with the setup employed.

The split cylinder test has been investigated for early age concrete. It is concluded that the test is a poor choice at very early ages since the prediction of the tensile strength is wrong by a factor 2 or more. The test will only work after 24 hours for normal hardening cement and 48 hours for slow hardening cement.

Chapter 2

Development of Properties in Early Age Concrete

This chapter aims at giving an overview of the body of knowledge in terms of development of material properties for concrete in early age. This walk-through of the different material properties will later be applied for comparison with experimental values and as estimates in the finite element analysis, when necessary, for properties, which have not been determined separately in this project.

A very important reference in this context is the work carried out by Byfors (1980), in which the development of almost all properties of concrete has been reviewed in literature and where independent experiments of these properties have been carried out.

2.1 Properties Related to Thermal Dilations

The properties governing the thermal dilations are the heat of hydration, the specific heat capacity, the thermal conductivity and the thermal dilation coefficient.

2.1.1 Heat of Hydration

The hydration of Portland cement is often measured utilizing conduction calorimetry, (Double, Hellawell & Perry 1978). In principle, the method involves the measurement, as a function of time, of the rate of heat evolution from a cement paste sample maintained under near-isothermal conditions. This type of calorimetry will yield quantitative rate of heat evolution profiles for the cement paste under investigation as shown in Figure 2.1. In principle, the curve illustrates five stages of hydration. The first, sharp and highly exothermic peak shown in the figure is primarily due to the immediate hydration of free lime and the dissolution of other alkalis in the cement. This peak is usually one magnitude higher than the second peak shown on the border between stage III and IV, see e.g. Double et al. (1978). This stage is followed by the induction period, stage II. In this stage little heat is dissipated, which is thought to be brought about by need to achieve a certain concentration of ions in solution before crystal nuclei may form from

which hydration products may grow. This is known as nucleation control, see e.g. Young (1997). After achievement of a critical concentration in the pore solution of ions, the rate of hydration of the cement again increases in stage III since now the rate of hydration is controlled by the rate of reaction. As hydration continues, the thickness of the layer of hydration products formed on the surface of the cement grains eventually slows down the reaction rate since water must diffuse through this layer to reach the unhydrated cement and through which the ions must diffuse to reach the growing crystals. Thus, the rate of reaction becomes diffusion controlled (stage IV and V).

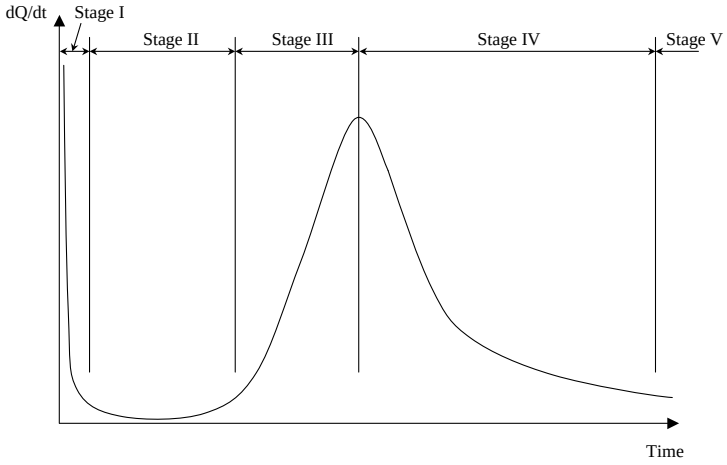

Figure 2.1 *Typical rate of heat evolution diagram for ordinary Portland cement paste. After (Young 1997)*

Thus, a number of mechanisms are involved in the shape of the curve shown in Figure 2.1. The rate of heat evolution curve has been modelled by a number of functionals in literature. One of the first and simplest approaches was proposed by Avrami (1939):

$$V = 1 - e^{-(t/\tau)^n} \tag{2.1}$$

This equation in general relates to may phase transformations that occur by a process of nucleation and growth of transformed products. The term V is the volume fraction transformed at the time t, τ is a factor including growth rate and nucleation terms while the value of the dimensionless factor n is related to geometry of the problem and the particular growth rate and nucleation laws involved, see (Avrami 1939, Double et al. 1978). The derivative, dV/dt, of this function, scaled with a thermal conversion constant, may be plotted in the rate of heat evolution diagram, Figure 2.1, with a good correlation. It turns out that relations of this type in general may be used to describe not only the rate of heat evolution, but also the development of the strength and stiffness of concrete. A variation of Equation 2.1 is:

$$V = e^{-(\tau/t)^n} \tag{2.2}$$

which produces results similar to Equation 2.1. This version is also often associated with the growth mechanisms occurring in cementitious systems.

Another concept for determining the heat of hydration is to measure the temperature rise of a hydrating sample under adiabatic conditions. This was illustrated in Figure 1.2. This experiment measures the total heat release, Q as a function of time, and the output may be modelled using Equation 2.1. This curve represents basically an integration of the curve in Figure 2.1 and vice versa, differentiating the former will yield the latter curve. However, the latter curve is not produced under isothermal conditions and the comparison is only valid if a proper maturity concept is introduced, i.e. the dependency of rate of reaction on temperature is considered.

2.1.2 Specific Heat Capacity

The value of the specific heat capacity, c, as a function of the age of the concrete was first investigated by Löfkvist (1946). Experiments were conducted on different types of cement, aggregates and curing conditions for early age concrete. Based on the experimental results it was concluded that no significant change of the heat capacity occurs during hardening.

On contrary, a change with maturity was found by Hansen, Hansen, Kjær & Pedersen (1982). The experiments were carried out on cement pastes employing rapid hardening cement from a maturity age of 4 hours to 160 hours. As stated in Hauggaard-Nielsen (1997), these results may be utilized on concrete if the aggregates have a constant water content since in this situation their heat capacity will remain constant. The heat capacity of the concrete may then be calculated based on a composite formula, (Høyer 1990). The heat capacity depends on the water content in the pores, and Hansen et al. (1982) found that it decreases with maturity, and determined the change to range from approximately 1.92 kJ/kg℃ at 1.5 hours to 1.65 kJ/kg℃ at 120 hours. One reason is that water has a higher heat capacity than the hydration products, thus resulting in a decrease when the water is consumed in the hydration reactions.

A literature study carried out by Høyer (1990) concluded on the background of Löfkvist (1946) that the heat capacity may be kept constant, and unchanged, for early age and hardened concrete. This was also concluded by Byfors (1980). A value of approximately 1.0-1.1 kJ/kg℃ was stated by the authors. However, in another study by Schutter & Taerwe (1995), the heat capacity was found to decrease with the degree of hydration. This paper focused on the evolution of the thermal characteristics of early-age concrete as a function of the state of the hardening process. The specific heat was determined for hardening cement paste samples made with blast furnace slag cement. It was concluded that the specific heat decreases linearly with the degree of hydration.

The specific heat capacity does also depend on the mix composition, temperature and the moisture content. The dependency on temperature was investigated by Espinosa-Paredes, Garca, Santoyo, Contreras & Morales (2002) in the temperature range from 28 ℃ - 200

℃. They found that the specific heat capacity increases with temperature. However, the capacity decreases with decreasing moisture content, quite clearly caused by the decrease of water in the system, (Byfors 1980). Finally, it has been found by Fu & Chung (1997) that the addition of silica fume may increase the specific heat capacity of cement paste.

2.1.3 Thermal Conductivity

The conductivity plays an important role for the temperature gradients in early age concrete, and the subject achieves increasing attention in the research community. The topic was investigated by Löfkvist (1946) who stated that there are not significant differences between the conductivity of early age concrete compared with matured concrete. This was also the conclusion in Høyer (1990) who states that a value of 8.0 W/m℃ may be applied. Also Byfors (1980) stated that the conductivity may be kept constant, and listed a value of 2.4 W/m℃.

However, in the work by Gibbon & Ballim (1998) a dependency of the maturity of the concrete was found, showing that the conductivity decreases with age. Measurements were taken from onset of hydration and continued in the first week, and the decrease was in the order of 10-40%. It was also shown that the conductivity is dependent on type of aggregates and type of cement. A formula for determination of the conductivity of concrete based on knowledge of the conductivity of the mortar in the concrete and the conductivity of the aggregates was presented.

Dependency of conductivity on moisture content and temperature was demonstrated in Bouguerra (1999). It was found that the conductivity increases with moisture content and decreases with temperature. This result is, with regard to the dependency of moisture, confirmed by Khan (2002). Finally, Fu & Chung (1997) found that silica fume may effectively decrease the conductivity.

2.1.4 Thermal Dilation Coefficient

The thermal dilation coefficient is known to be dependent on many different parameters, i.e. type of cement, cement content, aggregates, water-cement ratio, age, temperature and relative humidity, (Høyer 1990, Neville & Brooks 1990). In fact, the thermal dilation coefficient has two components, namely the true thermal dilation coefficient, where the dilation is caused by the molecular movements, and the hygrothermal expansion coefficient. The latter arises from the increased water vapor pressure in the pores with increased temperature of the paste. This increase results in an expansion of the paste. The latter term makes the thermal dilation coefficient dependent of the humidity with a maximum at intermediate values, see Neville & Brooks (1990), since no increase in the water vapor pressure is possible for a totally dry paste, or a fully saturated paste.

For concrete in early age, Löfkvist (1946) found that the dilation coefficient is lower in the cooling phase than in the heating phase of the hydration. The values determined ranged

from approximately 12 10^{-6}/°C in the heating phase to 6 10^{-6}/°C in the cooling phase. A decrease was also found by Alexanderson (1972) who determined values ranging from 70 10^{-6}/°C at 4 hours to 12 10^{-6}/°C at 120 hours. The results are reprinted in Figure 2.2.

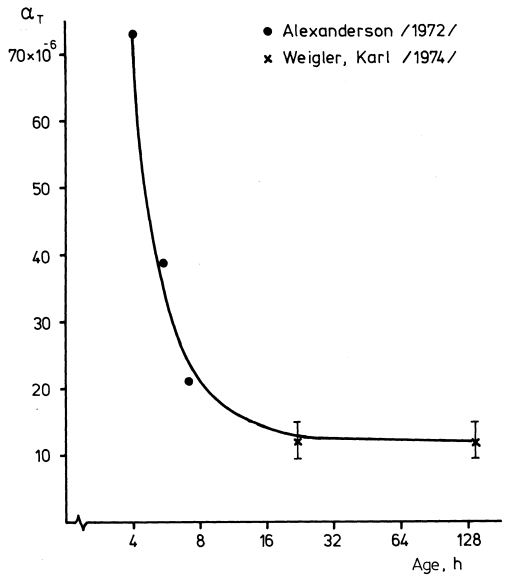

Figure 2.2

The thermal dilation coefficient was determined experimentally for early age concrete by Emborg (1989). It was concluded that the coefficient was slightly higher in the heating phase compared with the cooling phase, i.e. the result, which was found by Löfkvist (1946). Later works include (Laplante & Boulay 1994), who also found that a hysteretic effect exists between the heating branch and the cooling branch of the temperature dependency of the thermal expansion coefficient. The results shown in Figure 2.2 were also verified with an initial value of 22 10^{-6}/°C at 9 hours decreasing to 12 10^{-6}/°C at 16 hours whereafter the coefficient was found to be constant. In the work by Khan, Cook & Denis (1998) experiments were conducted from an age of 16 hours. They did not find a dependency of the coefficient of thermal expansion on age, which is in agreement with the findings by Laplante & Boulay (1994). However, in (Bjøntegaard & Sellevold 2001) a minimum of the coefficient was reported at 12 hours, whereafter it started to increase again. Finally, the work of Kada, Lachemi, Petrov, Bonneau & Aïtchin (2002) does also indicate that the coefficient of thermal expansion decreases from with age. Here an investigation of the water-cement ratio has been carried out. It is found that for a water-cement ratio of 0.45, the initial value of the coefficient is 25 10^{-6}/°C at 8 hours while it decreases and becomes constant at a value of 8 10^{-6}/°C at 14 hours. Approximately the same result is found for a concrete with a water-cement ratio of 0.35. However, for a water-cement ratio of 0.30 there is a minimum of the coefficient at 14 hours with a value of 3 10^{-6}/°C whereafter it increases to 8 10^{-6}/°C, which is the constant value. The initial value at 8 hours for this mix was 12 10^{-6}/°C.

The dependency of the thermal dilation on temperature was determined in (Vodák, Černý, Drchalová, Š Hošková, Kapičková, Michalko, Semerák & Toman 1997). The conclusion was that there is a linear variation of the coefficient with temperature for mature concrete. The temperatures in which the measurements were taken ranged from 20 ℃ to 200 ℃.

2.2 Properties Related to Non-Thermal Dilations

Volumetric dilations due to shrinkage have several origins. The fresh concrete may experience plastic shrinkage caused by premature drying in combination with a low rate of bleeding. The cracking pattern will resemble the well known patterns seen in soil exposed to drying. The plastic shrinkage takes place in the first 30 min. to 6 hours after casting, (Neville & Brooks 1990), and may be fully avoided if the initial curing conditions are improved.

After the concrete has set, shrinkage contraction due to drying may still occur. It can be significant and cause cracking if restrained as explained in Chapter 1. This long term drying shrinkage may cause volumetric changes in the concrete for many years after casting due to the low water vapor diffusivity of concrete resulting in a prolonged period of time before equilibrium has been reached. However, by choosing proper curing conditions this contribution to the early age shrinkage of concrete may be eliminated. In fact, concrete should not be exposed to loss of water due to drying in early age.

The final cause for early age dilations is due to the autogenous deformation. This dilation is a result of the chemical shrinkage due to the hydration, and is, after set, further increased by the formation of partially saturated pores in which the thereby built-up capillary stresses deforms the skeleton and result in an outer shrinkage.

2.2.1 Autogenous Dilation

The magnitude of autogenous deformation for concrete is dependent on, among other parameters, the water-cement ratio. For high water-cement ratio concretes no self-desiccation will take place, and thus, since this is the major governing mechanism, the autogenous deformation will remain insignificant. However, when the water-cement ratio is below 0.40-0.45, (Jensen & Hansen 2001*a*), self desiccation will start to be appreciable and the magnitude will increase with decreasing water-cement ratio. For low water-cement ratio cement pastes the magnitude may amount more than 1000 μ-strain after a few weeks of hardening, (Jensen & Hansen 2001*a*).

Quantitative measurements of the autogenous deformation on cement paste as a function of time from the addition of water may readily be obtained by use of the dilatometer developed by Jensen & Hansen (1995). For concrete, other methods apply, see e.g. Altoubat (2000), but it is difficult to make measurements as early as in the dilatometer.

Also the content of silica fume has a significant influence on the magnitude of autogenous deformation in early age. Figure 2.3 shows the autogenous shrinkage for cement pastes with varying silica fume content. It is seen how the magnitude of deformation at 330 hours is doubled when the content of SF is increased from 3 % to 10 %.

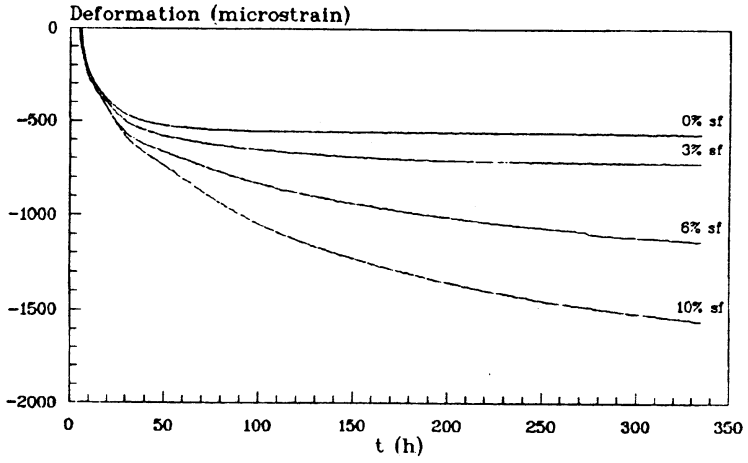

Figure 2.3 *Autogenous deformation after setting of cement pastes with w/c=0.35; time measured from water addition; deformation fixed to 0 at time of setting; temperature 30* ℃*. (Jensen & Hansen 1996)*

The autogenous deformation is a product of the self-desiccation of the paste. The relation between the relative humidity of a paste with water-cement ratio of 0.25 and the autogenous deformation was studied by Jensen & Hansen (1996). The results show that a depression of the RH is followed by autogenous shrinkage. If the RH is not depressed, no significant deformation will occur.

The autogenous shrinkage was modelled by Auperin (1989) with the following formulation, see also Høyer (1990):

$$\varepsilon_s = \varepsilon_s(\infty) e^{-(\tau_e/(M+k))^{\alpha}} \tag{2.3}$$

where $\varepsilon_s(\infty)$, τ_e, k and α are material parameters and M is the maturity of the sample. Note the similarity with Equation 2.2, which arises from the fact that the fundamental mechanisms governing the problem are growth-related. Equation 2.3 was fitted in (Auperin 1989) with a good result. A similar formulation using Equation 2.1 was proposed in (Tazawa et al. 2000).

The magnitude of autogenous shrinkage is also dependent on the temperature of the mix. This was investigated by Tazawa et al. (2000) and in general they found that increasing

temperature decreases the autogenous deformation. The dependency on temperature was also investigated by Jensen & Hansen (1999).

2.3 Mechanical Properties

Besides detailed knowledge of the early age volumetric dilations, also the mechanical properties must be determined in order to be able to model the behavior of early age concrete. The compressive and tensile strengths determine whether failure will occur, while modulus of elasticity gives an estimate of the stresses, which are building up as a result of the volumetric dilations and the degree of restraint. Also Poisson's ratio must be known in order to make 2D and 3D generalizations suitable for finite element modelling.

2.3.1 Compressive Strength

The development of the compressive strength is probably one of the most intensively studied parameters of concrete. This is due to the fact that this parameter, along with the modulus of elasticity, is the most important one in structural analysis. Literature surveys of the development of the compressive strength may be found in (Byfors 1980, Høyer 1990), as well as in text books like (Herholdt, Justesen, Nepper-Christensen & Nielsen 1985, Neville & Brooks 1990, Young, Mindess & Darwin 2002).

The development of the compressive strength is dependent mainly of the water-cement ratio, type of cement, additives, puzzolans and curing conditions (temperature and moisture). Figure 2.4 show examples of the development of compressive strength in early age and up to 28 days. Also this development shows the characteristics common to growth problems, and often a formulation like Equation 2.2 is employed for modelling. However, in (Byfors 1980) a different formulation was chosen, which fits the experimental results well, but lacks a background in growth-problems.
A common framework for describing compressive failure of concrete is the theory of plasticity, see Nielsen (1999*b*). The plastic yield surface used is the modified Mohr-Coulomb yield surface. This surface is determined by three parameters, namely the cohesion, the friction angle and the tensile strength. While the development of the tensile strength is investigated in literature, see next section, information of the development of the cohesion and the friction angle is lacking. The compressive strength may be applied in this determination, but then one of the parameters must be fixed or known in advance. However, a single paper has been found, (Baudeau 1995), in which the friction angle for fresh concrete before set is measured. The measuring technique adopted was the triaxial test. The experiments were conducted on concrete with a water-cement ratio of 0.46 and a maximum aggregate size of 15 mm, and it was assumed that the cohesion was zero. It was found that the friction angle was independent of the transverse pressure and equal to 38.6°. This value is almost the same as found for mature concrete, see e.g. Nielsen (1999*b*). Thus, in a preliminary analysis, this value may be kept constant and the cohesion can be determined from the compressive strength.

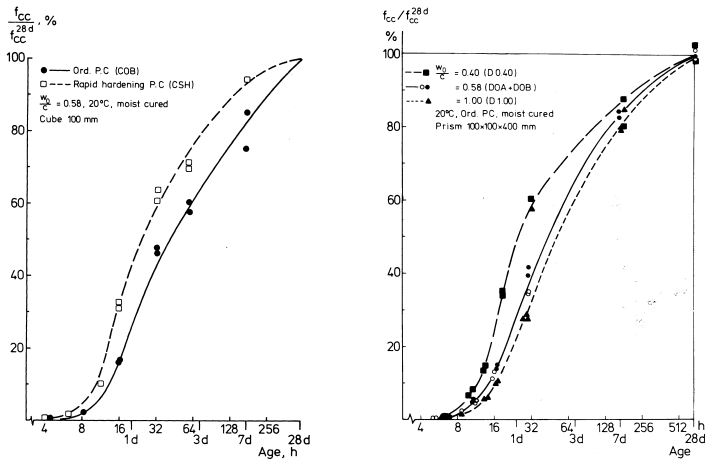

(a) (b)

Figure 2.4 *Relative compressive strength gain in concrete with rapid hardening respectively ordinary Portland cement (a) and relative strength as function of water-cement ratio (b). (Byfors 1980)*

2.3.2 Tensile Strength

The development of the tensile strength of concrete is of outmost importance for the prediction of the crack initiation. The uniaxial tension test, which is believed to give the best estimate of the tensile strength is not widely used due to the difficulties concerning conducting the test. Instead several indirect methods have been developed, e.g. the split tensile test (also known as the Brazilian test) and the three point bending test (which gives the modulus of rupture). However, the interpretation of these indirect test methods often relies on linear elastic formulas combined with correction factors determined empirically. This fact make the use of the methods unreliable if the tensile strength in unusual situations, like e.g. concrete in early age or fiber reinforced concrete, are to be determined. This is due to the fact that the correction factors are compensating for the actual behavior of the concrete, which is not linear elastic and ideal-brittle, but quasi-brittle. And the brittleness of the concrete is significantly changed in early age and for fiber reinforced concrete compared with matured, normal strength and fiber-free concrete.

Experimental results based on the uniaxial tension test are few in the literature. This is caused by the difficulties of conducting the test, due to the problems with self-weight and frictional forces, which become significant in early age. Specimens, which are tested in upright position are influenced by self-weight while specimens that lay down are influenced by friction against the subbase. The latter may, however, be reduced by the use of teflon sheets. Furthermore, the results are often reported as function of the compressive strength or the splitting tensile strength. Although this seems relevant from a practical viewpoint it blurs the development of the uniaxial tensile strength since the behavior of the other test methods change with brittleness and age.

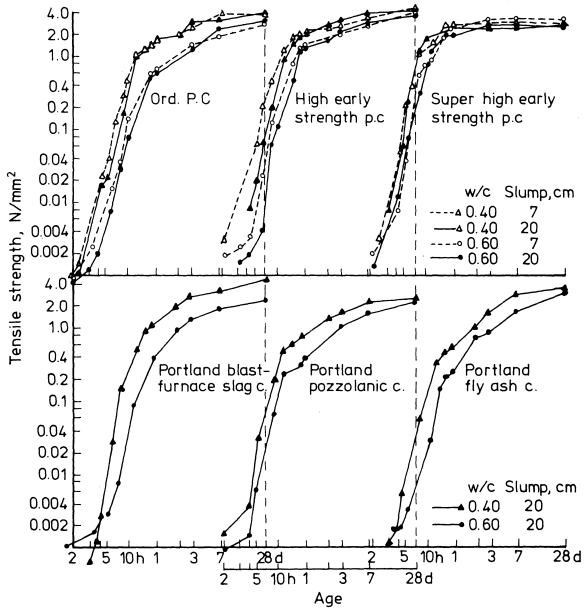

Figure 2.5 *Uniaxial tensile strength gain for varying cement types and water-cement ratios. (Kasai 1971)*

The uniaxial tension test was conducted by Kasai (1971) and the results are reprinted in Figure 2.5. The figure shows the development of the uniaxial tensile strength at early ages starting at 2 hours. The results are very interesting - note especially that the tensile strength is very low in the beginning (2 hours). It is also interesting that the tensile strength increases with a higher rate than the compressive strength at very early age, see (Kasai 1971).

In the work by Byfors (1980) a large number of uniaxial tension tests were conducted on concrete with different water-cement ratios, cement type and curing conditions. The experiments started at 8 hours and progressed for one month. The results were similar to the ones obtained by Kasai (1971).

Besides the direct and indirect methods, also fracture mechanical test methods are increasingly applied to determine the tensile strength. These methods include crack mouth opening displacement (CMOD) controlled uniaxial tension tests, three point bending tests and wedge splitting tests. A fracture mechanical interpretation of the three point bending test in combination with a method for extraction of the tensile strength (inverse analysis) was applied by Wittmann, Roelfstra, Mihashi, Huang & Zhang (1987). Here the experiments were started at an age of 2 days and continued through 28 days. In the experimental time period results showed the same growth-like behavior as seen elsewhere in literature.

2.3.3 Modulus of Elasticity

The short-term stiffness or modulus of elasticity of concrete at early ages is developing in a way similar to the development of compressive and tensile strength. Usually the determination follows one of two different methods. Either a specimen is subjected to uniaxial compression or tension and a extensometer or displacement gage is employed to measure the dilation. Otherwise, non-destructive methods may be applied like measurement of the dynamic modulus of elasticity using ultrasound. The use of non-destructive methods is motivated by the difficulties arising in connection with the application of traditional methods in combination with early age concrete. Conversion of the dynamic result into the static equivalent one is possible, see e.g. (Byfors 1980) or (Nagy 1997).

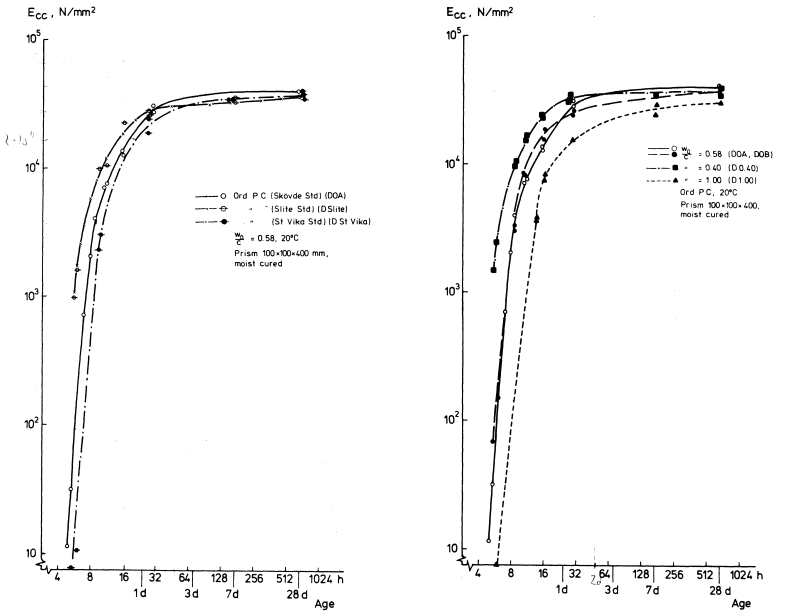

(a) (b)

Figure 2.6 *Development of secant modulus of elasticity of concrete at early ages; different types manufacturers type of ordinary Portland cement (a) and influence of water-cement ratio (b). (Byfors 1980)*

Figure 2.6 shows the results obtained by Byfors (1980). The specimens were moist cured measuring 100x100x400 mm^3. A measuring frame was mounted on the specimen using screws with flat ends in order to facilitate mounting in early age. Two extensometers attached to the measuring frame monitored the dilation. Figure 2.6b shows the influence of water-cement ratio, which, as expected, increases with decreasing w/c-ratio. Furthermore, the growth-nature of the increase in modulus of elasticity is observed. It is interesting that it has been possible to conduct the experiments at an age of only 5 hours where the secant modulus has been as low as 10 N/mm^2.

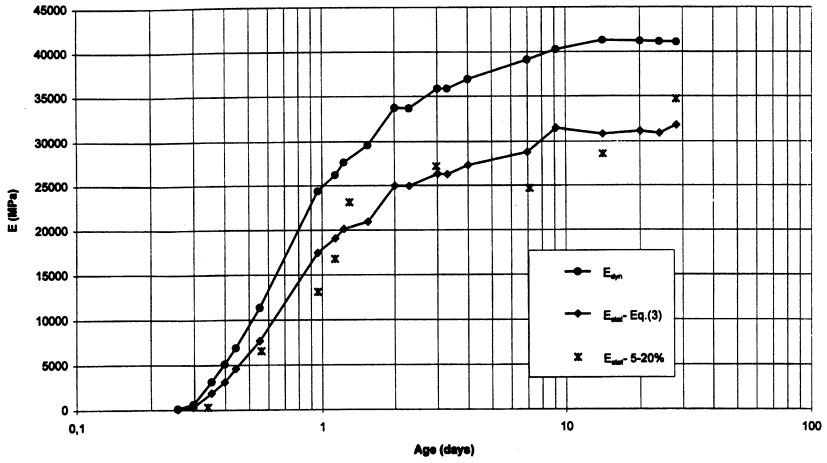

Figure 2.7 *Development of dynamic and static modulus of elasticity with age. w/c=0.54. Ordinary Portland cement, Type II. (Nagy 1997)*

The results shown in Figure 2.7 were obtained by Nagy (1997). The non-destructive ultrasound method was applied to determine the dynamic modulus together with a conventional method for determination of the static modulus. Development in modulus of elasticity employing the ultrasound method was also investigated by Boumiz, Vernet & Tenoudji (1996).

2.3.4 Poisson's Ratio

In (Byfors 1980) it was found that not very many researchers had investigated the development of the Poisson's ratio for early age concrete. The reason for this is that Poisson's ratio is not normally utilized in structural calculations. It is, however, gaining increased importance since finite element generalizations are dependent on this value and since such modelling is widely used today. Two investigations are mentioned in (Byfors 1980), where one of these, (Plank 1971) is claimed to have found a decrease with age, while the other, (Günzler 1970), apparently did not find any change. The insensitivity to age was also found in a later work by Oluokun, Burdette & Deatherage (1991).

It was however discovered in the work by Byfors (1980) that the Poisson's ratio does change with age. Figure 2.8 shows this evolution in relation to the compressive strength of the concrete at the same age. Initially, the Poisson's ratio is high as shown in the figure, which is comprehendible since liquids have a Poisson's ratio of 0.5. It is interesting to see that the Poisson's ratio appears to have a minimum at an intermediate age of approximately 10 to 16 hours (corresponds to $f_c \approx 1$ MPa depending on mix). Then, after arriving at this minimum value, the Poisson ratio again increases.

Other authors in literature have investigated the development of the dynamic Poisson's ratio through the ultrasound measuring technique, see (Boumiz et al. 1996). A result of this investigation is reprinted in Figure 2.9. The figure shows the same decrease in

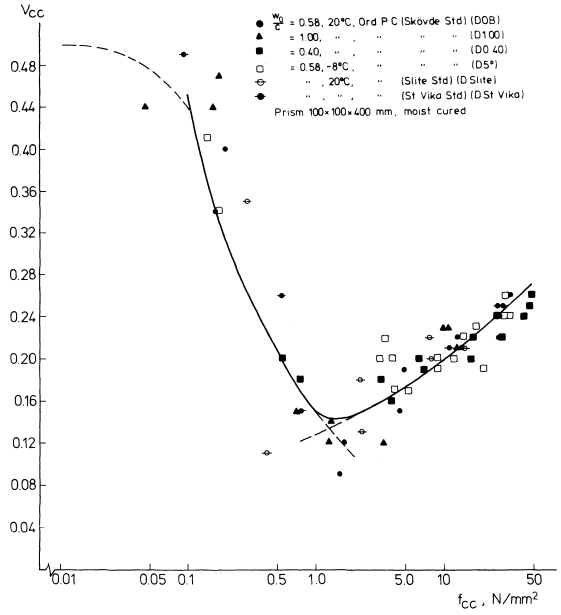

Figure 2.8 *Relation between Poisson's ratio and compressive strength. (Byfors 1980)*

Poisson's ratio as found by Byfors (1980), but on the contrary there does not seem to be a subsequent increase. However, the ultrasound method and the thereby determined dynamic Poisson's ratio is known to predict values higher than the static Poisson's ratio, but this fact can probably not explain the lack of increase in Poisson's ratio as it was found by Byfors (1980).

2.4 Creep and Relaxation

Creep and relaxation of concrete is a vast and complicated subject, which has been and is undergoing intensive research. Important textbooks about the subject include (Neville, Dilger & Brooks 1983), (Neville 1995), (Bažant 1988). Creep and relaxation of concrete arises from the fact that it behaves as a viscoelastic material. The initial instantaneous deformation measured at load application is followed by a time-dependent deformation, which is dependent on the mix proportions, humidity, temperature, age at load application, sign of load, magnitude of load and duration of load. Also changes of these variables, the rate of change and the sign of the change may inflict the magnitude of time-dependent deformation, usually resulting in a larger deformation.

The contributions of the time-dependent deformations are often separated into the viscoelastic part and the viscous (visco-plastic) part. Figure 2.10 shows a schematic representation of the deformation process in conjunction with creep. The material in the figure is non-ageing and kept at isothermal, sealed conditions in a state of quasi-equilibrium. As mentioned and shown in the figure, instantaneous elastic deformation will take place at

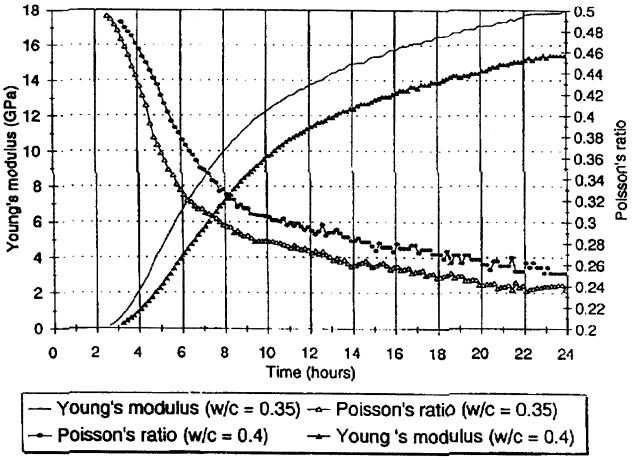

Figure 2.9 *Development of dynamic Poisson's ratio and dynamic modulus of Elasticity with age. (Boumiz et al. 1996)*

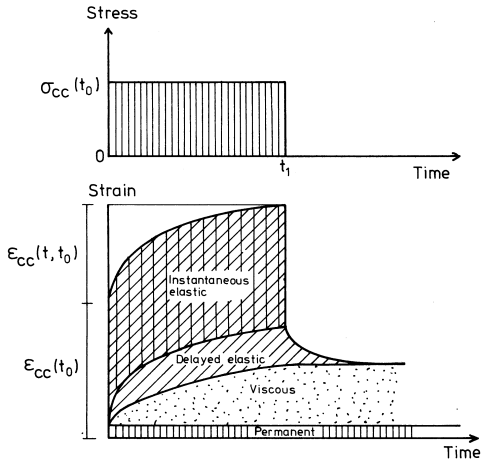

Figure 2.10 *Schematic representation of deformation process on conjunction with creep. (Byfors 1980)*

the time of load application. This deformation is fully instantly recoverable and does not change with time. However, during the load application, a delayed, or viscoelastic, deformation builds up. This deformation is believed to be associated with moisture movements in the microstructure inflicted by the macroscopic stresses in the material, (Neville et al. 1983). This deformation is asymptotically fully recoverable if the load is removed, e.g. at time t_1, see Figure 2.10. The viscous, or viscoplastic, deformation is also time-dependent and increases in magnitude with the duration of load application. This deformation, given the assumptions mentioned above, is caused by viscous flow in the material, i.e. sliding or shear of the gel particles lubricated by layers of adsorbed water. This deformation is not, by itself, recoverable; only inversion of the stress exerted on the material may, with time, result in a recovery. Finally, as Figure 2.10 shows, a part of the deformation is permanent. The permanent deformation is caused by damage, i.e. cracking of the material. The magnitude of this contribution is dependent on the stress level in the material.

This schematic representation of the contributions to the time-dependent deformations of concrete has been given several mathematical interpretations in literature. Depending on whether concrete is regarded as a viscoelastic solid or viscoelastic fluid, the two most simple models are the Kelvin solid chain and the Maxwell fluid chain, see e.g. (Flügge 1975). These two models consist of a spring and a dashpot in parallel connection or series connection, respectively, and they are, in combination, capable of capturing the principal effects shown in Figure 2.10.

The assumptions stated in combination with Figure 2.10 does of course not resemble the real situation for concrete. The most important effect, which changes the picture is the aging of concrete that inevitably always requires that aging of the viscoelastic parameters is regarded. Several aging creep models are proposed in literature such as the triple power law by Bažant & Chern (1985), which is empirically based on aging characteristics of concrete, while the solidification theory, (Bažant & Prasannan 1989*a*, Bažant & Prasannan 1989*b*) is based on a model of the concrete aging (solidification as a consequence of hydration).

The aging effects of the viscoelastic response in concrete are pronounced at early ages. This was seen by Brameshuber (1988) who applied large creep coefficients,

$$\varphi(t,t') = \frac{\varepsilon_{creep}(t,t')}{\varepsilon_{elastic}(28days)} \tag{2.4}$$

for early age concrete. If the concrete was loaded at an age of $t' = 6$ hours, $\varphi(t,t')$ could reach values of 200 in 4 hours of loading. However, it was also found that the value of the creep coefficient declined rapidly in this very early age, and $\varphi(24,12) = 40$. The results of Brameshuber (1988) are shown in Figure 2.11. It is notably that the magnitude of creep in compression and tension differs. However, this is in contradiction with Hauggaard, Damkilde, Hansen, Hansen, Christensen & Nielsen (1997) who concluded that creep in tension is comparable with creep in compression. This is again in contradiction with Neville (1995) who states that creep of mass concrete in uniaxial tension for mature concrete may be 20 to 30 % higher than under a compressive stress of equal magnitude. And the difference may be as large as 100 % for concrete loaded at early ages. Then, again, Neville (1995) notes that contradictory evidence exists, (Yonekura, Kusaka & Tanaka 1988). Also Emborg (1989) notes that the literature is in contradiction on whether compressive creep and tensile creep is comparable, but for simplicity similarity was preferred in that study.

It appears prudent, on this background, to assume that tensile creep experiments should be carried out in order to arrive at the tensile creep properties at early age. Otherwise, a too low magnitude of creep may be assessed resulting in unnecessary conservative calculations of the risk of early age cracking.

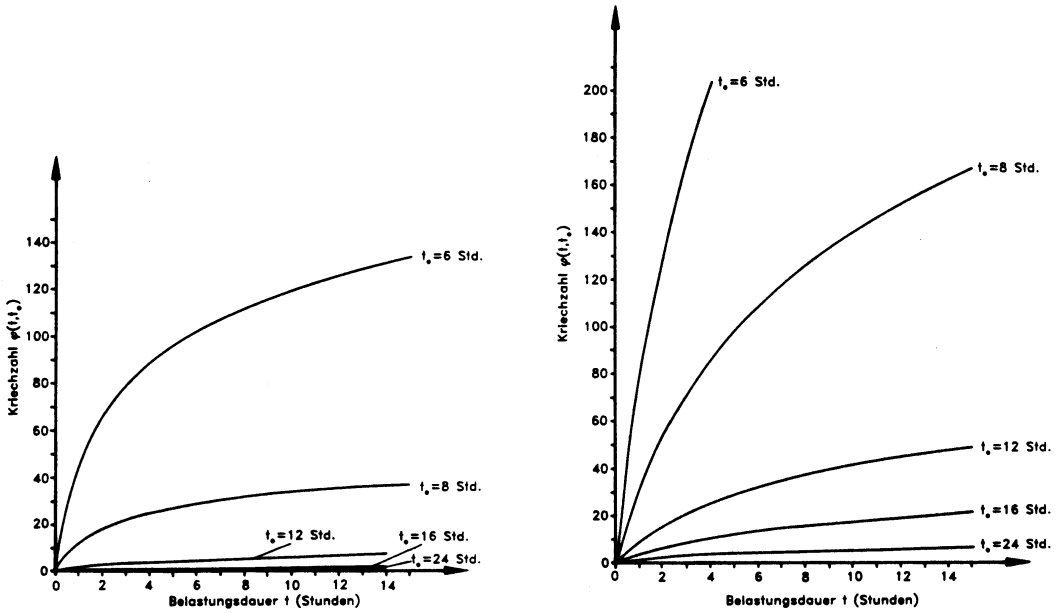

Figure 2.11 *Creep coefficients as function of age at load application and load duration, in compression (a) and in tension (b) Model used in (Brameshuber 1988)*

The magnitude of early age creep, however, independent of sign of loading, is seen in the literature to be very large. This was seen in the references given above, and also in the work by Westman (1995). Specific creep compliance of more than 700 10^{-6}/MPa was determined at an age of 13.2 hours. Also high creep compliance was determined by e.g. Byfors (1980) (in compression) and Østergaard, Lange, Altoubat & Stang (2001) (in tension) for early age concrete.

The temperature has an important influence on the magnitude of creep and relaxation in early age concrete. Magnitude of creep is influenced by the temperature and changes in the temperature. Higher temperature results in higher creep, see Neville et al. (1983). The puzzling thing about transitional thermal creep is that temperature changes seem to increase creep independent on the sign of the temperature change, see e.g. (Neville et al. 1983, Hauggaard et al. 1997, Hauggaard, Damkilde & Hansen 1999). Figure 2.12 shows this effect for unsealed creep of flexure specimens. The upper figure shows the case where the temperature rises in three steps, while the lower shows the case where temperature decreases in three steps. In the work of (Bažant, Hauggaard, Baweja & Ulm 1997, Bažant, Hauggaard & Baweja 1997) this transitional thermal creep was modelled utilizing a micro-prestress assumption implemented in the solidification theory, see also Hauggaard et al. (1999). They arrived at fine predictions.

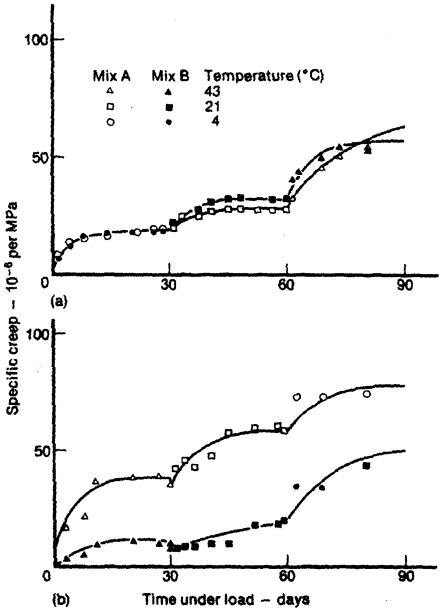

Figure 2.12 *Creep at variable temperatures. Upper figure shows the change of magnitude of creep for increasing temperatures, while the lower figure shows the change of magnitude of creep for decreasing temperatures (Neville et al. 1983)*

Also moisture in terms of drying and re-wetting may change, notably increase, the magnitude of creep of concrete. An effect, which, like the thermal transitional creep, causes an increase in the magnitude independent of the sign of the change of moisture content. This type of increase of the creep was investigated by Pickett (1942). The results in Figure 2.13 are a reprint of this work. Despite the rather poor reproduction in this thesis both the full and the dotted lines in the figure are seen. The full lines correspond to the time periods where the concrete is submerged in water, while the dotted lines represent the time periods where the concrete is subjected to drying. The experiments were conducted on three point bending beams and the results represent the midpoint deflection. Beam B is initially, until the unloading, fully submerged in water, while beam C is subject to drying. It is clearly seen that beam C has a higher magnitude of creep than beam B. The highest amount of creep, however, is seen neither in beam C or B, but in beam D, which after 40 hours is subject to drying and re-wetting cycles. Thus, the change of environment does increase creep, despite the sign of the change.

The drying effect on creep is often referred to as the Pickett effect, see e.g. (Altoubat 2000), or the drying creep, while the magnitude of creep under sealed conditions is called the basic creep. The drying creep is, in fact, hardly a material parameter, but rather an effect of the drying pattern dependent on the geometry of the sample and the thereby built up stresses in the material. Also cracking due to the tensile stresses built up in the perimeter of the material is inflicting on the magnitude of drying creep.

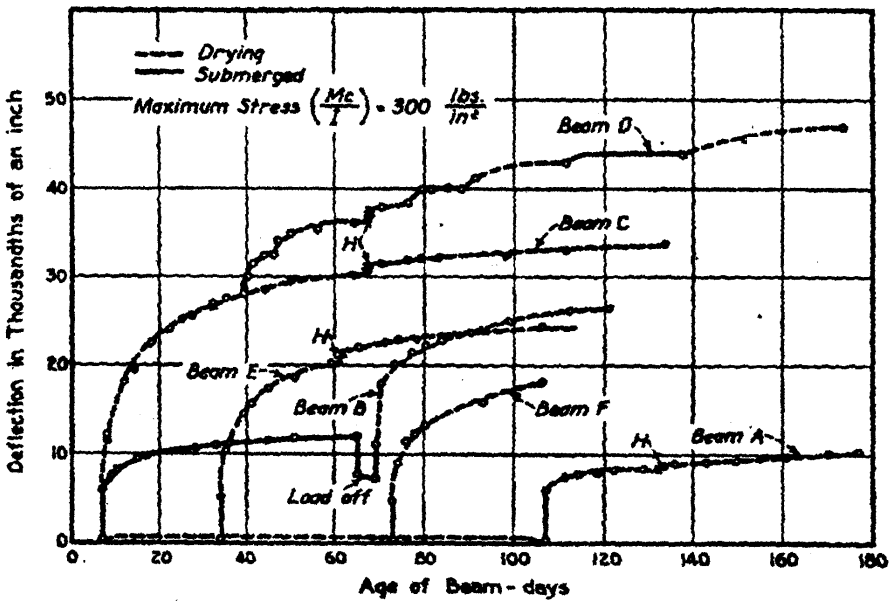

Figure 2.13 *Creep at variable relative humidity (Pickett 1942)*

2.5 Fracture Properties

The review of properties so far has been focused on the behavior prior to cracking. The sources of the volumetric deformations in concrete have been identified and quantified. This, in combination with knowledge of the mechanical properties and the time-dependent deformations, has prepared the ground for pre-cracking analysis of concrete at early ages.

However, as already stated in the introduction, it very interesting not only to be able to control the pre-cracked situation, but also to possess methods for analysis of the cracked stage, thus enabling the engineer to answer the question: How deleterious would cracking actually be in this situation?.

In order to do so, knowledge of the parameters governing not only crack initiation, but also the crack propagation must be obtained and prepared for implementation in a modelling framework.

The development of the tensile strength has already been described in this chapter. This material property is often employed as the crack initiation criterion for concrete, i.e. cracking occurs when $\sigma_{11}(t) = f_t(t)$, where $\sigma_{11}(t)$ is the maximum principal stress at any point of time t, while $f_t(t)$ is the tensile strength at the same point of time, t.

The propagation of this initial crack is governed by the fracture energy, $G_f(t)$, and the shape of the stress-crack opening relationship, $\sigma_w(t)$ i.e. a function describing the stress transfer in the crack as function of its opening. The fracture energy is a material parameter and describes the energy necessary to fully propagate the crack over a unit measure

of area, while the stress-crack opening relationship gives information on how the fracture energy is distributed as a function of the crack opening.

The characteristic length, L_{ch}, introduced by Hillerborg, Modéer & Petersson (1976) gives an estimate of the brittleness of the concrete. This parameter may be interpreted as a measure of the elastic strain energy needed to propagate the crack one unit measure of area, see Equation 2.5:

$$L_{ch} = \frac{G_f E}{f_t^2} \tag{2.5}$$

Development in early age of the fracture mechanical properties is not investigated by very many researchers in literature. However, some important contributions exist.

2.5.1 Fracture Energy

In an early work by Petersson (1980), experiments on normal concrete; varying type of aggregates, water-cement ratio, paste content, maximum aggregate size and age at testing, were conducted. In the age variation, three point bending tests were performed at 2, 7, 28 and 91 days on a mix with a water-cement ratio of 0.50. It was found that the fracture energy increases with age in the period of 2-91 days, see Figure 2.14. The increase in fracture energy is comprehendible since it corresponds to the increased number of bonds forming in the concrete as hydration proceeds. However, besides the fracture of bonds, also the aggregate pull-out is playing an important role. In (Petersson 1980) the investigation was conducted on a concrete with water-cement ratio of 0.50, thus the paste is weak and the aggregates will experience pull-out instead of fracture. Otherwise, if the paste is strong, the aggregates may start fracturing at a certain age, possibly resulting in a decrease in fracture energy.

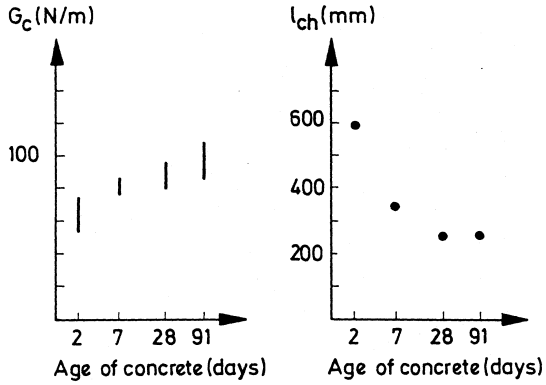

Figure 2.14 *Development of fracture energy and characteristic length with age of concrete (Petersson 1980)*

This was the effect in (Gettu, Garcia-Álvarez & Aguado 1998) where a decrease in fracture energy was found in a high strength concrete with silica fume addition. The test method

was the three point bending test (TPBT), while the concrete had a water-cement ratio of 0.30 and a 28-day compressive strength of approximately 60 MPa. In this experiment, the fracture energy decreased with age, an effect which the authors ascribed a mechanism of less bond cracking and more aggregate rupture, (Gettu et al. 1998).

In a paper of Wittmann et al. (1987), an investigation of the influence of water-cement ratio, age at loading and rate of loading using the three point bending test was conducted. The age was varied from 2-28 days while the selected water-cement ratios where 0.40-0.65. The rate of loading was varied from $10^{-3} - 10^{1}$ mm/min. In the experiment with age variation a constant water-cement ratio of 0.50 was chosen. The fracture energy was found to increase throughout the period. A similar result was obtained by Zollinger, Tang & Yoo (1993) who investigated fracture toughness with a water-cement ratio of 0.53 from 12 hours until 28 days employing the TPBT setup. Also Schutter & Taerwe (1997) investigated the development of fracture energy at early ages, but as a function of the degree of hydration. The age at testing ranged from 1-28 days and the water-cement ratio was 0.50. It was found, corresponding to the other findings of high water-cement ratio concretes that the fracture energy increases with age. Also the effect of the type of cement was investigated in this study and it was found that blast-furnace cements (CEM III/B 32.5 and CEM III/C 32.5) has a lower rate of development and a lower final value than an ordinary Portland cement (CEM I 52.5).

The fracture energy is also dependent on the rate of loading. In (Wittmann et al. 1987) it was found that G_f apparently has a minimum at intermediate rates of loading, in this case of approximately 10^{-2} mm/min while both lower and higher rates result in a increase of the fracture energy.

An important work was conducted by Brameshuber (1988), see also (Brameshuber & Hilsdorf 1987) and (Brameshuber 1989). Here three point bending experiments, among many other investigations, were conducted from 4 hours until 28 days with a water-cement ratio of 0.54. An increase of fracture energy with age was found.

Finally, Hariri (2000) has investigated the development of fracture mechanical properties and the width of the fracture process zone of early age concrete as function of degree of hydration. It was found that G_f increases with age for concretes with water-cement ratios of 0.29/0.49/0.50/0.55.

2.5.2 Characteristic Length

The characteristic length, L_{ch}, which as mentioned expresses a measure of the brittleness of the concrete is generally found to decrease with age, indicating a increase in brittleness. The decrease was found by almost all authors, see e.g. (Petersson 1980) and Figure 2.14. However, only Brameshuber (1988) made a detailed study on concrete as young as 4 hours. It was found that the decrease is not monotonic, but has moments of low values succeeded by an subsequent increase. This is depicted in Figure 2.15. Apparently, a low

value of L_{ch} is determined for very early age (4 hours), whereafter it increases and reaches a value of 300 mm at 5 hours. Then, a decrease is measured resulting in a minimum of 150 mm at 7 hours, then a new increases follows whereafter it steadily drops to a value of 90 mm. This is interesting since it gives an indication of how the crack may evolve if cracking occurs at any particular age. The tendency of higher brittleness of early age concrete was also found by Wong & Miller (1990) under mixed mode conditions.

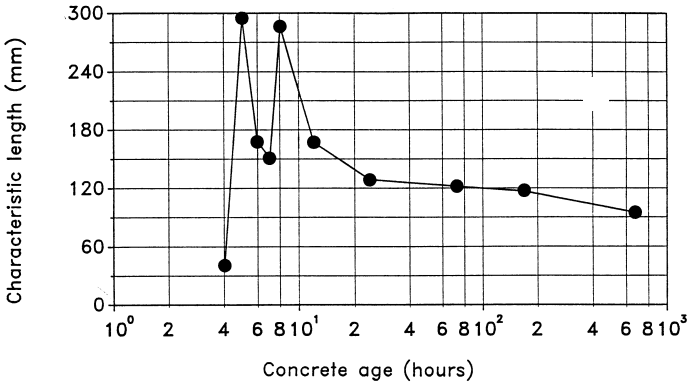

Figure 2.15 *Development of characteristic length with age of concrete (Brameshuber 1988)*

The influence of the rate of loading on the fracture mechanical properties was explored by Wittmann et al. (1987). From these results is can be concluded that the characteristic length decreases with increasing rate of loading.

2.5.3 Stress-Crack Opening Relationship

Only Wittmann et al. (1987) has investigated the development of the shape of the stress-crack opening relationship with age. This investigation was conducted with the TPBT setup on a 0.50 water-cement ratio concrete. It was assumed that the pre-crack behavior and the stress-crack opening relationship could be described as shown in Figure 2.16. Here, the pre-cracked behavior is assumed linear-elastic until the tensile strength, f_t, is reached. Then, the concrete cracks and follows the bilinear stress-crack opening relationship as shown in the figure. The parameters a_1 and a_2 are the normalized slopes of the relationship while the parameter b_2 is the cutoff on the y-axis of the second part of the relationship. In (Wittmann et al. 1987), all these parameters were found to decrease with age, corresponding to an increased brittleness of the concrete.

2.6 Concrete-Reinforcement Bond Properties

Bond of reinforcement in early age concrete is a problem not very well investigated. Development of the strength of bond for concrete at early ages has been investigated in (Sule & van Breugel 2001). The experiments comprised pull-out tests at 8 hours, 24 hours, 31 hours and 28 days and the average shear vs. end slip was measured. It was reported that

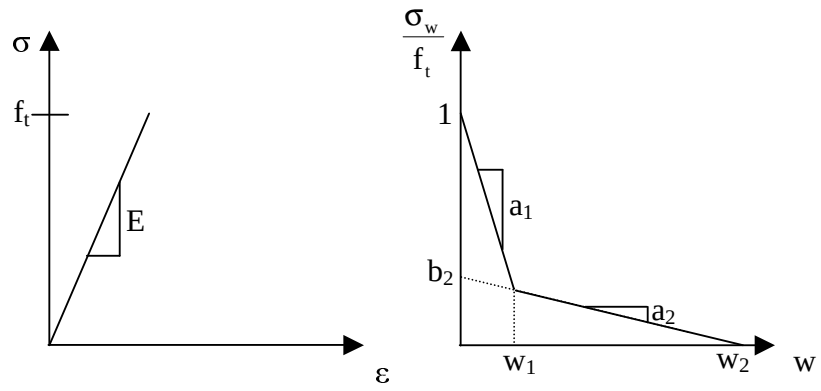

Figure 2.16 *Approximation of the stress-crack opening relationship by a bilinear function*

no significant bond strength had developed at 8 hours. At an age of 24 hours significant bond properties had developed with an average shear stress of 14 MPa for an end slip of 0.1 mm and 23 MPa for an end slip corresponding to 1.0 mm. At 28 days the shear stress transfer at 0.1 mm had increased to 22 MPa.

Chapter 3

Fracture Mechanics for Concrete

Analysis of reinforced concrete structures is almost always conducted with the assumption that the concrete tensile strength is zero, i.e. disregarded. Then, the calculations are performed on the cracked cross-section using either the elasticity or the plasticity theory. This approach is straight forward and leads in general to a safe design. However, these models do only approximately capture the behavior of concrete, and for this reason many empirical rules and provisions have been implemented in the building codes, see e.g. (Hawkins 1985).

The key issue is the lack of implementation of the fracture behavior of concrete. Concrete failure is not governed by a simple strength criterion, but by the growth of cracks. These cracks start growing already at low levels of an external load and are initially occurring around internal air voids, aggregates, shrinkage cracks, pores etc. These initial cracks will continue to grow while increasing the external loading and coalesce into larger cracks; and eventually the crack growth will localize and result in failure of the concrete structure.

Fracture mechanics provides a tool for analysis of not only the crack initiation situation, but more important, based on a energy consumption criterion, also how the cracks will propagate. This framework is able to explain many previously unexplained empirical rules and provisions in the building codes. This was shown in (Hawkins 1985) where requirements like minimum reinforcement and ductility limits etc. in the ACI Code were explained on the background of fracture mechanics. Also the size effect, i.e. the fact that the apparent strength and load-deflection behavior of a concrete element depends on its size, may be explained by fracture mechanics.

However, it took several years before an appropriate fracture model was devised for concrete. A short historical overview of this development will be given in the next sections, succeeded by presentation of the fictitious crack model suited for concrete.

3.1 Linear Elastic Fracture Mechanics

The first explanation of the mechanism of fracture in brittle materials was given by Griffith (1920). Based on the analysis of a sharp crack in a sheet of brittle material, e.g. glass, with a constant remotely applied stress, it was demonstrated that the stresses near the crack tip tend to approach infinity. Thus, the stress state in the vicinity of the crack tip proved to be crucial for the load capacity of the sheet. A new energy based failure criterion was formulated on basis of the analysis of the stresses and deformations near the crack tip. It was shown that in order for the crack to advance, a certain amount of potential energy must be accumulated in the system, available for release into the crack tips. Analysis of this energy balance condition resulted in a formula for the maximum applicable remote tensile stress, σ_c:

$$\sigma_c = \sqrt{\frac{EG_c}{\pi a}} \tag{3.1}$$

where E is the modulus of elasticity, a the initial crack length and G_c is the critical energy release rate. The critical energy release rate, G_c, is a new material parameter and describes the amount of energy needed to fully separate a unit area of crack surface. Equation 3.1 gives the criterion for crack growth. If $\sigma < \sigma_c$ no cracking will occur since the energy stored in the system is lower than the critical amount. However, if $\sigma \geq \sigma_c$ the crack will advance catastrophically since any extension of the crack length, a, will lower the critical stress, σ_c. Equation 3.1 explains the fracture of brittle materials, which in reality always have some intrinsic cracks like imperfections, pores, dislocations etc. It is also seen that if the size of the intrinsic cracks is reduced, the critical stress at which the cracks propagate may be increased.

Later, Irwin (1957) showed that the stresses near a sharp crack tip always show the same fundamental variation, namely a r^{-}-singularity, where r is the distance to the crack tip ($r << a$, and a is the crack length). This singularity is independent of the boundary conditions, geometry and loading. It is also independent of the opening mode of the crack; for which three fundamental different types exist, see figure 3.1. Mode I corresponds to the opening mode which was investigated originally by Griffith (1920).

All these modes exhibit the same singularity near the crack. However, the central issue is the scaling of this singularity. This is best illustrated by the equations describing the stresses and deformations near the crack, see Equations 3.2-3.3. Here, the stresses and displacements near the crack tip are given in polar coordinates with origin at the crack tip, at a distance r and angle θ. The parameter κ is equal to $(3 - 4\nu)$ in plane strain and $(3 - \nu)/(1 + \nu)$ in plane stress conditions. The factor K_I is denoted the stress intensity factor and is dependent on the boundary conditions, geometry and loading mode of the system. Expressions for the stresses and displacements in the mode II and mode III opening configurations, similar to the ones given in Equations 3.2-3.3, may be derived, see e.g. Karihaloo (1995). Also for these opening modes a square root r singularity will

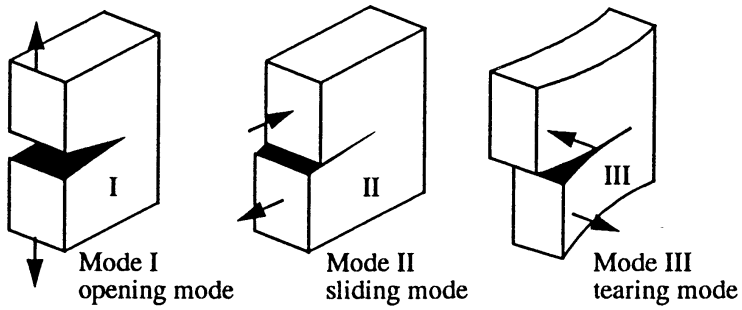

Figure 3.1 *Fundamental crack opening modes; Opening mode (mode I), sliding mode (mode II) and tearing mode (mode III). (Karihaloo 1995)*

be found, but the stress intensity factor will correspond to the loading of these situations, i.e. K_{II} and K_{III}.

$$\begin{aligned}
\sigma_{xx} &= \frac{K_I}{\sqrt{2\pi r}} \cos\frac{\theta}{2}\left(1 - \sin\frac{\theta}{2}\sin\frac{3\theta}{2}\right) \\
\sigma_{yy} &= \frac{K_I}{\sqrt{2\pi r}} \cos\frac{\theta}{2}\left(1 + \sin\frac{\theta}{2}\sin\frac{3\theta}{2}\right) \\
\sigma_{xy} &= \frac{K_I}{\sqrt{2\pi r}} \cos\frac{\theta}{2}\sin\frac{\theta}{2}\cos\frac{3\theta}{2}
\end{aligned} \tag{3.2}$$

$$\begin{aligned}
u &= \frac{K_I(1+\nu)}{E}\sqrt{\frac{2r}{\pi}}\cos\frac{\theta}{2}\left(\frac{\kappa-1}{2} + \sin^2\frac{\theta}{2}\right) \\
v &= \frac{K_I(1+\nu)}{E}\sqrt{\frac{2r}{\pi}}\sin\frac{\theta}{2}\left(\frac{\kappa-1}{2} - \cos^2\frac{\theta}{2}\right)
\end{aligned} \tag{3.3}$$

The postulate given by Irwin (1957) is now that the value of the stress intensity factor K_I determines whether or not a given crack will propagate under the actual circumstances. If the stress intensity factor reaches a critical value, K_{Ic}, which is assumed to be a material parameter, propagation will occur, - and the propagation will be catastrophical, i.e. uncontrolled for a constant load. However, if the external loading results in a K_I lower than the critical value, K_{Ic}, no crack propagation will occur. This postulate is called the Irwin criterion for fracture of brittle materials.

If a geometry and loading corresponding to the example investigated by Griffith (1920) is considered, the critical stress intensity factor at each tip of the crack will be equal to:

$$K_{Ic} = \sigma\sqrt{\pi a} \tag{3.4}$$

This relation leads to a very important result. By inserting Equation 3.1 into 3.4 it is seen that the two approaches essentially lead to the same result:

$$G_c = \frac{K_{Ic}^2}{E} \tag{3.5}$$

However, since it is much easier to determine the critical stress intensity factor, the Irwin approach is often preferred over the Griffith approach, and handbooks for stress intensity factors have been made, see e.g. (Tada, Paris & Irwin 1985).

The theory of brittle fracture as presented by Griffith and Irwin represents the actual fracture situation in brittle materials well. However, there are some conceptual problems with the fact that the stresses near the crack tips are assumed to approach infinity. This is in contradiction with what would be expected in the real situation where the material has a tensile strength. It is also violating fundamental assumptions for elasticity regarding small strains. A proposal for overcoming these problems was proposed by Barenblatt (1962). It was here assumed that a certain distribution of high closure stresses are acting in a zone near the crack tips. This distribution is generally unknown, but it is assumed that the distribution is such that the crack faces close smoothly, i.e. such that the stress intensity factor is zero. This smooth closure condition may be formulated mathematically and it can be shown that, as long as the zone over which the closure stresses are acting is small ($<<$ a), knowledge of the actual distribution of the closure stresses is unimportant. The model is essential corresponding to Griffith and Irwin's crack models, see e.g. (Karihaloo 1995), but the important issue is that it presents a hypothesis of what physically happens close to the crack tips. A crude estimate of the length of this fracture process zone, L_p, is (see e.g. (Karihaloo 1995)):

$$L_p = \frac{1}{\pi}\frac{EG_c}{f_t^2} \tag{3.6}$$

Another approach towards understanding of what happens in the fracture process zone, i.e. the zone where the energy is dissipated due to formation of new crack, was presented by Dugdale (1960). Here it was assumed that the process zone is finite and in the same order of magnitude as the crack itself. It was also assumed that the material under consideration has a yield capacity sufficient to cause a constant closing stress on the crack faces. Thus, in this model the closing stresses are known. This problem may also be formulated mathematically and solved such that the extension of the fracture process zone is determined from the smooth crack closure condition.

The cohesive crack models, i.e. the models by Barenblatt (1962) and Dugdale (1960) formed the basis for fracture mechanical modelling of concrete in the work by Hillerborg et al. (1976). In this model, known as the fictitious crack model; where fictitious refers

to the imaginary extension of the real crack into the fracture process zone; it was assumed that the length of the process zone has a finite size which is comparable with the crack length. However, now it is also assumed that the cohesive stresses in the process zone are varying and known. This will be explained in more detail in Section 3.2. First, the breakdown of linear elastic fracture mechanics if applied to concrete will be explained.

One of the first attempts to apply linear fracture mechanics to concrete was conducted by Kaplan (1961), and followed by many other authors, see e.g. a review in (Karihaloo 1995). The experiments comprised measurements of the critical energy release rate or the critical stress intensity factor utilizing the relevant formulas for the given situation. Like almost all other authors, Kaplan (1961) arrived at the conclusion that the determination of G_c depended on the specimen size. This result contradicted the postulate that G_c is a material property. One example of this variation, expressed in K_{Ic}, by Tian, Huang & Liu (1986) is given in Figure 3.2. Here, the variation of the critical stress intensity factor with the characteristic size of compact tension specimen is shown. It is clearly seen that K_{Ic} varies with the characteristic dimension W. However, as the figure also indicates, it appears that a plateau for K_{Ic} is reached for very large specimens.

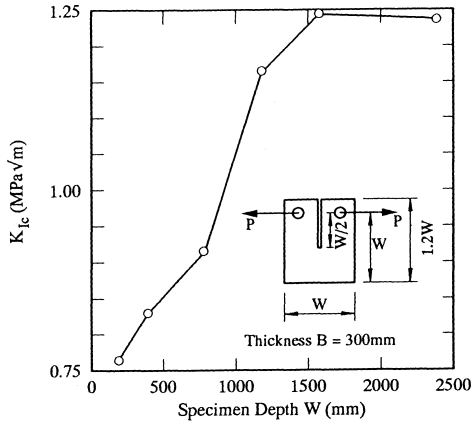

Figure 3.2 *Variation of K_{Ic} with specimen size, W, for concrete. Figure after (Karihaloo 1995), results from (Tian et al. 1986)*

The fracture toughness of cement paste and mortar was determined in a work by Ohgishi, Ono, Takatsu & Tanahashi (1986). The results are depicted in Figure 3.3. Here the critical stress intensity factors for both hardened mortar, with $d_{max} = 0.3$, and cement paste were determined on four point bending specimens. It is clearly seen that K_{Ic} is dependent on the size of the initial notch relative to a characteristic dimension of the beams, a/W. However, this dependency is only found for the mortar, not for the cement paste. This is interesting since, like the results by Tian et al. (1986), it indicates that the maximum particle size relative to the characteristic structural dimension, W, of the specimen has an influence on the result. If W is much larger than the maximum particle size, d_{max}, the critical stress intensity factor seems to be constant. However, if d_{max} is of the same order, or only differs from the specimen size by one or two decades, then a dependency of the dimensions of the specimen is achieved.

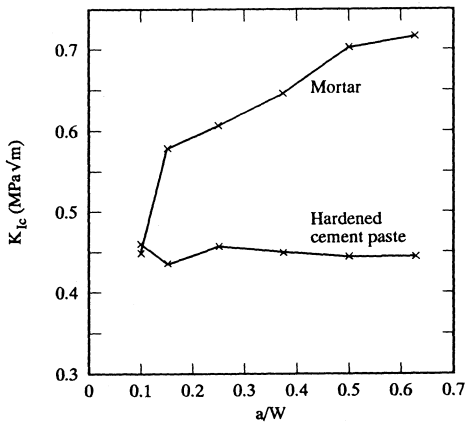

Figure 3.3 *Variation of K_{Ic} with notch depth, a, for hardened mortar and cement paste. Figure after (Karihaloo 1995), results from (Ohgishi et al. 1986)*

The work by Tian et al. (1986), Oluokun et al. (1991) and others, see e.g. Karihaloo (1995), proved that linear elastic fracture mechanics is not applicable to concrete when the structural size is too small. The theory was only found to be accurate if sufficiently large specimens were treated. This was adverse since "sufficiently large" in this context meant +2 decades larger than the maximum particle size. In (Karihaloo 1995), necessary specimen sizes of 45-135 times the maximum particle size are mentioned depending on the geometry. Thus, a fracture theory, which is able to describe the fracture behavior for normal sized specimens and applicable to all different sizes was needed. This theory was presented by Hillerborg et al. (1976), see the next section.

3.2 Non-linear Fracture Mechanics

The reason for the breakdown of linear elastic fracture mechanics is the fact that concrete has a very large fracture process zone; which is in violation with the basic assumption of the linear elastic fracture mechanics. This very long fracture process zone is caused by the heterogeneity of the material, with large aggregates inside the mortar/cement paste matrix. The aggregates act as nucleation spots for microcracking since differences in stiffness between the aggregates, sand particles and cement paste may cause stress concentrations. Furthermore, as the crack localizes, the aggregates may act as bridging particles due to the frictional pull-out during crack opening, thus ensuring a continued stress transfer over the crack even for large openings.

The basic conceptual differences are depicted in Figure 3.4. Linear fracture mechanics is applicable as long as the fracture process and the non-linear behavior zones are small. This is the situation in Figure 3.4a, where these zones are very small compared with the characteristic structural dimension. The model by Dugdale (1960) may be applied if the zone with non-linear material behavior is large, see Figure 3.4b, but this model still requires that the fracture zone is small (due to the constant closing stress criterion). Finally, as shown in Figure 3.4c, the situation in concrete differs in the way that the zone with non-linear behavior is small, while the fracture zone is large.

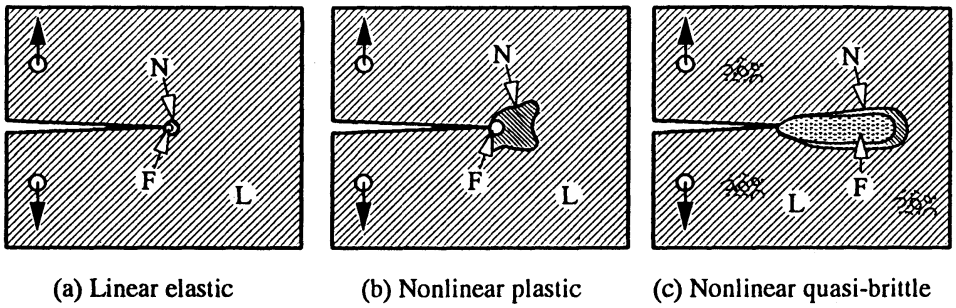

Figure 3.4 *Conceptual differences between materials suited for modelling with linear elastic fracture mechanics (a), non-linear plastic fracture mechanics ((Dugdale 1960)) (b) and non-linear quasi-brittle fracture mechanics (c). Linear elastic material is denoted with an L, non-linear material behavior with an N, while fracture behavior is denoted by F. Figure after (Karihaloo 1995), originally from (ACI 1991)*

Another way of showing these differences is given in Figure 3.5. This figure shows schematically the behavior of the three different material classes if they are subjected to e.g. a uniaxial tension test. The brittle material will be linear elastic almost all the way to the peak load, where suddenly, a crack will propagate through the specimen, causing an almost immediate unloading and failure. The ductile material shown in Figure 3.5b is characterized by a pronounced yield plateau. Thus, the non-linear behavior starts long before the unset of cracking. Furthermore, the fracture process zone will often be small in comparison with the non-linear zone, leading to the result that the properties of this zone may be ignored as in the model by Dugdale (1960). Finally, Figure 3.5c shows how a quasi-brittle material behaves. Here the non-linear behavior starts before the peak load is reached. This is due to microcracking in the material which make it more flexible, but does not weaken the material. As discussed earlier, this microcracking will occur at local sites where stress concentrations are present. Then, upon arrival at the peak load, crack localization will occur, and the stress transfer capability of the material starts to decline. In the beginning, this decline will be governed by localized microcracking in the material, but later frictional pull-out of aggregates, or fibres if present, will be responsible for the continued stress transfer.

The evolution of the fracture process zone is schematically shown in Figure 3.6. This figure shows a situation where a imaginary specimen is opened in Mode I. The thereby resulting stresses lead to a situation where all stages of crack propagation are seen. The outmost left part of the figure shows the situation before the tensile strength, f_t, is reached. Here microcracking occurs leading to a non-linear material behavior. Then, going right in the figure, at some point the tensile strength is reached, whereafter the continued microcracking start to localize and weaken the material. Proceeding to the right, it is now seen that the cracks coalesce and form macrocracks. These will have a tendency to run in the interfacial transition zones (ITZ), which are known to have a lower strength than the surrounding material due to higher water-cement ratio and higher porosity. It is also

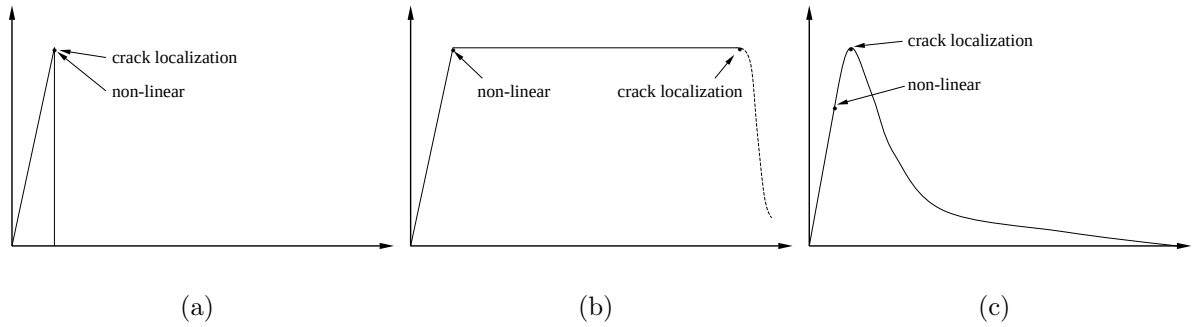

Figure 3.5 *Differences between brittle (a), ductile (b) and quasi-brittle materials.*

seen how aggregates may be responsible for bridging stresses since the crack may branch around, and thus, the aggregate maintains contact with both sides of the crack. Finally, to the left of the figure, it is seen that at some point of opening, w_c, the crack is no longer able to transfer stress.

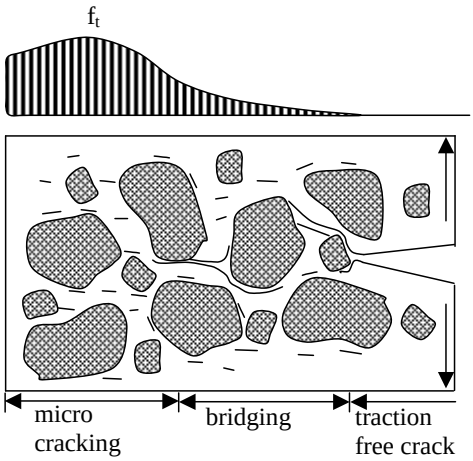

Figure 3.6 *Schematically drawing of the crack propagation in concrete. Scattered microcracking occurs before attainment of tensile strength, f_t, and continues thereafter in conjunction with aggregate bridging, whereafter, finally, a stress free crack is produced*

The concepts of Figure 3.6, i.e. the assumptions that microcracking, aggregate bridging, crack branching etc. exists and result in a long fracture process zone is supported by experimental evidence. One example of this evidence is given in Figure 3.7. This work was carried out by Nemati, Monteiro & Scrivener (1998), who conducted compressive tests on concrete cylinders and maintained the crack pattern at certain stress levels by intrusion of Woods metal. The intrusion agent, Woods metal, is characterized by a low melting point (around 70 ℃ - 90 ℃) and is well suited for intrusion in concrete. The Figures 3.7a-3.7c

show the extent of microcracking for normal strength concrete (NSC) (with $w/c = 0.528$) in the paste, around aggregates and in the ITZ, in the aggregates and around air pores. Also crack bridging and crack branching is seen in the figures. The picture in Figure 3.7d shows an example of cracking in a high strength concrete (HSC). Here, the microcracking is less pronounced; only few cracks are seen, travelling through the ITZ and the aggregate.

The length of the fracture process zone, L_p, has been estimated by several authors in the literature. In (Karihaloo 1995) values of L_p for a number of materials have been compiled. Here, a typical length of FPZ for glass is mentioned ($L_p = 10^{-6}$ mm), showing why this material is well described by LEFM, while the length of FPZ for mortar ($L_p = 100 - 200$ mm), normal concrete ($L_p = 200 - 500$ mm) and dam concrete ($L_p = 700$ mm), explains why LEFM fails and non-linear fracture mechanics must be applied.

3.2.1 Fictitious Crack Model

From the discussion above, it is seen to be conclusively necessary to include the fracture process zone in the modelling of fracture behavior of concrete. The first authors to do so was Hillerborg et al. (1976). Inspired by the cohesive crack models by Barenblatt (1962) and Dugdale (1960), it was proposed that concrete exhibits a similar behavior, where cohesive stresses result in a smooth closure of the crack tips. The crack was assumed to initiate when the tensile strength was reached anywhere in the structure. Thereafter, a certain distribution of cohesive closing stresses, $\sigma_w(w)$, would act over the crack faces as function of the opening, w, and decreasing with increasing crack opening, until $\sigma_w(w_c) = 0$. It is also important that Hillerborg et al. (1976) made no restrictions on the size of the fracture process zone. It may be as long as exemplified in the previous section.

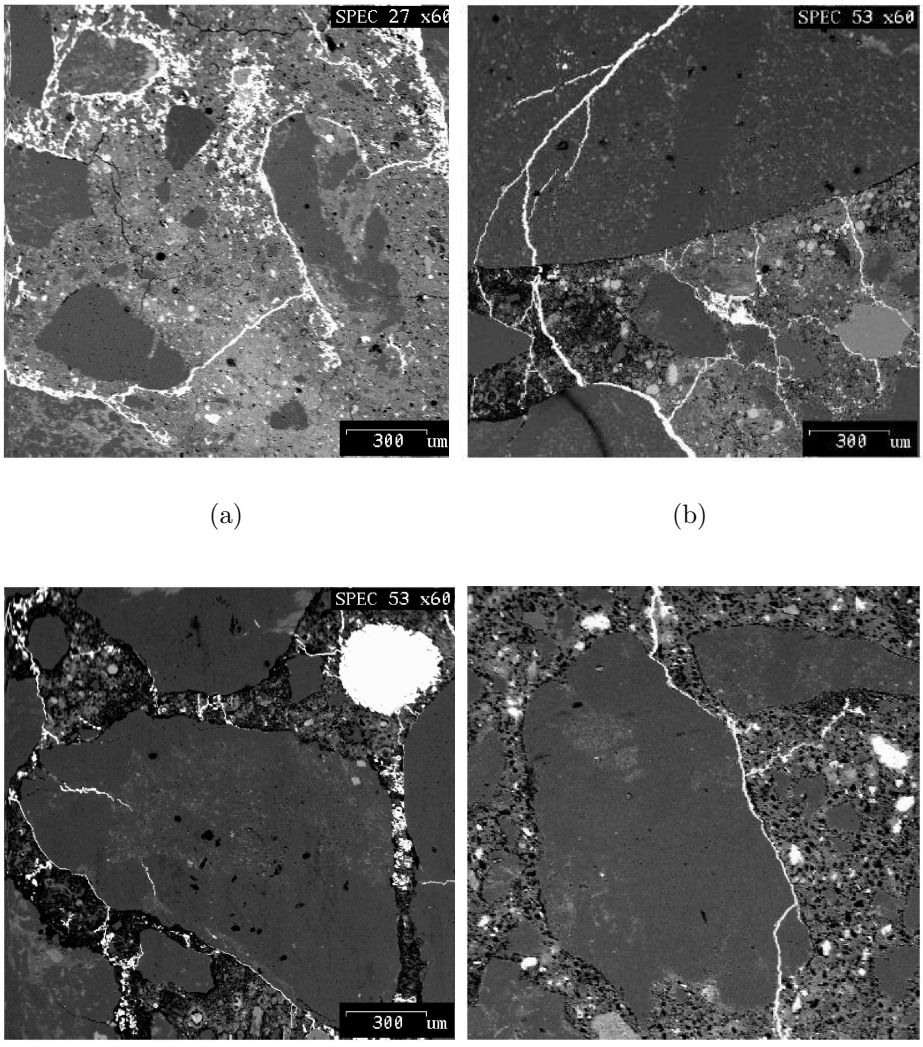

Figure 3.7 *Scanning Electron Microscopy (SEM) images of cracking in concrete. Normal strength concrete (NSC) with pronounced microcracking and localized cracks running in the ITZ and in the paste (a), cracking around and inside an aggregate (b) and cracking around an air pore (c). Cracking in HSC (d) shows less tendency to microcracking, and the crack travels through the ITZ and the aggregate itself. (Nemati et al. 1998)*

Given these assumptions, knowledge of the distribution of the cohesive closing stresses, must be known, since the FPZ is no longer small. The distribution of the cohesive stresses is often called the stress-crack opening relationship since the stresses transferred are assumed to be dependent on the opening of the crack, w. Knowledge of this relationship and employing the assumption that cracking occurs when the maximum principal stress reaches the tensile strength forms the basic information needed in Hillerborgs crack model, known as the fictitious crack model. The term "fictitious" is applied since the FPZ is viewed as an extension of the real stress free crack. However, FPZ is not a continuous crack, but rather distributed microcracking and aggregated bridging.

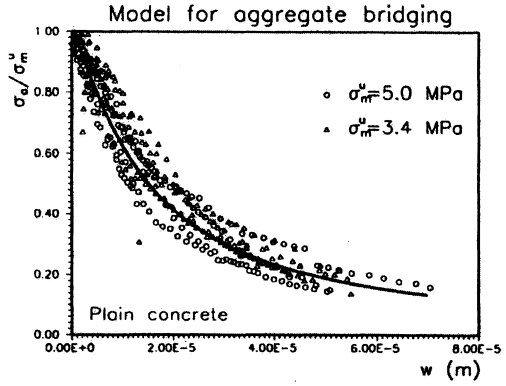

Figure 3.8 *Normalized stress-crack opening relationships for normal concrete. (Stang 1992)*

The shape of the stress-crack opening relationship has been determined by various authors in the literature. Results obtained by Petersson (1980), Cornelissen, Hordijk & Reinhardt (1986) and Stang (1992) are shown in Figure 3.8. This figure demonstrates that the shape of the stress-crack opening relationship is almost the same for a wide range of experimental data, including normal and high strength concrete. A simple empirical formula, able to fit the data shown in the figure, was provided by Stang (1992):

$$\sigma_w(w) = \frac{f_t}{1 + (w/w_c)^p} \tag{3.7}$$

where it was shown that $w_c = 0.015$ mm and $p = 1.2$ may be fixed for all the experimental results considered. However, many different stress-crack opening relationships have been used in literature, including linear, bilinear, exponential and polynomial formulations, see e.g. (Karihaloo 1995). Nevertheless, for many situations, a simple bilinear approximation as shown in Figure 3.9 suffices. Here, the non-linearity due to microcracking on the ascending part of the tension response of concrete has been ignored, while the stress-crack opening relationship is assumed to be bilinear with the normalized slopes a_1 and a_2 and the cut-off b_2.

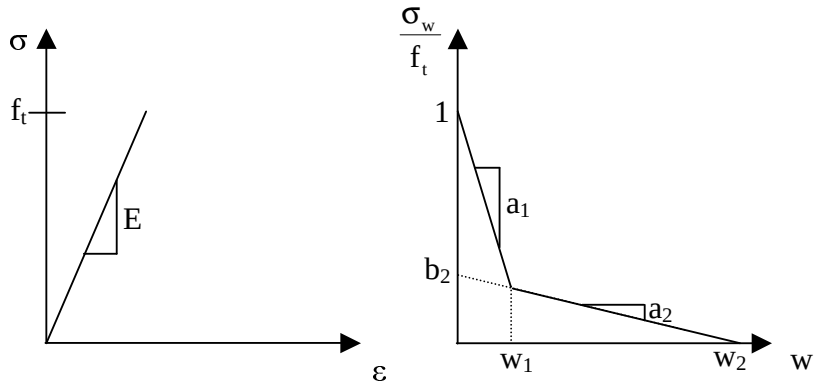

Figure 3.9 *Elastic (a) and cracked behavior of concrete, assuming that $\sigma_w(w)$ may be described by a bilinear relation*

3.2.2 Crack Band Model

A modification of the fictitious crack model by Hillerborg et al. (1976) was developed by Bažant & Oh (1983). It is assumed that the cracking occurs over a certain band width, h, instead of taking place discretely, as in the fictitious crack model. This assumption is justified by the fact that, as Figure 3.7a-d indicates, cracking in concrete is not occurring in a single plane, but is scattered over a certain width. Over this width, h, the inelastic deformation due to cracking takes place. Thus, the cracking is interpreted as a inelastic strain, which is related to the crack width w by the crack bandwidth h:

$$\varepsilon_{cr} = \frac{w}{h} \tag{3.8}$$

This model is well suited for implementation in finite element code since the strain due to cracking may be obtained from Equation 3.8, and thus the total strain of the element becomes:

$$\varepsilon = \varepsilon_e + \varepsilon_{cr} \tag{3.9}$$

where ε_e is the elastic strain. Hence, the cracking is assumed to be smeared over an entire element. It is therefore necessary to choose the band width equal to the element size in order to avoid mesh dependency of the results. An appropriate element size of 3 times the maximum particle size was estimated by Bažant & Oh (1983) based on experimental results. It is, however, also important to avoid internal element snap-back behavior, which imposes the following criteria on the choice of h:

$$\frac{d\sigma_w(w)}{d\varepsilon} \geq -E \tag{3.10}$$

where the derivative is calculated at the initial portion of the stress-crack opening relationship. The advantage of the crack band modelling is the easy implementation in finite element codes since the inelastic strain can be treated as any other non-linear problem. Also models for multidirectional cracking may be implemented. Furthermore, there is no need of incorporation of elements to describe the cracking behavior separately - this is included in the solid elements. And, finally, the crack path is not preferred in advance, as is often the case for discrete cracking.

3.3 Time-Dependency of Concrete Fracture

Similar to the viscoelastic behavior of the bulk material, concrete fracture is influenced by time-dependent mechanisms. The static stress-crack opening relationship shown in Figure 3.9 does only represent the constitutive behavior in its simplest form. Two different approaches are proposed in literature which both includes the time-dependent effects. One explanation is that the time effects occurring in the fracture zone arise from the rate-effect on the breakage of bonds on the atomic level, see e.g. (Wu & Bažant 1993) or (Bažant & Li 1997). The other approach takes origin in traditional hereditary law creep modelling of concrete and adopts e.g. a Kelvin chain unit to describe the time-dependent behavior, see (Hansen 1990) and (Santhikumar & Karihaloo 1996). These approaches will be explained further in the following.

3.3.1 Visco-Elastic Effects in Concrete Fracture

Creep of concrete has successfully been modelled by application of the Maxwell and Kelvin chains, see Chapter 4, and it seems obvious to expand this type of modelling to the time-dependent fracture of the material. The first author to use this approach was Hansen (1990) who developed a viscoelastic fictitious crack model based on a three parameter viscoelastic solid using the Kelvin chain. The differential equation for this case is given by:

$$(E_1 + E_2)\sigma + \eta\dot{\sigma} = E_1 E_2 \varepsilon + \eta\dot{\varepsilon} \tag{3.11}$$

where E_1 and E_2 are the age-independent spring stiffness, η is the viscosity of the dashpot while σ and ε are the stress and strain respectively. Solving Equation 3.11 assuming either constant stress σ_0 or constant strain ε_0 gives the creep and relaxation functions, respectively:

$$\varepsilon(t) = \sigma_0 \left[\frac{1}{E_1} + \frac{1}{E_2} \left(1 - e^{-t/\tau_1} \right) \right] \tag{3.12}$$

$$\sigma(t) = \varepsilon_0 \left[\frac{E_1 E_2}{E_1 + E_2} + \left(E_1 - \frac{E_1 E_2}{E_1 + E_2} \right) e^{-t/\tau_2} \right] \tag{3.13}$$

where $\tau_1 = \eta/E_2$ and $\tau_2 = \eta/(E_1 + E_2)$ are denoted retardation times. The idea proposed by Hansen (1990) is to modify Equations 3.12-3.13 to fit the situation valid in the cracked situation, see e.g. 3.9. To do so, the strain must be replaced by the crack opening w and furthermore the stiffness of the springs and the viscosity of the dashpot must be negative in order to simulate the descending stress as a function of the crack opening w. Thus, Equations 3.12-3.13 are modified to read:

$$\varepsilon(t) = (f_t - \sigma_0) \left[\frac{1}{M_1} + \frac{1}{M_2} \left(1 - e^{-t/\tau_1} \right) \right] \tag{3.14}$$

$$\sigma(t) = f_t - \varepsilon_0 \left[\frac{M_1 M_2}{M_2 - M_1} + \left(M_1 - \frac{M_1 M_2}{M_2 - M_1} \right) e^{-t/\tau_2} \right] \tag{3.15}$$

where $M_1 = E_1$, $M_2 = -E_2$ and $\eta' = -\eta$. Note that the term $-\sigma_0$ has been replaced by $(f_t - \sigma_0)$ in Equation 3.14 in order to obtain a positive opening for a given crack opening w, and likewise, f_t has been added in Equation 3.15 in order to arrive at positive, decreasing stresses with time.

The model by Hansen (1990) was extended in the work by Santhikumar (1998), see also (Santhikumar, Karihaloo & Reid 1998). In this work, a generalized Kelvin chain model with n chain units was adopted, and the solidification theory by Bažant & Prasannan (1989*a*) was implemented in order to account for the ageing of the concrete. In this work it was also assumed that the stress transfer as function of the crack opening could be described by the effective spring concept:

$$\sigma(w) = k(t)w \tag{3.16}$$

where the stiffness $k(t)$ of the springs is chosen in accordance with the solidification theory in order to account for ageing, while the stiffness is also dependent on the position on the static stress-crack opening relationship curve, see e.g. Figure 3.9. Thus, if the stress in the spring is below the static stress-crack opening, creep or relaxation depending on the loading conditions is allowed to take place until the failure envelope, $\sigma(w)$, is reached. Then, if at any point of time, $\sigma(w)$ is reached or violated, relaxation is required to take place until once again the stress is within or on the static $\sigma(w)$.

3.3.2 Rate-dependency of Concrete Fracture

The time-dependency of concrete fracture may also be explained by the rate effect on bond rupture. The hypothesis by Wu & Bažant (1993) is based on the assumption that the rate of breakage of bonds is governed by the Maxwell-Boltzmann distribution of the vibration frequency of atoms or molecules possessing a certain specified energy level U:

$$f = k_b e^{U/(RT)} \tag{3.17}$$

where k_b is a constant, R is the natural gas constant and T is the temperature. The potential of the bond forces, U, has a certain maximum, Q, and if the potential surpasses this threshold value, the bond will break. It is now postulated that, based on Equation 3.17, the rate of breakage of bonds may be formulated as, see also (Wu & Bažant 1993):

$$\dot{w} = \dot{w}_r \sinh[\psi(\sigma(w), w)] e^{(Q/(RT_0) - Q/(RT))} \tag{3.18}$$

where $\dot{w}_r$ represents a reference crack opening velocity, T_0 is the reference temperature, and $\psi(\sigma(w), w)$ is given by:

$$\psi(\sigma, w) = \frac{\sigma(w) - \sigma_r(w)}{k_1(\sigma_r(w) + k_0 f_t)} \tag{3.19}$$

in which k_1 and k_0 are constants and f_t is the tensile strength. The function $\sigma_r(w)$ is the stress-crack opening relationship for infinitely slow rate of crack opening displacement. Equations 3.18-3.19 may be rewritten such that the stress-crack opening relationship at the actual rate of crack opening is determined, assuming $T = T_0$:

$$\begin{aligned} \sigma(w) &= \sigma_r(w) + k_1[\sigma_r(w) + k_0 f_t] \sinh^{-1}\left(\frac{\dot{w}}{\dot{w}_r}\right) \\ &= \sigma_r(w)\left[1 + k_1 \sinh^{-1}\left(\frac{\dot{w}}{\dot{w}_r}\right)\right] + k_1 k_0 f_t \sinh^{-1}\left(\frac{\dot{w}}{\dot{w}_r}\right) \end{aligned} \tag{3.20}$$

This formulation was investigated by Wu & Bažant (1993) and later developed in other papers, e.g. (Bažant & Li 1997) and (Li & Bažant 1997). It was found, in combination with modelling of the bulk creep of the undamaged material, to be able to describe the real behavior seen in experiments, although the authors pointed at the need for further research. A value of k_1=0.01-0.08 was estimated by Wu & Bažant (1993) based on experimental experience.

The model was adopted in the work by Zijl, de Borst & Rots (2000) who made a finite element implementation and found good agreement with experimental results. The experimental results were adopted from Zhou (1992) who conducted creep failure tests on three point bending beams. The experimental data was fitted by Zijl et al. (2000) who found k_1=0.05, k_0=0.1 and $\dot{w}_r = 10^{-7}\text{s}^{-1}$. A simple alternative to the model expressed in Equation 3.20 was proposed by Zijl et al. (2000) in which it is assumed that the rate dependency is caused by a viscosity term:

$$\sigma(w) = (f_t + \mu_r \dot{w})\sigma_r(w) \tag{3.21}$$

in which μ_r is the viscosity. This formulation was also used to fit experimental data, but the agreement was not found to be as convincing as Equation 3.20. The best fit for the viscosity was found to be $\mu_r = 1500$ Ns/mm^2.

3.4 Fracture Mechanics and Early Age Concrete

The bilinear stress-crack opening relationship given in Figure 3.9 may be utilized for early age concrete without any modifications. This type of approximation of the real behavior was also the simplification adopted in (Wittmann et al. 1987) for the determination of stress-crack opening relationships for early age concrete. Also Brameshuber (1988) adopted the bilinear stress-crack opening relationship for early age concrete. Furthermore, this approximation is widely accepted in literature as capturing the main features of the stress-crack opening relationship, see e.g. (Rossi, Brühwiler, Chhuy, Jenq & Shah 1991) and (Olesen 2001*a*). However, other formulations exist, like e.g. the assumption in (Hillerborg et al. 1976) (linear), (Zijl et al. 2000) (exponential) etc. The linear assumption is probably too simple since it does not capture the tail of the curve, which describes the aggregate (or fiber, if present) pullout and which may contribute significantly to the fracture energy. Hence, if a linear function is adopted, the slope will be too low compared with the real behavior in order to keep the fracture energy constant, thus changing the predicted material behavior. Other simplifications of the stress-crack opening relationship exist, see e.g. the number of formulations in (Karihaloo 1995).

It is more troublesome to choose a concept for the rate dependency of the stress-crack opening relationship since here apparently two different methods are available in literature, see the Sections 3.3.1-3.3.2. However, a number of reasons point at the rate-dependency. It seems questionable to use negative spring stiffness and viscosity in the Kelvin chain as done by Hansen (1990), since this contradicts fundamental thermodynamic conditions. In the case of the model by Santhikumar (1998), this problem has been overcome, and a more general model developed. This model is shown to yield very good results in an application example where the time-dependent crack growth in a large concrete dam was investigated, (Karihaloo & Santhikumar 1999). However, this model does not consider time-dependency of the crack itself, but rather the aging viscoelastic behavior of the bulk

material in the vicinity of the crack. The fundamental stress-crack opening relationship is static and not changing while the creep and relaxation of the surrounding material is incorporated into the model and governs the time-dependent behavior. This approach does lead to fine results, but the viscoelasticity of the bulk material is mixed up with the properties of the crack. In a finite element analysis, where the viscoelasticity is accounted for elsewhere, it would not be the correct approach to include it in the stress-crack opening relationship.

Instead, it seems more promising to view the time-dependent properties of the crack as arising from the rate effect on the opening velocity. The validity of the two constitutive relations proposed in Section 3.3.2 will be investigated further in the Chapter 5.

The age dependency of the stress-crack opening relationship will be modelled using age dependent functions for each of the parameters in the stress-crack opening relationship:

$$\begin{aligned} f_t &= f_t(t) \\ a_1 &= a_1(t) \\ a_2 &= a_2(t) \\ b_2 &= b_2(t) \end{aligned} \tag{3.22}$$

All the short-term experiments will be conducted at almost the same and constant crack opening rates in order to yield reference curves, which may be applied as basis in the rate-dependent formulation employed to model the long term behavior.

The rate-dependency is in turn assumed to be age independent. This latter assumption is justified by the fact that the rate-dependency is accounting for the rate of breakage of bonds, and thus, not for the aging, i.e. not the number of bonds. Of course, the critical potential needed to break the bonds, Q, may change during aging due to changes in the hydration reactions, but a reasonable first assumption is that this does not happen, and that the significant ageing effects are captured by the functions given in Equations 3.22.

Chapter 4

Viscoelasticity for Concrete

The phenomenological aspects of creep and relaxation of concrete was explained in Section 2.4. It was then explained how the time-dependent deformations of bulk concrete is dependent on numerous factors like age at load application, load level, duration of load, temperature, humidity, changes of these parameters, etc., etc. This chapter aims at introducing the modelling framework, which has been used in literature with respect to these problems.

4.1 Creep and Relaxation

Time-dependent deformations of viscoelastic materials are often divided into creep and relaxation, depending on the boundary conditions. These differences are illustrated in Figure 4.1. For the situation where a constant load, σ_0, is applied, the deformation will increase with time as shown in the figure. This increase, whose mechanisms were explained in Section 2.4, is called creep. On the other hand, if a constant deformation, ΔL, is imposed on the structure, the stresses will decline with time as shown in the lower graph in the figure.

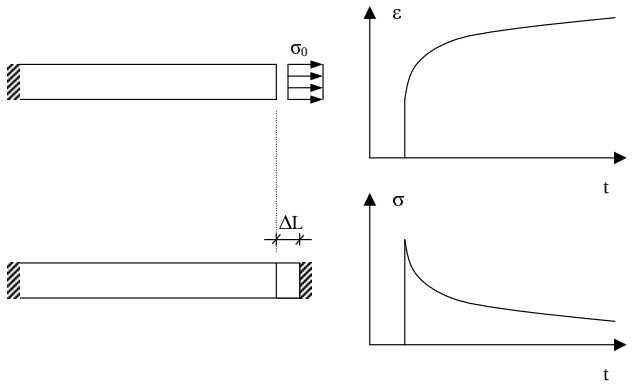

Figure 4.1 *Creep and relaxation of a viscoelastic material when subject to a constant load or a constant deformation, respectively*

If the material is non-ageing, the respond to both these conditions will be the same regardless of the time point of application. However, as well known, concrete is an ageing material, especially in the early ages, which greatly complicates the situation. If the material is assumed to be non-ageing, the time-dependent deformations may be described with a simple compliance function:

$$\varepsilon(t) = J(t - t')\sigma_0 \tag{4.1}$$

in which t denotes time, t' the time point of load application and $J(t - t')$ is the compliance, which is only dependent on the load duration, $t - t'$. If, on the other hand, a constant deformation is imposed on the structure, the time-dependent stress may be described employing a non-ageing relaxation function $R(t - t')$:

$$\sigma(t) = R(t - t')\varepsilon_0 \tag{4.2}$$

Equations 4.1-4.2 may be generalized to a random load or strain history utilizing the principle of superposition. This is clear since the respond to any load or deformation is independent of the magnitude of the load and since the compliance and relaxation functions are non-ageing, see e.g. (Lemaitre & Chaboche 1994) or (Flügge 1975). The relation between the compliance and the relaxation functions may be shown to be (Lemaitre & Chaboche 1994):

$$R(t - t')\frac{dJ(t - t')}{dt} = J(t - t')\frac{dR(t - t')}{dt} \tag{4.3}$$

Thus, if either $R(t - t')$ or $J(t - t')$ is known, the other function may be derived thereof using Equation 4.3.

In a real structure, the situation will of course not be as simple as the one depicted in Figure 4.1. In this case, besides the many couplings with other effects, the two situations will almost always be mixed such that both relaxation and creep will take place in a given situation, depending on the degree of restraint of the part of the structure under analysis.

Furthermore, concrete exhibits as known ageing, which makes the relaxation and creep functions age dependent, i.e. dependent on not only the load span, but also the time point of load application. Thus, the compliance is given by $J(t, t')$ instead of $J(t - t')$. This will be elaborated further in the next section.

4.2 Integral Modelling of Viscoelastic Behavior

The traditional models for concrete creep are integral in nature, i.e. they are based on a unique compliance function $J(t, t')$, which predicts the time-dependent deformations as function of time at application t' and duration of load, $(t - t')$. As already touched in Section 2.4, modelling of the time-dependent deformations are often conducted by application of rheologic models like the Kelvin or the Maxwell chains. Both the generalized Kelvin model with n chain units and the generalized Maxwell chain with n units are shown in Figure 4.2.

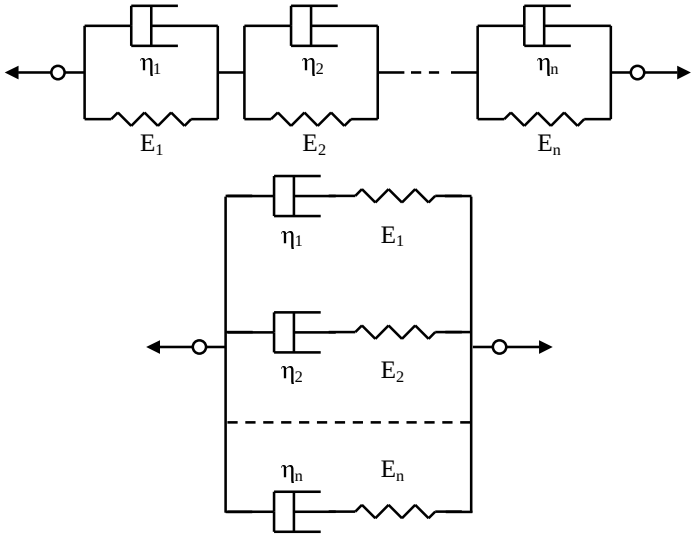

Figure 4.2 *Kelvin chain composed of n Kelvin units in serial connection (upper part) and Maxwell chain composed of n Maxwell units in parallel connection (lower part).*

This type of modelling is - phenomenologically - able to capture the time dependent deformations of concrete. An often applied variant is the Kelvin chain with three units, in which one dashpot viscosity, say η_1, and one spring stiffness, say E_3 are set to zero, while the rest, η_2, η_3, E_1, E_2 are fitted to available experimental data. This model is called the Burger model (see e.g. Figure 4.3) and may with success be applied to concrete, see e.g. (Nielsen 1999*b*), or cement paste, (Dela 2000), if ageing of the material is considered.

The reason for the age dependency are the progressing hydration reactions, which may change the behavior of the concrete in many years after casting, and also recrystallization and polymerization of the already formed hydration products, which in part is responsible for some of the long term ageing effects, (Bažant 1988). The ageing is especially important for early age concrete since the rapid change of all important material properties also causes fast changes of the time-dependent respond. One way the time-dependency of the viscoelastic respond may be implemented is by regarding the individual elements in the preferred rheological model as time-dependent, i.e. $E_n(t)$ and $\eta_n(t)$. Functions fitting this time-dependency may be found in literature; e.g. the dependency of the spring stiffness is often modelled employing the Avrami-type equation (Equations 2.1-2.2), see e.g. (Nielsen

1999*b*), and (Hauggaard-Nielsen 1997). The time-dependency of the viscosities may be taken into account by the logarithmic expression (Nielsen 1999*b*):

$$\eta(t) = F\frac{t}{1 + C/t} \tag{4.4}$$

where F and C are constants, which are fitted to experimental results. More complex functions may be found in literature, (Hauggaard-Nielsen 1997). The compliance function for the Burger model may be found in (Flügge 1975).

Another method of modelling the ageing of concrete, which appears more consistent is presented by Bažant & Prasannan (1989*a*). This principle is called the solidification theory and is based on a model for the concrete ageing. Here, the growth of the solidified volume fraction $v(t)$ is assumed to account for the ageing of the time-dependent respond. The compliance function based on the solidification theory is given by:

$$J(t,t') = q_1 + q_2 F(\sigma) Q(t,t') + q_3 F(\sigma) \ln\left[1 + \left(\frac{t-t'}{\lambda_0}\right)^n\right] + q_4 F(\sigma) \ln\left(\frac{t}{t'}\right) \tag{4.5}$$

in which:

$$\begin{aligned} F(\sigma) &= \frac{1 + (\sigma/f_c)^2}{1 - (\sigma/f_c)^{10}} \\ Q(t,t') &= \int_{t'}^{t} \left(\frac{\lambda_0}{\tau}\right)^m \frac{n(\tau - t')^{n-1}}{\lambda_0^n + (\tau - t')^n} d\tau \end{aligned} \tag{4.6}$$

where λ_0, m and n are material constants, which based on experimental experience can be fixed to $\lambda_0 = 1$ day, m=0.5 and n=0.1, (Bažant 1988). The function $F(\sigma)$ accounts for the damage, which is only notable for stress levels higher than σ/f_c=0.7. The parameter f_c is the compressive strength while the coefficients $q_1 - q_4$ are constants fitted to experimental creep data.

General stress-histories may be taken into account in the integral creep models by the principle of superposition. In this case, the strain at the time t may be determined as:

$$\varepsilon(t) = \int_0^{\infty} J(t,t') d(\sigma(t') + \sigma_0 J(t, t' = 0) \tag{4.7}$$

where the stress increment $d(\sigma(t'))$ is imposed at time t', at which time point the compliance function is given by $J(t,t')$. Furthermore, an initial contribution σ_0 has been added

to Equation 4.7. However, not all effects concerning creep of concrete may be superimposed. The principle is only applicable if basic creep is considered, the stresses are low (less than 40% of the strength), the strains are monotonically increasing and the stress distribution shows no sudden changes, (Bažant 1988). More general conditions must be modelled using an incremental approach.

4.3 Incremental Modelling of Viscoelastic Behavior

The incremental approach towards the modelling of the time-dependent deformations of concrete has several advantages. It is, first of all, less demanding with regard to the memory of the materials. In the integral approach, knowledge of the entire load-deformation history must be known since it is required in order to solve Equation 4.7, while the incremental approach only requires storage of the present stress and strain and a few state variables, like e.g. the total stress and strain, see e.g. (Hauggaard-Nielsen 1997) or (Altoubat 2000). Besides this fact, also the limited applicability of the principle of superposition, as already discussed in the previous section, impedes the integral type of modelling. These problems are accentuated in early age concrete where the non-linearities in the creep behavior are more pronounced.

Figure 4.3 shows an example of one often applied rheological model used for concrete, i.e. the Burger model. This model was adopted by Hauggaard-Nielsen (1997) who made an incremental formulation. The derivation of the incremental formulation is summarized here.

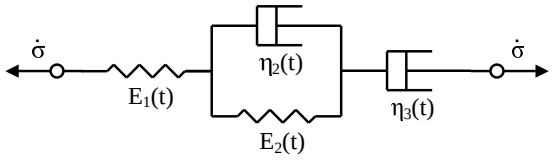

Figure 4.3 *The Burger rheological model for incremental ageing viscoelasticity*

The rheologic model shown in the figure captures the main types of time-dependent deformation in concrete. It has a spring, whose stiffness, E_1, accounts for the instantaneous deformation occurring upon application of a load. The reversible time-dependent viscoelastic deformations are accounted for by the single Kelvin unit. This unit will, over time, increase the deformation, but if the load is removed, the process is reversed and the strain of the unit will asymptotically approach zero again. Finally, the single dashpot, η_3, accounts for the irreversible or viscoplastic deformation. The stiffness and viscosities of the single elements in the Burger model are assumed to be time-dependent, i.e. $E_1(t)$, $E_2(t)$, $\eta_2(t)$ and $\eta_3(t)$. As the figure shows, in the incremental approach only the stress increment and the strain increments are considered. The total strain increment of the model is determined by adding the different contributions from the individual elements:

$$\dot{\varepsilon} = \dot{\varepsilon}_1 + \dot{\varepsilon}_2 + \dot{\varepsilon}_3 \tag{4.8}$$

The strain increments from each unit may now be determined. The strain increment of the single spring with the stiffness $E_1(t)$ is given by:

$$\dot{\varepsilon}_1 = \frac{\dot{\sigma}}{E_1(t)} \tag{4.9}$$

where $\dot{\sigma}$ is the stress increment. The stress increments in the individual elements of the Kelvin unit are given by:

$$\dot{\sigma} = \dot{\sigma}_2^s + \dot{\sigma}_2^d \tag{4.10}$$

where $\dot{\sigma_2^s}$ denotes the stress increment in the spring of the Kelvin unit while $\dot{\sigma_2^d}$ is the stress increment in the dashpot of the Kelvin unit. The stress increment in the spring is readily obtained as:

$$\dot{\sigma}_2^s = E_2(t)\dot{\varepsilon}_2 \tag{4.11}$$

The stress increment of the dashpot in the Kelvin chain is determined by differentiating the total stress in the element at the time t. The total stress in the element is given by:

$$\sigma_2^d = \dot{\varepsilon}_2\eta_2(t) \tag{4.12}$$

and by differentiation, the stress increment is determined:

$$\dot{\sigma}_2^d = \dot{\varepsilon}_2\dot{\eta}_2(t) + \ddot{\varepsilon}_2\eta_2(t) \tag{4.13}$$

Knowing the stress increments of both the elements in the Kelvin chain, Equations 4.11 and 4.13, insertion in Equation 4.10 gives:

$$\begin{aligned} \dot{\sigma} &= E_2(t)\dot{\varepsilon}_2 + \dot{\varepsilon}_2\dot{\eta}_2(t) + \ddot{\varepsilon}_2\eta_2(t) \\ &= \eta_2(t)\ddot{\varepsilon}_2 + \left(E_2(t) + \dot{\eta}_2(t)\right)\dot{\varepsilon}_2 \\ &= \dot{\sigma}_1^s \end{aligned} \tag{4.14}$$

where the stress increment of the single spring is denoted by $\dot{\sigma}_1^s$. Rearranging Equation 4.14 gives:

$$\ddot{\varepsilon}_2 + \frac{E_2(t) + \dot{\eta}_2(t)}{\eta_2(t)}\dot{\varepsilon}_2 = \frac{\dot{\sigma}_1^s}{\eta_2(t)} \tag{4.15}$$

This differential equation may be solved in time steps assuming that the material properties are constant within each step, i.e. the central value of the material property within the time step is used. By doing so, $\dot{\eta}_2 = 0$, and Equation 4.15 may be reduced to:

$$\ddot{\varepsilon}_2 = \frac{1}{\bar{\eta}_2}\left(\dot{\sigma}_1^s - \dot{\sigma}_2^s\right) = \frac{\dot{\sigma}_2^d}{\bar{\eta}_2} \tag{4.16}$$

where $\bar{\eta}_2$ denotes the value of the viscosity at the middle of the time step, and where the latter equality is obtained by differentiation of Equation 4.11. Integration of Equation 4.16 yields:

$$\dot{\varepsilon}_2 = \frac{\sigma_2^d}{\bar{\eta}_2} \tag{4.17}$$

The strain increment of the single dashpot is obtained similarly to Equation 4.11:

$$\dot{\varepsilon}_3 = \frac{\sigma_3^d}{\bar{\eta}_3} \tag{4.18}$$

Thus, finally the stress increment of the Burger model is obtained by inserting the results from Equations 4.9, 4.17 and 4.18 in Equation 4.8:

$$\dot{\sigma} = E_1(t)(\dot{\varepsilon} - (\dot{\varepsilon}_2 - \dot{\varepsilon}_3)) \tag{4.19}$$

This model was found by Hauggaard-Nielsen (1997) to be sufficient in the modelling of concrete at constant temperature. For varying temperatures, the model was extended with a concept called microprestressing and applied with good correlation to experimental results, see (Hauggaard-Nielsen 1997).

4.4 Viscoelasticity and Early Age Concrete

It turns out that traditional creep models are not able to capture the pronounced creep behavior of early age concrete. This was found by Emborg (1989) who concluded that the predictions in early age of the triple power law for creep of concrete, (Bažant & Oh 1983), did not match experimental findings on normal concrete. However, by applying certain correction functions, a very fine agreement was obtained, see e.g. (Emborg 1989). Later, in the work by Westman (1995), a similar approach was adopted and found to be suited for the early age modelling of high performance concrete.

In the case of the compliance function based on the solidification theory, Equation 4.5, Østergaard, Lange, Altoubat & Stang (2001) found that also this formulation does not match the large creep of early age concrete. However, a simple modification of the coefficient associated with the ageing viscoelastic compliance term, q_2, was determined as sufficient for the inclusion of early age basic tensile creep:

$$q_2 = q_2' \frac{t'}{t' - q_5} \tag{4.20}$$

Conclusively, it is demonstrated that the integral models have trouble capturing the creep of early age concrete. Such shortcomings are overcome if the incremental approach is adopted.

Chapter 5

Test methods for early age concrete

This chapter will give a detailed description of the conduction and interpretation of the most common test geometries for fracture mechanical testing of concrete. The reason for the extensive character of this chapter is that no consensus exists on exactly how fracture mechanical testing at early ages should be conducted. Most researchers use the three point bending test in ordinary fracture testing, but this test method is not, due to problems with self-weight, the most suited method for early age concrete.

Many researchers use the split cylinder test in order to obtain an estimate on the tensile strength of the concrete - but how does this test method, for which the interpretation is exclusively based on simple linear elastic formulas, behave if the material changes significantly, as is the case for early-age concrete. Does the split cylinder test stand a finite element modelling in which the constitutive properties are selected such that early age concrete is simulated?

A very promising test method for determination of early age fracture mechanical properties is the wedge splitting test. This is due to the limited self-weight problems, which may, with very simple means, be eliminated entirely. However, not very many researchers have been engaged in the development of this test method - so how should the interpretation be carried out, and how reliable are the results, which may be obtained from the test method?
Besides these considerations there is still no consensus on whether or not the indirect test methods such as the three-point bending test and the wedge splitting test may at all be employed for the determination of the stress-crack opening relationship. Some researchers believe that local minimums may restrict inverse analysis from being carried out, while others are concerned about the energy dissipated outside the final, critical crack in the indirect methods. For these reasons, research based on the indirect testing methods still has be validated and calibrated using the only apparently simple direct testing method, namely the uniaxial tension test. Therefore, this method will be described together with the numerous problems associated with the practical conduction of the test. Problems, which have lead to advanced technical solutions over the years at different research institutions; and which have resulted in different opinions on how to conduct the experiment.

5.1 Uniaxial tension test

The uniaxial tension test is one of the few test methods, which through a simple interpretation directly yields the stress-crack opening relationship for the material under analysis.

This, however, only holds true if the test is conducted under very well controlled conditions, a fact, which has resulted in some debate in the literature. The key issue in the controversy is the influence on the experimental result of the actual propagation of the crack through the specimen and how this propagation is influenced by rotations at the specimen boundary. Some researchers believe that the specimen boundary should be free to rotate, see e.g. (van Mier 1986), (van Mier 1997), (van Mier & Shi 2002), (van Mier & van Vliet 2002) etc. Other researchers believe that not only the specimen boundary but more important also the material in the vicinity of the crack, i.e. the crack planes, must be prevented from rotating, see e.g. (Zhou 1988), (Hillerborg 1989), (RILEM 2001), (Østergaard & Stang 2002). Due to this inconsistency in the research community, a very detailed walk-through of the mechanisms in the uniaxial test method will be carried out here.

Concrete is well known for the inherent inhomogeneity of the material, see e.g. Figure 3.7. Due to this fact and due to different stiffness and Poisson's ratios of the constituents, significant differences in the stress distribution may be measured if a tiny sample of the material is subjected to a uniaxial uniform strain, see left part of Figure 5.1. However, a very useful assumption, which is often applied is that the material macroscopically may be described as homogeneous, see e.g. (Stang 1984). Thus, if a sufficiently large sample is considered, the stress variations will be acceptably small. The necessary volume is called the representative volume element (RVE). If the volume under consideration is smaller than the RVE, the calculations may still be conducted utilizing microstructural models like e.g. the lattice model, (van Mier 1997). Sufficiently large volumes may be modelled employing a macroscopic assumption implemented in e.g. standard finite element software. Now, a strip of concrete larger than the RVE is considered, see right part of Figure 5.1. The properties of this strip are varying, but the variations will be small. However, if subjected to a uniaxial displacement field, any crack will naturally start to propagate at the weakest spot. The presence of a notch may complicate the picture due to stress-concentrations and consequently the crack in a uniaxial tension test usually starts to propagate at the perimeter of the specimen, regardless of the position of the weakest spot.

An imaginary uniaxial tension test is now conducted using the aforementioned strip of concrete, see Figure 5.2. The strip of concrete is attached to a material, which is wider and thus subject to a lower stress level, but has the same stiffness and Poisson's ratio as the concrete strip. The boundaries of this material are free to rotate during the experiment. Furthermore, this material is attached to a testing machine whose properties do not disturb the stress distributions in the specimen, and controls the translation of the attached material in a stable way. Due to the notch, which has been introduced by the attachment of the wider material, the concrete strip starts to crack at one of the crack tips, e.g. the left one as shown in situation 1 in Figure 5.2. Now, this side of the con-

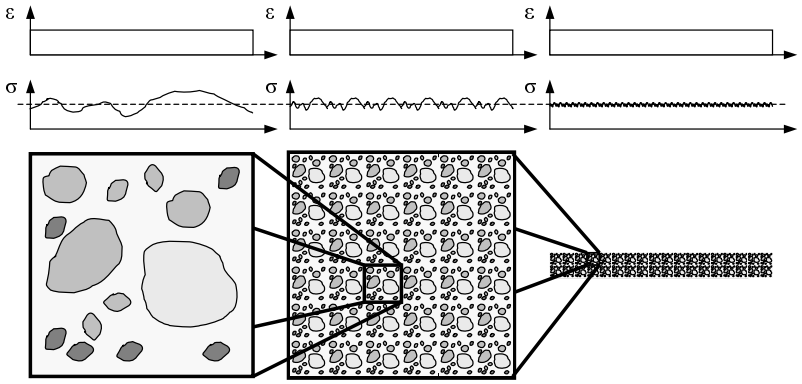

Figure 5.1 *The concrete strip being tested must be a representative volume element (RVE)*

crete strip is weakened and the crack will propagate further into the strip from the same side, e.g. situations 2 and 3. Actually, the crack may in this situation propagate entirely through the strip from one side, situation 4, since the rotational freedom can do nothing to prevent it. The consequence of this fact is that the crack opening displacements of the crack varies over the entire width of the strip. Thus, the stress-crack opening relationship may not be derived directly from the global load-deformation curve, since the underlying averaging may not be true. This fact is evident from the literature, see e.g. (Zhou 1988), (Hillerborg 1989) or (Østergaard & Stang 2002). It shall also be demonstrated using the finite element method later in this chapter.

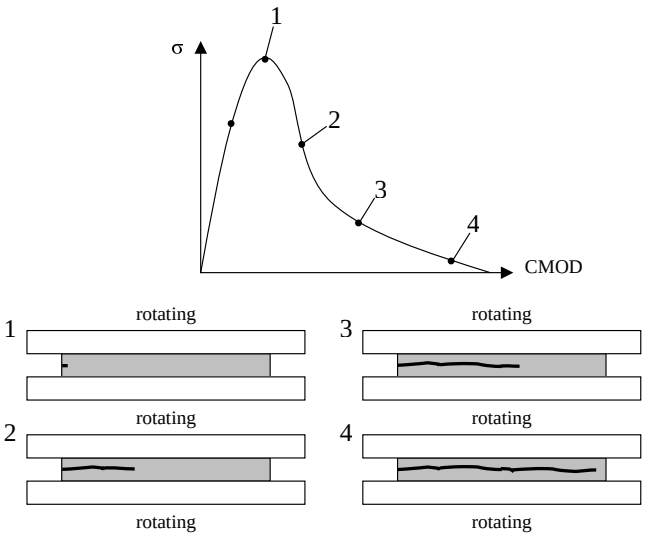

Figure 5.2 *Fracture of RVE with no rotational stiffness of the boundary planes*

Hence, a system where the crack boundary planes are free to rotate is unsuitable. Therefore, this rotation must somehow be eliminated. This is, unfortunately, very difficult as experienced by many researchers, and as a result, often only a partial restriction of the

rotations is achieved. The outcome of an imaginary experiment on the concrete strip in the situation where partial rotation of the crack boundary planes is possible is shown in Figure 5.3. In this case a significant hump (by some authors called a "bump") will be seen on the global load-deformation curve. This is demonstrated in the figure. The cause of the hump was explained first by Zhou (1988) and Hillerborg (1989) who found that, depending on the rotational stiffness of the crack boundary planes, instability may occur resulting in a situation where inclined crack planes are in equilibrium with the external normal force and moment. This is the case shown in Figure 5.3, situation 2. But at some point of crack opening, this equilibrium cannot be maintained anymore and the boundary planes will rotate back to the parallel orientation. This causes as a consequence crack closure in the first crack, while a second crack opens up on the other side. Now, rapidly, this second crack propagates through the specimen and reaches the tip of the first crack, situation 3 and 4. Of course, as noted by van Mier (1997), these two crack systems may not coalesce perfectly into one crack, which is caused by the heterogenous nature of concrete, but this fact cannot explain the hump seen in the curve. The hump is solely due to the fact that the crack boundary planes are allowed to experience some rotation, as demonstrated by Østergaard & Stang (2002), and as shall be demonstrated later. In fact, the two crack systems will rapidly start to behave as one discrete crack, and any secondary cracking will soon experience crack closure.

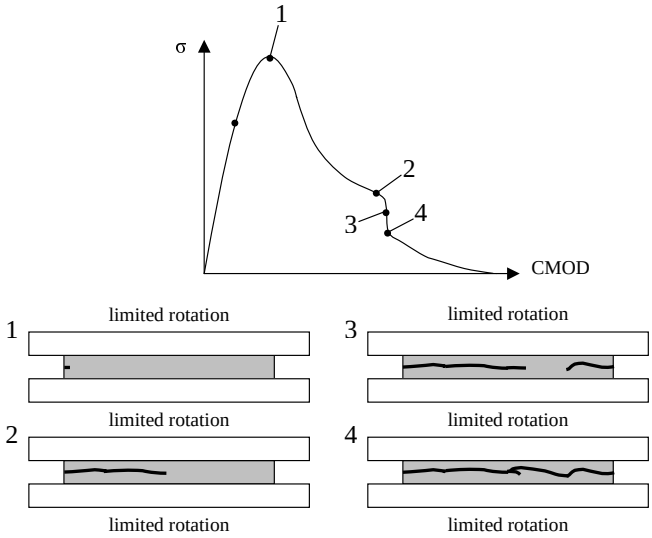

Figure 5.3 *Fracture of RVE with insufficient rotational stiffness of the crack boundary planes*

The reason for the fact that the hump is not seen in the case of no rotational stiffness, see Figure 5.2, is very simply that no moment can build up and thus, no moment will ever be present to counteract the rotation. This was also demonstrated by Hillerborg (1989). However, when a limited rotational stiffness is present, humping occurs. This can *not* be employed as an argument against rotational stiffness, but *only* as an argument for increased rotational stiffness.

Figure 5.4 demonstrates the case where the rotational stiffness is sufficient to suppress the rotation of the boundary planes. In this case, as in the two former cases, the crack initiates at the tip of one of the notches, here the left notch, see situation 1 in the figure. However, since the crack boundary planes are prohibited from rotation, the crack will almost immediately propagate through the concrete strip, as shown by the close occurrence of situations 2, 3 and 4. The only delay of this process will be the heterogeneity of the material, which by assumption has a limited influence. Now, the crack planes are strictly parallel and all points on the crack experience the same opening for a given load. Thus, a very simple procedure may be applied in order to derive the stress-crack opening relationship, i.e. subtraction of the elastic deformation from the measured global load versus local deformation curve. This fact was demonstrated in (Zhou 1988) and also in (Østergaard & Stang 2002) and will be elaborated further later. Note that the hump theoretically still will be present, since the crack uses a little time to propagate from one side to the other, but the influence on the stress-crack opening relationship is vanishing.

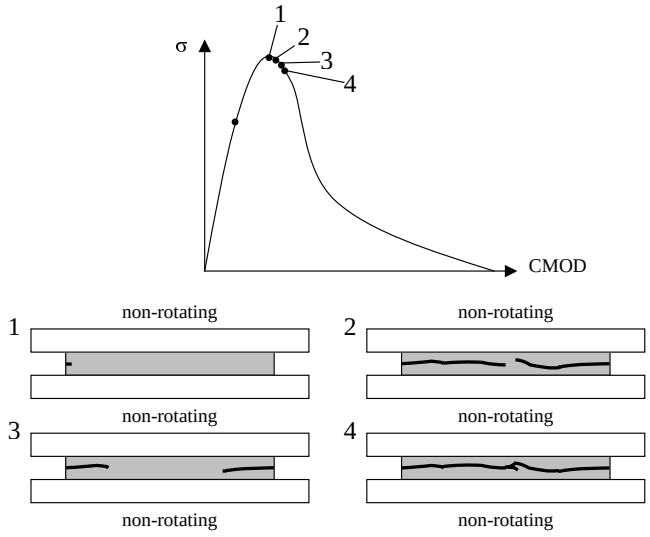

Figure 5.4 *Fracture of RVE with infinite rotational stiffness of the boundary planes*

Thus, it has been demonstrated that the crack boundary planes must be parallel in the uniaxial tension test. Lack of or insufficient machine rotational stiffness will influence the result and make the results questionable.

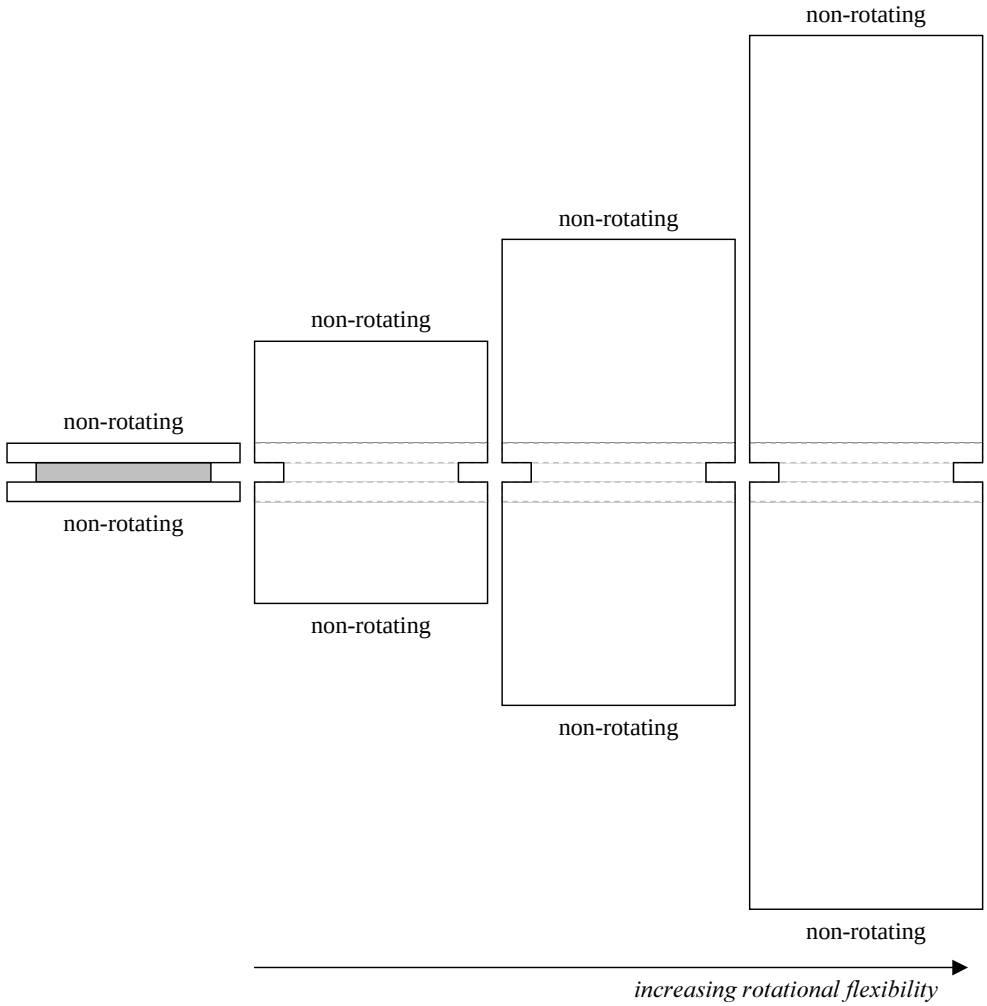

Figure 5.5 *Influence of the specimen length on the rotational flexibility of the crack boundary planes*

The imaginary experiment discussed so far in the Figures 5.2-5.4 does not represent a real situation. In practice, it will not be possible to obtain a uniaxial stress field in such a short concrete strip. The specimen must be given a certain length. The influence of this specimen length is illustrated in Figure 5.5. The situation on the left represents the concrete strip. This strip is now build into a specimens with different lengths, see the three specimens to the right. All these specimens are build into a testing machine, which is supposed to be able to suppress any rotation at the specimen boundaries, see the figure. However, as the specimen gets longer and longer, it also achieves a higher and higher rotational flexibility at the crack boundary planes. In fact, a too long specimen may result in some rotational capability of the crack planes, thus resulting in the situation shown in Figure 5.3. This situation occurred for van Mier (1986) who in a finite element model applied non-rotating specimen boundaries, but on a long and slim specimen (280 x 75 mm^2, 13 mm thick). Thereby it was, accidentally, achieved that the crack boundary planes were somewhat rotating, resulting in a hump; a fact that is very clearly seen in the results. Instead, it is more correct to use short specimens, as the one given as the second

specimen from the left in Figure 5.5. This specimen schematically resembles the RILEM standard uniaxial tension test specimen, see (RILEM 2001).

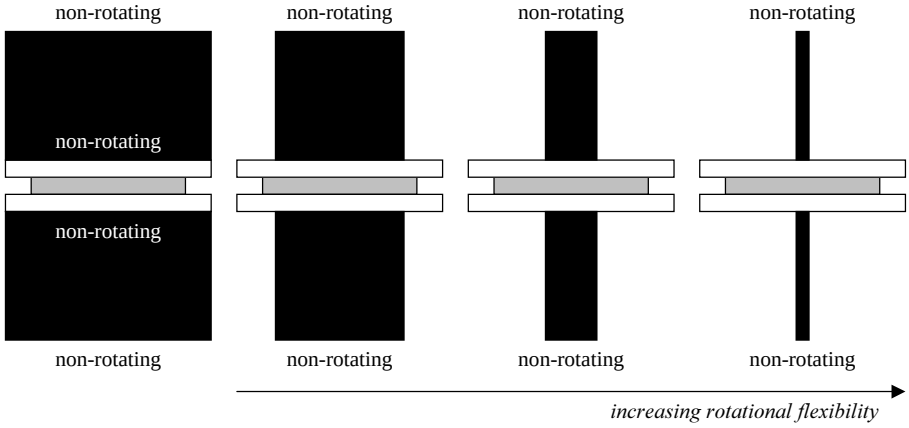

Figure 5.6 *Influence of the rotational stiffness of the testing machine on the rotational flexibility of the crack boundary planes*

The latter problem is the stiffness of the testing machine itself. This problem is illustrated in Figure 5.6 in which the rotational stiffness is symbolized by the thickness of the black areas. It is obvious that the *translational* testing machine stiffness is unimportant when modern closed-loop testing is utilized, since the local deformation measure around the crack controls the experiment. Thus, very flexible machines in the translational sense may be used as e.g. in (van Mier & Shi 2002), where cables were introduced between the specimen and the machine. However, the problem with the cited work is that also the *rotational* stiffness is very low (in fact close to zero). This is a misunderstanding since it again allows for rotation of the crack boundary planes and thus resulting in the situation shown in Figure 5.2. The correct situation is the one where the rotational stiffness is sufficiently large to suppress any rotations of the crack boundary planes.

The influence of the rotational stiffness of both the specimen and the testing machine was investigated by Zhou (1988) and Hillerborg (1989), who derived approximate formulas for the necessary stiffness. The actual stiffness of the testing system may be determined from:

$$\frac{1}{k_i} = \frac{1}{k_m} + \frac{h_i}{EI_0} \tag{5.1}$$

where k_i is the rotational stiffness of either the upper or the lower part of the test arrangement, k_m is the rotational machine stiffness, h_i is the length of the lower, or upper, part of the specimen, E is modulus of elasticity and I_0 is the moment of inertia outside the crack. It is seen that both a too low rotational machine stiffness and a too long specimen may lower the stiffness of the arrangement. Stability is according to Hillerborg (1989) achieved if:

$$k_i > 2I_0 \left(-\frac{d\sigma}{dw} \right) \tag{5.2}$$

where $d\sigma/dw$ is the steepest slope of the stress-crack opening relationship, which is negative (descending branch).

Besides the problems described above, also loading eccentricity affects the outcome of the uniaxial tension test. This was demonstrated by Zhou (1988) who conducted finite element analysis with varying load eccentricity on the specimen. The investigation was conducted with rotating boundary conditions. The results are shown in Figure 5.7. As the figure shows, the influence of loading eccentricity is significant. It is clear that if rotations are eliminated by selecting a rotationally very stiff testing machine, the influence of the loading eccentricity will also be reduced.

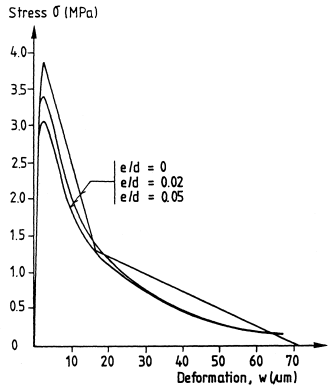

Figure 5.7 *Influence of loading eccentricity on the output of the uniaxial tension test. (Zhou 1988)*

5.1.1 Finite element modelling

The uniaxial tension test has been modelled in the commercial finite element package DIANA, see e.g. (DIANA 2000). The model is used to demonstrate the influence of the rotational stiffness of the testing machine. The mesh applied is shown in Figure 5.8a. This mesh proved in a h-convergence analysis to yield satisfactory results. A conceptual drawing of the model including the testing machine stiffness is given in Figure 5.8b. The modulus of elasticity of the concrete is given by E_c, while the steel end platen has the stiffness E_s. A short rod models the rotational stiffness of the testing machine, and the modulus of elasticity is chosen such that the rotation for a given moment in the testing machine equals the rotation at the end of the rod for the same moment, i.e.:

$$E_k = \frac{2K_r L}{I} \tag{5.3}$$

where L is the length of the rod, K_r the rotational stiffness, I moment of inertia and E_k the equivalent modulus of elasticity of the rod.

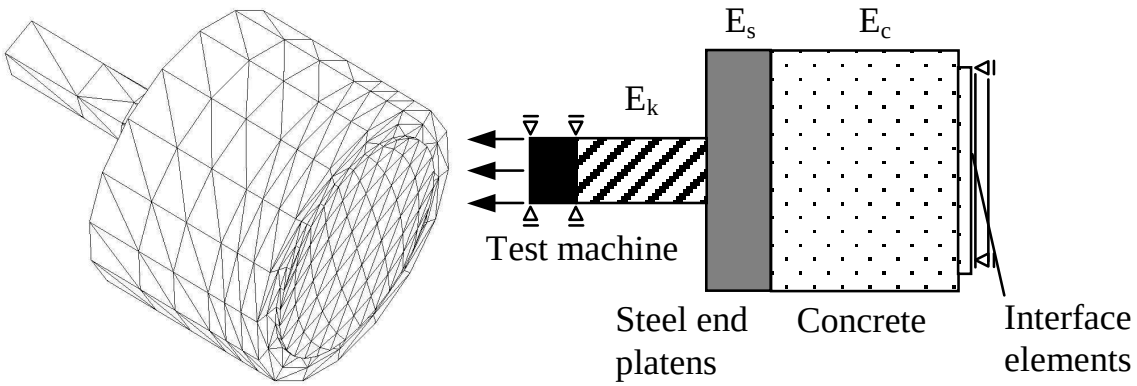

Figure 5.8 *Three dimensional finite element mesh employed in the analysis (a) and a schematic drawing of the model (b)*

The model was utilized to investigate the influence of the rotational stiffness of the testing machine on the result from the experiment.

Influence of Machine Stiffness

The graphs in Figures 5.9a-b and 5.10a-d show clearly the consequence of the choice of rotational stiffness on the output from the numerical uniaxial tension tests. The curves display the constitutive input as the thick red curve while the output is shown as the thick green curve. The displacements of four nodes around the perimeter placed with a gage length of 40 mm and individually spaced by 90 degrees are also shown. The average displacement of these nodes form the basis for calculation of the green curve:

$$w = u_{avg}(\sigma) - u_{avg}(\sigma_{max}) + \frac{\sigma_{max} - \sigma}{K_i} \tag{5.4}$$

in which K_i is the initial flexibility of the specimen, u_{avg} is the average displacement at the stress σ and $u_{avg}(\sigma_{max})$ is the average displacement at peak stress, σ_{max}.

The factor K is a reference stiffness, K=35.7 kNm/rad, which is the rotational stiffness measured for the experimental setup in this project in a non-prestressed configuration. In the prestressed configuration, the stiffness equals approximately $7K$ (see also Section 5.1.2). The parameters for the stress-crack opening relationship were preferred as:

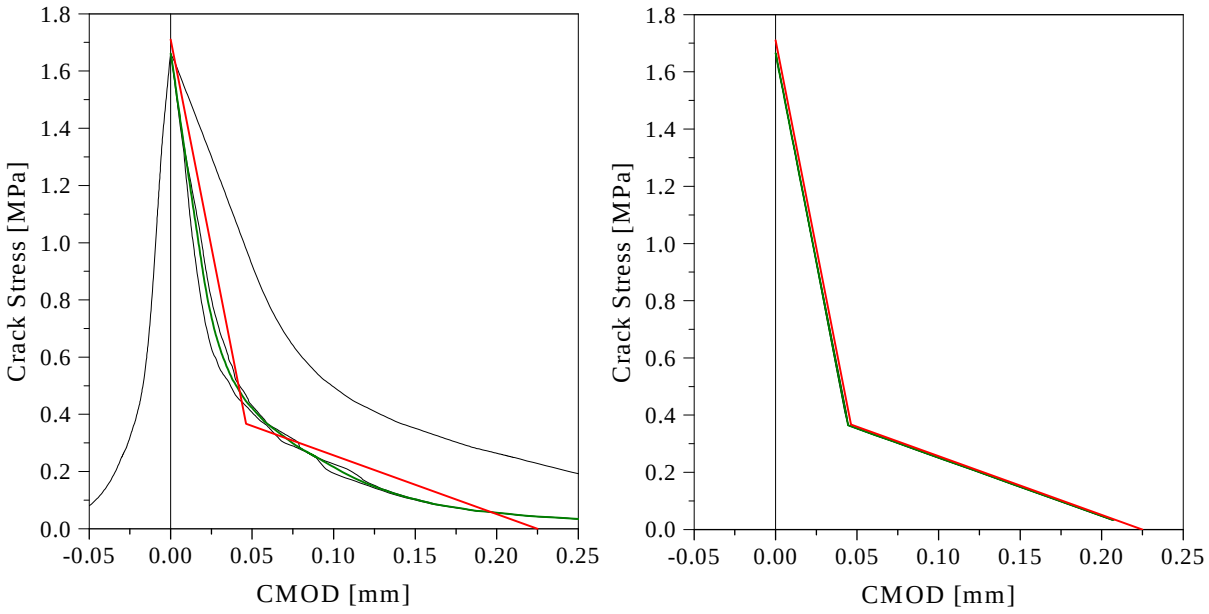

(a) (b)

Figure 5.9 *Results from finite element calculations, zero rotational stiffness (a) and very high stiffness (10K) (b)*

$$\begin{aligned} f_t &= 1.71\ MPa \\ a_1 &= 17.0\ mm^{-1} \\ a_2 &= 1.20\ mm^{-1} \\ b_2 &= 0.27 \\ E &= 30000\ MPa \end{aligned} \tag{5.5}$$

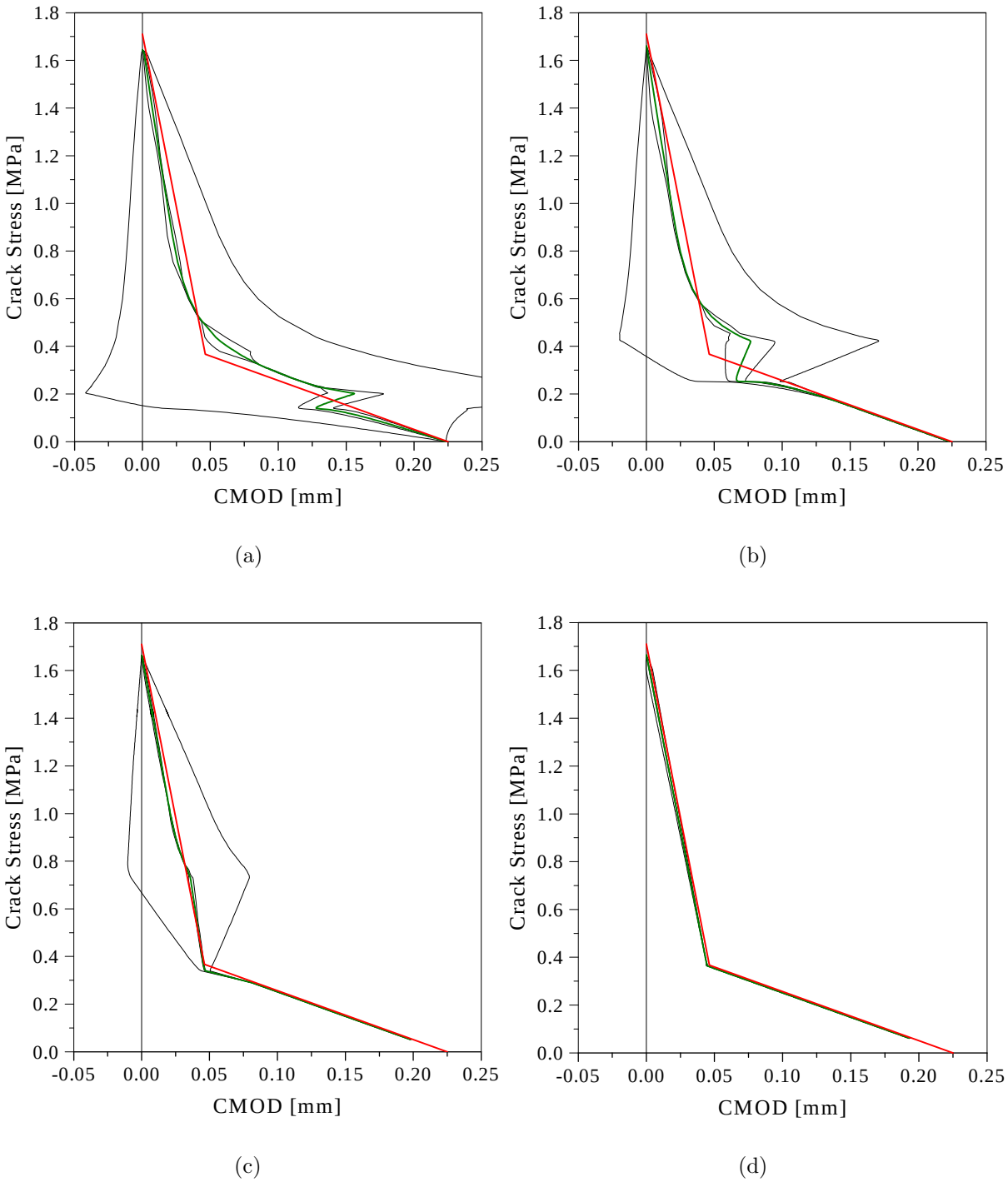

Figure 5.10 *Results from finite element calculations with insufficient rotational stiffness, 0.4K (a), K (b), 4K (c) and 7K (d)*

The consequence of choosing a system with no rotational stiffness at all is clearly seen in Figure 5.9a. This results in significant rotation of specimen, which makes the simple formula for calculation of w, Equation 5.4, unprecise and wrong. Thus, zero rotational stiffness is a poor choice if a determination of the parameters in the fictitious crack model by Hillerborg et al. (1976) is the goal of the investigations. In this case, sufficiently high stiffness must be sought for. A situation where this has been achieved is depicted in Figure 5.9b. A stiffness of 10 times the reference stiffness gives a stable experiment in which the constitutive output equals the input. The only difference in this case is the influence of the notch at which stress concentrations results in a lowering of the peak load and thus in a too low experimental tensile strength. However, the error on tensile strength for all the simulations in Figures 5.9-5.10 is below 3 %.

In the case where some rotational stiffness is present in the system, the typical hump is seen in the results. This is clearly seen in Figure 5.10a-c. Figure 5.10d does also show a small hump, but the rotational stiffness in this case is so high that it is almost suppressed and in any case not influencing the result. The graphs also show that the position of the hump moves upwards as the rotational stiffness increases. For low stiffness (0.4K and 1.0K), it is occurring on the tail of the stress-crack opening relationship, while higher stiffness (4K) moves it upwards to the first part of the curve, until it vanishes.

This discussion shows the importance of non-rotating crack boundary conditions. It also indicates that the results by van Mier, Schlangen & Vervuurt (1995) were not obtained under non-rotating conditions as claimed, but rather under conditions, which resulted in a hump. The results of some experiments of that work are given in Figure 5.11. The striking similarity with finite element results of this work is clearly seen.

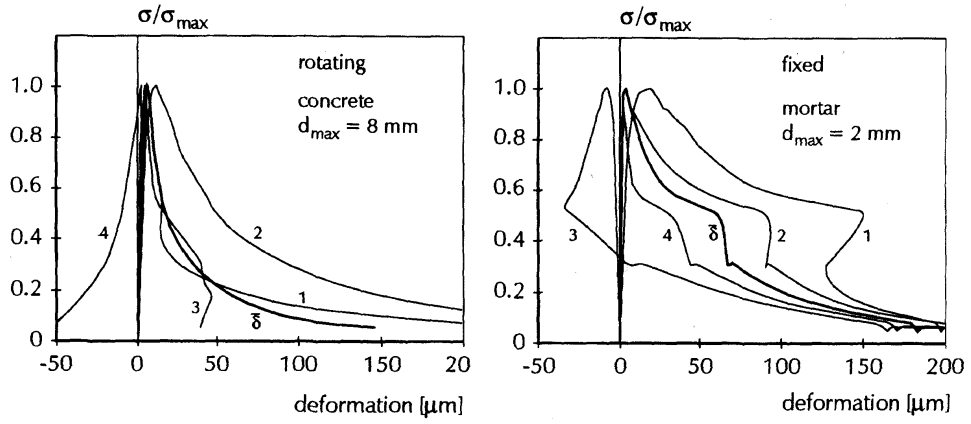

(a) (b)

Figure 5.11 *Experimental results by van Mier et al. (1995), picture from (van Mier 1997), with zero rotational stiffness (a) and insufficient rotational stiffness (b)*

5.1.2 The Experimental Setup

The standard RILEM uniaxial tension test specimen, see (RILEM 2001), has been adopted in this project. A schematic drawing of the dimensions is given in Figure 5.12. The dimensions fulfill the requirements described in the sections above. Thus, the specimen is short with a length equal to the diameter of the unnotched specimen. The notch is sawn on the mature specimen in order to reduce any boundary effects during casting in the notched region. Furthermore, the specimen is sawn out from samples twice the length of the final specimen. It is thereby achieved that any possible boundary effects in the mould at the ends are eliminated. The sawing is conducted with outmost care ensuring that the specimen is undamaged and such that the saw cuts are perpendicular to the specimen axis.

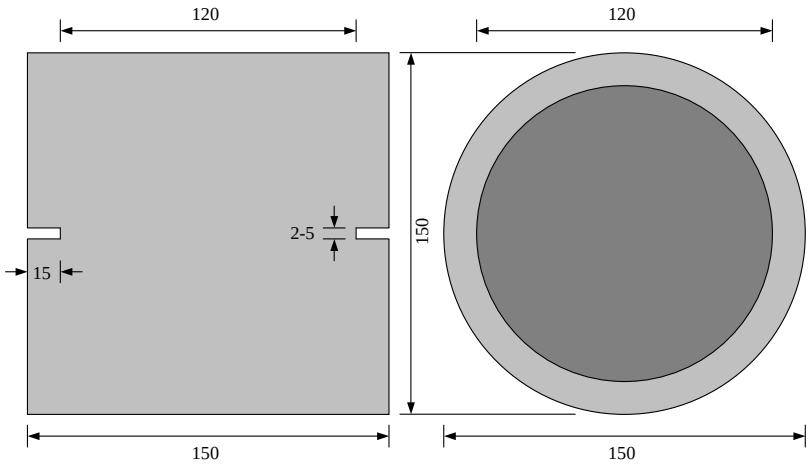

Figure 5.12 *Dimensions of the RILEM uniaxial tension test specimen*

Figure 5.13a shows the end platen, which is glued onto the specimen. The end platen is made of steel and 30 mm thick. The glue is a high strength fast setting epoxy resin, which, within a few minutes, achieves a tensile strength of about 30 MPa. The second end platen shown in the figure is attached to the first one and acts as a connection and alignment part. Figure 5.13b shows the wedges applied to establish a prestressed connection between the testing machine and the first end platen. The establishment of this prestressing will be explained later. Figure 5.13c demonstrates how the parts are assembled. The second end platen is screwed into the first one and the alignment of the specimen with regard to the testing machine is ensured by the tight connection between the wedges and the second end platen. Note also the steel rod, which is inserted into the testing machine grips and is instrumented in order to monitor the prestressing during the experiment.

(a)

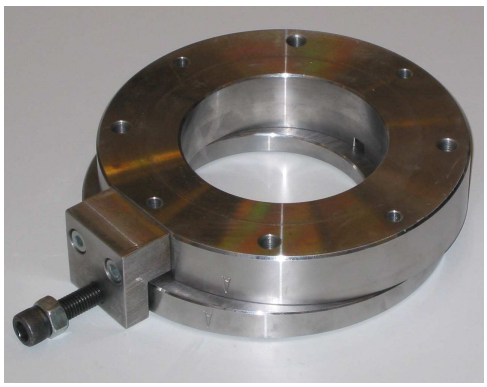

(b)

(c)

Figure 5.13 *One end platen is glued onto the concrete specimen while another is screwed into the first platen (a); the wedges are used in the testing machine in order to make a prestressed connection between the machine and the first end platen (b); The second end platen is fitting snugly into the wedges such that eccentricities are minimized (c). Figure (c) also shows the steel rod onto which the testing machine grips are fastened. The steel rod is instrumented with strain gages in order to monitor the prestressing during the experiment*

Figure 5.14a shows the situation where the test specimen has just been inserted into the testing machine. One end platen is glued onto the specimen outside the testing machine in a arrangement, which assures a fine alignment between the platen and the specimen. The second glued connection will be made in the testing machine as shown in order to rule out any risk of introducing a redundant moment in the arrangement. Figure 5.14b shows how the prestressing of the wedges is carried out. Here, four instrumented water screws are mounted in the screw holes in the inner wedge parts. The instrumentation was made to be able to measure, and equalize, the tension in the water screws. A tensile force well above the peak load of the experiment is then imposed on the setup. This tensile force was set to 110 kN, and meanwhile, the wedges are displaced. The highest loss of prestress after full unloading was less than 20 %. Thereby, concrete with a tensile strength well above 7 MPa could be tested without loss of prestress.

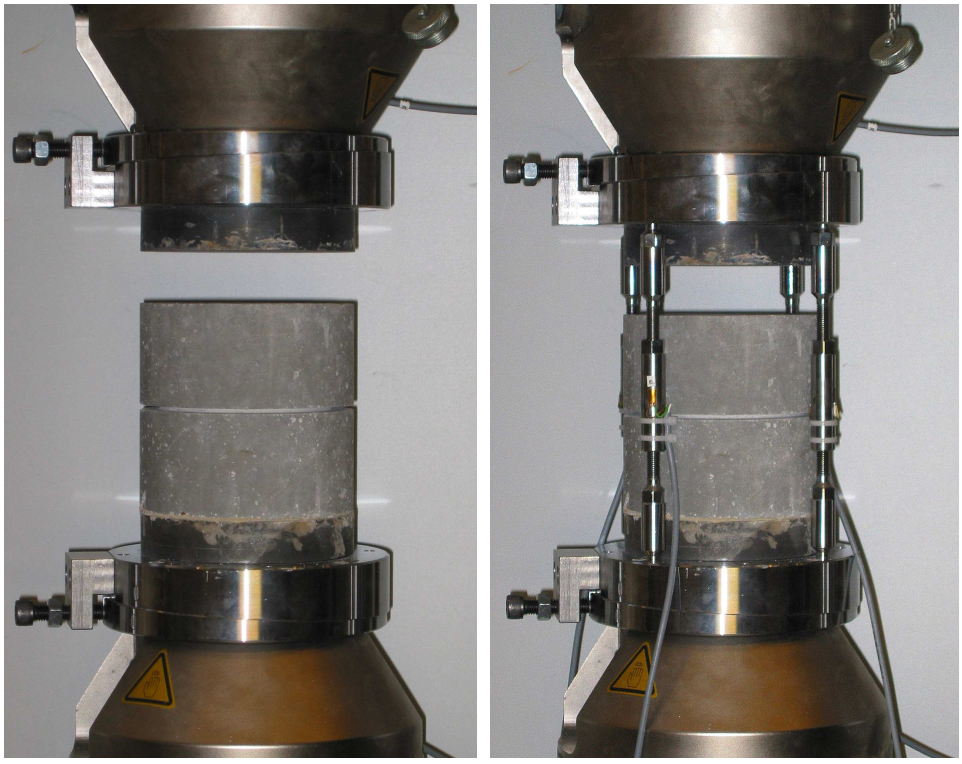

(a) (b)

Figure 5.14 *One end platen is glued onto the concrete specimen outside the testing machine whereafter the arrangement is put into the testing machine(a); the prestressing is thereafter achieved by four turnbuckles, which are screwed into the inner wedge part (b)*

Figure 5.15a shows the final situation where both end platens are mounted on the specimen and where the wedges are prestressed. The figure also shows the rig, which is employed to make measurements of the crack opening during the experiment. The gage

length is 40 mm and three LVDT's and three extensometers are applied . Figure 5.15b shows a detail of this rig. Both LVDT's and extensometers are utilized to measure the opening displacement. The averaged signal from the extensometers are used during the experiment in the closed-loop control of the experiment, while the LVDT's record the opening at each location independently such that the rotations during the experiment are measured.

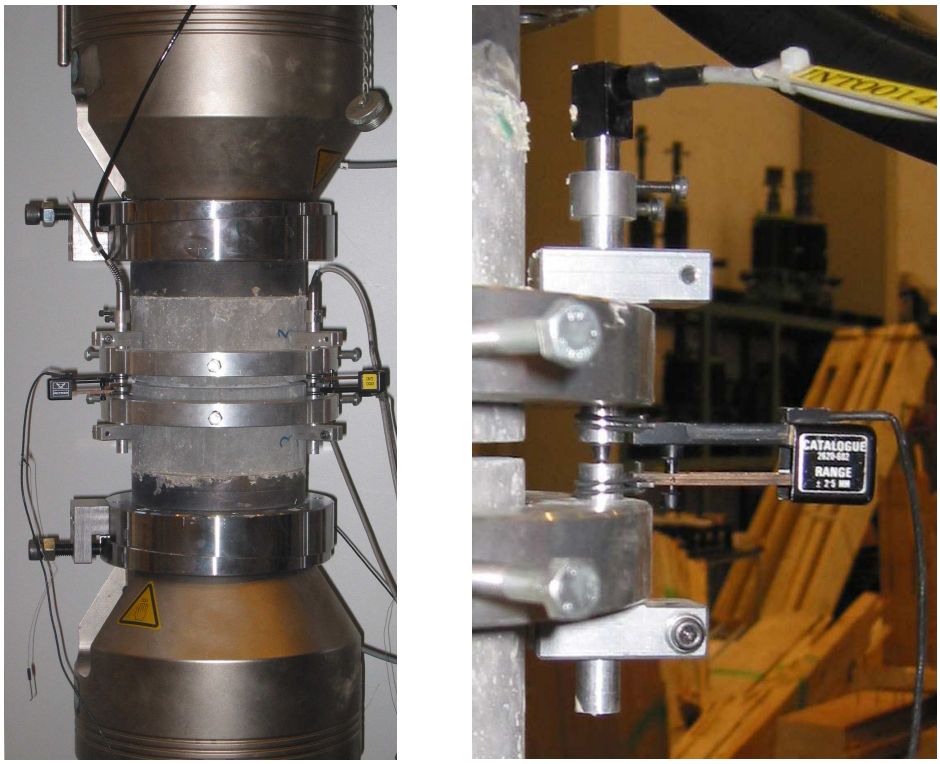

(a) (b)

Figure 5.15 *The final uniaxial tension test setup (a); and a detail of the measuring system, which is able to measure opening displacement at the crack employing both extensometers (experiment control gages, only the average value is logged) and LVDT's (where the individual signals are logged (b)*

The rotational stiffness of the arrangement is measured both for the situation where the wedges are applied and a prestressed connection established, and also in the situation where the wedges are removed. The latter measurements were conducted by Olesen (2001*b*), and the same technique is adopted here for the prestressed configuration, i.e. by mounting a steel bar eccentrically on the end platens and measuring the rotations of these as function of the tensile force. The testing machine employed was the 250 kN Instron 8502 machine. Table 5.1 gives the results. It is seen how the stiffness perpendicular and parallel with the two testing machine steel columns are almost identical when the wedges are not prestressed. This indicates that the short steel rod, connecting the end platen

and the grip, is the limiting factor in the rotational stiffness. However, when the prestressing is active utilizing the wedges, there is a clear difference between the two axes. Furthermore, the stiffness is now significantly increased by seven times. This is sufficient for many situations as shown through the finite element modelling in the previous sections.

Table 5.1 *Rotational stiffness, K_r, of an 250 kN Instron 8502 testing machine in different configuration, parallel and perpendicular to the two steel columns of the machine*

	K_r (parallel) [kNm/rad]	K_r (perpendicular) [kNm/rad]
No prestress	37.8	35.7
Prestressed	546	251

Higher levels of rotational stiffness have been reached in literature, see e.g. (Hordjik 1991) where approximately 1000 kNm/rad was achieved in an advanced setup. For normal concrete, however, the stiffness achieved in this project, see Table 5.1, is sufficient.

5.1.3 Usability with Early Age Concrete

The uniaxial tension test can only with great difficulty be conducted for early age concrete. Some researchers adopt the dog-bone setup, see e.g. Figure 1.5. This was the approach of e.g. Altoubat (2000). This setup may be used from the very set of the concrete since the mould may be used in the loading arrangement. However, usually the setup is only used for determination of the tensile strength and time-dependent deformations. Some of the explanation is the fact that the specimen in the usual configuration is too long and also the difficulty achieving a sufficiently rotationally stiff arrangement. Also frictional effects against the subbase plays is an argument in disfavor for this setup.

Gluing, as prescribed in the RILEM uniaxial tension test standard is impossible on a very early concrete sample. Therefore some authors have developed alternative setups using specially fitting shoes made of the mould in order to get a firm grip around the specimen, see e.g. (Hauggaard-Nielsen 1997). These setups may theoretically be modified such that the stress-crack opening relationship is determined. However, in this thesis, the wedge splitting test has been adopted for early age concrete and the uniaxial tension test will only, at a mature stage, be applied for verification and calibration of results obtained from the WST. The UTT specimen is simply not well suited for early age concrete.

5.2 Split cylinder

Originally, this research focused on the possibility of obtaining an estimate of the tensile strength by use of the split cylinder test. The need for an individual determination of the

tensile strength was indicated in the work by e.g. (Rossi et al. 1991) who used the wedge splitting test to obtain stress-crack opening relationships for mature concrete. They did not trust the estimate on the tensile strength obtained by their inverse analysis method and made an independent determination of the tensile strength using the split cylinder test.

However, since early age concrete fundamentally is a different material than mature concrete, it was decided to make an in-depth analysis of the split cylinder test method such that no misinterpretations would occur. The results of these investigations are published in the paper by Olesen, Østergaard & Stang (2003), see also Østergaard, Olesen & Stang (2001), and repeated here.

5.2.1 Introduction

The split cylinder test, also known as the Brazilian split test, is widely accepted as a standard test method for assessing the uniaxial tensile strength of concrete and similar materials. It was first described by Carneiro & Barcellos (1949) and it is performed by loading a cylindrical specimen along diametrically opposed generators until failure, see Figure 5.16. It was shown by Timoshenko & Goodier (1970) that the diametrically loading of the cylinder induces an almost uniform tensile stress normal to the plane of loading, and the failure load is interpreted as the load at which these tensile stresses reach the uniaxial tensile strength of the material. The tensile strength based on this interpretation is known as the splitting tensile strength. For a perfectly brittle material the splitting tensile strength would coincide with the uniaxial tensile strength. However, concrete is not a perfectly brittle material but a so-called quasi-brittle material. The load is furthermore usually distributed over a small strip, which results in a disturbance of the stress field. These effects results in the well-known fact that, for normal strength concrete, the splitting tensile strength overestimates the true uniaxial tensile strength. Thus, the splitting tensile strength is normally reduced by an empirical factor in the range of $0.6 - 0.9$ when estimating the uniaxial strength, see e.g. (Herholdt et al. 1985).

The failure of the split cylinder specimen is characterized by a splitting crack beginning at the center line and propagating towards the loading points. If the material is sufficiently brittle the splitting will continue until the specimen is divided into two halves. In this case the ultimate load is governed by the tensile strength as well as the tension softening behavior of the material. However, if the material is not sufficiently brittle the splitting process will not be completed before a compressive crushing/sliding failure develops, which then governs the ultimate load. Concrete failing in compression may be modelled as a rigid-plastic material with a Mohr-Coulomb friction yield criterion, (Nielsen 1999*b*). Upper-bound solutions exist for the rigid-plastic failure of the split cylinder test and will be given later. These solutions are characterized by the formation of wedge-like regions under the loading strips, simultaneously splitting the rest of the specimen. The compressive failure of concrete in the form of the Coulomb friction hypothesis may also be implemented in a finite element model as will be demonstrated.

Figure 5.16 *The outcome of a split cylinder test when performed on an early age concrete. Ordinary normal strength concrete specimen, 12 hours old, diameter 100 mm, length 200 mm, width of loading strip 10 mm.*

5.2.2 Linear Elastic Solution

A circular disk with a diameter D acted upon by two equal and diametrically opposite forces P is a classical problem in elasticity. The state of stress in the plane of loading is uniform tension perpendicular to this plane (Timoshenko & Goodier 1970), and the magnitude of these tensile stresses is given by:

$$\sigma = \frac{2P}{\pi D} \tag{5.6}$$

In the split cylinder test the loads are applied over a certain width ($2a$) as shown in Figure 5.17. This will affect the state of stress, and if it is assumed that the loads are distributed evenly over the loading strips, the tensile stress at the center of the disk should be modified according to the following expression (Tang 1994):

$$\sigma = \frac{2P}{\pi D}\left[1 - \left(\frac{2a}{D}\right)^2\right]^{\frac{3}{2}} \tag{5.7}$$

In the case of the split cylinder test we have that $P = P_c/L$, where P_c is the total load on the cylinder and L is the length of the cylinder. For a perfectly brittle material the

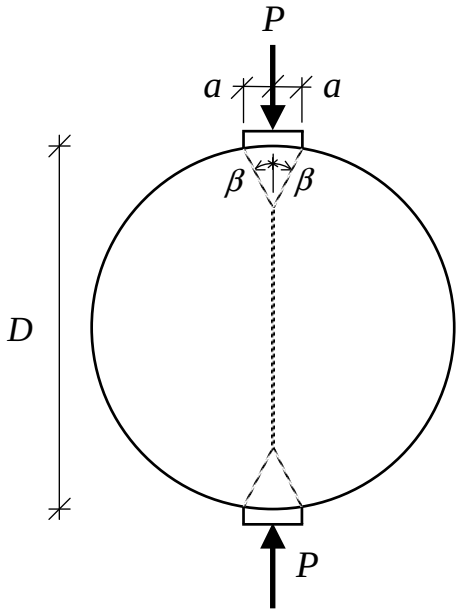

Figure 5.17 *Yield lines of the assumed plastic failure mode.*

ultimate load of the split cylinder is given by Equation 5.7 with $\sigma = f_t$, the uniaxial tensile strength.

5.2.3 Ideal Plastic Solution

An ideal rigid-plastic solution to the split cylinder test is presented by Nielsen (1999*b*) based on a solution by Chen & Drucker (1969). Here concrete is modelled as a modified Mohr-Coulomb material with a sliding failure condition given by the angle of friction φ and the cohesion c. The sliding failure condition is overruled by a separation failure condition stating failure when the tensile stress reaches the uniaxial tensile strength. The solution is based on a failure mechanism with yield lines as shown in Figure 5.17. The cylinder is separated into four rigid parts. The two opposite wedge shaped parts translate towards each other, and the other two parts translate horizontally apart. Based on this mechanism the following optimal upper-bound solution to the load-carrying capacity of the cylinder may be found:

$$P = 2af_t \left[\frac{D}{2a} \tan(2\beta + \varphi) - 1 \right] \tag{5.8}$$

where β is given by:

$$\cot\beta = \tan\varphi + \frac{1}{\cos\varphi}\sqrt{1 + \frac{\frac{D}{2a}\cos\varphi}{\frac{f_c}{f_t}\frac{1-\sin\varphi}{2} - \sin\varphi}} \tag{5.9}$$

Here, the uniaxial compressive strength f_c has been introduced. The above upper-bound solution is only valid as long as the two wedge shaped parts do not overlap, which is the case if $\cot\beta \leq D/(2a)$. An exact solution based on a slip line field was given by Izbicki (1972) The solution given above is, however, only deviating from the exact solution by a few percent for the present applications. Hence, the above simple solution is applied here.

5.2.4 Finite Element Implementation

One quarter of a cylinder is modelled by finite elements in the finite element program DIANA (2000). The elements are three-node triangular isoparametric plain strain elements (type T6EPS), and the mesh is shown in Figure 5.18a. It is assumed that a crack may develop in the vertical plane of symmetry, thus, interface elements (type L8IF) are attached at the vertical face of the quarter cylinder. Symmetry boundary conditions are specified along the vertical and horizontal sections defining the quarter cylinder, i.e. deformations normal to these sections are suppressed. All vertical displacements of the nodes on the loaded horizontal surface of the loading strip are tied together to ensure synchrony.

For concrete in solid elements the constitutive behavior is described by a linear elastic model in combination with a Mohr-Coulomb yield criterion. According to Nielsen (1999*b*) the angle of friction for concrete may be set to 37°, and consequently the cohesion is given by $c = f_c/4$, where f_c is the compressive strength. These values have been applied here, and the angle of dilation set equal to the angle of friction. In order to suppress relative deformations in the elastic phase prior to cracking, the interface elements are given high spring stiffness values (30000 N/m^3) with respect to relative normal and shear deformations. After crack initiation the normal relative deformation is governed by a bilinear stress-crack opening relationship as described in Figure 3.9, and due to symmetry the shear modulus is of no importance, and it is set equal to the pre-crack modulus. It should be emphasized that the relative displacement of an interface element only represents half the crack opening. The material of the loading strip elements are modelled as linear elastic with a modulus of elasticity equal to 1000 MPa.

The FEM formulation of the split cylinder test constitutes a highly nonlinear problem with snapping effects. However, the DIANA software provides a number of advanced facilities enabling a successful solution of the problem. The iterative scheme applied is called Newton Regular based on the tangent stiffness matrix and the arc length method. The problem is solved under an adaptive load step control, and the convergence criterion is based on an energy norm.

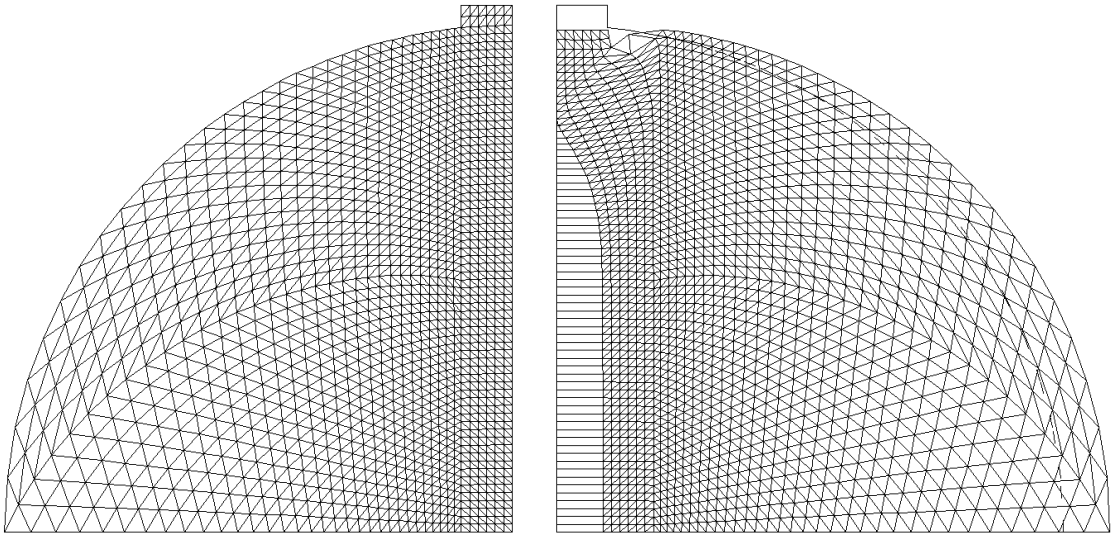

(a) (b)

Figure 5.18 *(a): Finite element mesh, D = 100 mm, L = 200 mm, a = 5 mm. (b): Deformation plot at extreme deformation to illustrate combined cracking and yielding, plain strain condition, f_t = 2 MPa, E = 30 GPa, a_1 = 20 mm^{-1}, a_2 = 0.2 mm^{-1}, b_2 = 0.1.*

Figure 5.19 shows the results of a number of FE-calculations of the split cylinder test. The figure depicts load versus deformation. The load is normalized with respect to the linear elastic load at crack initiation, P_e, and the deformation is the total compression of the specimen. Different materials are represented differing only by the value of the tension softening parameter a_1. The remaining material parameters were kept constant at values representing a normal strength concrete: f_t = 2 MPa, E = 30 GPa, a_2 = 0.2 mm^{-1}, b_2 = 0.1. The softening parameter a_1 describes the initial toughness of the material, and a value of a_1 = 20 mm^{-1} would apply to normal strength concrete. For large values of a_1, i.e. $a_1 > 5$ mm^{-1} we observe snap back of the load deformation curve, for smaller values of a_1, however, there is no snap back behavior. All curves shown in Figure 5.19 exhibit a behavior where the first part is linear until a crack is initiated in the center of the cylinder. This crack propagates towards the loading points as the load is increased. However, the crack also opens and as a consequence the crack bridging stresses decrease according to the stress-crack opening relationship, where the a_1 parameter plays an especially important role. At some point the load peaks and drops while the crack opening continues. During crack opening redistribution of stresses in the whole specimen takes place, and at large crack openings the load is primarily carried through compression and bending of the almost separated semi-cylinders. The carrying capacity at this stage is governed by the Mohr-Coulomb yield criterion, which is responsible for the second part of the load deformation curve. After the load has dropped to this curve it increases again as the deformation increases. In the end the load approaches a constant yield level.

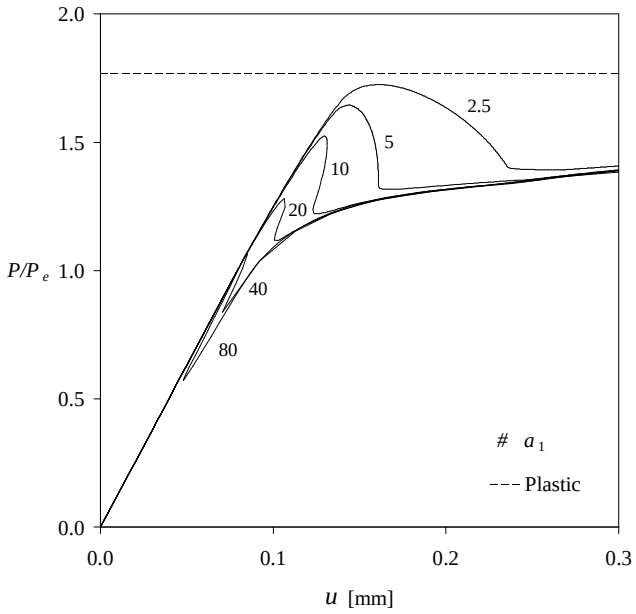

Figure 5.19 *Normalized load versus specimen compression u. FE-solutions for different values of the softening parameter a_1. Load level for the ideal rigid-plastic solution indicated by the broken line. $D = 100$ mm, $L = 200$ mm, $a = 5$ mm, $f_t = 2$ MPa, $E = 30$ GPa, $a_2 = 0.2$ mm^{-1}, $b_2 = 0.1$.*

The finite element load deformation curves are obtained by controlling the crack opening. However, split cylinder tests are normally performed in load control, thus only the ascending part of the curve may be obtained, i.e. only the first peak load is found from the test. On the other hand, if the test was deformation controlled the full load deformation curve could be obtained only for materials with a sufficiently low value of the softening parameter a_1, ruling out the risk of snap-back.

In Figure 5.18b the deformed finite element mesh is plotted at an extreme load step with extreme deformations for $a_1 = 20$ mm^{-1}. The figure illustrates the almost plane opening of the splitting crack, which, however, is prevented from penetrating all the way through the cylinder due to compressive stresses below to loading strip. Furthermore, it illustrates the plastic deformations in a region near the loading point. Note that a wedge like region immediately below the loading strip is formed in support of the simple failure mode assumed in the ideal plastic solution.

In Figure 5.20a finite element results for load deformation curves are shown for different values of the tensile softening parameter b_2. The remaining material parameters have been kept constant at $f_t = 2$ MPa, $E = 30$ GPa, $a_1 = 20$ mm^{-1} and $a_2 = 0.2$ mm^{-1}. The softening parameter b_2 defines the level of the second part of the stress-crack opening curve, and is the one parameter, which is most directly influenced by the addition of fibres to concrete. Thus, for normal strength concrete the addition of 1% by volume of fibres would increase the value of b_2 from approximately 0.1 to 0.5-0.7. The curve representing $b_2 = 0.1$ is identical to the curve shown in Figure 5.19 representing $a_1 = 20$ mm^{-1}. A

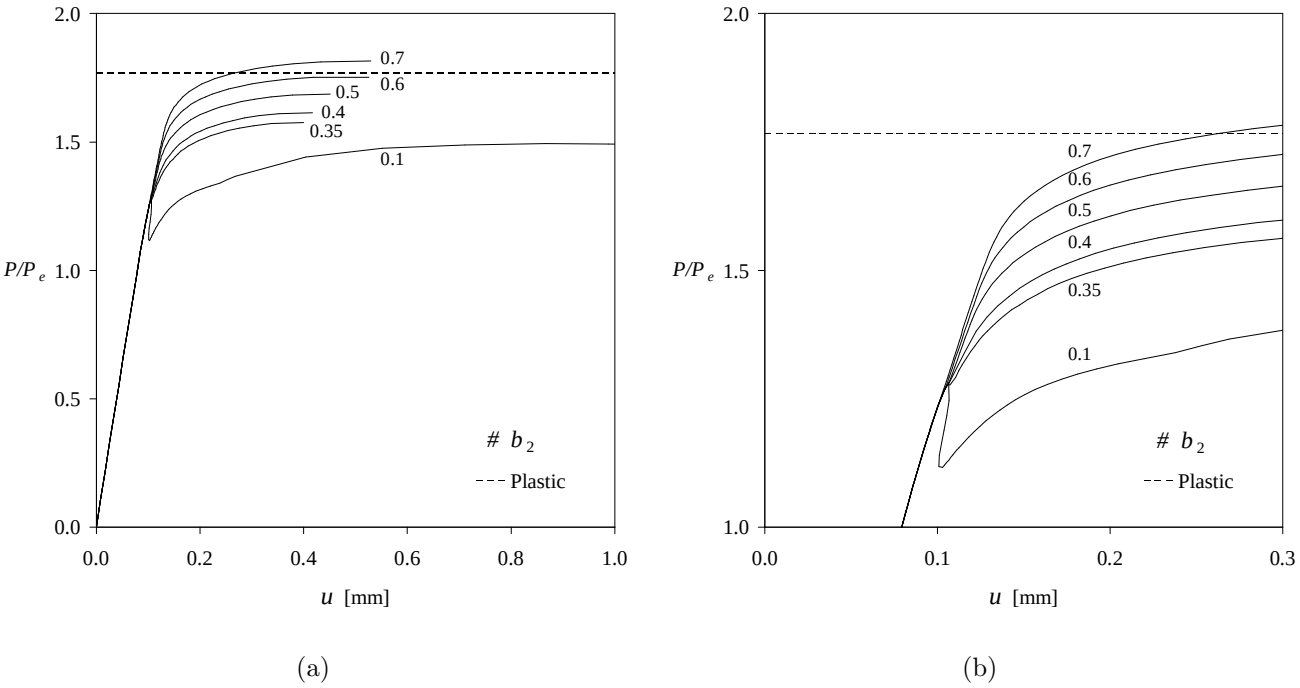

Figure 5.20 *Normalized load versus specimen compression u. (a): FE-results for different values of the softening parameter b_2. Load level for the rigid-plastic solution indicated by the broken line. $D = 100$ mm, $L = 200$ mm, $a = 5$ mm, $f_t = 2$ MPa, $E = 30$ GPa, $a_1 = 20$ mm^{-1}, $a_2 = 0.2$ mm^{-1}. (b): Close-up of curves shown in (a).*

close-up of results is shown in Figure 5.20b. We note that $b_2 = 0.35$ marks the point of transition from a situation with a distinct peak preceding the plastic behavior. Thus, for values of $b_2 < 0.35$ the capacity of the split cylinder test in load control is determined by the peak governed by the magnitude of a_1, whereas the capacity for larger values of b_2 is determined by the plastic yield capacity.

5.2.5 Semi-analytical model

A simple model has been developed for the analysis of the splitting of a cylinder. The model is based on the so-called nonlinear hinge model (Olesen 2001*a*), which is an analytical solution to the crack propagation in a rectangular prismatic body due to moment and normal force loads. The model is based on the fictitious crack model (Hillerborg et al. 1976) with a bilinear tension softening curve. Another fundamental assumption of the hinge model is that it is modelled as independent incremental layers, thus neglecting the shear stiffness of the hinge. The hinge solution is expressed in terms of the normalized angle of rotation $\theta = \varphi h E/(s f_t)$, where φ is the angle of rotation of the rigid boundary lines of the hinge, see Figure 5.21 (c), and where h is the height of the hinge, E is the elastic modulus and s is the length of the hinge. The hinge solution is summarized in

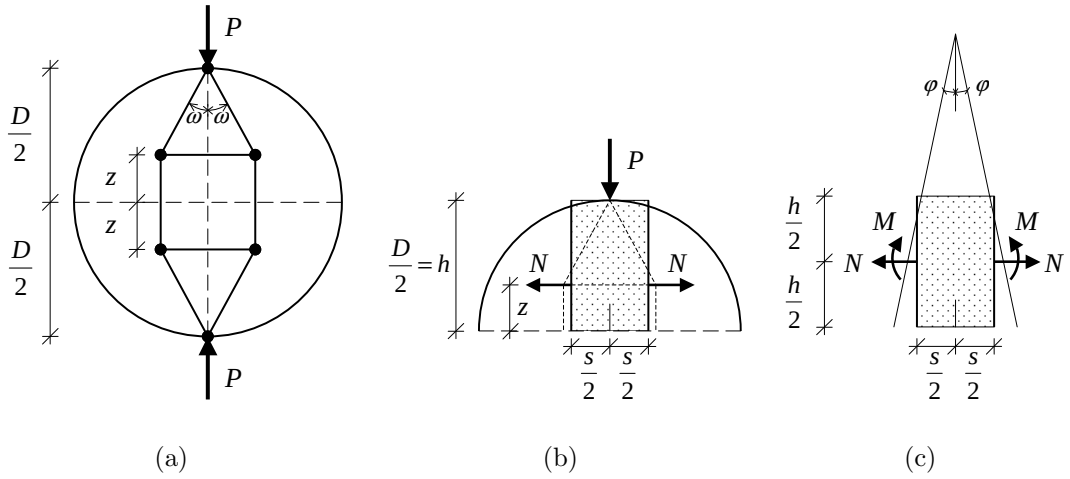

Figure 5.21 *Geometry and loading of the WST-specimen. (a): Strut and tie model. (b): Incorporation of the hinge element. (c): Loaded hinge and definition of hinge deformation angle φ.*

Appendix A and it furnishes the relative crack depth $\alpha = d/h$ and the normalized moment $\mu = 6M_h/(f_t h^2 t)$ as functions of the relative normal force $\rho = N_h/(f_t h t)$, where M_h and N_h are the hinge moment and normal forces, respectively, and d is the depth of the crack and t is the width of the hinge. The solution comprises four distinct phases, the elastic pre-crack phase and three cracked phases differing in how much of the softening curve that has been activated.

The simple split cylinder model assumes that the state of stress in the cylinder caused by the diametrically opposite loads may be replaced by the strut and tie model shown in Figure 5.21 (a), where ω denotes the strut inclination angle and z denotes the distance of the horizontal tie from the center of the cylinder. Now the hinge element is incorporated in place of the horizontal tie, and the tie force is referred to the mid-height of the hinge producing a moment loading of the hinge. The loads are thus given by:

$$N = \tfrac{1}{2} P \tan\omega, \qquad M = N\left(\tfrac{1}{2}h - z\right) \tag{5.10}$$

Thus far the simple split cylinder model has only considered one half of the cylinder. In order to model the cooperation of the two halves an elastic interaction is ensured by a rotational spring counteracting the rotational deformation φ of the hinge. Equilibrium of the hinge and spring system requires that:

$$M = M_h(\varphi, N) + K_e \varphi \tag{5.11}$$

where K_e is the stiffness of the rotational spring. In normalized terms (5.11) reads:

$$\mu = \mu_h(\theta, \rho) + k_e\theta \tag{5.12}$$

where k_e is given by:

$$k_e = \frac{6K_e}{Eh^2t}\frac{s}{h} \tag{5.13}$$

The value of k_e may be established by comparison with FEM results. The strut inclination ω is tuned such that crack initiation in the simple model coincides with the elastic solution, i.e. the load at which the elastic stress in the most stresses fibre of the hinge equals f_t, coincides with the load at which the elastic solution (5.7) produces $\sigma = f_t$. Thus, the strut inclination ω is given by:

$$\tan\omega = \frac{1}{\pi}\left[1 - \left(\frac{a}{h}\right)^2\right]^{\frac{3}{2}}\left[\frac{3}{2h}\frac{h-2z}{1+k_e} + \frac{1}{2}\right]^{-1} \tag{5.14}$$

Due to the coupling between the loads M and N and the nonlinearity of the hinge solution the equilibrium equation (5.12) must be solved iteratively.

The parameters of the hinge model have been calibrated against finite element predictions of the peak load for different values of the softening parameter a_1 ranging from 7.5 mm^{-1} to 320 mm^{-1}. This calibration furnished the following values: $z = 0$, $k_e = 0.44$ and $s = 2.62D$.

In Figure 5.22, results obtained with the simple hinge based model are compared with finite element results. The finite element results are equivalent to the results shown in Figure 5.19 except that the normalized load has been plotted versus the CMOD, i.e. the opening of the crack at the center of the cylinder. The hinge model does not take into account the limited compressive strength of the material, and the ideal plastic solution may be exceeded. However, later the simple model is combined with the ideal plastic model, truncating the hinge solution by the plastic solution when appropriate. The comparison between the finite element and the simple model results show remarkable agreement considering the simplifications made. The simple model captures the initial behavior and gives a good prediction of the peak load, however, the solution is truncated due to break down of the analytical expressions.

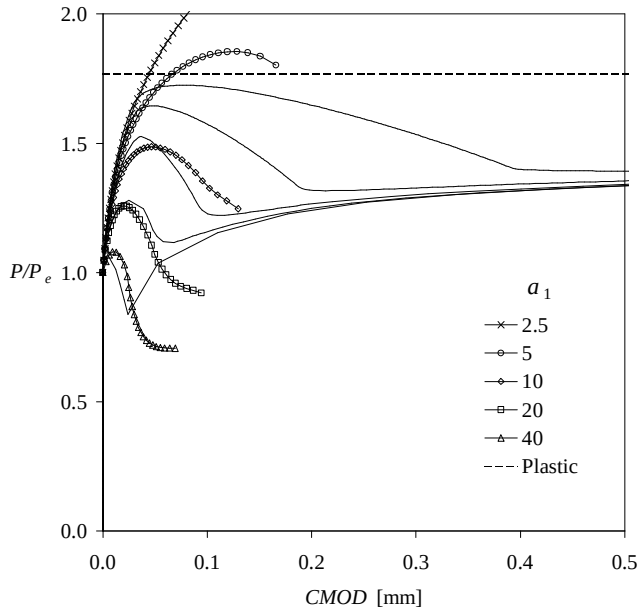

Figure 5.22 *Normalized split load versus* CMOD. *Hinge solutions compared with FE-solutions for different values of the softening parameter a_1. Load level for the rigid-plastic solution indicated by the broken line. $D = 100$ mm, $L = 200$ mm, $a = 5$ mm, $f_t = 2$ MPa, $E = 30$ GPa, $a_2 = 0.2$ mm^{-1}, $b_2 = 0.1$.*

In Figure 5.23 results obtained with the simple hinge based model are again compared with finite element results. In this case the finite element results are equivalent to the results shown in Figure 5.20 except that the normalized load has been plotted versus the crack opening at the center, CMOD. The same comments as given above apply here. The hinge model predicts the same initial behavior, however, it predicts a higher value of the b_2 parameter corresponding to transition point mentioned in the previous section, namely a value of approximately 0.6.

5.2.6 Numerical study

A numerical study of the expected outcome of the split cylinder test has been performed applying the different methods described in the previous sections. It has been assumed that the test is performed in load control, thus the expected maximum load P_{max} is taken as the first peak of the load deformation curve if a peak is predicted; if no peak is predicted then the ultimate load in the plastic region is taken. The influence of the material parameters a_1 and b_2 is studied, as well as the influence of the cylinder diameter D and the width of the loading strip a. For this study the modulus of elasticity has been calculated from the empiric expression: $E = 15000 f_t$, and the compressive strength has been calculated from the empiric expression: $f_c = (f_t/0.35)^2$ with strength units in MPa. Figures 5.24 through 5.27 show the results.

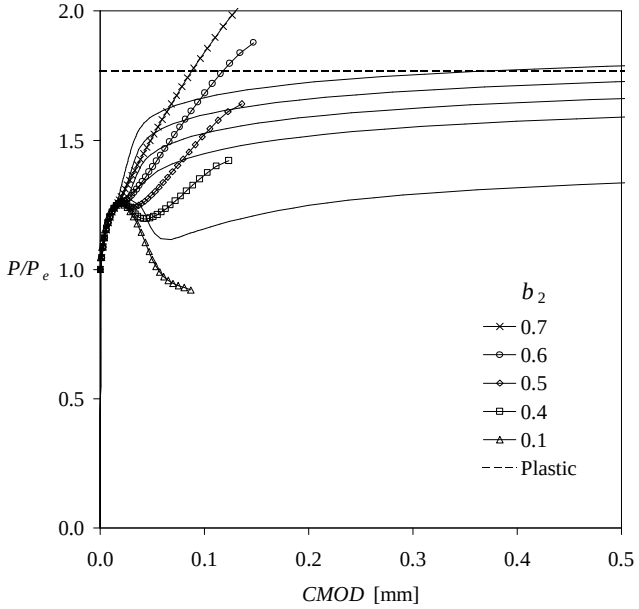

Figure 5.23 *Normalized load versus* CMOD. *Hinge solutions compared with FE-solutions for different values of the softening parameter b_2. Load level for the rigid-plastic solution indicated by the broken line. $D = 100$ mm, $L = 200$ mm, $a = 5$ mm, $f_t = 2$ MPa, $E = 30$ GPa, $a_1 = 20$ mm^{-1}, $a_2 = 0.2$ mm^{-1}.*

The figure legend "plastic" refers to the ideal rigid-plastic upper-bound limit given in (5.8), while the legend "Hinge" refers to the semi-analytical hinge based model, cut off by the ideal rigid-plastic upper-bound limit. The work by Rocco, Guinea, Planas & Elices (1999) is labelled "Rocco et al." Note that this solution is only shown within the range of applicability characterized by $0.4 \leq 2a_1 D f_t/E \leq 10$. Finally, the label "Tang" refers to the solution by Tang given in (5.7) while "FEM" refers to the finite element model presented here.

In Figure 5.24 the influence of a_1 is presented. High values of a_1 correspond to brittle materials, low values to plastic materials, and intermediate values correspond to quasi-brittle materials. It is obvious from the figure that the elastic solution only applies for high values of a_1, and that the ideal plastic solution only applies for low values. The finite element results demonstrate the transition from brittle to plastic behavior. This transition is reproduced nicely by the hinge model. Normal strength concrete is quasi-brittle material, and $a_1 = 20\text{mm}^{-1}$ is a representative value. From the results shown here it is obvious that the split cylinder test will overestimate the tensile strength of normal strength concrete.

Figure 5.25 shows the influence of the softening parameter b_2. As mentioned earlier large values of b_2 could be obtained if fibres are added to the concrete; the more fibres the larger the b_2-value. We observe that for small values of b_2 there is no influence of this parameter. The reason for this is that the first peak of the load deformation curve has been reached before the second part of the bilinear stress-crack opening relationship is

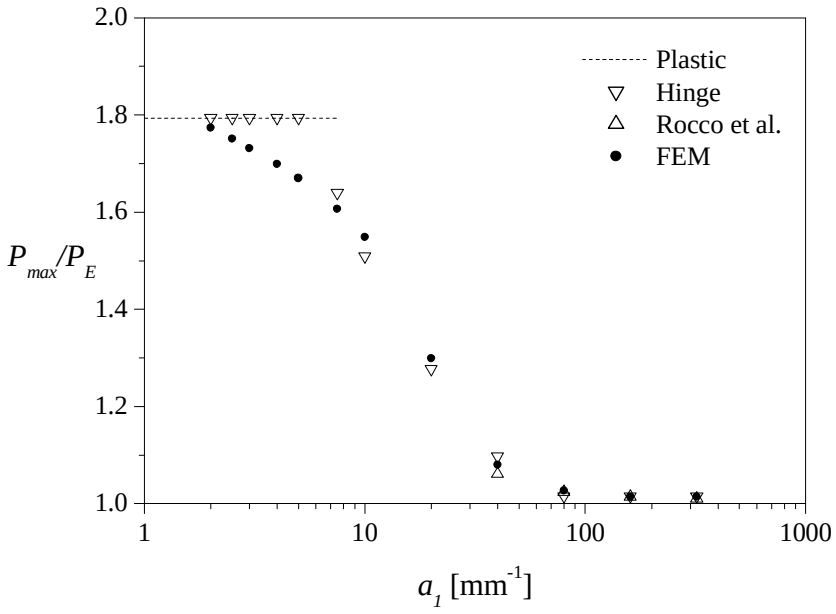

Figure 5.24 *Model results for the normalized split load versus softening parameter* a_1. $f_t = 2$ *MPa*, $E = 30$ *GPa*, $a_2 = 0.2$ *mm*$^{-1}$, $b_2 = 0.1$, $D = 100$ *mm*, $L = 200$ *mm and* $a = 5$ *mm*.

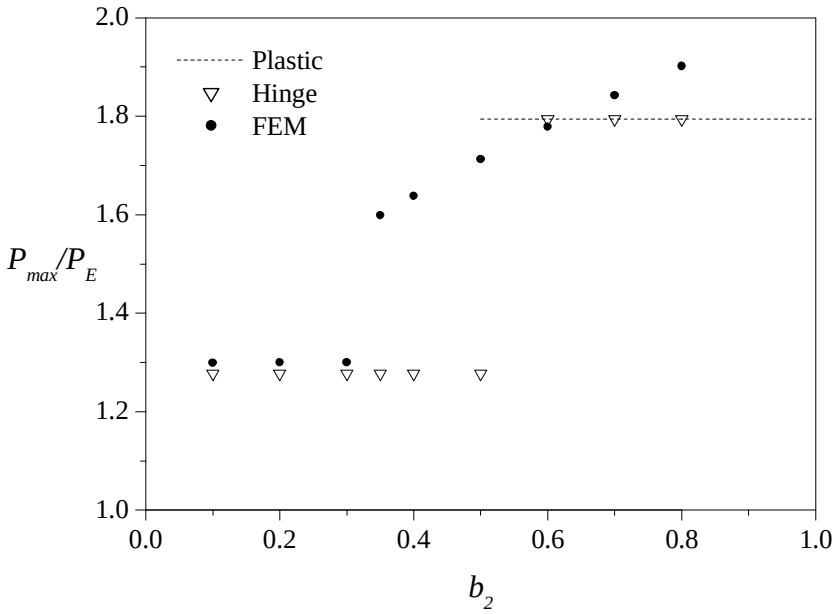

Figure 5.25 *Model results for the normalized split load versus softening parameter* b_2. $f_t = 2$ *MPa*, $E = 30$ *GPa*, $a_1 = 20$ *mm*$^{-1}$, $b_2 = 0.1$, $D = 100$ *mm*, $L = 200$ *mm and* $a = 5$ *mm*.

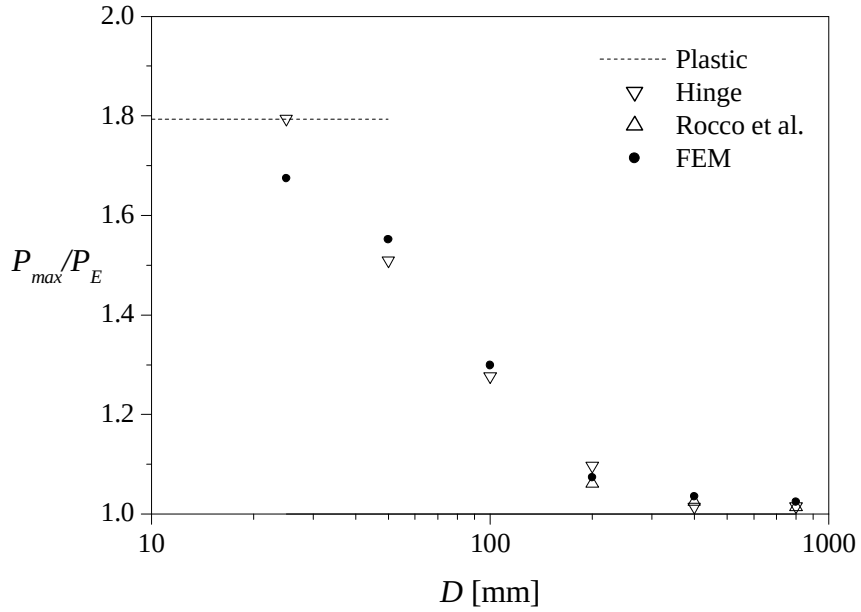

Figure 5.26 *Model results for the normalized split load versus diameter of the cylinder* D. $f_t = 2$ *MPa*, $E = 30$ *GPa*, $a_1 = 20$ mm^{-1}, $a_2 = 0.2$ mm^{-1}, $b_2 = 0.1$, $L = 200$ *mm and* $a/D = 0.1$.

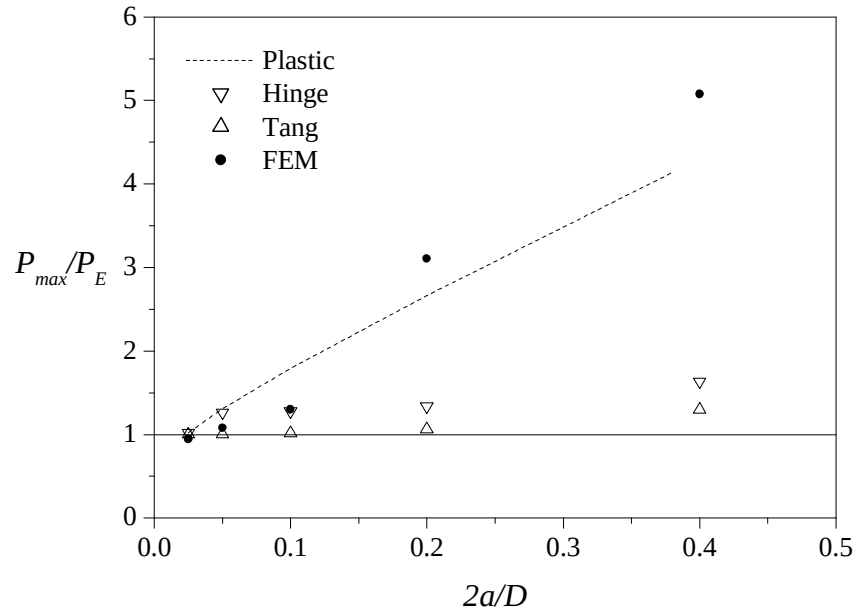

Figure 5.27 *Model results for the normalized split load versus relative width of loading strip* $2a/D$. $f_t = 2$ *MPa*, $E = 30$ *GPa*, $a_1 = 20$ mm^{-1}, $a_2 = 0.2$ mm^{-1}, $b_2 = 0.1$, $D = 100$ *mm and* $L = 200$.

activated. For larger values of b_2 the finite element load deformation curve does not exhibit a peak, see Figures 5.20 and 5.23. In such cases the maximum load is given by the plastic yield level, which is affected by the magnitude of b_2, therefore we observe a sudden jump from a constant level to an almost linear dependency. The FEM results exceed the upper-bound ideal rigid-plastic level, which is attributed to the fact that the FE-model does include the elastic deformations. The hinge based results exhibit a jump from the constant non-plastic level to the ideal rigid-plastic level, since, in the actual case, if the hinge solution does not exhibit a peak it will exceed the plastic level as may be seen from the load deformation curves.

The size effect is demonstrated in Figure 5.26 for material parameters corresponding to normal strength concrete. We observe a transition from plastic behavior to brittle as the size increases from small to large values. It is worth noting that the simple model is in good agreement with the FEM predictions.

Finally, the influence of the width of the loading strip is presented in Figure 5.27. The FEM results exhibit a transition from brittle behavior to plastic behavior as the relative strip width is increased from narrow to wide. For wide loading strips the FEM results exceed the ideal rigid-plastic solution. Apart from the effects of including the elastic deformations in the FE-model, this is attributed to the possible interaction between the stress fields in the two wedge-like regions below the loading points. The linear elastic influence given by Tang is also shown, and it is seen to be negligible for the present material and geometry. The simple hinge model does not capture the effect of strip width as predicted by the finite element model, this is due to the fact that the loads on the cylinder are modelled as point loads, although the effect by Tang is incorporated.

5.2.7 Useability with Early Age Concrete

The investigation clearly shows the possible dangers associated with the application of the split cylinder test for early age concrete. The problems arise from the fact that the fracture mechanical properties at early age may be significantly different from those valid for mature concrete. The matrix material is most likely more tough, which results in a lower value of a_1. As the analysis demonstrates, this may fundamentally change the behavior of the specimen, thereby altering the peak load and rendering the simple linear elastic solution wrong. Also the aggregate pullout may be much more tough in early age, resulting in a higher b_2 value compared with mature concrete. This concern, which may result in a fundamental alteration of the peak load, must also be addressed before the test method may be applied to early age concrete.

The potential problems arising in early age is clearly demonstrated in Figure 5.16. Here the compressive failure wedge is very long and steep and the tip is in fact placed at the center of the original specimen. Thus, it is indicated that the actual failure for this specimen, which was 12 hours old at testing, is significantly different from the linear elastic assumption.

However, if these matters are solved, either by an experimental demonstration of the invariability of the test method at early ages, or by derivation of correctional expressions, the method is very well suited for use at early age. This is primarily due to the easiness of the handling of the specimen and the simplicity of the test method.

5.3 Wedge Splitting Test for Short-Term Testing

The wedge splitting test is very interesting for many reasons. The idea of this test, which is a special form of the so-called compact tension test, is to split a small cube with a groove and notch in two halves while monitoring the load and crack mouth opening displacement (CMOD). Originally, this test was designed for determination of the fracture energy, G_f, however by application of a suitable model, the stress-crack opening relationship may also be extracted. The test is especially well suited for early age concrete since there are almost no problems with self-weight. The test is also very stable since the specimen stores very little elastic energy during testing. Finally, this test method is well suited for inverse analysis.

5.3.1 Interpretation of the WST

The idea of employing the WST-geometry for determination of fracture energy for concrete was originated by Linsbauer & Tschegg (1986) and further developed by Brühwiler & Wittmann (1990). In the original configuration the fracture energy needed to split the specimen could be calculated from the area under the P_s-CMOD curve, where P_s is the split load. Extension to methods able of estimating the stress-crack opening relationship for concrete for which the tensile strength was independently estimated were described by e.g. (Rossi et al. 1991). More general methods for inverse analysis may be found in Østergaard, Olesen, Stang & Lange (2002).

If the hinge model, see Appendix A, is applied to the WST-specimen, it allows not only for an accurate determination of the fracture energy, G_f, but it also makes it possible to make a fast and objective determination of the softening curve. This is due to the detailed analytical expressions that opens up for phased analysis and inverse calculation. The major concern when using the hinge element is whether the assumption about rigid vertical boundaries is acceptable. If deformations in the boundary planes play a significant role for the shape of the P-CMOD curve, the model might be too simple and thus, unprecise in its predictions. This concern will be addressed by comparing hinge model results with FEM-calculations.

Figure 5.28 shows the principal experimental setup. The vertical loading of the wedge and the opening at load line (using a clip gage) are recorded during experiments. Closed loop CMOD control may be utilized to control the experiment. However, constant rate of displacement of the wedge is often satisfactory since the experiment is very stable, see e.g. (Brühwiler & Wittmann 1990).

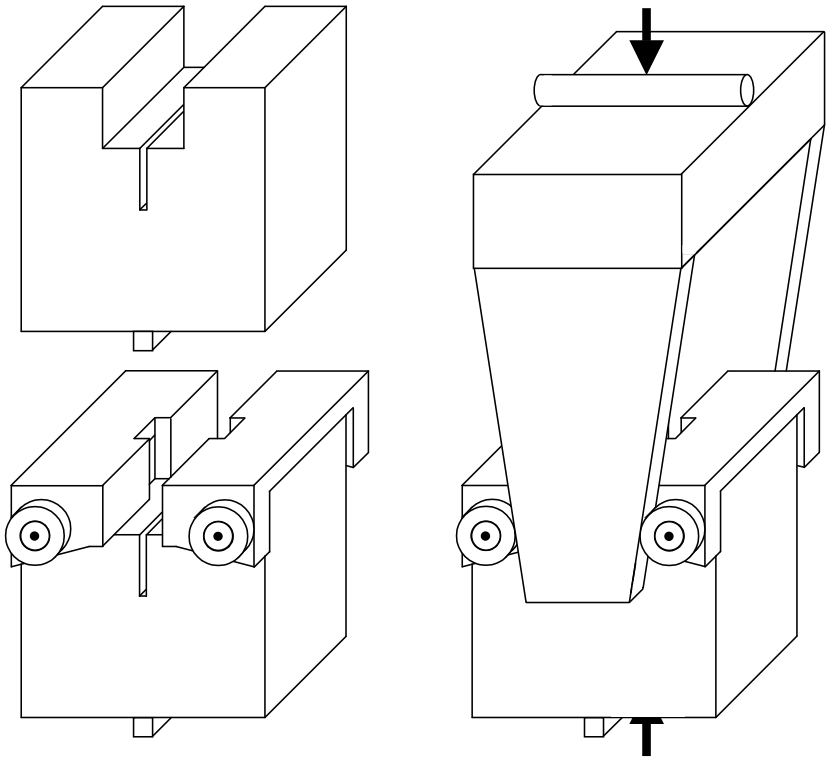

Figure 5.28 *Upper left: Specimen placed on line support; lower left: mounting of two loading devices with roller bearings; right: wedge in place between roller bearings.*

Figure 5.29a shows the geometry of the WST-specimen. The side length of the cube is L and the thickness $t = L$. The initial notch length is a_0 while the ligament length is h. The coordinates for the center of the roller bearings are described by d_1, which is the horizontal distance from the center line, and d_2, the distance from the bottom of the specimen. These must be known since the resultant of the wedge forces passes through this point.

Figure 5.29b shows how the hinge element is incorporated into the WST-specimen. From investigations on three point bending specimens (see e.g. (Ulfkjær, Krenk & Brincker 1995)), the band width is expected to be in the order of $h/2$, which is within the boundaries of the WST-specimen. As shown, the hinge is placed up-side down with crack initiation at the bottom of the notch. As indicated, CMOD is calculated from the opening measured at a distance b from the bottom of the specimen.

Figure 5.29c shows the loading of the specimen. The resultant acting on the specimen from the roller bearings is resolved into a splitting part and a vertical part. The figure also shows loading due to self-weight, mg, acting a distance e from the center line. Usually, self-weight of WST-specimens is ignored in the interpretation of experimental results, since for mature samples the influence is negligible. However, if experiments are

performed on samples in early age self-weight should be considered. Finally, Figure 5.29c shows the sectional forces, P_{sp} and P_v, acting in the symmetry plane.

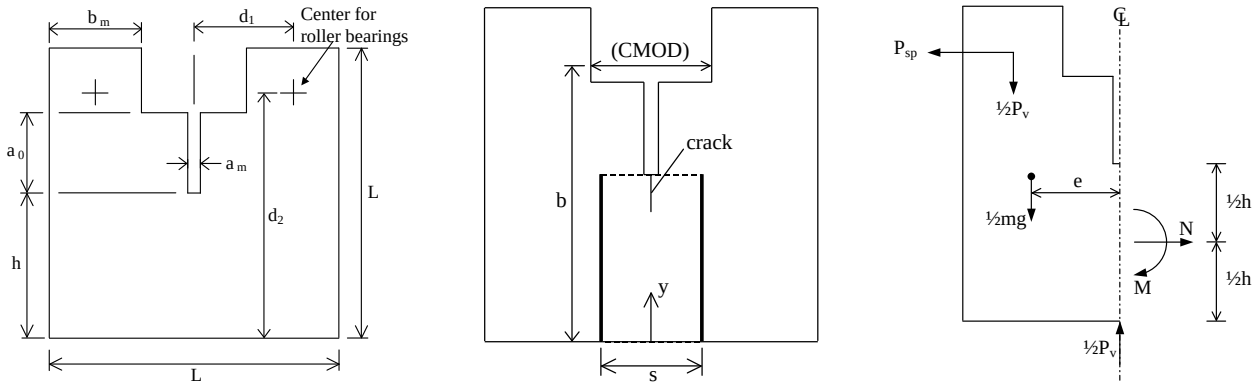

Figure 5.29 *Geometry and loading of the WST-specimen (a), incorporation of the hinge element (b) and loading (c)*

The relationship between the splitting force P_{sp} and the vertical force P_v may be derived by looking at the forces acting on the wedge, see e.g. (Rossi et al. 1991), and is given by:

$$P_v = k\ P_{sp} \tag{5.15}$$

where k is dependent on the friction in the roller bearings and the wedge angle:

$$k = \frac{2\tan\ \alpha_w + 2\mu_c}{1 - \mu_c\ tan\ \alpha_w} \approx 2\ tan\ \alpha_w \tag{5.16}$$

where μ denotes the coefficient of friction in the roller bearings, while α_w is the wedge angle. The rough equality is only valid if the friction in the roller bearings is negligible. According to Rossi et al. (1991), manufacturers of roller bearings give μ-values ranging from 0.1 % to 0.5 %. Ignoring friction in this range generates an error ranging from 0.4 % to 1.9 %.

From Figure 5.29c, expressions for the moment M and the normal force N in the symmetry plane are now determined from the equilibrium equations

$$N = P_{sp} \tag{5.17}$$

$$M = P_{sp}\left(d_2 - \frac{h}{2}\right) + \frac{1}{2}P_v d_1 + \frac{1}{2}mge \tag{5.18}$$

where m = mass of specimen and g = gravity. Using the fact that cracking initiates at $\theta = 1 - \rho$, see e.g. Appendix A, the magnitude of the load, P^0_{sp}, where cracking begins may be calculated by insertion of Equations (5.17)-(5.18) and (A.5). The result is given by Equation (5.19):

$$P^0_{sp} = \frac{f_t h^2 t - 3mge}{6d_2 + 3d_1 k - 2h} \tag{5.19}$$

In the cracked phases, an iterative scheme must be applied when determining the actual load, P_{sp}, for a given angular deformation of the hinge, since no explicit expression can be derived. This can be done in several ways but the best strategy may depend on the known information. This will be explained further in the next section on solution strategies.

The crack mouth opening displacement (CMOD), here defined as the opening of the specimen at the line of loading, depends on three different contributions. One contribution is caused by the elastic deformation of the specimen, δ_e. The second contribution is opening due to the presence of the crack, δ_{COD}. In the cracked phases, opening due to the presence of the crack, δ_{COD}, will be a major term. Finally, the third contribution is due to a geometrical amplification, which arises from the fact that there is a certain distance, $b-h$, from to the crack mouth, located at h, to the line where CMOD is measured, located at b. This contribution, δ_g, is caused by the rotation of the crack faces. Thus, CMOD, is given by:

$$CMOD = \delta_e + \delta_{COD} + \delta_g \tag{5.20}$$

The first term in Equation (5.20) may be determined from handbooks on stress analysis of cracks. According to Tada et al. (1985), δ_e is given by:

$$\delta_e = \frac{P_{sp}}{Et} v_2 \tag{5.21}$$

where v_2 is a function of the ratio between the length of initial notch and distance from the loading line to the bottom of the specimen. In this case, the ratio is given by $x = 1 - h/b$, and:

$$v_2 = \frac{x}{(1-x)^2}\left(38.2 - 55.4x + 33.0x^2\right) \tag{5.22}$$

Equation (5.21) only takes the elastic opening due to the splitting force into account, while the opening caused by the vertical force is neglected. In the cracked phases this simplification will not result in any significant error since the elastic opening is very small compared with the opening due to cracking. In the elastic phase, finite element calculations have shown that the error is negligible.

The opening due to the presence of the crack is derived by Olesen (2001*a*), see also Appendix A, and is given by:

$$\delta_{COD} = \frac{sf_t}{E}\frac{1 - b_i + 2\alpha\theta}{1 - \beta_i}, \qquad \beta_i = \frac{f_t a_i s}{E} \tag{5.23}$$

where b_i and β_i must be chosen in accordance with the actual phase of crack propagation.

The opening due to the distance between the load line and the bottom of the notch, may be calculated from the expression for the crack opening, given by (see (Olesen 2001*a*)):

$$w(y,\varphi) = \frac{2(y - y_0)\varphi - \zeta_i}{1 - \beta_i}, \qquad \zeta_i = \frac{f_t b_i s}{E} \tag{5.24}$$

where ζ_i must be preferred in accordance with the actual phase of crack propagation. It is now assumed that δ_g is governed by the mean angle of the crack surfaces relative to the vertical line of symmetry. This angle, denoted the crack angle, φ_{cr}, is for all phases given by:

$$\varphi_{cr} = \frac{\delta_{COD}}{2\alpha h} \tag{5.25}$$

However, due to an artifact of the model, the angle of the crack faces are not equal to zero at crack initiation, instead they instantly assume a certain angle, φ_{cr}^0. This angle may be derived by differentiating Equation (5.24):

$$\varphi_{cr} = \frac{1}{2}\frac{\partial w(y,\varphi)}{\partial y} = \frac{\varphi}{1-\beta_i} \tag{5.26}$$

Thus, φ_{cr}^0 is given by:

$$\varphi_{cr}^0 = \frac{\varphi_{0-I}}{1-\beta_1} \tag{5.27}$$

where φ_{0-I} represents the angular deformation of the hinge at initiation of the crack. The corrected crack angle is given by $\bar{\varphi}_{cr} = \varphi_{cr} - \varphi_{cr}^0$ and thus, δ_g is given by:

$$\delta_g = 2\bar{\varphi}_{cr}(b-h) = 2\ (b-h)\left(\frac{\delta_{COD}}{2\alpha h} - \frac{sf_t}{hE}\ \frac{\theta_{0-I}}{1-\beta_1}\right) \tag{5.28}$$

where φ in the latter expression has been replaced by the normalized angle θ. Note that Equation (5.28) will not represent a good solution for high values of β_i. However, this will only be a problem for materials that exhibit an extreme brittleness in the first part of the softening regime. A different solution of the hinge problem suited for this case may be found in Olesen (2001*a*), where the stress-crack opening relationship is described by a drop-linear form. It is also important in this connection to consider the influence of the b_2-parameter. If b_2 is high, such as e.g. in a fiber reinforced concrete, the influence of a_1 vanishes since the first part of the stress-crack opening relationship becomes short. Thus, a poor determination of a_1 in such cases is not detrimental for the method.

The fracture energy, G_f, may be calculated utilizing the crack mouth opening displacement at the load line and the rotation of the upper part of the specimen. From the derivation of δ_g it is known that the rotation of the upper part of the specimen is governed by the corrected crack angle. Figure 5.30 shows the deformation of the upper part of the specimen.

The horizontal displacement is given by $u = 1/2\ CMOD$, while the vertical displacement is calculated as $v = d_1 \sin\bar{\varphi}_{cr}$. Thus, $dv \cong d_1 d\bar{\varphi}_{cr}$, and the energy, dW, dissipated during a displacement of the load point by $(du,\ dv)$ is given by:

$$dW = 2\left(P_{sp}(u)du + \frac{1}{2}P_v(v)dv\right) \tag{5.29}$$

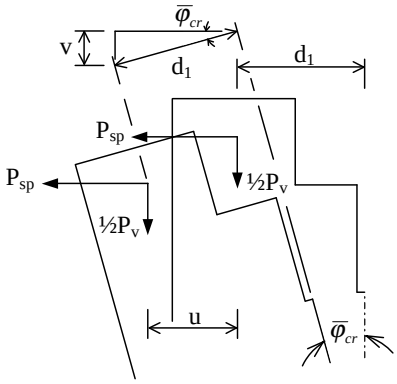

Figure 5.30 *Displacement of load point*

where the loads are written as functions of their displacements. Equation (5.29) may be rewritten, employing the relation between the horizontal and the vertical displacement and the relation between the loads. This yields:

$$dW = 2\left(P_{sp}(u)\ du + \frac{1}{2}\left(k\ P_{sp}(u)\right)\ d_1\ d\bar{\varphi}_{cr}\right) \tag{5.30}$$

Thus, G_f is calculated by integrating Equation (5.30) and dividing by the area of the ligament:

$$G_f = \frac{2}{ht}\int_0^{u^{max}} P_{sp}(u)\ du + \frac{kd_1}{ht}\int_0^{\bar{\varphi}_{cr}^{max}} P_{sp}(u)\ d\bar{\varphi}_{cr} + \frac{mge}{ht}\tan\left(\frac{hE}{sf_t}\theta^{max}\right) \tag{5.31}$$

where the latter term is due to work done by the gravity. The normalized angular deformation, θ^{max} is defined as the deformation at which only the dead weight can be sustained by the hinge. Note that since $u = \frac{1}{2}CMOD$ is a function of θ and $\bar{\varphi}_{cr}$, see Equations (5.20)-(5.28), Equation (5.31) cannot be simplified. Equation (5.31) may be solved using a numerical integration scheme.

Solution Strategies

In the cracked phases, an iterative scheme must be applied when determining the actual load, P_{sp}, for a given angular deformation of the hinge, or known value of CMOD, since no explicit expression can be derived. This can be done in several ways. The most obvious way is to make a small increment in θ and then on the basis of this value, find a solution for P_{sp}. This can be done by using a root-finding algorithm. The equation that must be solved is given by:

$$\mu_{ext}(P_{sp}) - \mu_{int}^{j}(\theta, P_{sp}) = 0 \tag{5.32}$$

where $\mu_{ext}(P_{sp})$ represents the external loading of the hinge, given by Equation (5.18), while $\mu_{int}^{j}(\theta, P_{sp})$ is the internal normalized moment capacity of the hinge, where the analytical expression depends on the actual phase of crack propagation, j (see (Olesen 2001*a*)).

The above described procedure results in solutions for the splitting force, P_{sp} for given values of θ, whereas CMOD is unknown. If experimental observations are made and the purpose is to find solutions for P_{sp} for certain values of CMOD, this constraint may be utilized when solving the equations. Instead of guessing values of θ, it is more obvious to solve for P_{sp} and θ employing two non-linear equations describing the restraints on the load, P_{sp} and crack mouth opening displacement, CMOD. The first of these two equations is identical to Equation (5.32), while the second reads:

$$CMOD^{obs} - CMOD(P_{sp}, \theta) = 0 \tag{5.33}$$

where $CMOD^{obs}$ is the observation made for CMOD, while $CMOD(P_{sp}, \theta)$ is determined from Equation (5.20).

5.3.2 Inverse Analysis on the WST

The previous section described how the global load-crack mouth opening displacement curve may be determined knowing the stress-crack opening relationship. This is a necessary step towards the real interesting problem, which is to conduct an inverse analysis and thereby determine the stress-crack opening relationship from the global load-crack mouth opening displacement curve.

It is, however, difficult to determine the stress-crack opening relationship from inverse analysis. Strategies based on the finite element method has been developed by Roelfstra & Wittmann (1986) and Wittmann et al. (1987), who assumed the fracture mechanical properties to be those, which minimize a function describing the error between the finite element curve and the experimental curve. A different method utilizing the direct sub-structure method by Brincker & Dahl (1989) was explored in (Ulfkjær & Brincker 1993). They investigated different optimization strategies and found methods that could be employed for the inverse analysis. Kitsutaka (1997) developed a method for stepped inverse analysis, where the optimum softening inclination is determined for the current step of analysis. All former values of the stress-crack opening relationship were fixed. The result is a poly-linear stress-crack opening relationship, which closely approximates experimental values. A similar approach was explored by Nanakorn & Horii (1996).

The method presented here is based on the hinge model described in the Appendix A. The method is attractive due to its inherent simplicity and the short computation time. Furthermore, this approach does not have problems of finding local minimums, which was found to be a problem in the method by Ulfkjær & Brincker (1993).

The idea is to use a stepwise inverse analysis, where the optimization problem is solved in steps corresponding to the different phases of crack propagation. This is possible due to the analytical solution, which distinguishes clearly between the different phases. First, the optimization is conducted in the elastic phase with the modulus of elasticity as the only free parameter, and only with the observations belonging to the elastic phase. This first part, named Step I, see Equation (5.34)-(5.35) will result in a fast and reliable determination of the modulus of elasticity since the selected observations are governed by the modulus of elasticity only due to the fact that no crack has formed yet. It is important to realize that the initial guess on the tensile strength will determine how many observations to include in the optimization. But with reasonable initial guesses and by globally re-running the optimization process (including all steps) this is a minor problem, since the global iterations will converge at the true phase change point.

Having determined an estimate for the modulus of elasticity, the next step is to formulate an optimization strategy for the cracked phases. Using the bilinear stress-crack opening relationship, it turns out that the best strategy is to separate the problem into two, such that f_t and a_1 are determined first (Step II), while a_2 and b_2 are determined subsequently (Step III). This is due to results showing that local minima may be avoided using this approach. In contrast to Step I, all observations must now be included in the optimization. If only observations belonging to the actual phase (e.g. phase I) were considered, a spurious solution may be found. This solution represents the minimum where the constitutive parameters have been selected such that no observation belongs to the considered phase. Considering all observations in the cracked phases, and using the mean square of differences between observations and predictions as an error norm, the optimization problem reads:

Step I - Determination of E

$$\min_{E} \ \frac{1}{N^0_{max}} \sum_{0}^{N^0_{max}} \left(P_{sp} - \hat{P}_{sp} \right)^2 \tag{5.34}$$

$$\text{subject to} \qquad E \ > \ 0 \tag{5.35}$$

Step II - Determination of f_t and a_1

$$\min_{(f_t,a_1)} \frac{1}{N_{max}} \sum_{0}^{N_{max}} \left(P_{sp} - \hat{P}_{sp}\right)^2 \tag{5.36}$$

$$\text{subject to} \qquad f_t > 0 \tag{5.37}$$

Step III - Determination of a_2 and b_2

$$\min_{(a_2,b_2)} \frac{1}{N_{max}} \sum_{0}^{N_{max}} \left(P_{sp} - \hat{P}_{sp}\right)^2 \tag{5.38}$$

where N^0_{max} and N_{max} represents the last observation made belonging to phase 0 and the total number of observations made, respectively.

Note that the observations on the P-CMOD curve must be placed equidistantly with regard to the arch length in the normalized coordinate system in order to arrive at a precise result when conducting the inverse analysis. This is due to the fact that no part of the curve should be weighted higher than any other part. Only this approach will result in a good determination of all the constitutive parameters. If one part of the curve has a higher weight in the optimization, the determination of the parameters which dominate the curve shape of this part will dominate the landscape of the object function, and an ill determination of the rest of the parameters and also a poor fit of the rest of the curve may be the result. One example is the peak of the curve for a normal concrete without fibers. This part of the curve is dominated by f_t and a_1. Thus, if emphasis is placed on this curve part, either through observation density or by the particular selection of the object function, the fit of this curve part may be excellent on the expense of the rest of the curve.

The proposed method is simple and precise and will in general not find local minima. In other methods such as presented by Roelfstra & Wittmann (1986), finite element analysis is applied to calculate the predicted responses for a given set of parameters, and the optimization problem is set up for the entire curve. A possible problem with such an approach is that the correlation between e.g. the modulus of elasticity and the error norm for the entire curve is weak. Another problem is that this five dimensional optimization problem may be more liable to finding local minima. This problem was described in the work by Ulfkjær & Brincker (1993).

The proposed method shows the importance of a detailed analytical model for the purpose of performing inverse analysis. Of course, this method might still suffer from finding local minima, but as indicated on the contour plots in Figure 5.31 and 5.32, the method seems to be very robust. Figure 5.31 shows a contour plot where the error function in Step II has been calculated for different choices of f_t and a_1. The correct parameters in the case

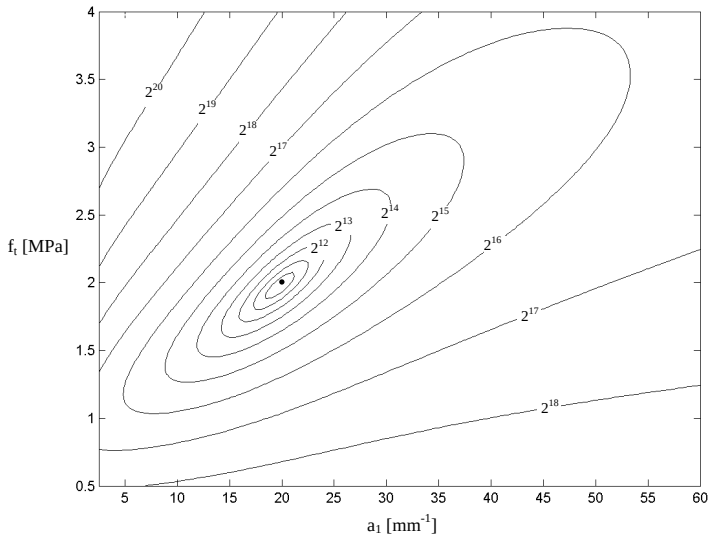

Figure 5.31 *Contour plot for error norm in Step II as function of f_t and a_1. $E \equiv 30$ GPa, $a_2 \equiv 0.2$ mm^{-1} and $b_2 \equiv 0.1$*

shown are $f_t = 2.0$ MPa, $a_1 = 20$ mm^{-1}, $a_2 = 0.2$ mm^{-1}, $b_2 = 0.1$ and $E = 30000$ MPa. The error function has been calculated by comparing the "experimental" curve, which is generated employing the correct values for constitutive parameters, with the estimated curve, which uses the actual estimates for f_t and a_1 and the correct values for the fixed constitutive parameters. Both curves are generated using the hinge model. It is seen in Figure 5.31 that no local minima exist. This is very important since it means that any initial guesses in phase I will eventually lead to the correct values. The error function for Step III, see Figure 5.32, is also seen to behave very smoothly without local minima. Thus, the result is not sensitive to the initial guess. However, as noted before, other reasons make good initial guesses important, e.g. in order to achieve a fast convergence.

Figures 5.31 and 5.32 only show the contour plot near the global minimum. In order to make a more thorough testing of the robustness of the method and to determine whether any other minima exist near or far away from the global minimum, many different start guesses have been tried using different P-CMOD curves, generated either by FEM or real experiment. Up to 25 start guesses, ranging from $0.1\lambda - 10\lambda$, where λ is global solution for the actual parameter, have been examined in the optimization algorithm. They do all arrive at the same and correct solution. Only requirement is that the initial guess on the constitutive parameters does not violate the physics of the problem or the definitions given in e.g. Figure A.1.

The method described above is easily applied to the three and four point bending specimen, as well as other test geometries where the hinge model can be used. The method has already been implemented for the three point bending test by the author, see Section 5.5, and the results are promising with regard to precision of the results and the fact that no local minima have been encountered during the inverse analysis. The method has also been tested on experimental results obtained with the wedge splitting test, (Østergaard,

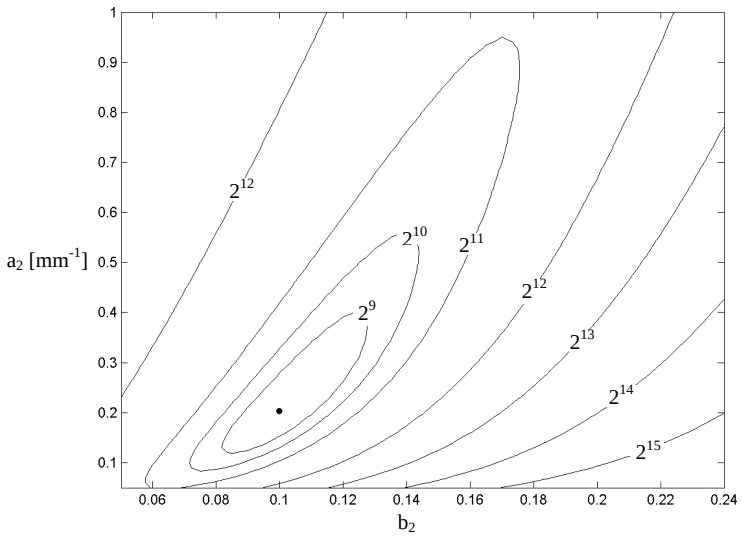

Figure 5.32 *Contour plot for error norm in Step III as function of a_2 and b_2. $E \equiv 30$ GPa, $f_t \equiv 2$ MPa and $a_1 \equiv 20$ mm^{-1}*

Lange & Stang 2002), see also Chapter 6.

5.3.3 Implementation in MatLab

A set of programs have been written in MatLab. These programs are capable of conducting both forward analysis and inverse analysis. The basic principles of the programs depend on whether an experiment has been conducted. If no experimental results are available, the algorithm simply makes steps in θ and finds the solution for P by solving Equation (5.32). This is relevant for e.g. parameter investigations. For the case where experimental observations are known, the program is a little different. Now, Equation (5.32) is solved together with Equation (5.33), and instead of making increments in θ, the loop covers all observations, and returns corresponding values for P_{sp}. Thus, the program returns predictions for P_{sp} for a given estimate on the parameters in the stress-crack opening relationship and a set of CMOD-values. This has been utilized in the algorithm for inverse analysis. The inverse analysis algorithm applies the simplex algorithm to fulfill (5.34-5.38). For each guess that the simplex algorithm generates, the forward analysis program is run. The simplex algorithm utilized is included in the MatLab Optimization Toolbox.

The code is available in Appendix B. It will be utilized for the interpretation of experimental results.

5.3.4 Finite Element Modelling

In order to verify the applicability of the hinge model to the WST-specimen and to determine the correct band width parameter, s, the WST-specimen has been modelled utilizing

the finite element method. Both 2 and 3 dimensional analysis has been conducted. The three dimensional analysis was carried out in order to investigate the effects of load distribution on the specimen in the thickness direction, see e.g. (Østergaard, Stang & Olesen 2002*a*). However, the analysis showed that this was unimportant and that the 2D modelling is able to fully capture the behavior of the specimen.

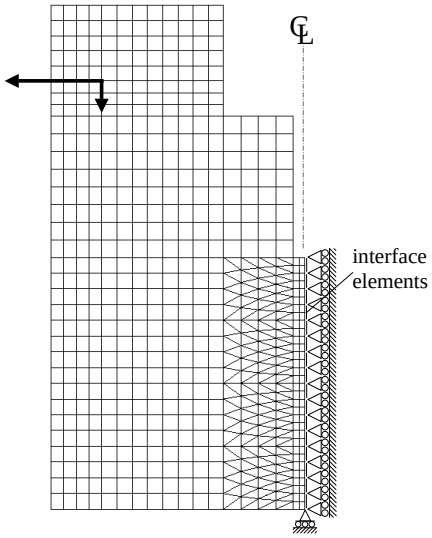

Figure 5.33 *Mesh utilized in FEM-analysis of WST-specimen*

Figure 5.33 shows the 2D mesh applied in the analysis. The geometry of the mesh represents one-half of the specimen shown on Figure 5.29a. The thin lines shown on the symmetry line, between the mesh and the supports, represents interface elements used to model the crack. These interface elements have been given a bilinear softening branch of the same type as shown in Figure A.1. This is possible in the applied FEM-package, DIANA, see e.g. the DIANA manual, (DIANA 2000), which furthermore allows for a stable CMOD control of the calculations. The quality of the mesh has been verified in a convergence analysis checking the invariability of the peak load, curve shape and the fracture energy. Based on this investigation, the mesh is found to be useful and precise.

5.3.5 FEM validation of interpretation and inverse analysis

In literature, see e.g. (Ulfkjær et al. 1995), modelling of the three point bending specimen has shown that the hinge parameter s for normal concrete can be fixed to $0.50h$, where h is beam depth. The present work shows that a dependency of the softening response exists for the wedge splitting test. The dependency is not strong, as shown in Figure 5.34, where load-CMOD curves have been drawn for different values of s and compared with the FEM-model. As shown, varying s from $0.2h$ to $1.20h$ only offsets the peak loads by +14% and -8%, respectively. The value of s/h that minimizes the error norm calculated

for the entire curve is $s/h = 0.84$ and is shown in the figure too. For this value of s the hinge solution is seen to be very close to the result generated by the finite element model.

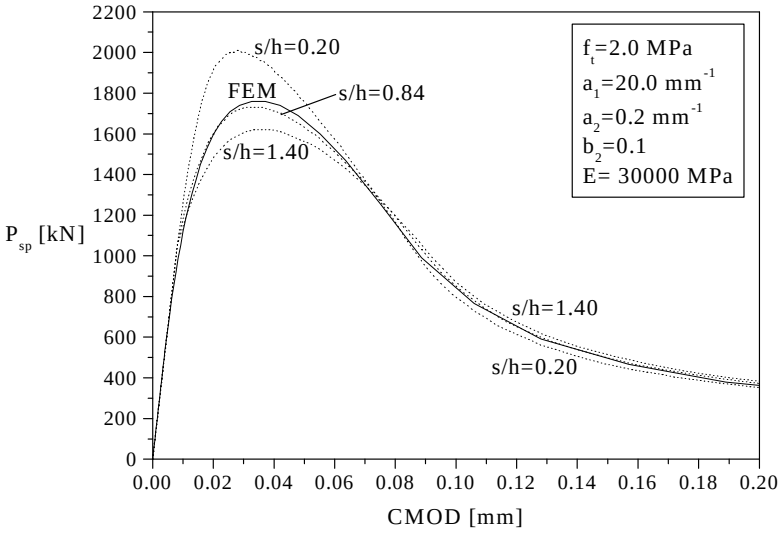

Figure 5.34 *Load-crack mouth opening curve generated by FEM-model (full line) and by hinge model (dotted lines) for different choices of s.*

The dependency of s seems reasonable due to the fact that the elastic energy stored in the crack band increases with increasing band width and thus, results in a more unstable crack growth, yielding a lower peak value, while the overall curve behavior is unchanged, except for the amount needed to keep the fracture energy, G_f, constant.

In general, s will be a function of the geometry of the wedge splitting specimen and the elastic and fracture mechanical properties represented by β_i and ζ_i, and thus, a calibration for s will be necessary for a given specimen geometry and for material properties similar to the those the actual investigation aims at determining. In general, this work has shown that small values of b_2 gives the best results from the inverse analysis. To show how the best fit value of s changes given a change in the f_t/E-ratio, model curves have been generated employing the finite element model. These 'experimental' curves have been employed in an inverse analysis algorithm, which optimizes for s only. All other parameters were fixed to the correct values. The result is shown in Figure 5.35, where the optimal choices of s are shown. The change of s as function of the f_t/E-ratio following Figure 5.35 is given in Equation (5.39). However, it must be stressed that s is also a function of the remaining parameters in the stress-crack opening relationship, and of the geometry of the wedge splitting specimen.

$$s/h = 2100\frac{f_t}{E} + 0.69 \tag{5.39}$$

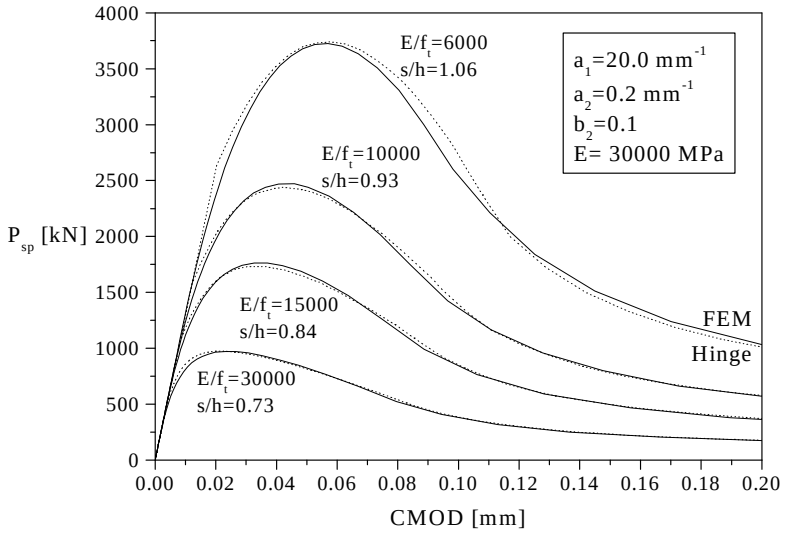

Figure 5.35 *Hinge model (dotted line) and finite element model (full line) results compared for different choices of f_t/E-ratio.*

The validity of choice of s and the general applicability of the concepts to fiber reinforced concrete is illustrated in Figure 5.36. This figure shows how the FEM-results are closely correlated to the hinge results for low and moderate fiber contents, which is for $b_2 \leqq 0.5$, while higher fiber contents results in significant differences with regard to curve shape and stress level for corresponding crack mouth opening displacements. This can somewhat be compensated for by optimizing with regard to the band width parameter, s, but the correlation will not be perfect. This is partly ascribed to the fact that high values of b_2 represent some violation of the model assumptions, since the boundary planes of the hinge may not remain plane in these cases and since the crack planes may possibly deviate much from the assumed bilinear shape. However, the curves are still so well correlated that the results will be useful in many cases.

More problems will be encountered in the case of inverse analysis for a FRC-material with high values of b_2. Now phase I is very short and it contains only few observations. This results in problems for the optimization algorithm and a poor determination of f_t and a_1. These parameters should probably in such cases be determined from tests on the pure matrix material and the result used for the determination of b_2 and a_2 for the fiber reinforced material. However, if an approximate determination of these parameters is sufficient, the proposed method can still be applied. Especially an accurate determination of a_1 for FRC with high fiber effect is not very important since the stress-crack opening curve is relatively unaffected by this parameter in such cases. In fact, for many cases, the simple drop-linear stress-crack opening relationship described in (Olesen 2001*a*) may be applied.

Figure 5.37 illustrates the robustness of the method for different choices of f_t and a_1. In all cases, the initial guesses were generated by an initialization algorithm, and the algorithm has found the solution without encountering local minima.

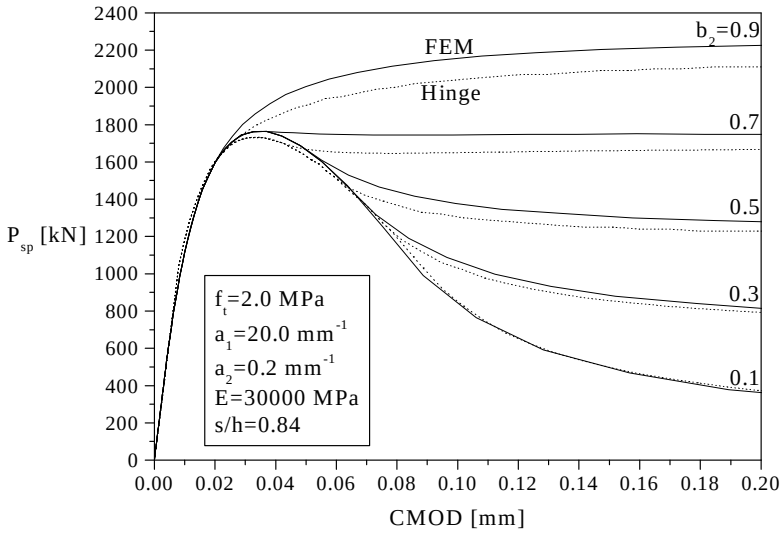

Figure 5.36 *Load-crack mouth opening curve generated by FEM-model (full line) and by hinge model (dotted line) for different choices of* b_2.

Table 5.2 *Results from inverse analysis with different values of* f_t *and* a_1, s/h=*0.84. Fixed parameters were selected to* a_2=*0.2* mm^{-1}, b_2=*0.1 and* E/f_t=*15000. The varied input values are given in the left part of the table while the output values for all the parameters are listed in the right part.*

$f_t[MPa]$	a_1 $[mm^{-1}]$	f_t [MPa]	a_1 $[mm^{-1}]$	a_2 $[mm^{-1}]$	b_2 [-]	$\frac{E}{f_t}$ $[10^3]$
2	20	2.03	20.59	0.229	0.105	14.1
3	30	2.95	29.86	0.247	0.110	14.8
4	40	3.86	39.50	0.272	0.117	15.0
5	50	4.72	48.46	0.287	0.121	15.4
5	20	5.06	20.52	0.230	0.103	14.3

The performance of the method in terms of the number of iterations needed to achieve convergence is demonstrated in Figure 5.38a. In this particular case 4 global iterations were needed to satisfy the convergence criteria. The error relative to the constitutive input of the finite element model is shown in Figure 5.38b. This result is also satisfying since the error on most parameters is below 5% and since the largest error, that of a_2, occurs for a small value of a_2.

Table 5.2 shows the results of the inverse analysis with varying f_t and a_1 in tabular form. The results are all based on the same s/h value, which has been determined on the basis of the first result in the table. It is seen that the error on the results increases with increasing f_t and a_1. This error is partly due to the fact that s is optimized for the case where $f_t = 2$ MPa and $a_1 = 20$ mm^{-1}. It is seen that the largest error on the determined parameters is that of a_2.

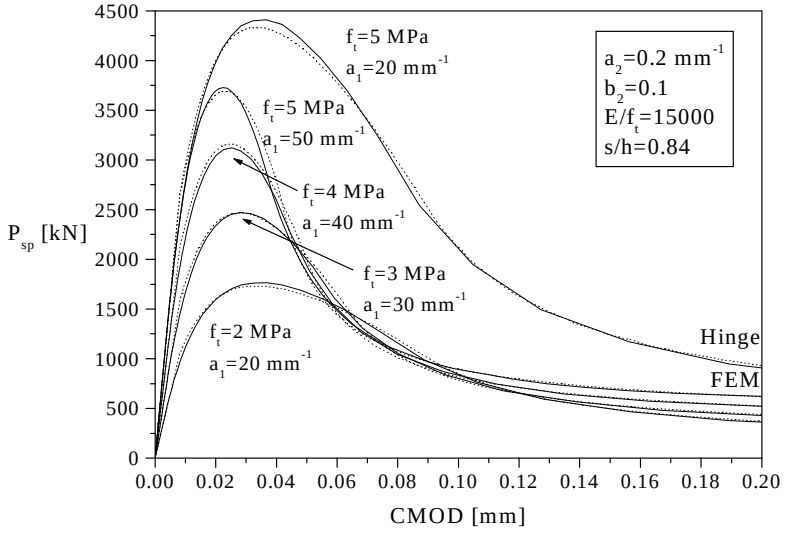

Figure 5.37 *Load-crack mouth opening curve generated by FEM-model (full line) and results from inverse analysis for different choices of f_t and a_1.*

Table 5.3 *Results from inverse analysis with different values of b_2, s/h = 0.84. Fixed parameters were selected to f_t=2 MPa, a_1=20 mm^{-1}, a_2=0.2 mm^{-1} and E/f_t=15000. The varied input values are given in the left part of the table while the output values for all the parameters are listed in the right part.*

b_2	f_t $[MPa]$	a_1 $[mm^{-1}]$	a_2 $[mm^{-1}]$	b_2 [-]	$\frac{E}{f_t}$ $[10^3]$
0.1	2.03	20.59	0.229	0.105	14.1
0.3	2.02	19.73	0.225	0.311	14.3
0.5	1.99	17.72	0.226	0.522	14.6
0.7	1.93	3.92	0.226	0.740	15.2
0.9	2.44	114.7	0.186	0.767	11.6

The inverse analysis algorithm has also been applied to stress-crack opening relationships with different values of b_2, see Table 5.3. For low values of b_2, the results from the inverse analysis are seen to be close to the input parameters. However, for b_2=0.9 the result is poor. Especially the determination of a_1 is poor, as explained before. Investigations on such materials may be better if they are combined with investigations on the pure matrix material. However, as long as the value of b_2 is kept $b_2 \leqq 0.5$, the method produces good results.

To verify that the method is also applicable for early age concrete, finite element P-CMOD curves for different values of f_t have been calculated. The results from the inverse analysis based on these curves are shown in Table 5.4. The f_t/E-ratio has been kept constant, which will approximately be the case for concrete during hardening. The stress-crack opening relationship has also been kept constant. In all cases the initial guess on f_t and

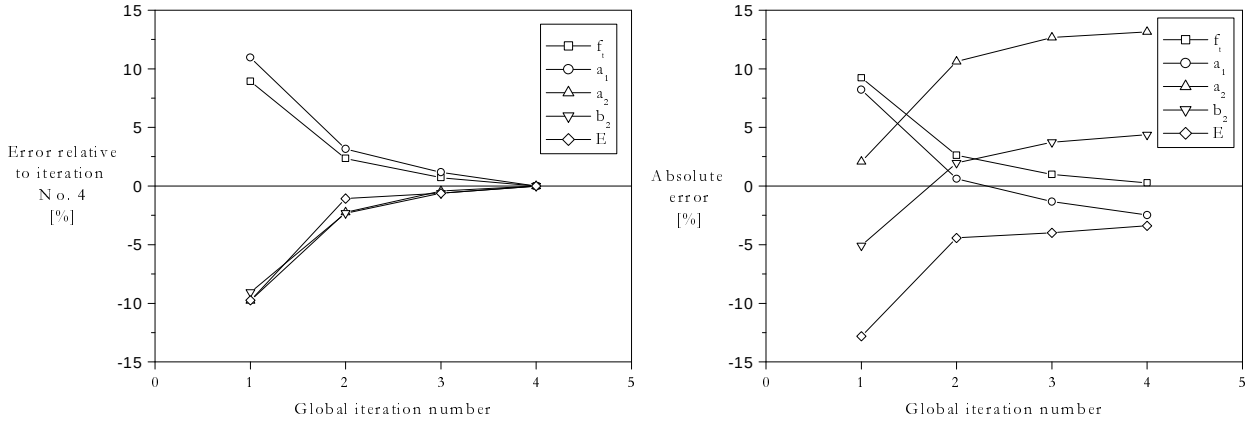

(a) (b)

Figure 5.38 *Relative error on results from the inverse analysis (a), used as convergence criteria and absolute error on results in relation to the constitutive input of the FEM-model (b). f_t=2 MPa, a_1=20 mm^{-1}, a_2=0.2 mm^{-1}, b_2=0.3, E=30 GPa*

Table 5.4 *Results from inverse analysis with different values of f_t, s/h = 0.84, and E/f_t=15000. Fixed parameters were selected to a_1=20 mm^{-1}, a_2=0.2 mm^{-1} and b_2=0.1. The varied input values are given in the left part of the table while the output values for all the parameters are listed in the right part.*

f_t $[MPa]$	f_t $[MPa]$	a_1 $[mm^{-1}]$	a_2 $[mm^{-1}]$	b_2 [-]	$\frac{E}{f_t}$ $[10^3]$
0.1	0.109	20.33	0.157	0.120	13.3
0.5	0.513	20.52	0.201	0.105	14.1
1	1.02	20.51	0.218	0.104	14.2
2	2.03	20.59	0.229	0.105	14.1

a_1 were generated by an initialization script. The method converged to the global minimum in all the cases shown in Table 5.4 without encountering local minima. The results also show that the method of inverse calculation produces good results for low values of f_t.

5.3.6 The Experimental Setup

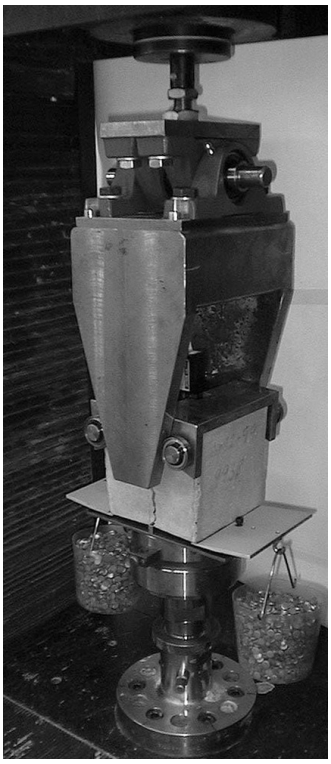

(a)

Figure 5.39 *Photo of the wedge splitting setup*

Figure 5.39 shows the experimental wedge splitting setup. Two measures have been taken in order to eliminate even the slightest self-weight loading of the ligament. First, the wedge has been connected to the crosshead such that this element is not resting upon the loading devices, which greatly reduces the dead load. Second, small weights attached to a teeterboard are imposing a reaction on the specimen from below. This reaction has been balanced such that the moment load in the ligament from the self-weight of the specimen and the deadweight from the loading devices is zero. The rest of the setup closely follows the schematic drawing given in Figure 5.29.

5.3.7 Usability with early age concrete

It is demonstrated in the previous sections that the wedge splitting test is very well suited for determination of fracture properties early age concrete. This is due to a number of facts:

1. Self-weight problems can be eliminated
2. Small specimen size gives small temperature gradients
3. Inverse analysis can be conducted
4. Easy to handle even at very early age

5.4 Wedge Splitting Test Setup for Long-Term Testing

The experimental investigation of time-dependent effects on the fracture of concrete is a subject, which not many authors have dealt with. The results presented here was first published in (Østergaard, Stang & Olesen 2002*b*).

5.4.1 Wedge Splitting Test and Cracked Hinge Model

If the normal force, N, acting on the hinge is constant over time and the rate effect model given by e.g. Equation 3.21 is employed, the maximal elastic moment that can be sustained by the hinge for a unit thickness is equal to:

$$M_{el} = \frac{1}{6}\left(f_t + k\dot{\varepsilon}(y = h/2)\right)h^2 - \frac{1}{6}Nh \tag{5.40}$$

where it has been assumed that a rate effect exists on the tensile strength in the elastic state, thus ensuring continuity of stress at the fictitious crack tip. Given this assumption, the angular deformation of the hinge at the onset of cracking will be:

$$\varphi_{el} = \frac{12sM_{el}}{Eh^3} \tag{5.41}$$

while the strain rate will be given by:

$$\dot{\varepsilon}(y) = \frac{12(y - y_0)}{Eh^3}\dot{M} \tag{5.42}$$

By requiring that the sides of the hinge element are straight, and that the incremental springs are attached to the sides, the following geometric condition must be fulfilled:

$$(y - y_0)\varphi = \frac{s}{E}\sigma\left(w(y), \dot{w}(y)\right) + w(y) \tag{5.43}$$

where y_0 is the neutral axis. Equation 5.43 may be rewritten to:

$$\sigma\left(w(y), \dot{w}(y)\right) = \frac{E}{s}\left((y - y_0)\varphi - w(y)\right) \tag{5.44}$$

By combining Equation 5.44 with the constitutive condition, Equation 3.21 and solving for the two unknown properties, $\sigma\left(w(y), \dot{w}(y)\right)$ and $w(y)$ one arrives at the following result:

$$\sigma\left(w(y), \dot{w}(y)\right) = \frac{E\left(b_i - a_i(y - y_0)\varphi\right)\left(f_t + k\dot{w}(y)\right)}{E - sa_i\left(f_t + k\dot{w}(y)\right)} \tag{5.45}$$

$$w(y) = \frac{E(y - y_0)\varphi - s\left(f_t + k\dot{w}(y)\right)b_i}{E - s\left(f_t + k\dot{w}(y)\right)a_i} \tag{5.46}$$

The position of the neutral axis may be determined from the equilibrium equations. The resultant of the compressive stresses, N_c, elastic tensile stresses, N_t and the crack bridging stresses, N_f are given by:

$$N_c = \frac{\varphi y_0^2 E}{2s} \tag{5.47}$$

$$N_t = \frac{s\left(f_t + k\dot{\varepsilon}(y)\right)^2}{2\varphi E} \tag{5.48}$$

$$N_f = \int_{y^*}^{h} \sigma\left(w(y), \dot{w}(y)\right) dy \tag{5.49}$$

where y^* denotes the position of the tip of the fictitious crack, given by:

$$y^* = y_0 + \frac{s(f_t + k\dot{\varepsilon})}{\varphi E} \tag{5.50}$$

Thus, the neutral axis, y_0 can be determined from:

$$N = N_c - N_t - N_f \tag{5.51}$$

Now the moment relative to the center of the hinge may be determined. The moment is given by:

$$\begin{aligned} M &= \left(\frac{h}{2} - \frac{1}{3}y_0\right) N_c + \left(\frac{1}{3}y_0 + \frac{2}{3}y^* - \frac{h}{2}\right) N_t \\ &\quad + (y^* - \frac{h}{2}) N_f + \int_{y^*}^{h} \sigma\left(w(y), \dot{w}(y)\right)(y - y^*) dy \end{aligned} \tag{5.52}$$

where the external moment imposed on the hinge is given by Equation 5.53. The equation gives a condition for determination of the angular deformation of the hinge for the selected external moment M.

From the equations given above, rate dependent analysis of the cracked hinge may be performed. The analysis may be carried out by discretizing the hinge in a finite number of springs. When the crack propagates into a certain spring the first guess on the crack opening rate may be assumed to be zero. Thus, at the beginning of any time step, the strain and crack opening rates are known, and with these values as fixed, analysis may be performed. After the analysis, it must be controlled whether the opening rate is equal to the initial guess, and if not, a new guess on the rate must be made. In this way, analysis may be performed with a prescribed moment load history, and for a constant moment, the creep crack opening and crack growth may be determined. If the wedge splitting test is considered, the presence of the normal force may be included in the equations. Ageing of the hinge may be included using solidification theory for the ageing of the hinge parameters, e.g. (Bažant & Prasannan 1989*a*).

5.4.2 The Experimental Setup

In the process of selecting the design of the experimental setup, applicability to early age concrete has been a major goal. Thus, the uniaxial specimen and the three point bending specimen were quickly disregarded. With regard to the uniaxial specimen, the reason was the difficulties in establishing a pure uniaxial state of stress, and problems with casting of the notch and measuring the crack opening displacement. For the three point bending specimen, self-weight was the problem. None of these problems are associated with the wedge splitting test, although a more complex model for interpretation is needed compared with e.g. the uniaxial tension test. A picture of the setup is shown on Figure 5.40.

The picture shows how the specimen is inserted between two rigid frames. On the upper frame two loading shelves are attached. The right one of these is designed to completely eliminate loading of the specimen from self-weight caused by the frame and wedge, while the left one imposes a certain load with a magnification factor of four. As shown, the loads are applied with certain eccentricities relatively to the line of rotation. This has

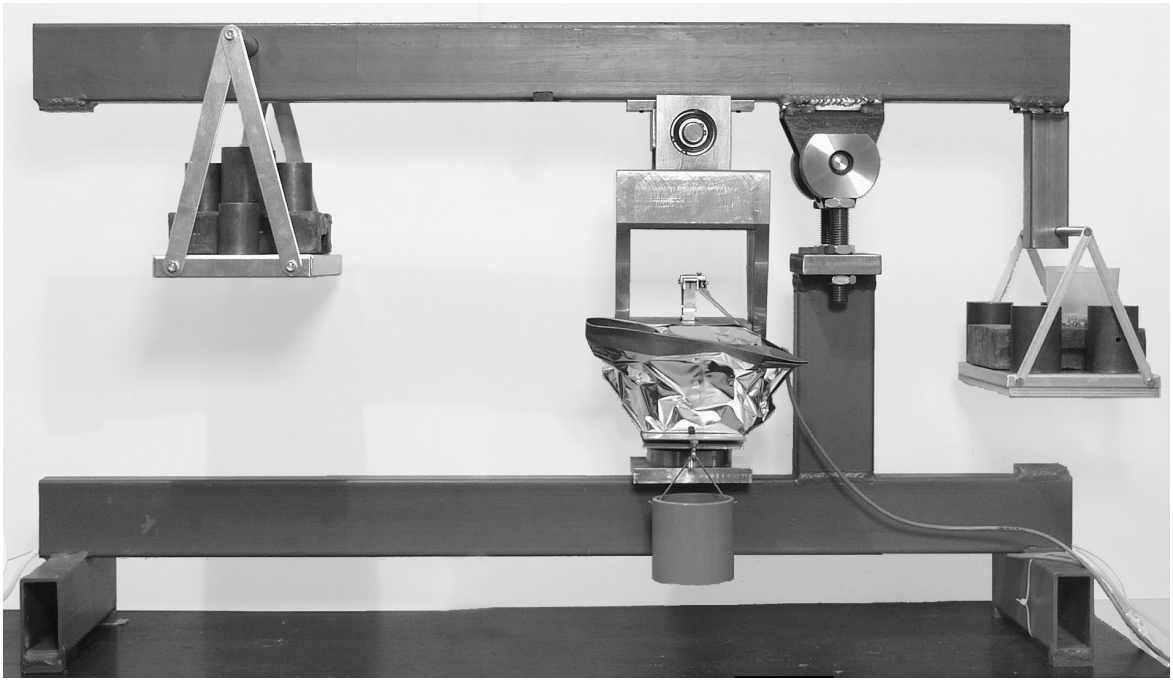

Figure 5.40 *Creep crack growth setup*

been done in order to eliminate changes in the self-weight compensation and loading with changes of the angle of the upper frame during crack opening. Figure 5.41 shows the loads acting on the frame in the self-weight situation.

The rotation of the frame will result in a change in the lever arms of the loads with respect to the point of rotation. This change will be a function of the length of the arm, L_i and the eccentricity, e_i, where i represents one of the four loads under consideration. Taking moment with respect to the point of rotation, and following the orientation of the eccentricities shown on Figure 5.41 gives:

$$\begin{aligned}(P_b L_b + \tfrac{1}{2} q L_1^2)\cos\theta - (P_b e_b + q L_1 e_h)\sin\theta \\ = (P_w L_w + \tfrac{1}{2} q L_2^2)\cos\theta - (P_w e_w - q L_2 e_h)\sin\theta\end{aligned} \tag{5.53}$$

This equation will remain valid for any θ if the coefficients of $\cos\theta$ on both sides, and of $\sin\theta$ on both sides, are equal. Thus, two equations must be satisfied:

$$P_b L_b + \frac{1}{2} q L_1^2 = P_w L_w + \frac{1}{2} q L_2^2 \tag{5.54}$$

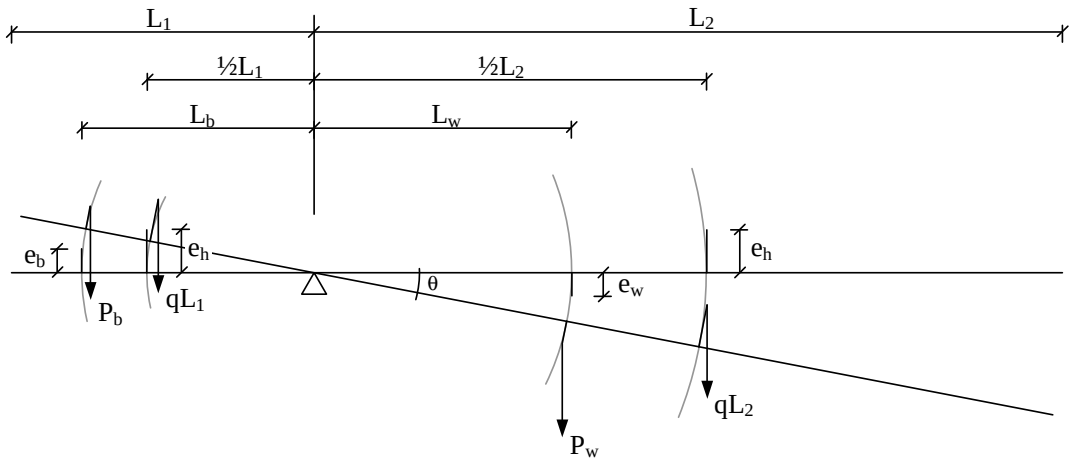

Figure 5.41 *Loads acting on the frame for an arbitrary angle θ in the unloaded situation*

$$P_b e_b + qL_1 e_h = P_w e_w - qL_2 e_h \tag{5.55}$$

Hence, all parameters except for two may be free. These two parameters must satisfy Equations 5.54 and 5.55. It must also be ensured that the ratio between the external loading and the load acting on the wedge remains constant for any angle θ. Figure 5.42 illustrates the problem. The specimen will rotate an angle φ when the frame rotates an angle θ, and thus, the ratio between the loads will change. However, this change can be minimized in the relevant θ-range by selecting suitable values for the free parameters.

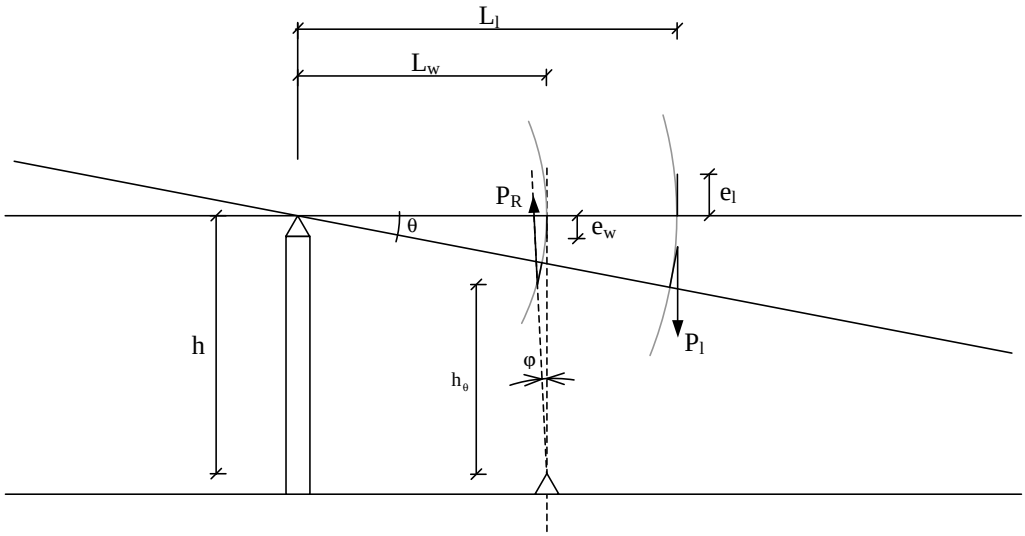

Figure 5.42 *External loading P_l and reaction P_R from the wedge for an arbitrary angle θ*

The length h_θ is given by:

$$h_\theta = h - L_w \sin\theta - e_w \cos\theta \tag{5.56}$$

Equation 5.56 may be applied to determine the angle φ:

$$\tan\varphi = \frac{\delta_w}{h_\theta} = \frac{L_w - L_w\cos\theta + e_w\sin\theta}{h - L_w\sin\theta - e_w\cos\theta} \tag{5.57}$$

Taking moment around the point of rotation for the frame, the following ratio between the external load and the wedge reaction may be established:

$$\frac{P_R}{P_l} = \frac{L_l\cos\theta + e_l\sin\theta}{(L_w\cos\theta - e_w\sin\theta)\cos\varphi - (L_w\sin\theta + e_w\cos\theta)\sin\varphi} \tag{5.58}$$

By selecting the free geometric parameters, the variation between the ratio of the imposed load and the load acting on the specimen may be minimized. In the setup utilized in the present work, the variation is less than 0.1 %.

Returning to the picture of the setup, Figure 5.40, it is noted that the external supports are arranged such that no unwanted redundant forces can occur. This is ensured by a ball bearing below the specimen and a line support of the wedge above the specimen. Thus, the specimen including wedge and loading devices may rotate freely as the upper frame rotates. Furthermore, by the use of a line support just below the specimen, but above the ball bearing, the boundary conditions of the specimen during loading and crack opening is equal to those described in the literature for this test, e.g. (Rossi et al. 1991). Finally, small boxes with metal granulate are used below the specimen to completely eliminate the influence of specimen self-weight on the fracturing zone. This is important at very early ages (8-10 hrs).

The crack mouth opening displacement is determined using clip gages designed for the present setup. A picture of one of the gages is shown in Figure 5.43. The gages have been designed such that the output is proportional with the crack mouth opening in the entire measuring range. This has been achieved by requiring that the point of contact with the specimen and the center of the spur gear lie on a straight line intersecting with the pinned attachment points of the potentiometer. See e.g. the drawing in Figure 5.43. Self designed clip gages were used instead of commercial equivalents due to two important reasons. First, commercial clip gages are often very expensive and it was outside the economical frames of the present work to buy the required number of gages (4). Second, long term use of expensive equipment present a problem in most laboratories. The self designed gages have high precision and the costs are only a fraction of the commercial ones.

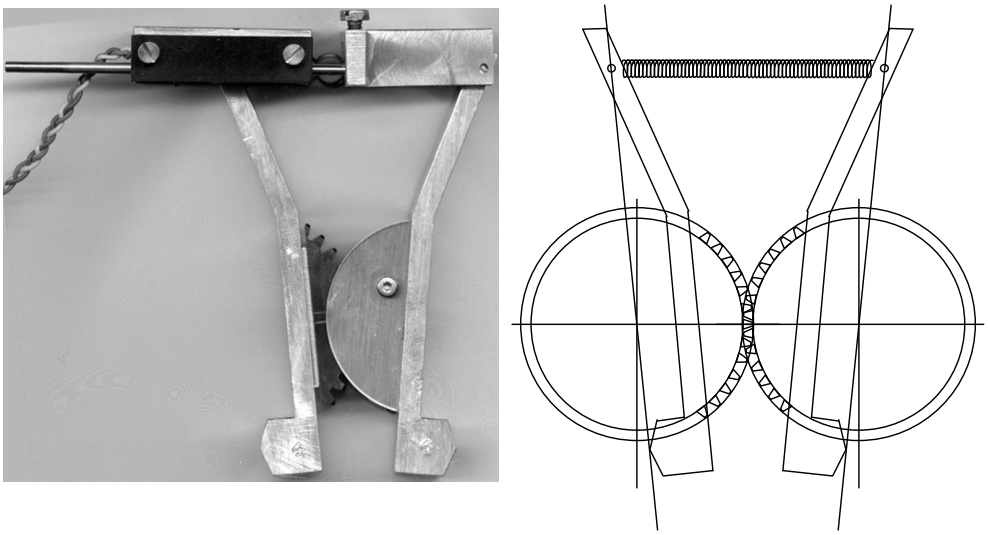

Figure 5.43 *Design of clip gage. The drawing shows how the point of contact with the specimen and the center of the spur gear lie on a straight line intersecting with the pinned attachment points of the potentiometer. This ensures a reading varying linearly with the crack mouth opening displacement, even for large deformations.*

Calibration of the loading frames and the clip gages has provided the proper proportionality constants between input and output, and shown that the desired properties for the setup have been achieved.

5.5 Three Point Bending Test

The three point bending test is widely applied for the determination of the fracture mechanical properties, especially fracture energy, but also the stress-crack opening relationship. Standards for determination of the fracture energy of concrete has been issued by RILEM, (RILEM 1985) and (RILEM 2000). These standards are mainly concerned with the determination of the fracture energy. However, papers addressing the issue of inverse analysis based on the test method have been published, see e.g. (Wittmann et al. 1987), (Brincker & Dahl 1989).

The use of the test method for early age concrete was attempted by Brameshuber (1988). However, complicated arrangements were necessary in order to compensate for the significant and detrimental influence of the self-weight of the beam. It seems in this sense much more promising to focus on the wedge splitting test for early-age concrete.

However, it is still relevant to incorporate investigations on this test method due to the widely spread use of it. Thus, the aim will be to implement the hinge solution and the method for inverse analysis in the three point bending test frame. Furthermore, by conducting independent experiments on three point bending beams, a basis for comparison of

results obtained with the uniaxial tension test and the wedge splitting test is established. This comparison, despite that it will necessarily be conducted on mature concrete, may yield a strong indication on whether the strategies proposed can be safely employed.

5.5.1 Interpretation and Inverse Analysis

Figure 5.44 shows the principal experimental setup. The clear span is denoted by L, the full height as H, while the beam thickness is denoted t. The initial notch length is given by a_0. During the experiment both the crack mouth opening displacement (CMOD) and the vertical displacement of the beam at the load point is measured. The CMOD is measured by gluing small measuring points onto the beam on each side of the notch, see Figure 5.44. A clip gage is mounted between these points, and usually, the experiment is controlled by requiring a constant rate of opening of the CMOD gage. This will in general, if the gage length is sufficiently short, result in a stable experiment. Besides the measurement of the CMOD also the midpoint deflection is measured. This information may directly be utilized for the calculation of the fracture energy, but may also like the CMOD measurements, be utilized in an inverse analysis algorithm from which the stress-crack opening relationship is derived.

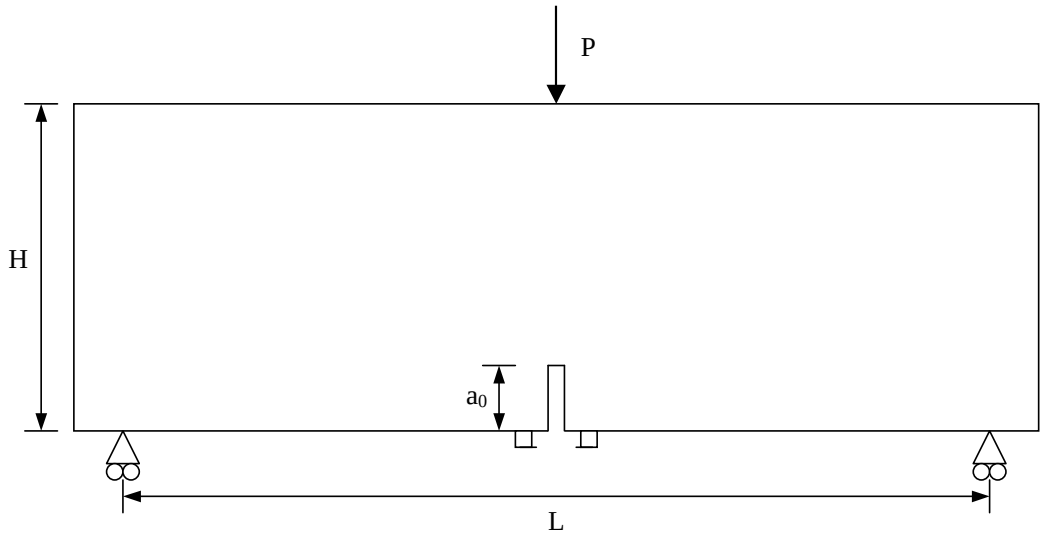

Figure 5.44 *Three point bending beam*

The required dimensions of the beam shown in Figure 5.44 are dependent on the maximum aggregate size, which is described in e.g. (RILEM 1985). Figure 5.45 shows how the hinge element is implemented in the beam. The hinge element, described in Appendix A, is inserted above the initial notch with a height $h = H - a_0$. The width of the hinge is given by s. From investigations in the literature, see e.g. (Ulfkjær et al. 1995), s is expected to be in the order of $H/2$.

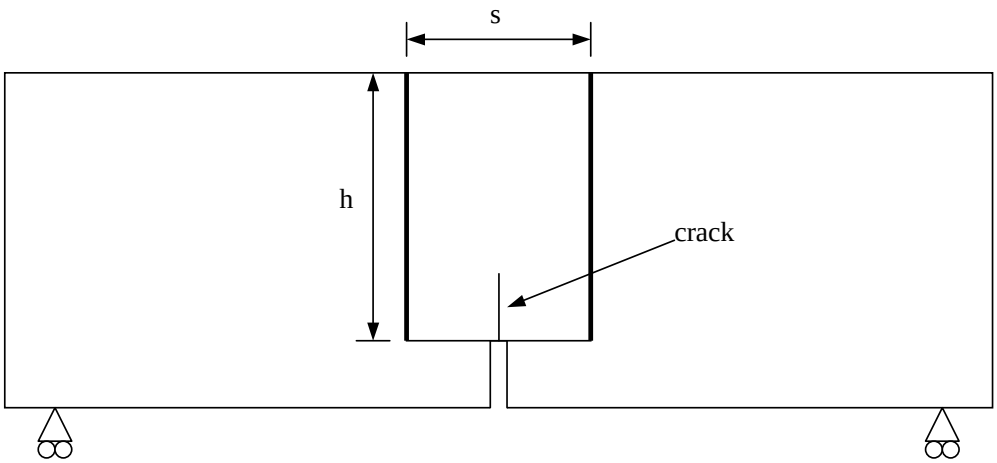

Figure 5.45 *Incorporation of hinge in the three point bending beam*

Figure 5.46 shows the loading on the hinge. It is assumed that no axial forces are imposed on the beam, such that $N = 0$. The hinge solutions in Appendix A are thereby greatly reduced, thereby also reducing the calculation time. The moment load M is given by:

$$M = \frac{1}{4}PL + \frac{1}{8}mgL \tag{5.59}$$

where P is the load. Self-weight is included in the expression and the mass is denoted by m and gravity by g. Using the fact that cracking initiates when the tensile strength f_t is reached in the bottom of the notch (disregarding any stress concentrations) leads to the following expression for the load P_0 at which cracking initiates:

$$P_0 = \frac{2}{3}\frac{t}{L}f_t h^2 - \frac{1}{2}mg \tag{5.60}$$

Calculation of the load in the cracked phases requires solving the hinge equations, see Appendix A. This is straightforward since it has been assumed that the normal force in the beam is constant and equal to zero.

The CMOD is calculated similar to the analysis of the wedge splitting test, see Equation 5.20. The elastic deformation of the specimen, just outside the notch, results in a opening given by Tada et al. (1985):

$$CMOD_e = \frac{6PLa_0}{EtH^2}v_1\left(\frac{a_0}{H}\right) \tag{5.61}$$

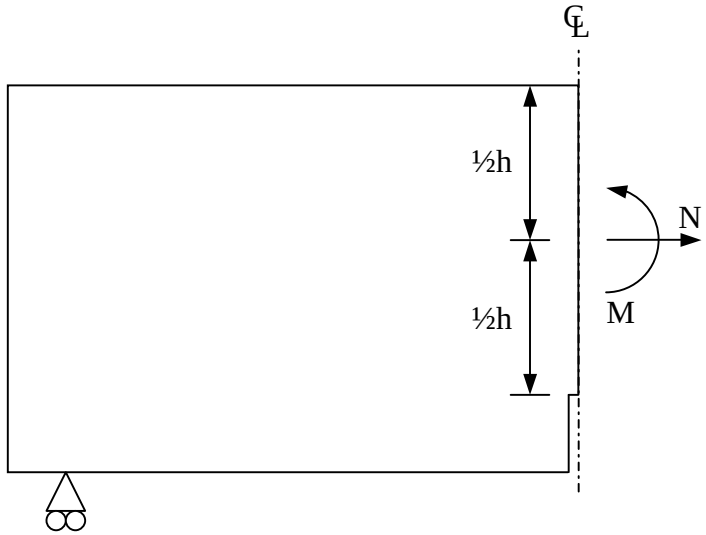

Figure 5.46 *Loads acting on the hinge*

in which:

$$v_1(x) = 0.76 - 2.28x + 3.87x^2 - 2.04x^3 + \frac{0.66}{(1-x)^2} \tag{5.62}$$

in which $x = a_0/H$. Note that Equation 5.62 is strictly only valid for $L/H = 4$, however, the dependency of L/H is weak. It is always necessary to mount two measurements points on the bottom of the beam in order to measure the CMOD. This was shown in the Figure 5.44. Figure 5.47 shows a detail of this situation. The small bricks have a height d. The contribution of these bricks is significant in the measurements and must be taken into account. According to Karihaloo & Nallathambi (1991), this may be done by simply assuming that the beam thickness is $H + d$ and the initial notch length is $a_0 + d$, thus modifying the variable in Equation 5.62 to read:

$$x = \frac{a_0 + d}{H + d} \tag{5.63}$$

However, Stang (2000) made the assumption that the crack sides are straight, which opens up for a straightforward geometrical correction of Equation 5.62:

$$v_1' = \frac{a_0 + d}{a_0} v_1 \tag{5.64}$$

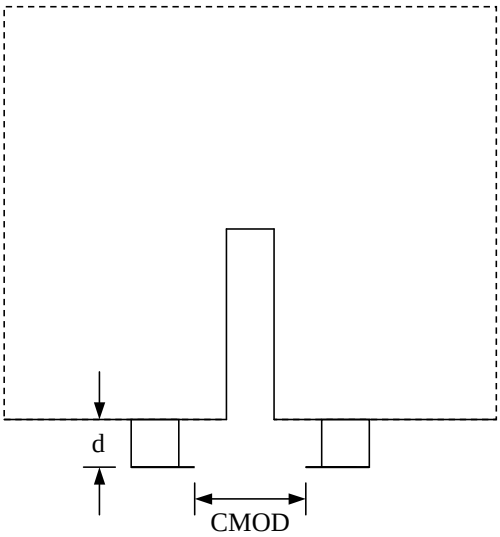

Figure 5.47 *Measurement points for CMOD*

in which v_1' is the corrected term to be inserted in Equation 5.61. Finite element calculations on the RILEM TPBT geometry shows however that none of these assumptions precisely capture the influence of the measurement bricks. The results of these calculations are given in Figure 5.48. The black curve represents the original expression given by 5.62, the red curve represents Equation 5.64, while the green curve is Equation 5.63. The blue and the turquoise curves are the average of the two assumptions, Equations 5.64-5.63 and the finite element results, respectively. It is seen that this averaging gives very fine results and thus, this assumption is adopted here.

The crack mouth opening displacement at the point of loading where cracking initiates, $CMOD_0$ may be determined from Equation 5.59 and Equation 5.61 and is given by:

$$CMOD_0 = 4a_0\frac{f_t}{E}\left(\frac{h}{H}\right)^2 v_1 - 3\frac{mg}{E}\frac{La_0}{tH^2}v_1 \tag{5.65}$$

in which v_1 is assumed to be calculated as the average of the two approaches given in Equations 5.64 and 5.63. Two more terms are contributing to the total CMOD in the cracked phases, namely the opening due to the crack opening displacement, $CMOD_{COD}$, and the geometrical opening, $CMOD_g$, due to the distance from the notch tip to the measurement points. This first term is the contribution due to the crack it self and is given in Appendix A, Equation A.14. The second contribution is given by Stang (2000):

$$CMOD_g = \frac{2(a_0+d)sf_t}{hE}(\theta - 1) \tag{5.66}$$

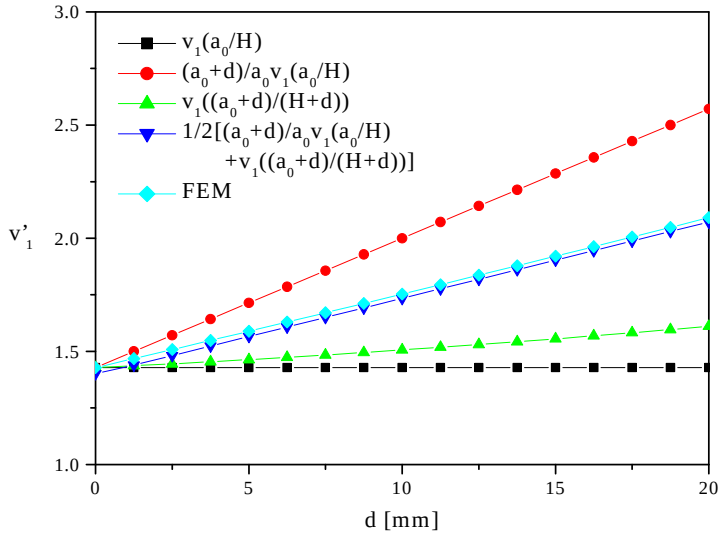

Figure 5.48 *Influence of the CMOD measurement points on the Tada expression*

in which the normalized hinge rotation, θ, is introduced (Appendix A).

The deflection in the elastic phase, u_e, is given by Tada et al. (1985):

$$u_e = \frac{1}{4}\frac{P}{Et}\left(\frac{L}{H}\right)^2\left(\frac{L}{H} + 6v_2\right) \tag{5.67}$$

where v_2 is a function of the initial notch to beam height ratio:

$$v_2(x) = \left(\frac{x}{1-x}\right)^2\left(5.58 - 19.57x + 36.82x^2 - 34.94x^3 + 12.77x^4\right) \tag{5.68}$$

in which $x = a_0/H$. Note that Equation 5.68 is strictly only valid for $L/H = 4$, but the dependency of L/H is weak. The deflection of the beam at the point of crack initiation, u_0, may be determined similarly to the calculation of $CMOD_0$:

$$u_0 = \frac{f_t}{E}L\left(\frac{h}{H}\right)^2\left(\frac{1}{6}\frac{L}{H} + v_2\right) - \frac{mg}{Et}\left[\frac{3}{4}\left(\frac{L}{h}\right)^2 v_2 + \frac{1}{8}\left(\frac{L}{H}\right)^3\right] \tag{5.69}$$

In the cracked phases, the presence of the crack must be included in the calculation of the deflection. This contribution is additive to Equation 5.67. The total deflection is given by Stang & Olesen (2000):

$$u = \theta + \left(\frac{L}{3s} \left(\frac{h}{H} \right)^3 + 2\frac{h}{s} \left(\frac{H}{h} \right)^2 v_2 - 1 \right) \mu(\theta) \tag{5.70}$$

Equations 5.59-5.70 form the basis for interpretation and inverse analysis of the three point bending test.

The calculation procedures for both the forward and the inverse analysis are entirely analogous to the description in the section on the wedge splitting test, although more simple since the normal force is now constant and equal to zero. The program code describing the implementation in MatLab is available in Appendix B.

5.5.2 Finite Element Modelling

A number of finite element calculations have been carried out in order to verify the applicability of the hinge and the validity of the analytical expressions. The investigations are split in two parts, where first the validity of the interpretation is demonstrated, second the quality of the inverse analysis. The mesh used in this first part of the analysis is shown in Figure 5.49. The elements applied are isoparametric, eight node plane stress elements with a linear elastic material description having $E = 30000$ MPa and $\nu = 0.2$. The crack is described by interface elements available in the FEM package used (DIANA).

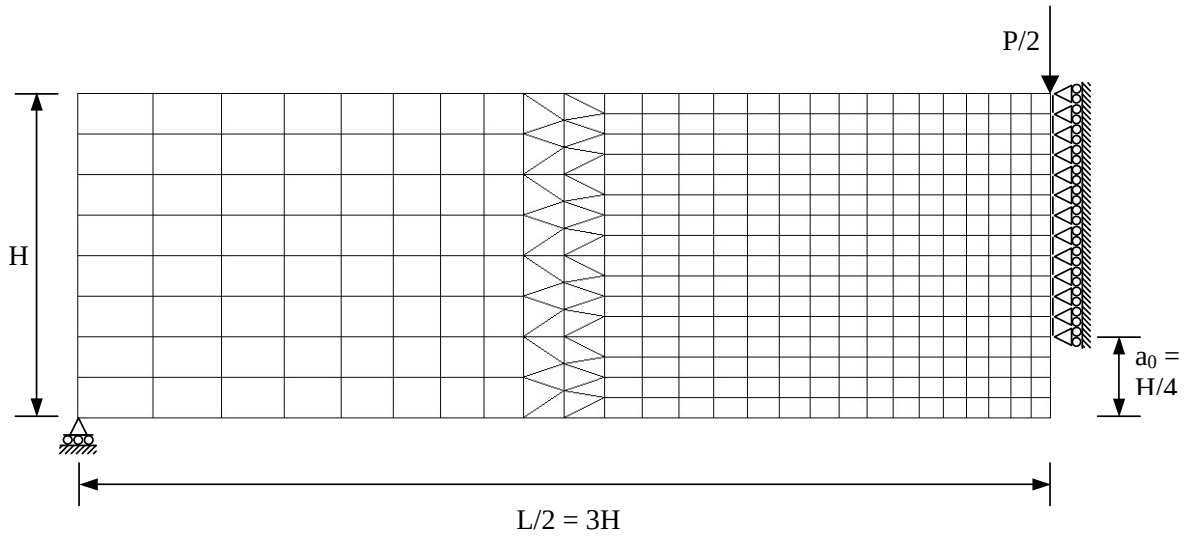

Figure 5.49 *Mesh employed in the finite element analysis of the three point bending test*

The interface elements are rigid until cracking occurs whereafter they obey the chosen stress-crack opening relationship. The shear retention factor is unimportant in this case since the cracking occurs on a line of symmetry. The dimensions are, as the figure shows, all proportional to the full height of the beam, H. The stress-crack opening relationship for all the beams in the Figures 5.50-5.52 are given by:

$$\begin{aligned} f_t &= 3.0\ MPa \\ a_1 &= 20.0\ mm^{-1} \\ a_2 &= 0.2\ mm^{-1} \\ b_2 &= 0.35 \text{ and } 0.70 \\ E &= 30000\ MPa \end{aligned} \tag{5.71}$$

where b_2 is changed in order to simulate different fiber contents. This variation was preferred since it was found in the section on WST that the b_2 parameter poses the greatest difficulties for the hinge model.

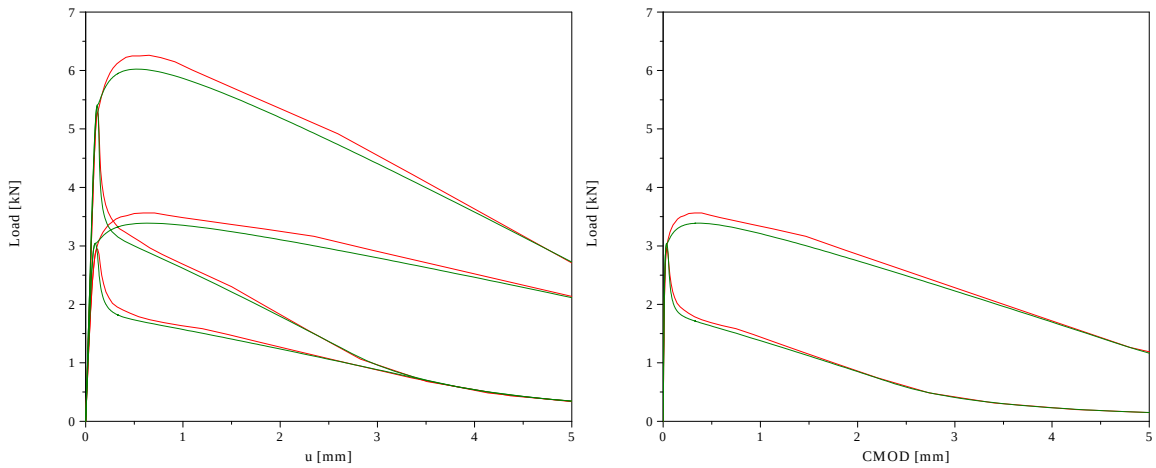

(a) (b)

Figure 5.50 *Comparison between the FEM results (red) and the hinge program results (green). Figure (a) shows deflection for unnotched and notched beams (lower curves) while figure (b) shows CMOD for notched beams.* $H = 100\ mm$

Figure 5.50 shows the correlation between FEM and the hinge analysis for small beams with H=100 mm. The graphs in Figure 5.50a depict the load-deflection relationship for both notched and unnotched beams, while Figure 5.50b only shows the load-CMOD relationship for notched beams. The hinge width parameter s is chosen in accordance with the literature, i.e. $s = 0.5H$, in all graphs. The correlation is seen to be very fine. The largest discrepancy between the curves is the level of load at the horizontal plateaus for the beams with high fiber content ($b_2 = 0.2$). The discrepancy is also seen to be smaller for the low fiber contents.

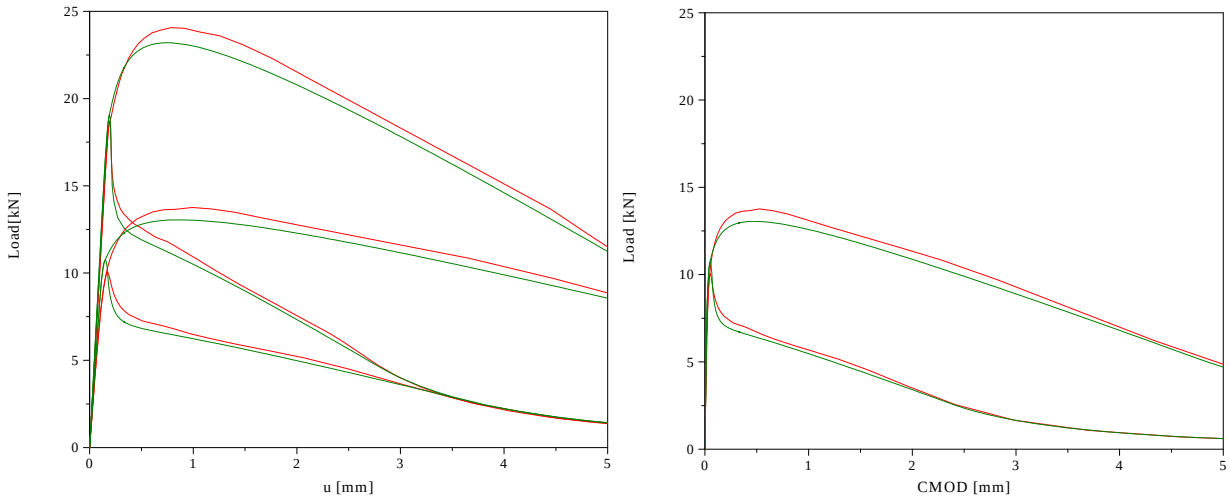

(a) (b)

Figure 5.51 *Comparison between the FEM results (red) and the hinge program results (green). Figure (a) shows deflection while (b) shows CMOD. $H = 200$ mm*

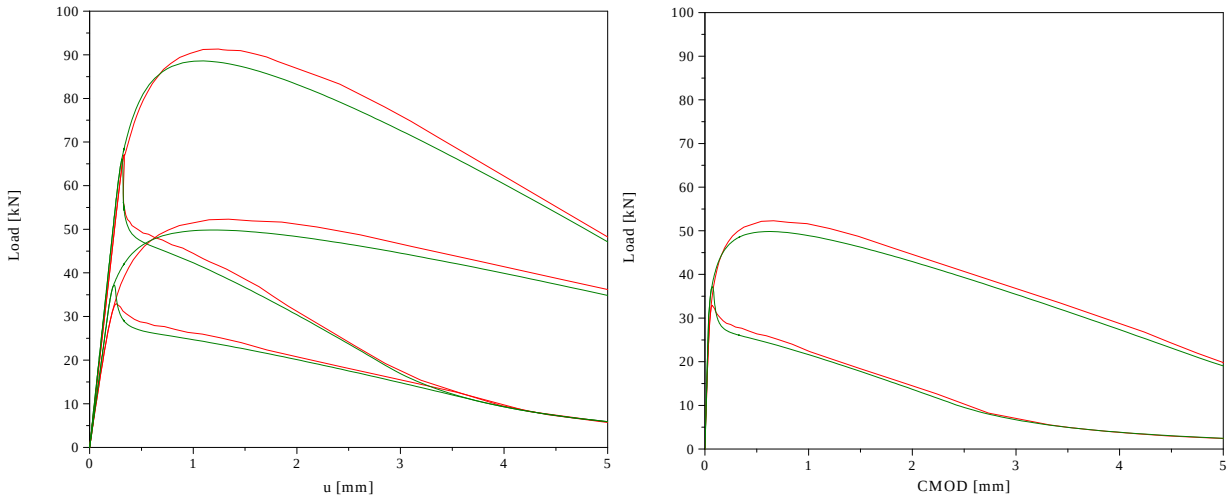

(a) (b)

Figure 5.52 *Comparison between the FEM results (red) and the hinge program results (green). Figure (a) shows deflection while (b) shows CMOD. $H = 400$ mm*

The same fine degree of correlation is seen in Figures 5.51-5.52 where beams with different sizes are investigated employing the same constitutive conditions as before, Equation 5.71. The results clearly demonstrate the applicability of the hinge model to analyze and predict the behavior of not only the three point bending test, but also the formerly investigated WST setup and the split cylinder. It is likewise also presumably applicable to other situations where normal force and bending moments prevail.

All the results from the finite element calculations have been subject to the inverse analysis algorithm proposed in Section 5.3. The first part of the investigation of the inverse analysis method for TPBT aimed at excluding the possibility of local minimums. Similar with the investigation for WST many different start guesses were tried, and they did all converge to the same global minimum.

Table 5.5 shows the results based on the P-u curves shown in Figures 5.50-5.52 with b_2=0.35. It is, first of all, seen that the majority of the results are reproducing the input quite well, but also significant differences are found. It is, however, not easy to see a clear pattern in the discrepancy between the input and the output values. The notched beam with a height $H = 200$ mm has a rather poor determination of all parameters while both the smaller and the larger beam with a notch give better results.

Table 5.5 *Results from inverse analysis with different beam sizes H; with and without notch, based on P-u curves. Value of* $b_2 = 0.35$, $s/H = 0.50$. *Fixed parameters were selected to* f_t=3 MPa, a_1=20 mm^{-1}, a_2=0.2 mm^{-1} *and* E/f_t=10000. *The varied input values are given in the left part of the table while the output values for all the parameters are listed in the right part.*

H	a_0	f_t [MPa]	a_1 [mm^{-1}]	a_2 [mm^{-1}]	b_2 [-]	$\frac{E}{f_t}$ [10^3]
100	0.00H	2.97	19.44	0.231	0.381	9.37
200	0.00H	3.15	23.53	0.218	0.361	9.37
400	0.00H	3.12	22.50	0.212	0.359	9.37
100	0.25H	2.63	12.85	0.253	0.422	8.97
200	0.25H	2.39	10.66	0.280	0.468	9.02
400	0.25H	3.14	24.67	0.219	0.365	8.76

Table 5.5 also shows that the unnotched beams give better results in comparison with the notched ones. This might partly be explained by the fact that $L/H = 6$ for the beams under investigation and thus, Equations 5.62 and 5.68 are not entirely precise. It is also noted that the average values for f_t and a_1 do yield values which are very close to the input values. This suggests that testing on different beam sizes and notch lengths may be beneficial for the precision of the inverse analysis.

Table 5.6 shows the results for beams with and without notch for $b_2 = 0.70$. These results have a better accuracy if compared with the inverse analysis conducted on the WST

Table 5.6 *Results from inverse analysis with different beam sizes H; with and without notch, based on P-u curves. Value of $b_2 = 0.70$, $s/H = 0.50$. Fixed parameters were selected to f_t=3 MPa, a_1=20 mm^{-1}, a_2=0.2 mm^{-1} and E/f_t=10000. The varied input values are given in the left part of the table while the output values for all the parameters are listed in the right part.*

H	a_0	f_t [MPa]	a_1 [mm^{-1}]	a_2 [mm^{-1}]	b_2 [-]	$\frac{E}{f_t}$ [10^3]
100	0.00H	3.08	26.42	0.208	0.709	9.37
200	0.00H	3.09	26.85	0.204	0.705	9.37
400	0.00H	3.09	26.71	0.203	0.703	9.37
100	0.25H	3.12	94.40	0.217	0.719	8.84
200	0.25H	3.11	85.60	0.210	0.712	8.87
400	0.25H	3.10	42.69	0.205	0.707	8.82

specimen for high values of b_2, see e.g. Table 5.3. Only the determination of a_1 for the small notched beams is poor, but this ill-determination is not crucial as discussed in the section on the WST testing.

Table 5.7 *Results from inverse analysis with different beam sizes H; with notch, based on P-CMOD curves. Notch length $a_0 = 0.25H$, $s/H = 0.50$. Fixed parameters were selected to f_t=3 MPa, a_1=20 mm^{-1}, a_2=0.2 mm^{-1} and E/f_t=10000. The varied input values are given in the left part of the table while the output values for all the parameters are listed in the right part.*

H	b_2	f_t [MPa]	a_1 [mm^{-1}]	a_2 [mm^{-1}]	b_2 [-]	$\frac{E}{f_t}$ [10^3]
100	0.35	2.88	17.33	0.235	0.392	8.67
200	0.35	2.69	15.79	0.250	0.422	8.67
400	0.35	2.47	13.71	0.264	0.455	8.67
100	0.70	2.92	15.41	0.224	0.760	8.66
200	0.70	3.01	27.47	0.217	0.740	8.59
400	0.70	3.13	40.76	0.206	0.720	8.51

More discrepancy between the input and the output values is found in Table 5.7. Here the P-CMOD curves are used as the input for the inverse analysis algorithm for all beam sizes and with both values of b_2. The poorest determination is seen to occur for the large beam with the low value of b_2.

In all the results given in Tables 5.5-5.7, the value of the width of the hinge, s, was kept constant. It is clear that an optimization for the best value of s would increase the accuracy of the results. However, this is not possible in the experimental situation, and the results show the discrepancy, which must be expected in such a real situation. It is also noted that the results in this section do all have a certain fiber effect included through the

high b_2 values. It is expected that the precision of the results, similar to the WST results, would increase if the value of b_2 was selected to be in the order of normal concrete, i.e. $b_2 = 0.1$.

5.5.3 The Test Setup

The experimental three point bending test setup is shown in the Figures 5.53-5.54. Figure 5.53 gives an overview of the entire setup. The beam corresponds to the RILEM TPBT beam with a clear span of 500 mm, and a 150x150 mm^2 cross-section. The supports are at each end able to rotate in direction of the beam axis and also perpendicular to the beam axis, as can be seen in Figure 5.53. Only the loading device mounted in the crosshead is build in. Thereby, no redundant forces will be built up in the system. A notch with a depth of $a_0 = 25$ mm is cut at the middle section of the beam, see the figure

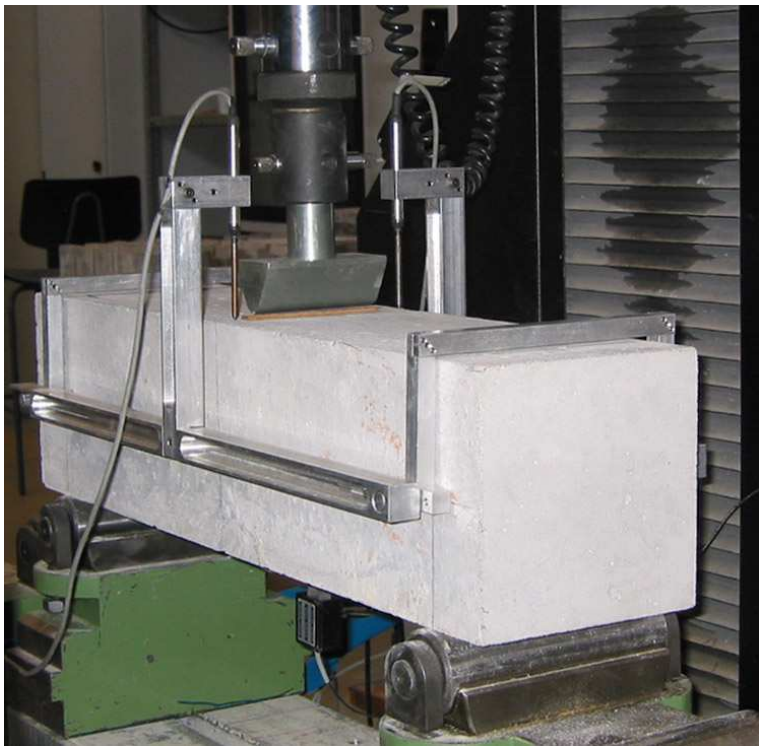

Figure 5.53 *The three point bending test setup.*

A rig is mounted on the beam from which the deflection is measured. This beam is applied in order to exclude false deflection due to deformation of supports etc. The rig is mounted on the centerline of the beam axis just above the supports, see e.g. Figure 5.54. The LVDT's, which are measuring the deflection at midpoint, are mounted on the rig; see Figure 5.53. The reference beam is able to rotate at the supports at one end, Figure 5.54b, and slip at the other, Figure 5.54a, thereby ensuring unrestricted adaption to the

(a) (b)

Figure 5.54 *Details of the reference beam.*

deformations in the beam. Two LVDT's are utilized for measuring the deflection of the beam, thereby eliminating stiff body rotations through averaging.

Also CMOD is measured during the experiment. This signal is furthermore used as the control signal for the closed loop testing of the beam. The CMOD is measured by mounting two small steel pieces on each side of the notch as illustrated schematically in Figure 5.47. The devices are mounted parallel to the beam axis with a gage length of $\delta = 10$ mm and the height is $d = 7$ mm. An Instron clip-gage is applied for the measurements.

5.5.4 Usability with Early Age Concrete

The three point bending test may be employed for early age concrete as it was done by e.g. (Brameshuber 1988). However special self-weight eliminating arrangements are needed due to the necessary dimensions, which result in high self-weight. The self-weight is regarded as high since the concrete must have attained a certain strength and thus a certain age before the self-weight is insignificant. If self-weight is required to contribute with less than 5% of the loading of the RILEM beam, the tensile strength of that beam must be 0.7 MPa before the experiment may begin, if the weight of the beam is 22 kg. Unless, of course, if special measures are taken.

These considerations lead to the conclusion that the WST is more suited for early age testing of concrete than the three point bending test. This is due, primarily, to the vanishing self-weight problems in the WST setup, which furthermore can be eliminated.

Chapter 6

Experimental Results

This chapter presents the experimental data, which were generated during the research project. The chapter starts with an introduction of the alternative variables, which may be used for the description of the development of properties. These encompass time, maturity and degree of hydration. Depending on the circumstances, all of these approaches may be applied, and they may all be precise.

The next section of the chapter describes the mix designs and the reasons for choice of mix parameters and variations of these.

A section follows, which is dedicated to the comparison between different testing geometries, i.e. split cylinder, WST, TPBT and UTT. The first section compares all the test geometries at a mature age (6 months) and it is demonstrated that the stress-crack opening relationship is indeed a material property. The second section compares split cylinder results with results obtained from the wedge splitting test at early ages. Thereby, it is demonstrated that the split cylinder test is a poor choice at early ages.

Early age fracture properties are then explored utilizing the wedge splitting test setup, which was described in the previous chapter, Section 5.3. The results are summarized and modelling of the development is attempted based on known formulations.

The results of the long-term testing in terms of the bulk and crack creep properties are introduced in the following section.

6.1 Maturity vs. Degree of Hydration

Development of properties of cement based materials must be described with respect to the influence of the temperature. This is due to the fact that the rate of all chemical reactions are temperature dependent. Due to the heat of hydration, see e.g. Section 2.1.1, isothermal conditions will usually not be achieved in an uncontrolled situation. It is, on the other hand, cumbersome to obtain isothermal conditions.

The age of cement based materials is therefore often described using the maturity concept. The maturity is simply equal to time for a sample stored under isothermal conditions at a given reference temperature. If the conditions are non-isothermal or if the sample is stored at a constant temperature different from the reference temperature, a maturity function is utilized to calculate the maturity. This maturity function is accounting for the dependency of temperature on the rate of reactions. Application of the maturity concept allows for a unique description of the development of properties of cementitious materials. However, the evolution of properties will naturally be nonlinear due to the nonlinearity of the rate of reaction, which is exemplified by Equation 2.1. The advantage is the easy calculation. The maturity may be calculated as:

$$M = \int_0^{\tau} \frac{f(\theta(t))}{f(\theta_0)} dt \tag{6.1}$$

in which M is the maturity with reference temperature θ_0, τ is the actual time for which the maturity is calculated, θ is the temperature and $f(\theta(t))$ is the maturity function. If the temperature is constant, $\theta(t) = \theta_0$, maturity is equal to time since $f(\theta(t)) = f(\theta_0)$. Varying temperatures give different maturities. Several maturity functions have been proposed in the literature. Important examples are (Høyer 1990):

$$f(\theta) = k\ \theta_C \tag{6.2}$$

$$f(\theta) = k\ 2^{\ \theta_C/10} \tag{6.3}$$

$$f(\theta) = k\ e^{-E/(R\theta_K)} \tag{6.4}$$

where k is a constant, θ_C is the temperature in Celsius, θ_K is the temperature in Kelvin, while R is the gas constant and E is the activation energy. Equation 6.2 is one of the first formulations, assuming that hydration only proceeds above 0 ℃. Equation 6.3 utilizes the well established fact that the rate of reaction doubles for every time the temperature is increased by 10 ℃. The latter equation, Equation 6.4, by Hansen & Pedersen (1977), is based on Arrhenius equation for thermal activation energy and has proven to be able to describe the temperature dependency in the range from -10 to 80 ℃.

Another approach is the use of the degree of hydration. This method is more consistent since the properties in fact are directly dependent of the amount of reaction, i.e. the degree of hydration. However, the method is more demanding since it requires additional experiments, e.g. measurements of the heat of hydration with time and also knowledge of the total heat liberation at $t \to \infty$.

All the specimens employed to generate experimental results in this thesis are, however, small and kept in near isothermal conditions at approximately 20 ℃. Thereby, no significant temperature changes occur during hydration and thus, it may be assumed that the time is equal to maturity. This is documented in Figure 6.1 where the temperature changes during one week of hardening has been documented using a temperature probe in the center of one representative specimen for which an early age high strength cement has been applied. The specimen was a cylinder with a diameter of 100 mm and a length of 200 mm. The probe was placed in the center.

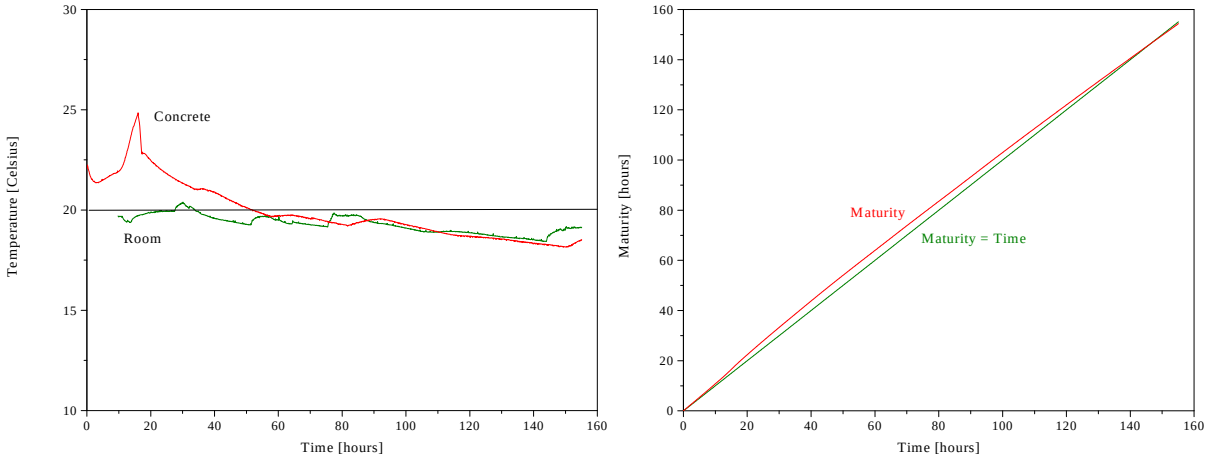

(a) (b)

Figure 6.1 *Temperature in the curing room and the concrete (a) and time versus maturity (b)*

The figure shows variations in the temperature of the curing room (which was in a basement). The temperature varies within two degrees Celsius and is caused by ambient temperature variations, since the room was not temperature controlled. The concrete temperature is seen to follow the expected variation (see e.g. Figure 2.1) within the first two days whereafter it follows the room temperature. Figure 6.1b shows the difference between the adopted maturity concept, $M = t$, versus true maturity, M, calculated employing Equation 6.1 and 6.4. The difference is small and does only introduce an error of less than 5%. This error will be smaller for normal cement and low heat cement.

6.2 Mix Designs and Mixing Procedure

6.2.1 Mix Designs

Table 6.1 shows the mix designs used in the experimental investigations. A vast number of parameter variations are possible due to the nature of modern high performance concrete, consisting of cement, fly ash, silica fume, additives, aggregates etc. Both the amount

and type of all these constituents may be varied. It is the purpose of this project to demonstrate the influence of water-cement ratio and cement type on the evolution of the fracture mechanical properties. Thus, all other parameter variations have been excluded. This choice has been made since the water-cement ratio significantly influences the brittleness of the concrete. Also the type of cement is very important for how a possible crack may evolve at early ages. This is not only due to the possible temperature gradients, but also to the composition of the cement itself.

Table 6.1 *Mix designs (kg/m^3). The letter P means powder and is given by $P = C + F + SF$. The maximum aggregate size was $d_{max} = 16mm$*

Mix	I	II	III	IV	V
Cement type (CEM)	II 52.5	II 52.5	II 52.5	I 52.5	I 42.5
Cement density	3100	3100	3100	3150	3200
Cement (C)	310.0	276	242.0	314	314
Fly ash (F) (0.20C)	62.0	55.2	48.4	62.8	62.8
Silica fume (SF) (0.05C)	15.5	13.8	12.1	15.7	15.7
Water	112.8	132.2	144.2	113.6	113.6
Air entraining agent (0.001P)	0.388	0.345	0.303	0.393	0.393
Plasticizer (0.006P)	2.33	2.07	1.82	2.36	2.36
Super plasticizer	6.2	3.1	0.0	7.1	7.1
FA, sea gravel, 00-04 mm	783.0	783.0	781.0	783.0	783.0
CA, sea gravel, 04-08 mm	343.7	343.7	342.9	343.7	343.7
CA, sea gravel, 08-16 mm	687.5	687.5	685.7	687.5	687.5
Aggregate content (%)	69.0	69.0	68.8	69.0	69.0
Apparent sand content (%)	43.4	43.4	43.4	43.4	43.4
Paste content (%)	25.5	25.6	25.1	25.6	25.5
Mortar content (%)	55.4	55.5	54.9	55.5	55.4
Water-cementitious materials ratio	0.307	0.394	0.480	0.307	0.307
Equivalent water-cement ratio	0.32	0.41	0.50	0.32	0.32

Table 6.1 shows how the variations in water-cement ratio and cement type have been achieved. Mix Nos. I, II and III are differing only in water-cement ratio. All other parameters have been kept constant. Mix Nos. I, IV and V differs only in the type of cement. These latter mixes therefore display the influence of type of cement. However, note that the amount of super plasticizer varies since it was necessary in Mix I, II, IV and V while it was unappropriate for Mix III. This variation may result in secondary effects like e.g. retardation in early ages.

6.2.2 Mixing Procedure and Curing for Early-Age Experiments

The concrete was mixed using a continuous pan mixer. First, the dry materials were mixed for 2 minutes, then water was added and the mixing continued for another minute before the admixtures were added. Total mixing time was 5 minutes.

Cylinders for determination of the split tensile strength were cast in PVC molds, while WST-specimens were cast in special wooden water-tight molds manufactured for this purpose. The groove and the notch in the WST-specimens were cast utilizing tapered PVC inserts. The concrete was compacted on a table vibrator for 2 minutes at 50 Hz.

The specimens were covered with plastic sheets immediately after casting and stored in the lab until testing. Only 15 minutes elapsed from addition of water and until the final covering of the specimens. Specimens that were used for tests before 24 hours were taken directly from the molds. At 24 hours, the specimens were demoulded and stored at 100% RH and laboratory temperature (20 ℃) until testing. The specimen temperature at the time of each test was recorded employing a thermocouple cast into the center of dummy specimen with dimensions corresponding to the cylindrical specimens.

6.3 Specimen type comparative study

6.3.1 Uniaxial tension test vs. WST, TPBT and SCT

The specimen type comparative study aims at comparing results obtained from wedge splitting tests, three point bending tests, uniaxial tension tests and split cylinder tests (SCT). This comparison will challenge the inverse analysis methods, which have been developed in the previous chapter. It will furthermore be determined whether the extraction of a specimen independent stress-crack opening relationship is possible.

The dimensions of the cylinders applied in this investigation are ∅100 x 200 mm. The geometry of the WST-specimens are shown in Figure 5.29a. The side length of the fundamental WST-cube is $L = 100$ mm, and the thickness $t = 100$ mm. The height of the ligament is $h = 50$ mm, while the splitting load is applied at $(d_1, d_2) = (40, 85)$ mm. The length of the notch is $a_0 = 28$ mm. Figure 5.29 shows the mean width of the notch, $a_m = 4.5$ mm, while the real notch is a little tapered in order to ensure easy decoding. The beams are cast according to the RILEM specifications, (RILEM 2000), and the span is 500 mm, while the cross section is 150x150 mm^2.

A total number of 5 UTT, 5 TPBT, 5 SCT and 10 WST were tested. The high number of WST specimens was preferred since it was expected that the scatter on these specimens would be large due to the ligament size vs. maximum aggregate size (50x100 mm^2 vs. 16 mm). The age at testing was 6 months in order to ensure that no ageing could cause any error on the results during the time period of experimental work (2 weeks). The specimens were cast similar to the description in Section 6.2.2, however, the curing was different. The specimens were, after an initial 24 hours curing period in the molds, covered with plastic and water cured for two months. They were then placed in the concrete lab and thus subject to the (small) temperature variations and drying conditions. This is probably not the most optimal conditions since it may cause drying stress in the specimens, and since this stressing will be different from one specimen type to another. However, the effect is probably minimal since the conditions were maintained for four months before testing.

The mix employed for this study was Mix I, see Table 6.1.

Figure 6.2 shows the results from the UTT experiments. One experiment has been discarded due to a poor glued connection between the specimen and the steel platen. This gluing has most likely resulted in an significant eccentric loading of the specimen, causing a too low peak load (approx. 2.8 MPa). The glued connection failed shortly after peak load, and after regluing a *higher* peak load was determined (approx. 3.0 MPa). Figure 6.2, therefore, only shows the results from the remaining four experiments.

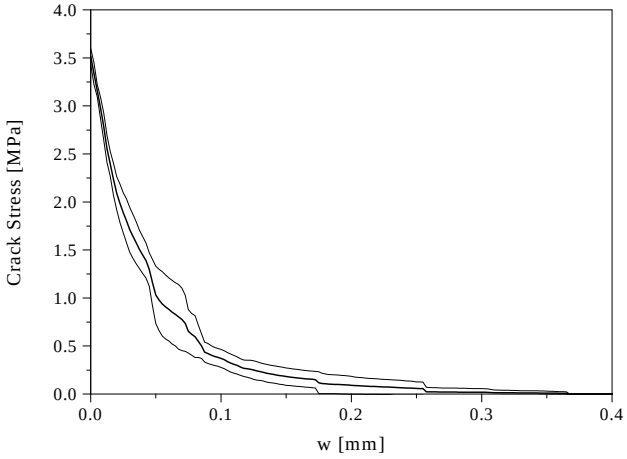

Figure 6.2 *Stress-crack opening relationships determined by the uniaxial tension test. The thick line represents the average of all experiments, while the thin lines show the standard deviation.*

Three features in Figure 6.2 are noted. First, the figure demonstrates an increased scatter at a crack stress of approximately 1 MPa. This is occurring due to the fact that all the curves show a hump. Thus, despite the effort to give the testing machine a higher rotationally stiffness, the stiffness was too low. This is in fact clear since the results from Section 5.1 demonstrate that the stiffness achieved is only sufficient if the tensile strength is lower than 2 MPa. However, the results are still useful, despite the hump, but a little too high initial slope of the stress-crack opening relationship must be expected, see e.g. Figure 5.10. The second thing to be noted in Figure 6.2 is sudden changes in stress level and scatter at the tail of the curve. This is simply caused by the termination of the individual experiments. Finally, note the very small scatter in determination of tensile strength.

The tensile strength determined from the uniaxial tension test is assumed to be the true uniaxial tensile strength of the material under investigation. Thus, in the comparison with the other test methods, this value is fixed and the inverse analysis algorithms for these methods are calibrated using this value. The free parameter in this calibration is the crack band width parameter, s. It turns out that this calibration is necessary in order to arrive at precise results. Figure 6.3 shows the results from the different testing methods after calibration. The dots represents the mean values while the bars are placed in a

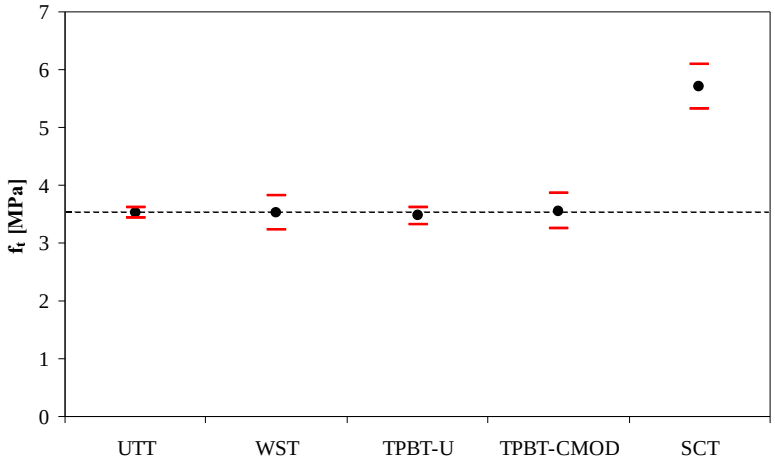

Figure 6.3 *Determination of tensile strength, f_t, from the different experiments. Split cylinder tests are denoted by SCT. The crack band width of the hinge is calibrated such that the values of f_t from WST and TPBT equals UTT.*

distance corresponding to the standard deviation. Only the tensile strength determined from the split cylinder test is different from the others, which is due to application of the simple linear elastic formula, Equation 5.6, known to predict too high values of f_t. Indeed, the ratio between this split tensile strength and the uniaxial tensile strength in Figure 6.3 is 0.61, which is expected from Section 5.2 and literature, e.g. (Herholdt et al. 1985). The agreement in tensile strength has been achieved by varying s. The values of f_t for the value of s determined by FEM and by the calibration, respectively, are shown in Table 6.2. This indicates that, ideally, both WST and TPBT experiments should be performed such that the right value of s can be determined. However, it also shows that the dependency of s is not very strong, and thus, if an error of 10-30% is acceptable, no further investigations are necessary.

Table 6.2 *Influence of s on the determination of f_t*

	s/h (FEM)	f_t	s/h (EXP)	f_t
WST	0.84	4.58	0.25	3.51
TPBT	0.50	3.05	0.95	3.51

Figure 6.4 shows the stress-crack opening relationships determined using the WST setup. The scatter is, as expected, higher in this experiment than e.g. for the UTT setup, but clearly within acceptable limits. Note that the curves shown in Figure 6.4 are produced from the bilinear curves determined from the inverse analysis, by averaging the stresses at certain crack openings, w. The underlying bilinear stress-crack opening curve does of course impose some restrictions on the average curve shown in the figure.

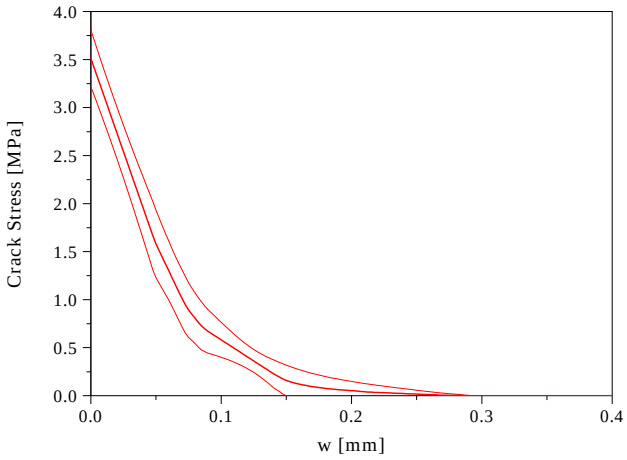

Figure 6.4 *Stress-crack opening relationships determined by the wedge splitting test. The thick line represents the average of all experiments, while the thin lines show the standard deviation.*

Figure 6.5 shows the results from the three point bending tests. The results obtained utilizing the midpoint deflection are shown in Figure 6.5a, while Figure 6.5b shows results based on the CMOD. The results are showing differences, which must, primarily, be caused by differences in the interpretation. However, also measurement scatter may contribute; but the total picture does resemble the fact that two different deformation measures are taken on the same beams.

The average curves for all the experiments with the UTT, WST, TPBT setups are shown together in Figure 6.6. The similarity in the first part of the stress-crack opening relationship between the WST, TPBT-U and TPBT-CMOD results is quite striking. The different experiments do in fact predict the same initial slope for the stress-crack opening relationship. The correlation is not as good for the tail. Here, the highest degree of correlation is found between the WST and the TPBT-U curves, while the TPBT-CMOD curve is higher. However, the largest discrepancy is between the UTT and the WST and TPBT curves. The UTT curve is almost permanently lying under the other curves. Some of the explanation is the hump as discussed earlier in this section, but other factors are probably also playing a role.

Despite the differences seen in Figure 6.6, there is no doubt that the results show that it is possible to determine practically similar stress-crack opening relationships from different test methods, and that the results obtained from the indirect methods are useful and close to the result, which may be obtained from the uniaxial tension test.

The modulus of elasticity may also be determined using the UTT, WST or TPBT tests, despite the fact that the methods probably are not the most suited ones in this regard. In order to arrive at the best possible determinations, finite element models were made for each setup. These FEM models were utilized to determine the exact elastic deformation at the point of deformation measurement for each setup. The results were applied in the

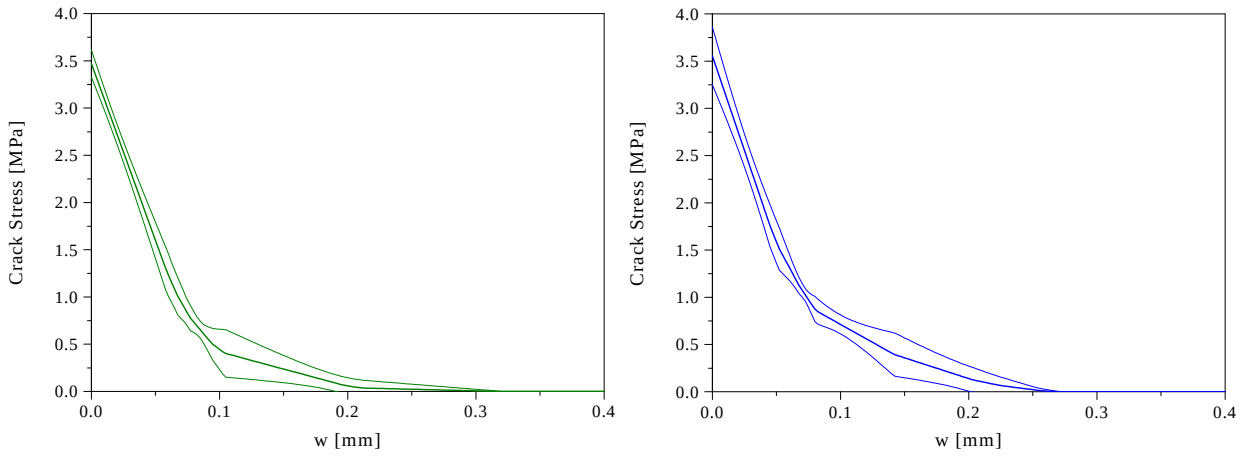

(a) (b)

Figure 6.5 *Stress-crack opening relationships determined by the three point bending test employing the deflection u (a), or the crack mouth opening displacement, CMOD (b). The thick line represents the average of all experiments, while the thin lines show the standard deviation.*

inverse analysis. In the case of the UTT test, the influence of translations of the measurement rig, see Figure 5.15a, was included in the calculations. The results are shown in Figure 6.7. The determination of E denoted by SCT was obtained employing the cylinders prepared for the SCT experiments. These cylinders were inserted between 10 mm thick soft fiber boards in a testing machine and subjected to a load varying from 0 to -3 MPa 5-7 times. Meanwhile, extensometers with a gage length of 50 mm measured the length change at the center of the specimen. An independent measurement of the modulus of elasticity was thus obtained from these experiments. The figure shows that this independent determination of E gives a higher value in comparison with the other test methods. However, with regard to the scatter most of the results are seen to fit quite nicely.

The fracture energy from the experiments are shown in Figure 6.8. It is seen that the values are not equal; the UTT experiments exhibit the lowest values, while the TPBT results based on CMOD show the highest values. It is not surprising that the values are different. The fracture energy is also found to be dependent on specimen size, experiment type etc. in the literature, see e.g. (Karihaloo 1995). In the cited work, different remarks are made to explain the varying values of G_f obtained from different experiments. One reason, which may apply in the present work is the possibility of varying widths of the fracture process zone due to the varying stress states near the crack.

Figure 6.9 shows the characteristic length determined from the different experiments and methods. It is notable that both the mean values and the standard deviation are quite high. It is also seen that the values varies for all four results. The scatter is probably

best explained by the fact that the characteristic length, integrally, includes all the other parameters determined in this study. Thereby, due to the law of sum of errors, the scatter will be large. The high values may be due to determination of fracture energies higher than the true ones, but it seems unlikely that the result from the uniaxial tension test has this flaw.

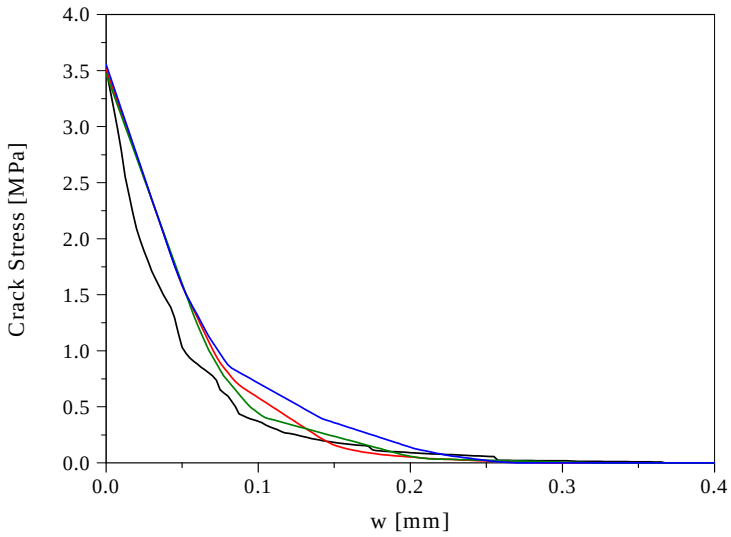

Figure 6.6 *Stress-crack opening relationships as determined from the different test methods. UTT is black, WST is red, TPBT-U is green and TPBT-CMOD is blue.*

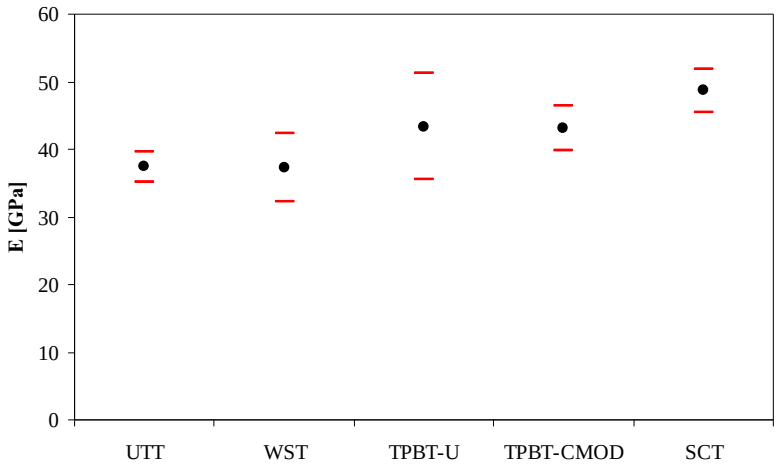

Figure 6.7 *Determination of modulus of elasticity, E, from the different test methods.*

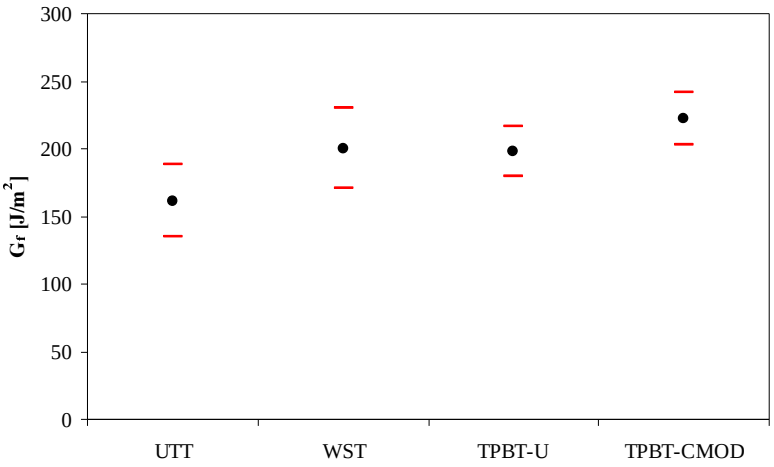

Figure 6.8 *Determination of fracture energy, G_f, from the different test methods.*

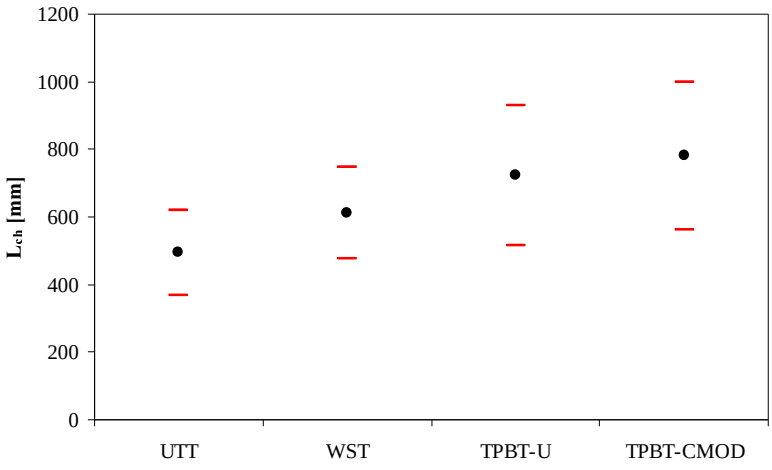

Figure 6.9 *Determination of characteristic length, L_{ch}, from the different test methods.*

6.3.2 SCT vs. WST at Early Age

The split cylinder test (SCT) has been conducted throughout this study in order to achieve a measure of the tensile strength of the materials under investigation. However, as demonstrated in Section 5.2, the outcome for early age concrete may not be a trustworthy result due to a different failure mechanism. Thus, as a consequence of this, SCT results have only been utilized for comparison with the WST results. The best estimate of the tensile strength is assumed to be obtained from the WST experiments since the inverse analysis algorithm is proven to yield precise results. Furthermore, the inverse analysis algorithm has been calibrated such that it, at least for the material analyzed in the previous section, produces the true uniaxial tensile strength as output. It is assumed that the calibration also holds true for early age concrete since the failure mode does not change and since the maximum aggregate size and the specimen dimensions are kept constant.

Figure 6.10 shows the influence of the water-cement ratio on the f_t/f_{sp}-ratio as function of the age at testing. Two WST and two SCT specimens were tested at each time point. From these results, four f_t/f_{sp}-ratios can be calculated that may be employed for calculation of the mean value and the standard deviation, shown in the figure.

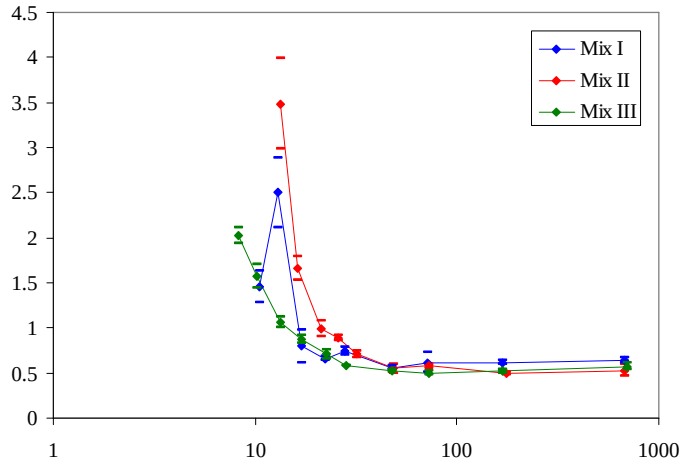

Figure 6.10 *The influence of ageing on the f_t/f_{sp}-ratio for different water-cement ratios*

First, the results for mature concrete are discussed, see Figure 6.10. Here, at an age higher than e.g. 100 hours, a ratio of 0.5-0.6 is obtained, which is expected from the literature. It is also seen that the low water-cement ratio concrete, Mix I, has a higher ratio than the two other mixes. This also makes sense since this mix is expected to be more brittle due to the low water-cement ratio. Thus, the results for mature concrete resembles the expected facts. However, the experiments conducted at early ages show a totally different result. Ratios as high as 4 are obtained for Mix II at 13 hours. Also Mix I and II are experiencing a development in the ratio, resulting in a decrease with age, and finally arriving at a constant value at approximately 24 hours. Figure 6.10 also indicates

that a maximum value at intermediate ages exist. This is seen for Mix I, but missing for Mix II and III. It is also seen in the results for different type of cement, see Figure 6.11. These experiments all show an initial increase of the ratio until a certain age after which the ratio again decreases and finally arrives at a constant value. For Mix I and IV this constant value starts at approximately 24 hours, while the concrete with slow-hardening cement, Mix V, has a ratio, which varies until 48 hours.

The high values of the ratio at the intermediate ages (12 and 24 hours respectively) may be explained by the transition of the material behavior, from a plastic material at early ages towards the quasi-brittle material at mature ages. This is indicated by the failure mode seen in Figure 5.16. The material is plastic and may possess different ratios between the governing properties, i.e. the tensile and the compressive properties. Thus, it is indicated that the compressive properties develop at a slower rate in the very early ages, thereby altering the failure mode towards a more pronounced compressive failure. This means that the failure load to a higher extent may be governed by the compressive properties, and thus the ratio may vary. The tensile strength derived from the experiment may then be lower than the true tensile strength of the material under analysis. Similar results of the relation between the uniaxial tensile strength and the split cylinder tensile strength was obtained by Altoubat (2000). This work also revealed a decreasing ratio in the time period from start of measurements (24 hours) and till an age of 100 hours whereafter the ratio was determined to be constant and equal to 0.8. It is noted that the effect is opposite to the predictions by the analytical and numerical models. This is most certainly due to lack of knowledge of the real compressive properties in early age (cohesion and friction angle).

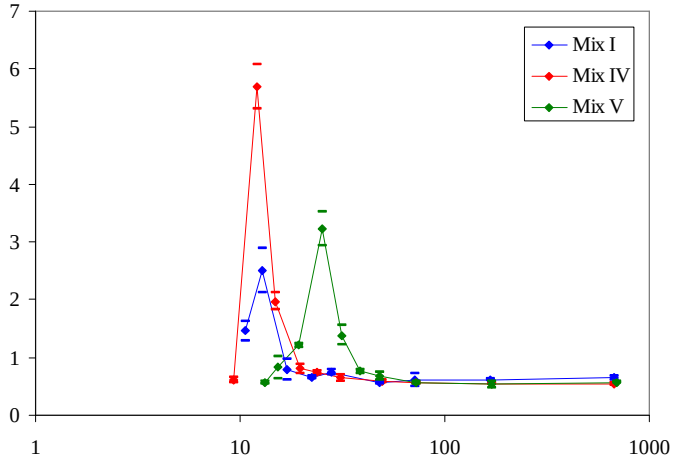

Figure 6.11 *The influence of ageing on the f_t/f_{sp}-ratio for different cement types*

Figure 6.12 shows the influence of curing on the ratio for Mix I. The curing conditions were either storage in a water tank, drying in the lab (at approximately 40% RH) or 100% RH in a sealed container with a water reservoir below the specimens. The specimens were

exposed to the different environments at 24 hours. The sealed condition, which is the reference condition in this work, is shown as the blue curve. It is clearly seen that the samples exposed to drying exhibits an increase in the ratio with age, while the ratio for the water immersed samples decreases. Also the sealed samples increase, but at a slower rate than the drying ones. This may be attributed to the self desiccation of the samples since the water-cement ratio is low. The development of the ratio is attributed to the fact that drying concrete is more brittle than wet concrete.

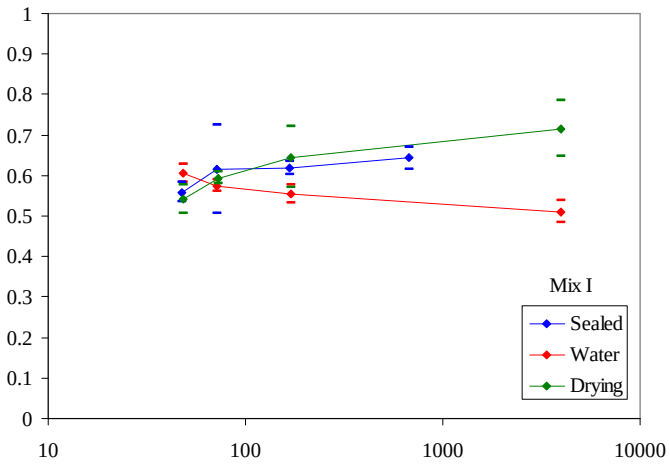

Figure 6.12 *The influence of ageing on the f_t/f_{sp}-ratio for different curing conditions*

It is noted that the drying of the samples will introduce a drying shrinkage stress in the WST samples, which will be different than the one arising in the SCT samples. However, the tests conducted at around 6 months, are probably not influenced significantly by this fact due to the smallness of the specimen.

The discussion above clearly shows that the split cylinder test is a poor choice for determination of the tensile strength at early ages. This is due to the mixture of parameters influencing the peak load in the split cylinder test. The WST test is free of this flaw since the failure mode is well defined and since all the parameters influencing the peak load are included in the model, i.e. the stress-crack opening relationship. The WST experiment also surpasses the SCT test by the fact that the entire load-deformation curve is obtained.

6.4 Results from Short-Term Experiments

This section introduces the results from the wedge splitting test for the five mixes described in Section 6.2.1. The results are all obtained using the value of s, which was determined to be the best one to fit the results in Section 6.3. The results presented will be the five constitutive parameters, which may be obtained from the wedge splitting test, namely the modulus of elasticity, E, and the stress-crack opening relationship, see e.g. Figure 3.9.

6.4.1 Development of Fracture Mechanical Properties

The development of the P-CMOD curves with age for Mix V is illustrated in Figures 6.13-6.14. These graphs are representative for the results obtained from the experimental work. The curves all have the same x-axis ranging from 0 to 4 mm, while the y-axis is changing.

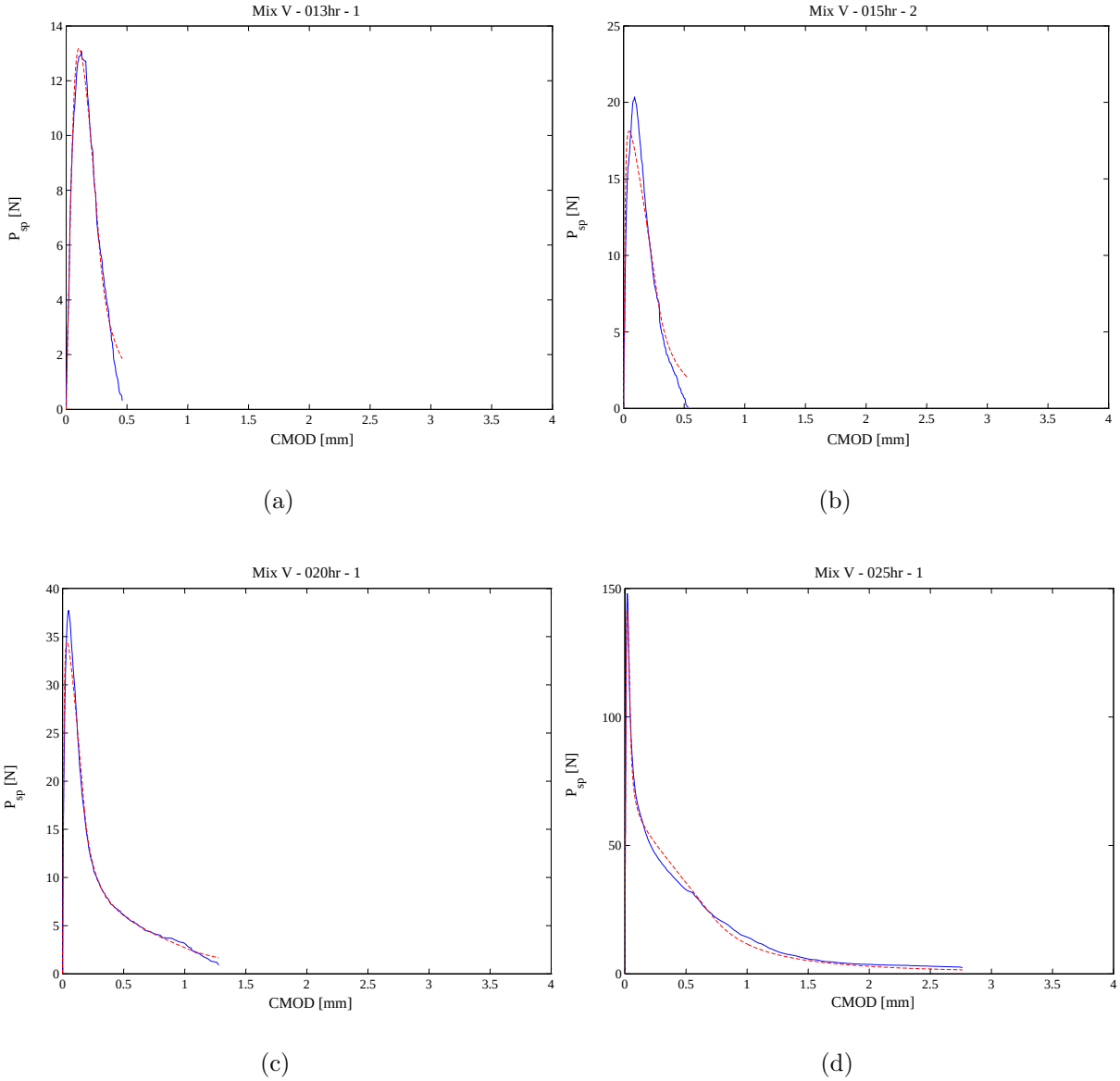

Figure 6.13 *Development of the WST P-CMOD curves with age for Mix V. The dashed red curve represents the results obtained from the inverse analysis while the blue curve is the experimental result.*

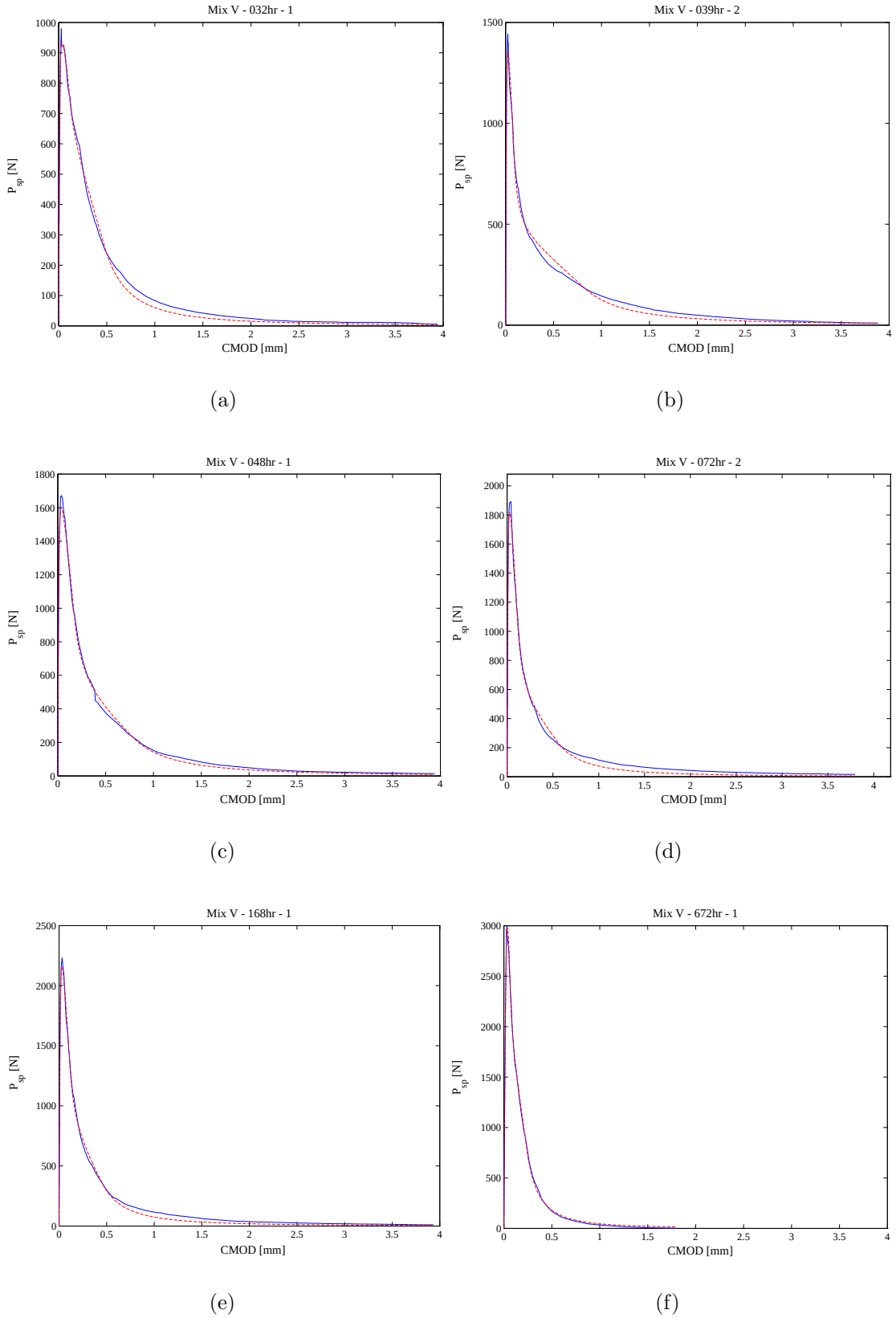

Figure 6.14 *Development of the WST P-CMOD curves with age for Mix V.*

Figure 6.13a shows the result obtained at an age of 13 hours. Here, the peak split load is 13 N. Self weight alone corresponds to a split load of more than 10 N, but it has been eliminated by the arrangement shown in Figure 5.39. It is thereby possible to make experiments on this very fragile sample. It is very interesting to see how relatively steep the descending branch is at this very early age. The specimen is pulled entirely apart at an opening of only 0.5 mm. This is changing with the age and a tail is already clearly visible at 20 hours, and a total opening of more than 2.5 mm is necessary at 25 hours. This may indicate a insignificant bond between the aggregates and the cement paste at 13-15 hours of age, which may be due to a higher water content in the interfacial transition zone, not yet consumed by the hydration reactions. Thus, it may be the cohesive properties of the paste, which entirely govern the strength of the sample.

This picture starts to change at 20 hours from which a tail becomes visible on the curves. This is most likely due to engagement of the coarse aggregates, which start to interact with the paste and thereby cause a tail on the curve while being pulled out. It is also interesting that this tail at an age of 28 days (672 hours) once again is reduced - now indicating that the aggregates are fracturing instead of being pulled out, see Figure 6.14f.

The results in Figures 6.13-6.14 also demonstrate the performance of the inverse analysis algorithm. The correlation is very good for almost all curves at any age. The major discrepancy is at 15, 20 and 25 hours where the peak load is a little underestimated. This may cause small errors on the determination of primarily the tensile strength and the initial slope of the stress-crack opening relationship. However, since the largest discrepancy is about 10% (15 hours), this is probably insignificant and in any case acceptable.

The fracture surfaces are also changing significant with the age of the concrete. At an age of 13 hours absolutely no aggregates are fracturing, which makes the surface very rough. It looks like clay pulled apart, revealing the aggregates as inhomogeneities, see e.g. the photos in (Østergaard, Lange & Stang 2002). The fracture surface is much more smooth at 28 days, which is due to the pronounced fracture of the aggregates.

The next section will go into detail with the development of the stress-crack opening relationship and the dependency of water-cement ratio, cement type and curing conditions.

Development of f_t

The development of fundamental properties of concrete like tensile strength, modulus of elasticity etc. is often described by growth functions like Equation 2.1. This approach is adopted here.

Figure 6.15 shows the development of the tensile strength for all the mixes in Table 6.1. Experiments were conducted such that especially the development in early ages is well described. The function applied for fitting the development is given in Equation 6.5:

$$f_t(t) = A_1 \left[1 - e^{-(t/\tau_1)^{n_1}}\right] + A_2 \left[1 - e^{-(t/\tau_2)^{n_2}}\right] \tag{6.5}$$

This function is seen to fit the results well. It is also seen that the uncertainty on the results is small. The 95% confidence intervals utilizing Equation 6.5 and based on the entire data set for all experiments are also shown in the figures. These confidence curves underline the fact that the uncertainty is small.

Figures 6.15a-c show the dependency of the water-cement ratio. It is seen that the strength at any age decreases as the water-cement ratio increases, which is expected. It is also seen that the strength development is a little faster in the very early age for the high water-cement ratio concrete (Figure 6.15c), which is due to the fact that no super plasticizer was added to this mix.

The dependency of type of cement is illustrated in Figures 6.15a, c-d. The cement used for Mix IV has a little slower rate of development than the cement used for Mix I. This fact is repeated in the figures. A slow-hardening cement was used for Mix V - and the tensile strength development for this mix is indeed seen to start at a later age and to be slower.

The best fitting parameters applied for the different concrete mixes are given in Table 6.3. The parameters show the tendency as already discussed above.

The need for the double exponential function for the description of the strength development is most likely caused by the addition of puzzolans. Especially the fly ash is known to contribute to the strength in a slower rate than the ordinary cement and silica fume and may thus cause the second strength gain seen in all the curves.

Table 6.3 *Parameters used to fit development of tensile strength.*

	Mix I	Mix II	Mix III	Mix IV	Mix V
A_1 [MPa]	2.31	1.45	1.28	2.00	1.52
τ_1 [hours]	18.5	20.6	16.6	18.8	34.3
n_1 [-]	4.38	4.71	3.49	4.39	5.95
A_2 [MPa]	1.68	1.24	1.36	1.57	1.56
τ_2 [hours]	245	254	437	210	207
n_2 [-]	1.64	1.02	0.848	1.26	1.97

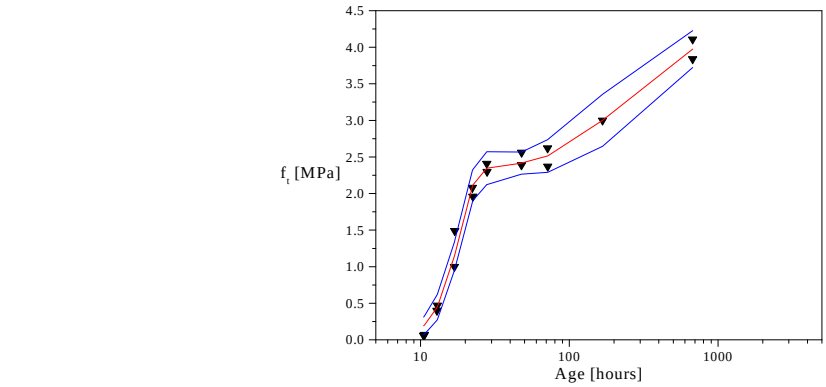

(a) Mix I

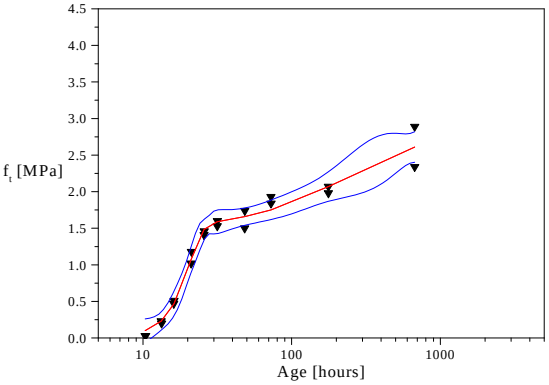

(b) Mix II

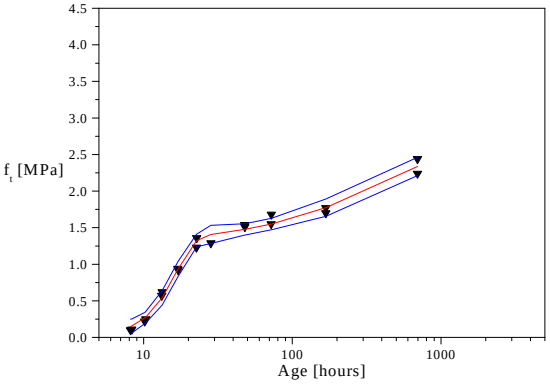

(c) Mix III

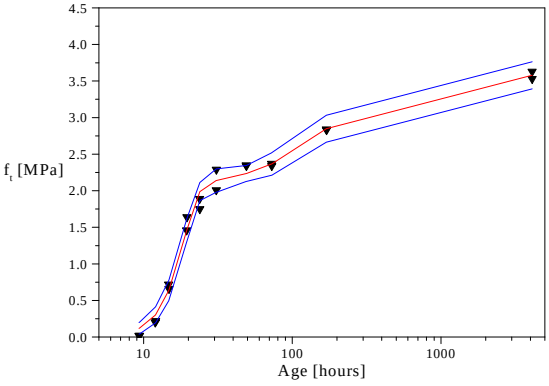

(d) Mix VI

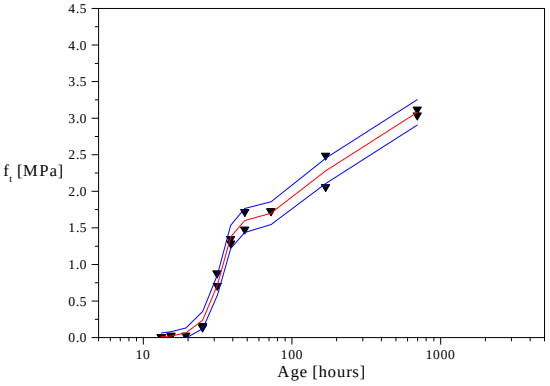

(e) Mix V

Figure 6.15 *Development of the tensile strength determined from WST. Downward triangles are experimental observations, while the red curve is the best fit employing Equation 6.5. The blue curves show the 95% confidence intervals*

Development of a_1

The development of the initial slope of the stress-crack opening relationship, a_1, with age is not investigated in the literature. No precedence is therefore established for the use of a relevant function describing the development. Figure 6.16 shows the development for all the mixes in this study. Three very important issues must be commented here. First, a decrease with age is seen on almost all the curves. The results in Figure 6.16c show this decrease most clearly, but the tendency is found in all the curves. Second, for Mix II, IV and V, an initial period with low values of a_1 is seen. Especially the curve showing the results from Mix V displays initially small values, which is due to conduction of a number of experiments at very low strength, see Figure 6.15e. Third, a slow change in the parameter with age is seen to continue throughout the period of testing.

Thus, the development of the initial slope of the stress-crack opening relationship should probably be fitted with a bell-shaped function. However, the experimental evidence for the initial small values is not strong. The fitting therefore omits these observations. Only the initial decrease and the second, slow, increase is included. These effects are captured with the exponential-linear function given below:

$$a_1(t) = p_1 e^{-t/\tau} + p_2 + p_3 t \tag{6.6}$$

in which t is time in hours, while p_1, τ, p_2 and p_3 are the fitting parameters.

Table 6.4 *Parameters used to fit the development of initial slope, a_1*

	Mix I	Mix II	Mix III	Mix IV	Mix V
p_1 [mm^{-1}]	5.23e5	1.09e3	4.83e1	6.79e4	5.88e1
τ [hours]	1.26	3.27	9.02	1.42	15.0
p_2 [mm^{-1}]	9.29	13.7	11.5	13.6	13.2
p_3 [mm^{-1}/hour]	1.0e-2	-7.4e-4	-4.5e-4	1.2e-2	8.5e-3

The proposed function using the fit parameters given in Table 6.4 are seen to fit the experimental results well as seen in Figure 6.16. The largest scatter is seen with Mix V, for which application of the function is rather doubtful. In fact, for this mix, another function may be chosen.

It is finally noted that the applicability of the function proposed should be verified by further experiments. This is due to the few results, which clearly show the assumed behavior and due to the relatively large scatter.

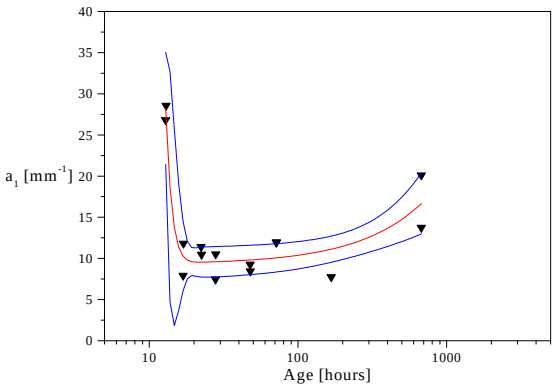

(a) Mix I

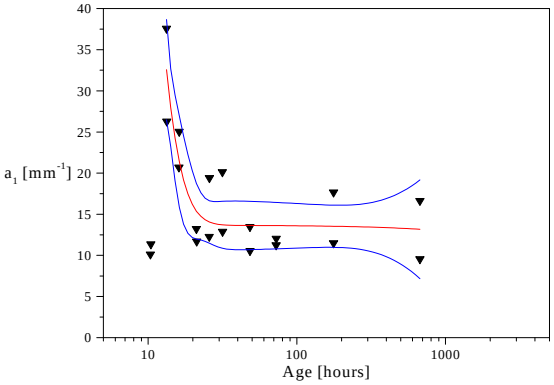

(b) Mix II

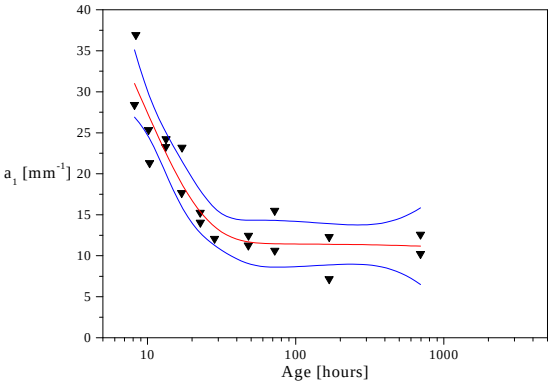

(c) Mix III

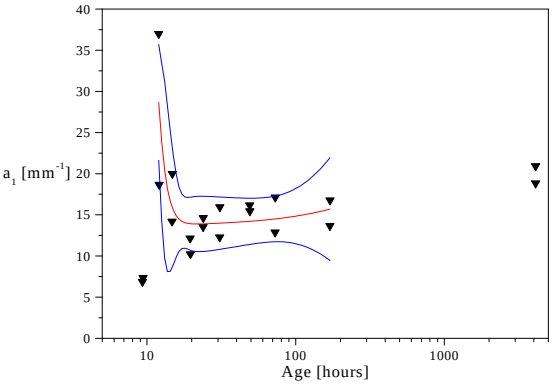

(d) Mix IV

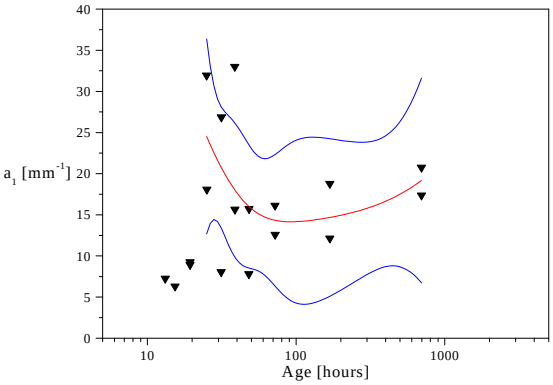

(e) Mix V

Figure 6.16 *Development of a_1 determined from WST. Downward triangles are experimental observations, while the red curve is the best fit using Equation 6.6. The blue curves show the 95% confidence intervals*

Development of a_2

The development of the second slope of the stress-crack opening relationship, a_2, is shown for all mixes in Figure 6.17. This parameter does not show a significant age dependency. If an age dependency is in fact present, the uncertainty of the results hides it. The only apparent age dependency is seen for Mix I but it is most likely caused by the high strength of the paste, causing the aggregate bridging to vanish. This statement is backed by the development in b_2 for Mix I (see Figure 6.18a), which is seen to approach one. Thus, the stress-crack opening relationship for this mix may with good accuracy be described employing a linear instead of the bilinear function applied. This renders a_2 and b_2 unimportant for Mix I.

It is assumed that a_2 is age independent, such that the value is unchanging with time. This assumption is applied for the fit curves shown in the figures, Figure 6.17. The fitting is furthermore only conducted for the initial part of the results for Mix I. The results are given in Table 6.5. The uncertainty of the value of a_2 is clear from the table.

Table 6.5 *Parameters used to fit the development of second slope, a_2*

	Mix I	Mix II	Mix III	Mix IV	Mix V
a_2 [mm^{-1}]	0.74	1.65	1.18	2.27	2.01

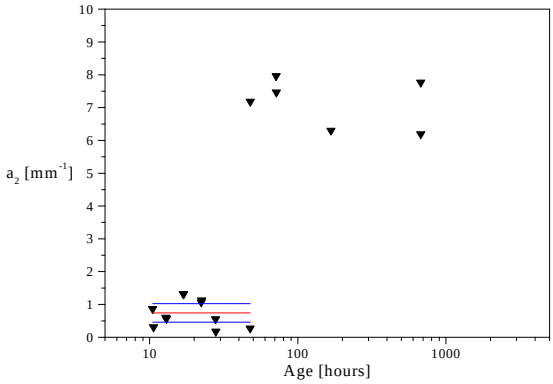

(a) Mix I

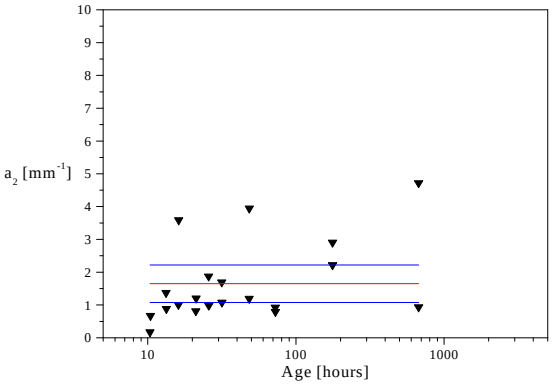

(b) Mix II

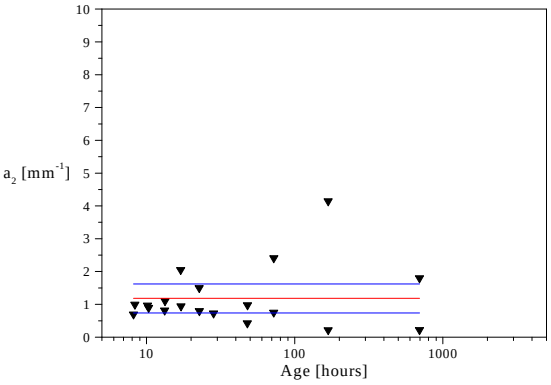

(c) Mix III

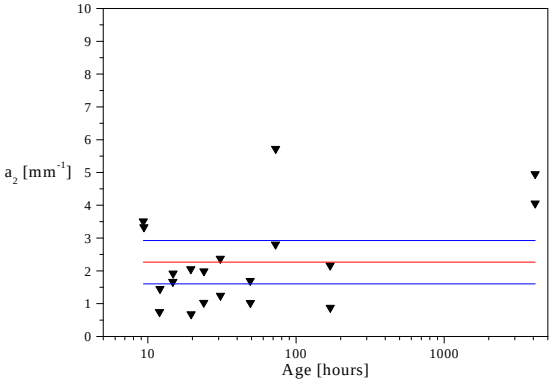

(d) Mix IV

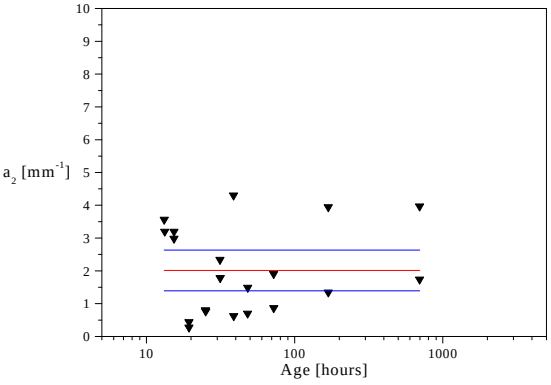

(e) Mix V

Figure 6.17 *Development of a_2 determined from WST. Downward triangles are experimental observations, while the red curve is the best fit assuming age independence. The blue curves show the 95% confidence intervals*

Development of b_2

The development of b_2 shows, like a_2, no pronounced age dependency. The uncertainty of the results is too large to reveal any age dependency. Similar to the change in a_2-value for Mix I, b_2 show an apparent aging. However, as discussed on the previous section, this is due to the strength development of the paste. Table 6.6 lists the best fit for all the mixes assuming no age dependency.

Table 6.6 *Parameters used to fit the development* b_2

	Mix I	Mix II	Mix III	Mix IV	Mix V
b_2 [-]	0.27	0.37	0.33	0.42	0.43

It is interesting that the value of b_2 only shows a little variation from one mix to another. The explanation may be that the heterogeneity for all the mixes is the same, thus resulting in approximately the same aggregate bridging. However, this only applies if aggregate bridging really plays a role in the fracture. This is not the case for the Mix I at mature ages.

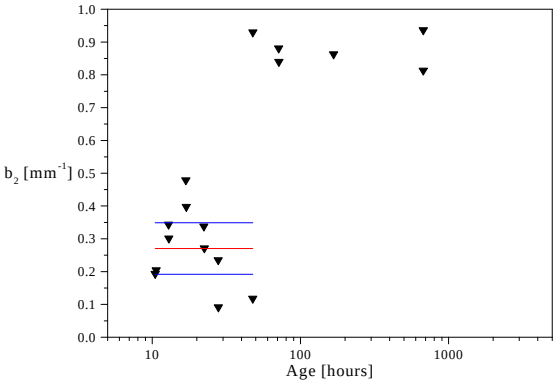

(a) Mix I

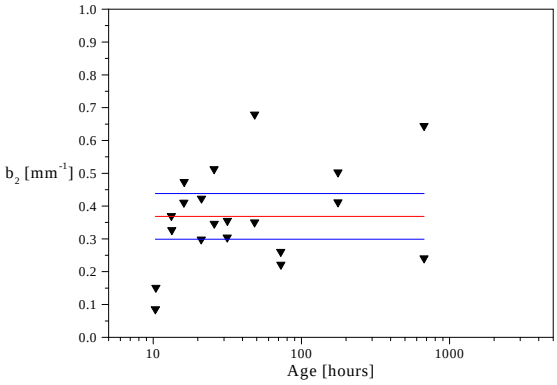

(b) Mix II

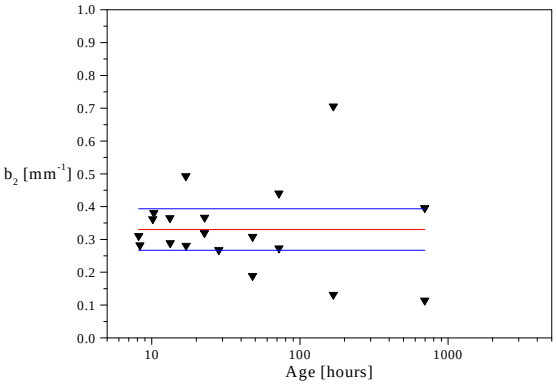

(c) Mix III

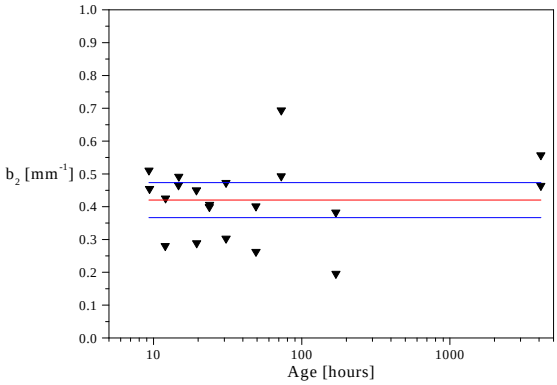

(d) Mix IV

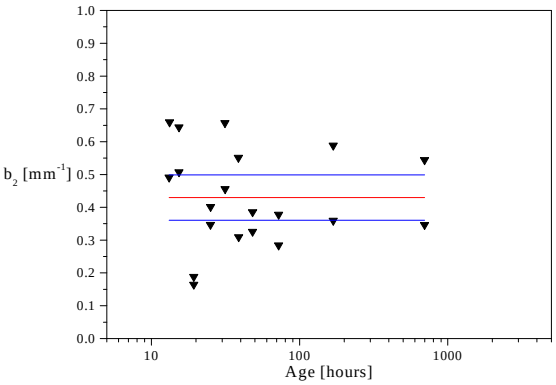

(e) Mix V

Figure 6.18 *Development of b_2 determined from WST. Downward triangles are experimental observations, while the red curve is the best fit assuming age independence. The blue curves show the 95% confidence intervals*

Development of E

The age dependency of the modulus of elasticity is, like the development of f_t, often assumed to be best described by growth functions similar to Equation 2.1. This assumption is also applied here, and a function similar to 6.5 is applied:

$$E(t) = A_1 \left[1 - e^{-(t/\tau_1)^{n_1}}\right] + A_2 \left[1 - e^{-(t/\tau_2)^{n_2}}\right] \tag{6.7}$$

The uncertainties for most of the results are small. However, the decrease seen for Mix I is most likely not a result of the real behavior and is therefore excluded from the analysis. Furthermore, also Mix II shows some scatter, especially at 28 days. The consequence of this is that the final value of E according to the fit function should be applied with care.

It is interesting that the development of modulus of elasticity is not correlated with the development of tensile strength for Mix I, IV and V at mature ages. For these results, further analysis and experimenting are recommended. This is due to the fact that either the experiment or the inverse analysis may cause an unknown error. It is, at least, not very trustworthy that the development of these two parameters decouple.

The parameters employed to fit the curves are shown in Table 6.7. The analysis showed that the use of the double exponential function for mix I and V where the ageing of the modulus of elasticity ceases represents an over-parameterization. Thus, for these mixes, only one exponential function is considered at seen in Table 6.7.

Table 6.7 *Parameters used to fit the development of modulus of elasticity, E*

	Mix I	Mix II	Mix III	Mix IV	Mix V
A_1 [GPa]	43.4	31.1	27.4	35.2	40.2
τ_1 [hours]	23.9	19.8	14.7	17.1	37.9
n_1 [-]	2.19	3.62	2.98	4.27	3.52
A_2 [GPa]	-	17.3	33.9	9.05	-
τ_2 [hours]	-	230	1077	60.5	-
n_2 [-]	-	0.93	1.43	2.23	-

The modulus of elasticity is an interesting bi-product from the main objectives, namely to determine the tensile strength and the stress-crack opening relationship. However, as the results clearly show, this method is also able to determine the modulus of elasticity with an acceptable accuracy. This is especially the case for Mix IV and V, which show a small scatter.

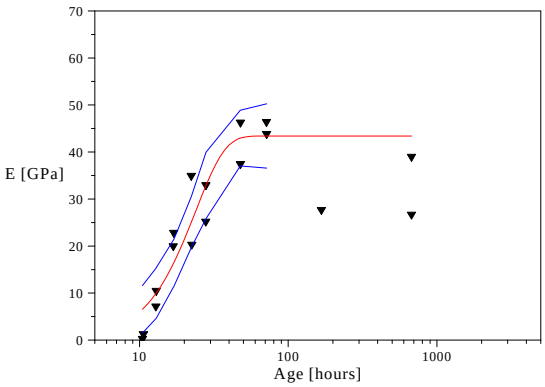

(a) Mix I

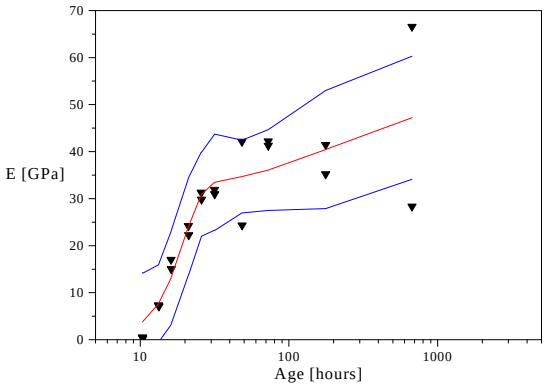

(b) Mix II

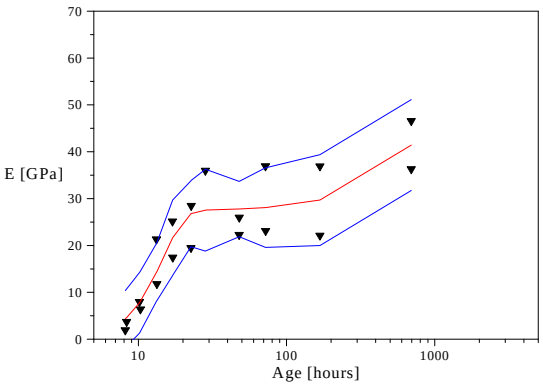

(c) Mix III

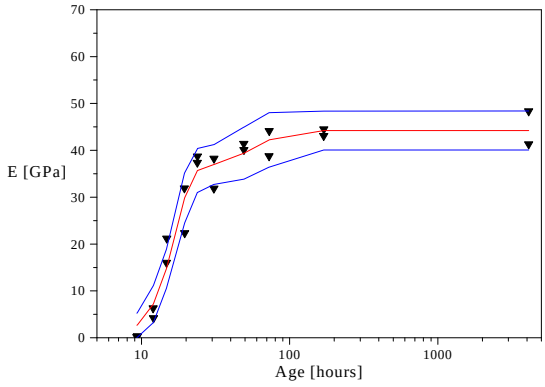

(d) Mix IV

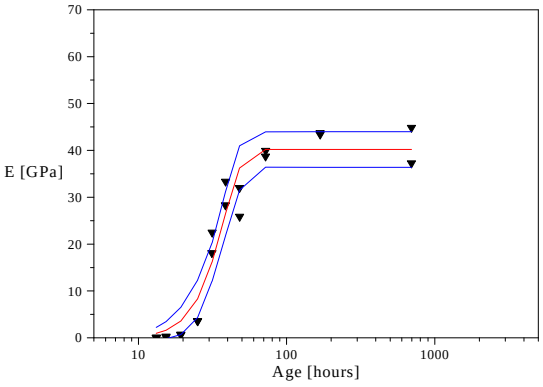

(e) Mix V

Figure 6.19 *Development of E determined from WST. Downward triangles are experimental observations, while the red curve is the best fit utilizing Equation 6.7. The blue curves show the 95% confidence intervals*

Development of G_f

The evolution of the fracture energy is another important issue which has received only limited attention in the literature. The development of fracture energy with time was investigated on cement pastes with and without silica fume by Dela (2000). In this work a growth function similar to Equation 2.2 was adopted. This function was proven to fit the development of fracture energy at early ages well. In this work, an equation similar to Equation 6.5 is adopted. This function is similar to Equation 2.2. Thus:

$$G_f(t) = A_1 \left[1 - e^{-(t/\tau_1)^{n_1}}\right] + A_2 \left[1 - e^{-(t/\tau_2)^{n_2}}\right] \tag{6.8}$$

Figure 6.20 show the development in fracture energy for all the mixes in this study. It is seen that the uncertainty is relatively small for most of the results. A continuing increase in the fracture energy for all mixes except for Mix IV is also observed. The missing development of the fracture energy for Mix IV at mature ages is uncertain, but the lack of data at mature ages may be part of the explanation.

Table 6.8 show the parameters, which are applied to fit the development in fracture energy. The second exponential function was unappropriate for Mix IV since it does not show an ageing after approximately 40 hours. Furthermore, it was necessary to fix τ_2 for Mix II and n_2 for Mix III to avoid spurious solutions caused by over-parameterization.

Table 6.8 *Parameters used to fit the development of fracture energy, G_f. Note that τ_2 for Mix II and n_2 for Mix III was fixed to 500 hours and 1, respectively*

	Mix I	Mix II	Mix III	Mix IV	Mix V
A_1 [J/m^2]	152	102	88	129	117
τ_1 [hours]	16.1	18.9	17.0	16.7	34.8
n_1 [-]	5.77	6.41	3.45	6.22	4.84
A_2 [J/m^2]	93	49	65	-	41
τ_2 [hours]	507	500	148	-	729
n_2 [-]	1.32	1.12	1	-	1.05

It is noted that the values of τ_1 and τ_2 for the different mixes results in the fact that the first part of the curve (the early age) is fitted by the first exponential only, and for this part, the second exponential is unimportant. Only the predictions upon approximately 50 hours is depending on the second exponential. Thus, the values for early age are almost unchanged if the second exponential function is omitted.

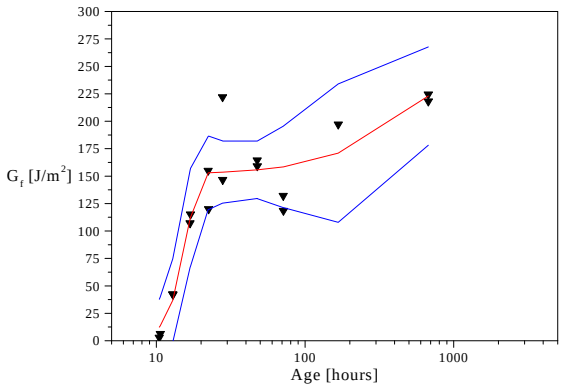

(a) Mix I

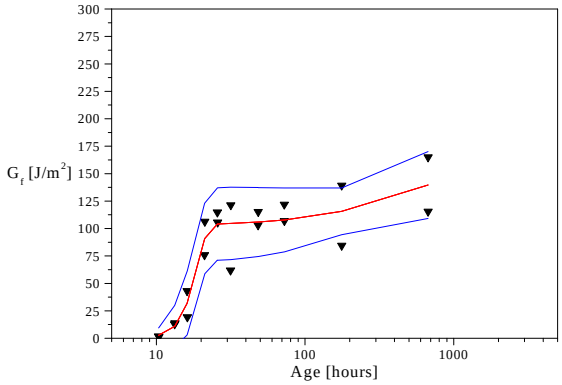

(b) Mix II

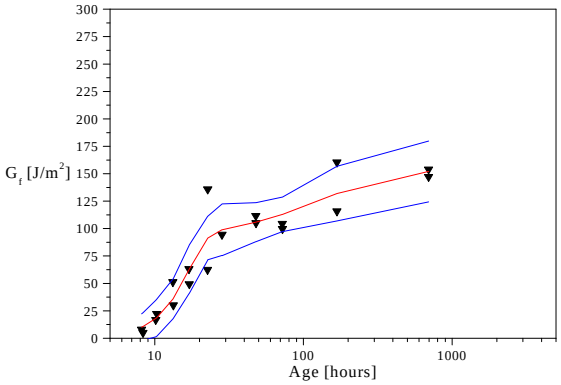

(c) Mix III

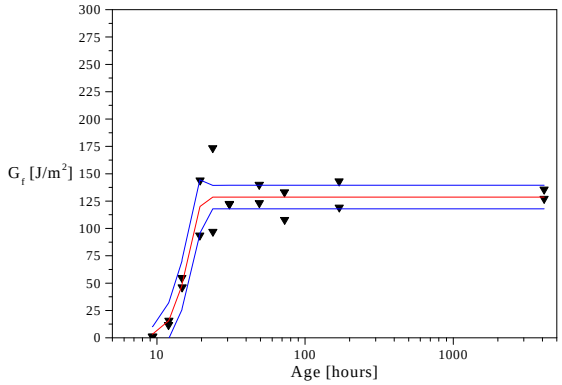

(d) Mix IV

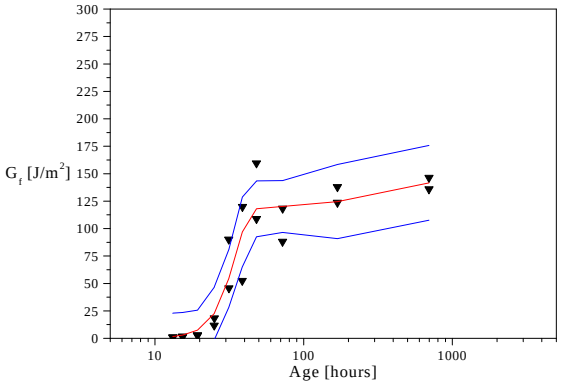

(e) Mix V

Figure 6.20 *Development of G_f determined from WST. Downward triangles are experimental observations, while the red curve is the best fit using Equation 6.8. The blue curves show the 95% confidence intervals*

Development of L_{ch}

The latter parameter, which has been determined in this study is the characteristic length, L_{ch}, which is defined by (see also Section 2.5):

$$L_{ch} = \frac{G_f E}{f_t^2} \tag{6.9}$$

Figure 6.21 shows the evolution of the characteristic length with time for all mixes in this study. The scatter is rather large for most results, which is expected since this parameter is calculated on basis of G_f, E and f_t, and thus incorporates the uncertainties from all these results according to the law of sum of errors. However, it is still possible to extract some very interesting features for the development of this parameter. First, focus is laid on the results for Mix I, IV and V since the scatter for these mixes is smallest. A clear decrease with age is seen, which is expected since the characteristic length is a measure of the brittleness of the mix. This decrease approaches values, which are expected for mature concrete. In this case, values of approximately 500 mm are found.

Another very interesting aspect of the evolution of the characteristic length is the low values at very early age, mostly pronounced for Mix IV and V. Such behavior was also found by Brameshuber (1988) and may mean that intermediate ages of high brittleness exist for maturing concrete. Especially Mix V underlines this observation since a number of experiments were conducted at a very low strength.

Finally, it is noted that all the concretes show a decrease in the overall characteristic length with age, despite the scatter. And also Mix II and III show an initial period of higher characteristic length than the succeeding time period.

Influence of Curing Conditions

The influence of curing conditions on the modulus of elasticity, stress-crack opening relationship, fracture energy and characteristic length has been investigated by subjecting a batch of specimens (Mix I) to either water curing or drying in the lab (approximately 50 % RH). These results are compared with the ones from the Mix I specimens, which were subjected to sealed curing, see the former section.

The specimens were initially cured 24 hours in the moulds whereafter they were subjected to the individual curing conditions. Wedge splitting tests were conducted at approximately 2, 3, 7 and 150 days. The prolonged curing before the latter tests was preferred such that the effect of the curing for sure would be significant.

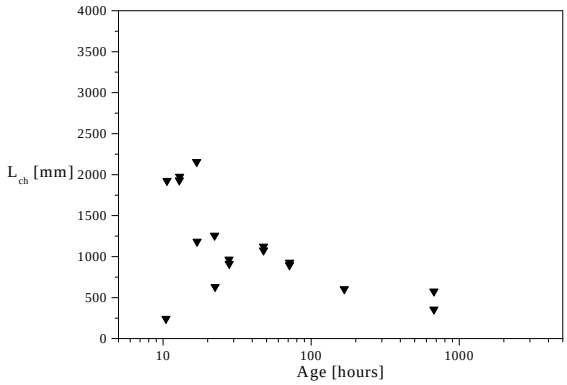

(a) Mix I

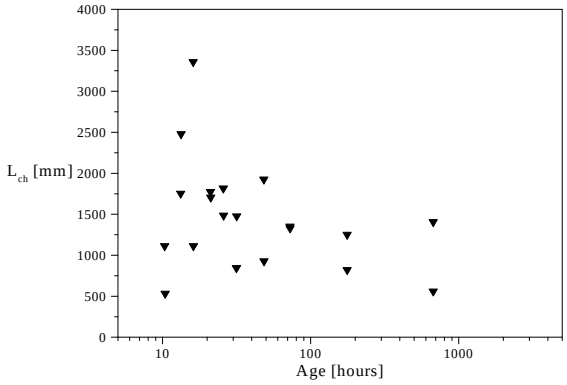

(b) Mix II

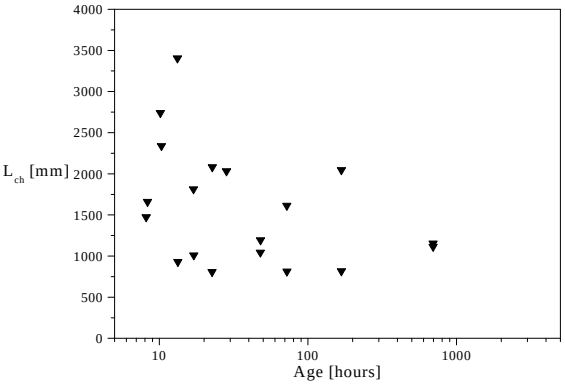

(c) Mix III

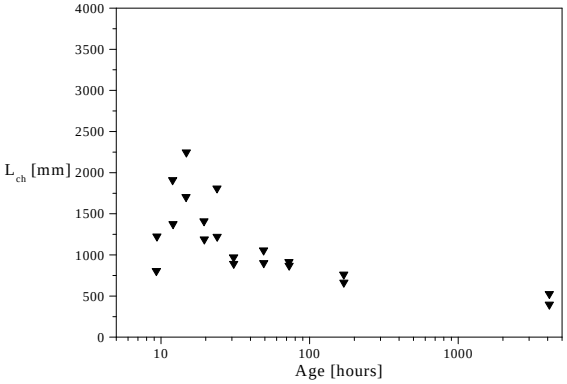

(d) Mix IV

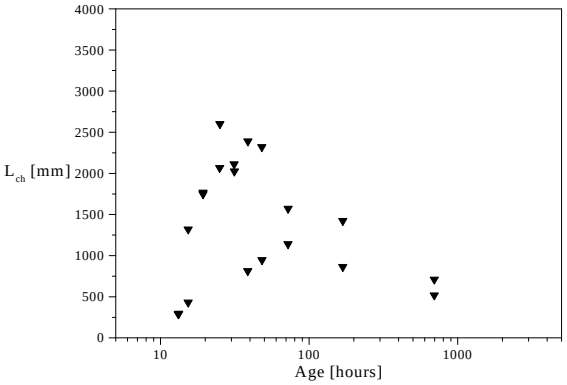

(e) Mix V

Figure 6.21 *Development of L_{ch} determined from WST. Downward triangles are experimental observations.*

The experience from literature is that the compressive strength of a drying sample is lower than that of a sample subjected to water curing, see e.g. Neville (1995), or recent papers by Bonavetti, Donza, Rahhal & Irassar (2000), Al-Khaiat & Haque (1998), Quillin, Osborne, Majumdar & Singh (2001). Also the modulus of elasticity is generally found to be lower for a sample subject to drying.

Figure 6.22a shows the tensile strength for the different curing conditions. It is first pointed out that the sealed specimens are from a different batch than the others, which may explain the departure of these results from the others. It is secondly observed that the tensile strength seems to be independent of the curing conditions for the wet and drying samples, however with a little higher strength for the water cured specimens. This is in contrast to the findings in literature. Another interesting observation is found in Figure 6.22b. It seems like the initial slope of the stress-crack opening relationship is higher for the water cured specimens than for the drying specimens. Higher a_1 generally results in a lower peak load of the experiment, thus in an ordinary load-controlled experiment, this fact lowers the apparent tensile strength. The conclusion is thus that the expected findings are missing - perhaps the scatter is too large, and conclusions may only be drawn if further experiments are conducted.

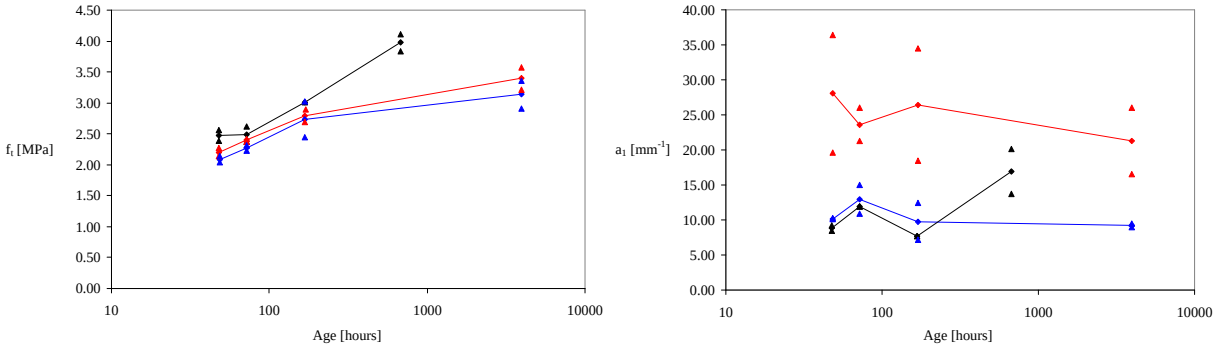

(a) (b)

Figure 6.22 *Development of f_t and a_1 determined from WST under different curing conditions. Triangles are individual observations while the diamonds connected by lines are the average values. Black=sealed, red=wet and blue=drying.*

Figures 6.23a-b show the influence of curing on a_2 and b_2. It is not possible to see any dependency of curing - perhaps due to the scatter on these results. Only a_2 appears to be a little higher for water curing. The same observation is made with regard to the modulus of elasticity, see Figure 6.23c. Although the scatter also here obscures the results, the water cured specimens do have a higher stiffness, which is in accordance with the results from the literature.

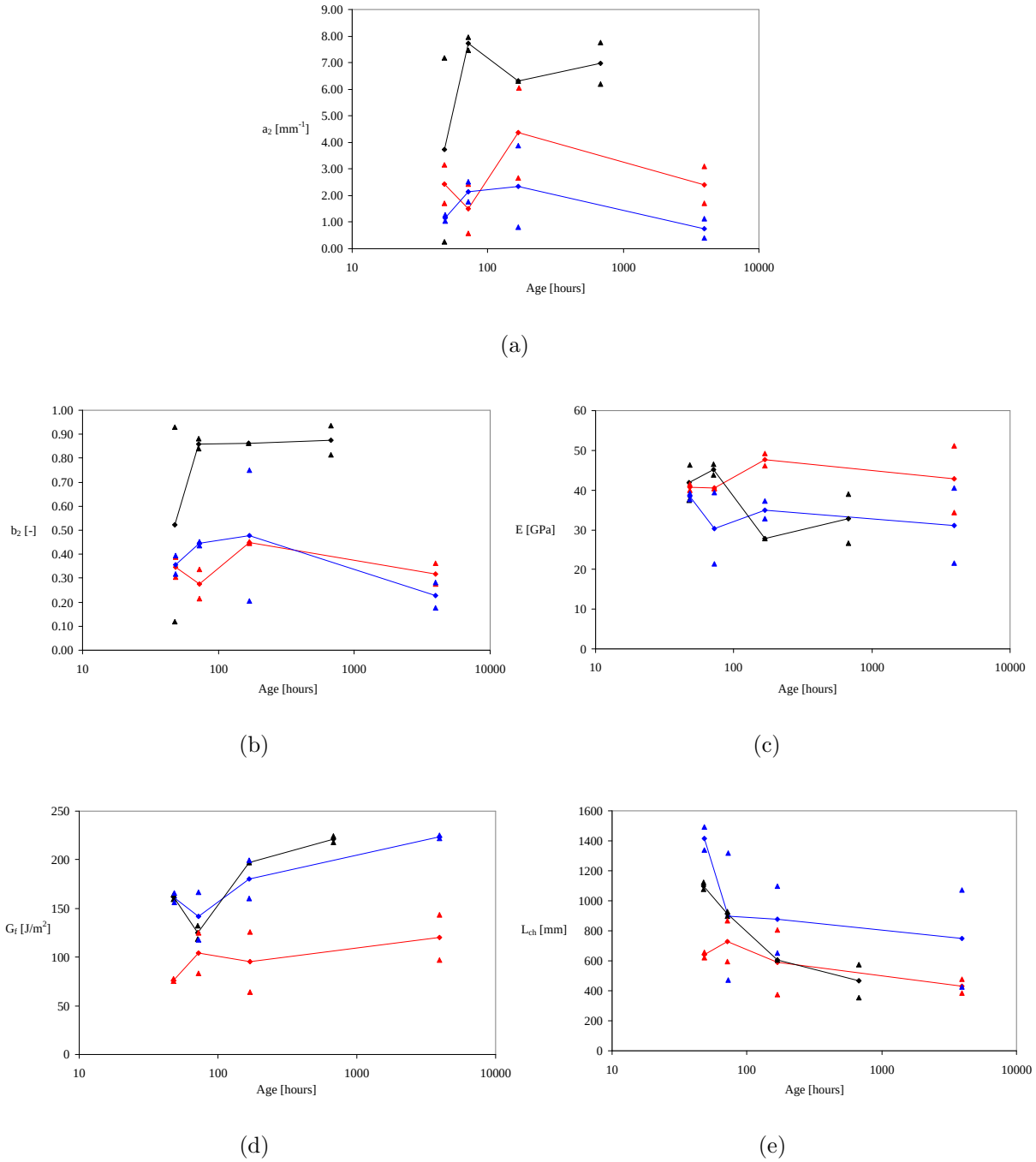

Figure 6.23 *Development of a_2, b_2, E, G_f and L_{ch} determined from WST under different curing conditions. Triangles are individual observations while the diamonds connected by lines are the average values. Black=sealed, red=wet and blue=drying.*

The fracture energy for the water cured specimens is found to be somewhat lower than for the drying specimens, see Figures 6.23d. No studies in the literature have been discovered, which could shed more light on this finding.

With regard to the characteristic length it is surprising that it seems to be higher for the drying concrete, see Figure 6.23e, than for the wet cured concrete. A guess a priori would say that it was the opposite. However, as the fracture energy is lower for wet curing, together with the fact that the tensile strength is almost unaffected, the result may be as seen. It is, unfortunately not possible to make a definite conclusion since the scatter is too high on the characteristic length, and thus, further experiments are recommended.

6.5 Results from Long-Term Experiments

This section aims at determining both bulk viscoelastic behavior and crack creep properties for some of the mixes described in Section 6.2.1.

6.5.1 Development of Bulk Creep Properties

The bulk creep properties have been determined employing the setup developed by Altoubat (2000). This setup is similar to the one described in Figure 1.5. Some of the results obtained with the setup have been published in (Østergaard, Lange, Altoubat & Stang 2001), using mix designs corresponding to those applied by Altoubat (2000). These experiments confirmed early age creep behavior also found by other authors, e.g. strong ageing of early age creep, see e.g. (Westman 1995).

This thesis does not focus on bulk creep of concrete, but it is necessary to obtain some ideas of the magnitude. This in order to be able to assess the influence in the models for crack creep behavior. The findings will be backed by comparison with the literature.

As discussed in Chapter 4, viscoelasticity of concrete may be described by various models. The first choice lies in the selection of the fundamental nature of the creep function, i.e. whether it should be integral or incremental. The incremental approach has several advantages as described in Chapter 4. However, also the integral type modelling has advantages since a lot of work has been done in this direction (e.g. the solidification theory by Bažant & Prasannan (1989*a*)), and since this type of modelling often is available in finite element codes like e.g. DIANA (DIANA 2000). DIANA offers the possibility of modelling creep of concrete by both ageing Maxwell and Kelvin chains containing up to 25 chain units. It is further more possible - phenomenologically - to include the influence of temperature. Thus, a vast range of creep problems may be modelled in DIANA, despite the fact that the physical connection is weak.

The ageing Kelvin chain implemented in DIANA is given by:

$$J(t,t') = \frac{1}{E_0(t')} + \frac{1}{E_1(t')}H_1(t,t') + \frac{1}{E_2(t')}H_2(t,t') + \ldots + \frac{1}{E_n(t')}H_n(t,t') \qquad (6.10)$$

where t is time, $E_0(t')$ is the instantaneous elastic deformation if the load is applied at an age of t', $E_n(t')$ is the spring stiffness of chain unit number n, while $H_n(t,t')$ is given by:

$$H_n(t,t') = 1 - \exp\left(\frac{t-t'}{\tau_n}\right) \tag{6.11}$$

where τ_n is the retardation time of chain unit n. The retardation time is linked to the viscosity of the dashpot η_n by $\tau_n = \eta_n/E_n$. Equation 6.10 will be employed to fit the creep data.

Variation of Age of Load Application

Experiments were conducted at $t' = 1$, 3 and 5 days at load levels, which initially were below 50 % of the tensile strength. Thus, any possible non-linearities at high load levels are avoided.

The results are given in Figure 6.24a-b. The ageing of the spring stiffness, $E_0(t')$, is given by Equation 6.7 utilizing the fitting parameters from Table 6.7. However, as already touched in Section 6.4, the experimental findings from the short-term experiments are not trustworthy beyond 100 hours since an apparent significant drop is measured (see also Figure 6.19a). This does also not fit the development which may be seen in Figure 6.24. Thus, the initial deformation in the creep experiments has been fitted by including the second exponential in Equation 6.7. The ageing of the stiffness of the remaining springs has also been modelled employing Equation 6.7, but for all these springs $A_2 = 0$ has been chosen. Different sets of retardation times τ_n have also been tried, using the experience from literature that they should be spaced by a decade, see e.g. (Bažant 1988) and (Altoubat 2000).

The fit shown in Figure 6.24 is obtained by 4 chain units. The first unit is simply a spring, i.e. the viscosity is set to zero, ensuring an instantaneous elasticity of the chain. This unit is described by Equation 6.7 using the fit parameters from Table 6.7 and with $A_2 = 20$ GPa, $\tau_2 = 100$ hours and $n_2 = 4$. The parameters of the remaining three units are given in Table 6.9.

Table 6.9 *Parameters used to fit the bulk creep behavior for Mix I*

	Unit 1, E_1	Unit 2, E_2	Unit 3, E_3	Unit 1, H_1	Unit 2, H_2	Unit 3, H_3
A_n [GPa]	180	280	360	-	-	-
τ_n [hours]	5	50	500	50	5	500
n_n [-]	1	1	1	-	-	-

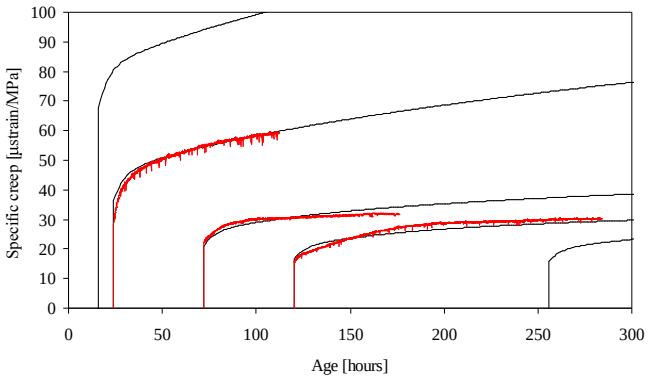

(a)

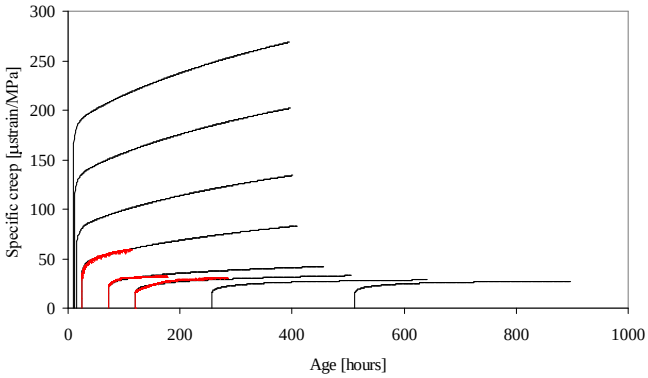

(b)

Figure 6.24 *Early age bulk creep for Mix I loaded at 1, 3 and 5 days (red curves). Black curves represents a fit employing the Kelvin chain.*

It is noted that only a limited number of experiments have been carried out and thus that the extrapolation and the curves drawn for different ages of loading may be unprecise. However, the behavior is similar to what is found in literature, see e.g. (Emborg 1989), (Westman 1995) and (Østergaard, Lange, Altoubat & Stang 2001). Furthermore, the functions applied are well established for creep behavior of concrete, see e.g. Equation 2.1 with regard to the ageing of the springs, or e.g. (Nielsen 1999*a*) with regard to the use of Kelvin type modelling.

The number of experiments carried out suffices for the purpose at hand, namely obtaining an estimate of the magnitude of creep in early age, which may be used to assess the influence of creep of the mixes under consideration. It is not an independent goal to contribute to the knowledge of early age creep, although the experiments do show some of the effects expected for early age creep and thus confirm results from literature. The experiments carried out do furthermore cover the primary time interval of interest, thereby fulfilling the goals setup initially.

Variation of water-cement ratio and curing conditions

A few other results from the creep experiments are reported. As expected from literature, (Herholdt et al. 1985), creep is found to increase with increasing water-cement ratio. This is illustrated in Figure 6.25 where the upper curve represents Mix III, which has a higher water-cement ratio than the lower curve, which is Mix I.

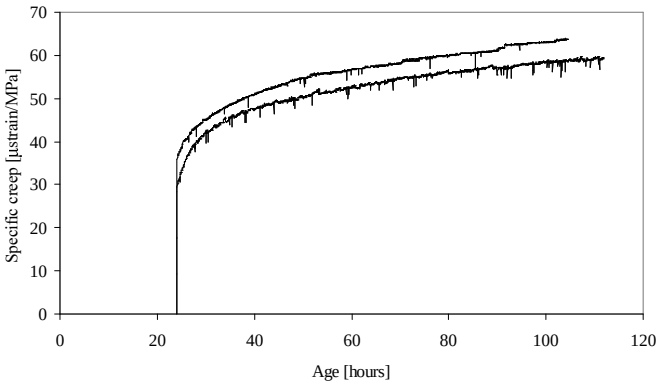

Figure 6.25 *Early age bulk creep for Mix I (lower curve) and Mix III (upper curve) loaded at 1 day.*

The influence of curing conditions is shown in Figure 6.26. Surprisingly, no effect is seen, which must arise from either experimental errors or from the possibility that the scatter is obscuring the expected picture. Due to the low number of experiments carried out, no scatter may be calculated. The only possible estimate on the scatter may be obtained from Figure 6.19, which show the scatter on the determination on the modulus of elasticity for the wedge splitting test.

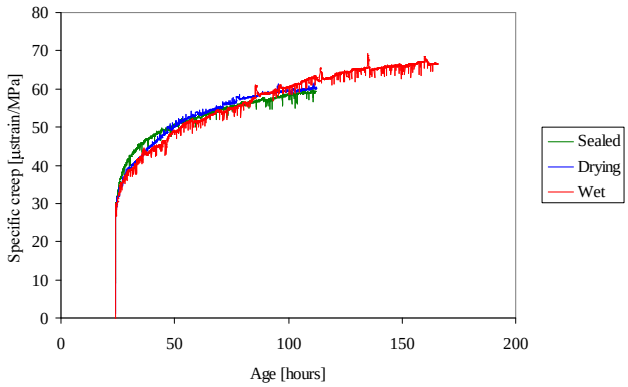

Figure 6.26 *Early age bulk creep for Mix I loaded at 1 day and subjected to different curing conditions.*

6.5.2 Development of Crack Creep Properties

The crack creep properties have been investigated in the long-term setup, which was described in Section 5.4. This section primarily aims at presenting the experimental

results and it is left for future work to implement the various theories for time-dependency of crack growth described in Chapter 4. This section primarily deals with the influence of the bulk creep on the results. This is due to the fact that it was discovered that this influence is dominating the behavior.
The loading levels for the long term experiments were estimated using the stress-crack opening relationships derived from the short term experiments, see Section 5.3. The load was selected such that the specimen was cracked, but still on the ascending branch of the load-crack mouth opening curve. A crack depth corresponding to half the crack depth at peak load of the short term experiment at the current age was selected. This in general corresponded to a load level equal to 80-90% of the peak load. Only Mix I is investigated. The repeatability of the setup was demonstrated in (Østergaard, Stang & Olesen 2002*b*).

Influence of Bulk Creep on the Crack Creep Results

The influence of creep in the bulk concrete on the total creep response obtained in the long-term setup has been evaluated utilizing the results from the previous section implemented in a finite element model of the wedge splitting specimen. The mesh applied in the finite element model is the same as previously employed, see Figure 5.33. However, the description of the crack is omitted, thereby assuring that only the deformations arising from the bulk of the specimen is modelled.

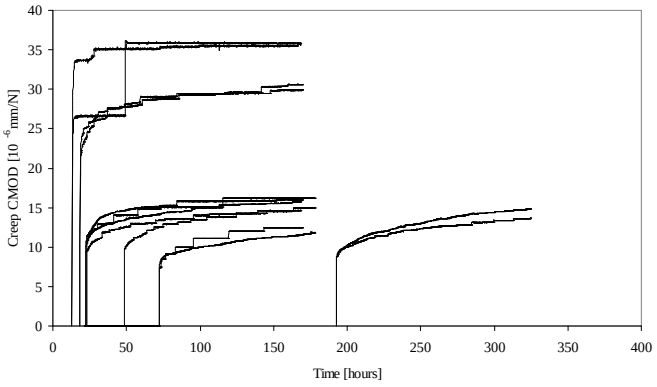

Figure 6.27 *Experimental results obtained by various ages of load application, 13, 17, 22, 48, 72 and 168 hours.*

Figure 6.27 show the experimental results obtained by application of the load at different ages. The y-axis is calculated by dividing the measured CMOD by the split load imposed on the specimen and multiplying by 10^6. Thus, the y-axis is a specific creep CMOD. It is seen on the figure that the specific creep CMOD is highest for the sample loaded at 13 hours, while the ageing results in a decrease in the time-dependent deformations. This behavior is probable since the creep of bulk concrete follows the same trend. Note that the rate of the creep of CMOD for the sample loaded at 13 hours very rapidly reaches zero. Thus, in this sample neither bulk creep or crack creep is measurable and it is therefore justified to assume that the fast development of the properties of this sample means that

the small load imposed at 13 hours rapidly becomes insignificant. It is also noted that the deformations measured in the experiments are small.

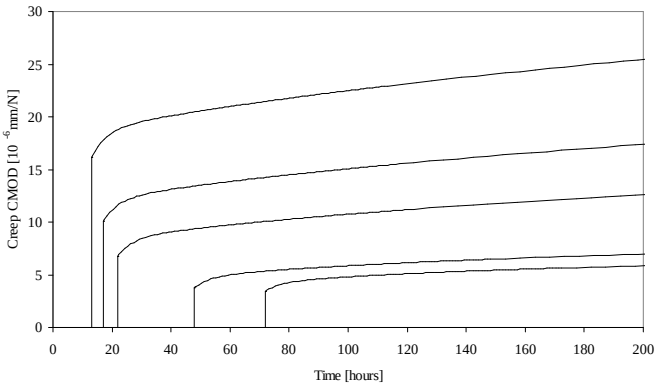

Figure 6.28 *Predicted magnitude of the bulk creep in the long-term setup.*

The influence of the bulk creep on the measurements are estimated by the finite element model as mentioned earlier. The results from these investigations are shown in Figure 6.28. These creep curves are obtained by use of the ageing Kelvin chain, which was calibrated in the section dealing with the bulk creep of the concrete mix. A behavior similar to the experimental findings in Figure 6.27 is seen, however, with the important difference that the initial deformations are different. The difference is clear in Figure 6.29, where the results are depicted together.

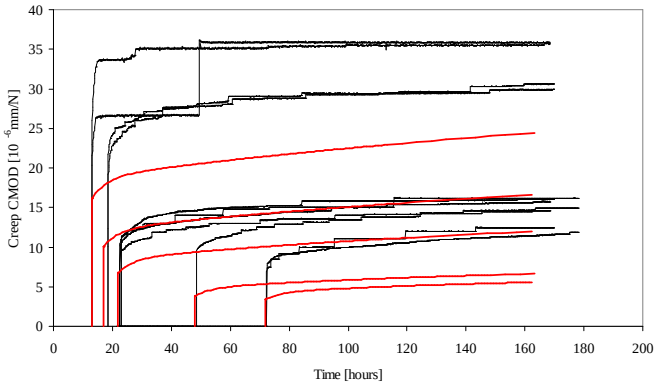

Figure 6.29 *The difference between the bulk creep and the experimental creep curves is primarily due to the initial higher opening in the experiment.*

It is important that the crack is omitted in the finite element results. These results do only capture the bulk creep. It is therefore surprising that the rate of creep in both the finite element results and in the experimental results seems to be the same. This is very clear in Figure 6.30 where the initial difference in deformation has been corrected. This initial difference is caused by the formation of a crack in the experiment, and may be

subtracted to facilitate a comparison between the results.

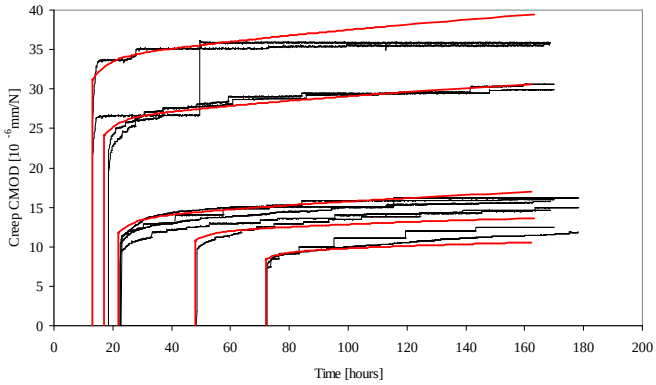

Figure 6.30 *Correcting the initial opening, which is due to the formation of a crack in the experiment shows that the curves are essentially the same.*

This may indicate that the crack is not growing or that the rate effect is insignificant. In fact, a possible explanation is that the ageing of the concrete means that the failure envelope expressed as the stress-crack opening relationship moves away from the actual stress state and thus that the stress state is more and more on the safe side and away from causing any failure or crack growth of the specimen.

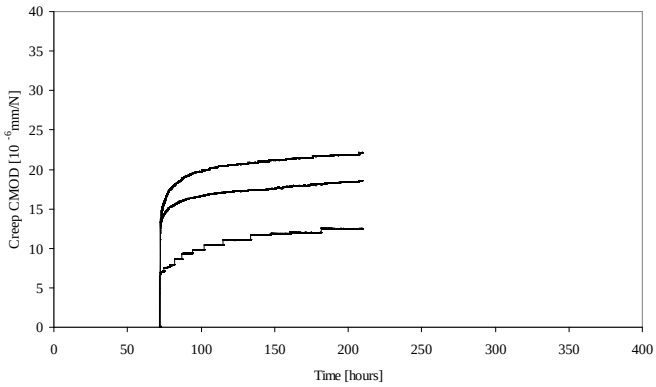

Figure 6.31 *Different load levels result in different initial openings, but the creep curves are essentially the same.*

Higher load levels were tried in order to induce failure or visible creep crack growth on the results. The results from this investigation are shown in Figure 6.31 where the lower curve correspond to the load level preferred earlier, i.e. a crack extension of 50 % of the extension at peak load. The upper curve is loaded to a load level corresponding to 95 % of the crack extension at peak load, while the intermediate curve is loaded to 65 % Again, a different initial deformation is seen, but the rate of deformation at later ages is the same, regardless of load level. No failure occurred for the specimen with the highest loading.

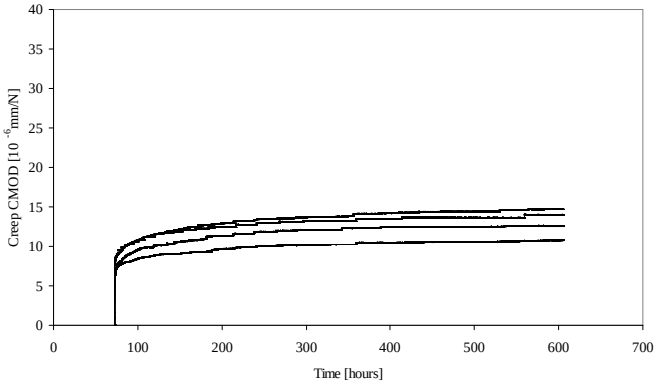

Figure 6.32 *These experiments were continued for three months (only the first month is shown), but no failure was observed.*

Other strategies were tried in order to see if failure or any measurable crack growth could be induced. Figure 6.32 shows the results from experiments which were conducted over an extended time period. The first month is shown in the figure, but the experiment was continued over three months. As the figure demonstrates, nothing interesting occurs during the testing period displayed. This was the case for the entire test duration.

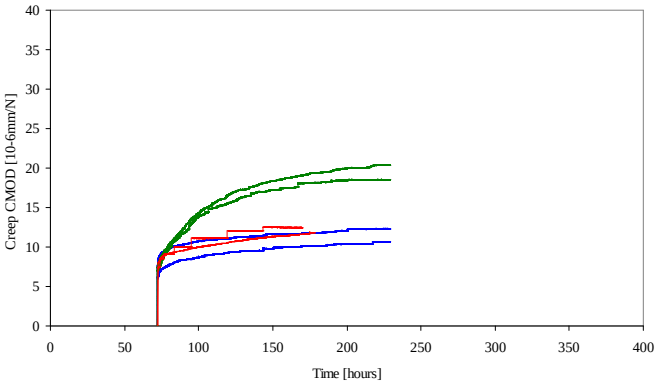

Figure 6.33 *Different curing conditions results in different magnitudes of creep, which is well established knowledge regarding creep of concrete (green=drying, red=sealed, blue=wet).*

Finally, Figure 6.33 shows the influence of the curing conditions. Different curing conditions were obtained by either filling the aluminium foil bag with water (water curing), or by removing it (drying in the lab RH (40 %)). The influence of curing conditions is most clearly seen on the drying samples, which in accordance with literature, show an increased magnitude and rate of creep. It is on the other hand difficult to see a difference between the sealed and the wet samples.

The investigations conducted in this section seems to indicate that the setup developed cannot be utilized for determination of the creep crack opening for early age concrete. This is due to the fact that no significant crack creep opening was measured. However,

another explanation may be that the time-dependent crack deformations, or crack rate effects, in early age concrete are insignificant. Perhaps the only important mechanism is the short term stress-crack opening relationship, and thus cracking is initiated only if the stress state violates the limitations imposed by this property at any age. Anyhow, if the rate effect for early age concrete was to be determined by conducting short-term experiments at different loading rates, say 10^{-3}-10^{2} mm/min, the ageing of the specimen *during* the experiment has to considered, which complicates the experiment and the interpretation significantly. A rate effect does of course exist, but it may be unimportant in early age concrete.

Chapter 7

Bond Between Reinforcement and Concrete

Traditional experiments of pull-out of reinforcing bars imbedded in concrete have been the subject of a large number of publications, see e.g. the extensive state-of-art report published by Féderation Internationale du Béton, (CEB-FIP 2000). The experiment is in principal conducted by establishing tension in the reinforcement while restraining the concrete. This situation is achieved by a number of different methods in the literature. The main objectives have been to determine the load carrying capacity of the connection under given circumstances along with the magnitude of the end slip between the reinforcement and the concrete as a function of the load transfer.

The pull-out experiments give results which mainly are useful in the design situation for mature concrete in the situation, where the structure is subjected to the calculated ultimate load, and where the deformations are large. The situation is different in the early age of concrete hardening since typically no mechanical loading will be present. Instead, only small scale deformations develop from temperature gradients, drying and autogenous shrinkage. An experimental setup, which simulates this situation is the specimen known as the tension stiffening rod, which has been adopted in this work.

Loading the tension stiffening rod using mature concrete results in complex cracking patterns as shown in Figure 7.1. The initial elastic stage shown in Figure 7.1a is followed by conical transverse and plane-vertical cracking as shown in Figure 7.1b. This cracking process is usually seen for deformed bars in which the ribs introduce large compressive stresses in the concrete combined with large tensile stresses at the tips of the lugs, (Goto 2001), (Tepfers 1973). Another result of the stresses is that ring or hoop stresses in the surrounding concrete will build up. Different stages will follow this situation, depending on the maximum possible confinement pressure which the concrete embedment may exert on the reinforcement. If the concrete is well confined, it will be able to carry the ring stresses, and the final failure will be a crushing of the concrete in the vicinity of the ribs of the reinforcement (Figure 7.1d). On the other hand, if the concrete cannot withstand the ring stresses, a through-splitting of the embedment will occur as shown in Figure 7.1c, see e.g. Goto (2001), Tepfers (1979), Noghabai (1995).

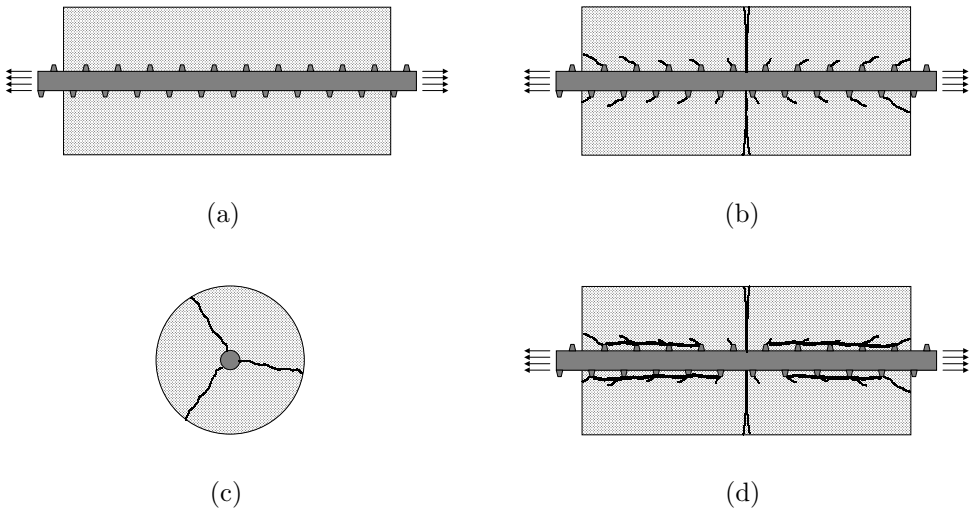

Figure 7.1 *Pull-out of reinforcement in concrete. Elastic stage (a), followed by primary (plane-vertical) and secondary (conical transverse) cracking (b). Finally, either a splitting of the concrete embedment(c) or a crushing of the concrete in front of the ribs of the reinforcing bar (d) may take place. Inspired by Noghabai (1995).*

The average shear stress along the interface versus the local slip, measured as the displacement discontinuity between a reference point on the concrete embedment and a point on the reinforcement bar being pulled out, are often used to interpret experimental results, see e.g. Rehm (1965), Tepfers & Olsson (1992), Noghabai (1995) and Magnusson (1997). This, however, is merely a means of representing the structural behavior of the reinforcement in the experiment rather than deriving a constitutive law governing the behavior of the interface, (CEB-FIP 2000, Page 7, 74). The introduction of a more fundamental shear-slip relationship is therefore justified.

The local shear-slip relationship has been modelled by various expressions in literature (CEB-FIP 2000). In Eligehausen, Popov & Bertero (1982) a trilinear function describing the cracked phases preceded by a nonlinear function accounting for the initial elastic phase and the first cracking was implemented for macroscopically well confined concrete, i.e. where the concrete does not undergo through-splitting.

Finite element modelling of the bond problem has also been given much attention in the literature. The models have been either full three dimensional or axisymmetric. The cracking has been modelled by different approaches including e.g. smeared cracking (Rots 1990), discrete cracking (Yao & Murray 1995) and element embedded cracks (Noghabai 1995). Also contact elements have been applied (Ichinose & Hayashi 1998). In Ichinose & Hayashi (1998), the constitutive behavior of the interface bond between two contiguous ribs was modelled using the Mohr-Coulomb failure envelope with and without dilatancy.

Bond of reinforcement in early age concrete is a problem not very well investigated. Development of the strength of bond for concrete at early ages has been investigated in Sule & van Breugel (2001). The experiments comprised pull-out tests at 8 hours, 24 hours, 31 hours and 28 days and the average shear end slip was measured. It was reported that no significant bond strength had developed at 8 hours. At an age of 24 hours significant bond properties had developed with an average shear stress of 14 MPa for an end slip of 0.1 mm and 23 MPa for an end slip corresponding to 1.0 mm. At 28 days the shear stress transfer at 0.1 mm had increased to 22 MPa.

The aim of the present paper is to introduce a constitutive modelling of the interface representing the bond properties between concrete and reinforcement. A shear-slip type constitutive relationship formulated as the shear transfer at any point along the reinforcement bar as a function of the relative slip at the same point will be introduced and applied both in an analytical model as well as in a finite element model. The model will be justified by analyzing the more complex case where a modified Mohr-Coulomb failure envelope is used to model the interface properties. Furthermore, in the Mohr-Coulomb case, the influence of the magnitude of the confinement pressure will be investigated.

Finally, an experimental setup which is suited for testing bond properties in concrete at early ages will be introduced. This setup features a self weight eliminating arrangement as well as a system to apply a well defined hydrostatic confinement pressure on the specimen. Also a few preliminary experimental results will be discussed.

The investigations will be focused on the behavior in the range of small deformations (local slips typically less than 0.1 mm) since this case is of principal interest for the early age situations due to the relevant loading cases in early age, which include volume changes and temperature gradients. This will be further explained in the following section.

7.1 Modelling of the Concrete-Reinforcement Interface

As already touched upon in the previous section, the loading of the reinforcement-concrete bond at early ages differs from the loading at later ages for a number of reasons. The primary reason is the scale of the deformations. The problem of interest with regard to mature concrete is often the ultimate limit state where a reinforcement bar is pulled out of the concrete. The results from such investigations are used in structural calculations e.g. for determining anchorage length. However, for early age concrete the problem at hand is different. Here, the loading will be intrinsic in nature, arising from temperature gradients and volumetric deformations due to hydration. This type of loading will result in small displacement discontinuities between the reinforcement and the concrete. Thus, the interesting properties of the interface are not obtained by a traditional pull-out experiment. Instead, it is suggested that the tension stiffening rod shown in Figure 7.1 is used.

Two alternatives for describing the constitutive relationship at the concrete-reinforcement interface will be discussed.

7.1.1 Modified Mohr-Coulomb Type Constitutive Condition

The primary constitutive law adopted in the analysis is the modified Mohr-Coulomb friction model. It is assumed that the interface behavior between concrete and reinforcement, regardless of the presence of ribs is governed by frictional behavior on the macro scale. The Coulomb friction model is outlined in Figure 7.2. The assumption is easily justified for plain bars without ribs, (CEB-FIP 2000). The concept is assumed also to be applicable for ribbed reinforcement, but only on a macro scale, and recognizing the fact that the constitutive parameters will be influenced by the geometry of the ribs, thus introducing a structural effect in the constitutive parameters.

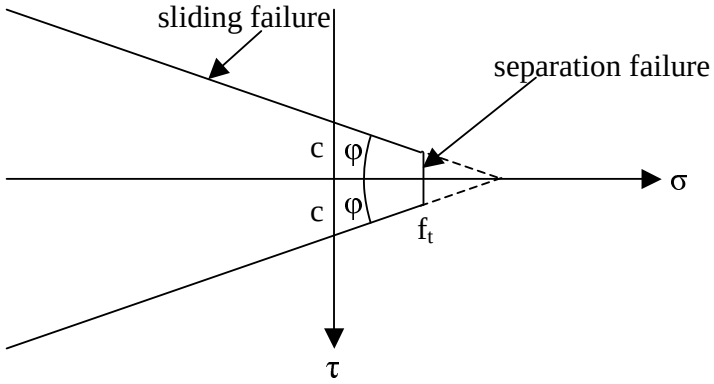

Figure 7.2 *Coulomb friction model with tension cut-off*

Typically normal stresses larger than the tensile strength is not allowed on the interface leading to introduction of the so-called tension cut-off as shown in Figure 7.2. The parameter c in Figure 7.2 is interpreted as the chemical adhesion between the bar and the concrete, while φ is the angle of friction. A modified version of the Mohr-Coulomb condition considers also the dilatation that will occur in interface during slipping. This is done by specifying the dilatation angle, ψ, and thus, the modified Coulomb friction model reads:

$$g = \sqrt{\tau^2} + \sigma \tan\psi \tag{7.1}$$

$$f = \sqrt{\tau^2} + \sigma \tan\varphi - c = 0 \tag{7.2}$$

$$\sigma \leq f_t \tag{7.3}$$

where Equation 7.1 describes the plastic potential surface from which the dilatation is determined. Equation 7.2 represents the sliding failure, while Equation 7.3 is the criterion for tension cut-off or separation failure.

The degradation, or softening, of the interface properties as function of the slip deformation, δ, between the concrete and the reinforcement should also be taken into account. Even though it is obvious that degradation takes place, quantification of the degradation is more troublesome. While the adhesion, c, is assumed to degrade rapidly and reach zero already for small openings ($c \approx 0$ for $\delta \ll 1$ mm), it is reasonable to assume that the degradation of friction will occur only slowly (φ =small for $\delta \gg 1$ mm) and presumably never reach zero.

By incorporating degradation of the Mohr-Coulomb parameters, the problem at hand will be fracture mechanical in nature, since they degrade over a certain characteristic length. Furthermore, the degradation functions of c, $c(\delta)$, and φ, $\varphi(\delta)$ will be material properties unique for the concrete and the surface properties of the reinforcement in question. The dilatation angle, ψ, is assumed to be constant, and dependent on rib geometry. For simplicity, the degradation functions $c(\delta)$ and $\varphi(\delta)$ are assumed to be linear, see Figure 7.3.

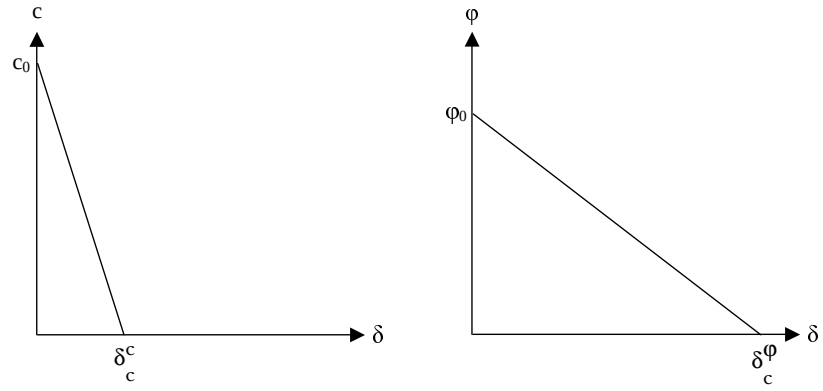

Figure 7.3 *Degradation functions of τ and φ as functions of δ*

Besides assessing the characteristics of the interface in the cracked state, an assessment of the elastic properties for the interface layer must be carried out. These parameters take the elastic properties of the interface region near the crack into consideration. It will be left to the parameter investigation to show the result of different choices since the knowledge of physical meaningful values is limited. These parameters should be determined from calibration with experiments. Finally, the tensile strength of the interface must be estimated. Knowledge of this parameter is limited, but it seems reasonable to assume that the value will be lower than the tensile strength of the bulk concrete.

7.1.2 Shear-Slip Type Constitutive Condition

Using the Mohr-Coulomb condition may be cumbersome under some circumstances, for instance in an analytical model. It is therefore relevant to try to simplify the relation without loss of generality or applicability. This can be achieved by application of an approach similar to the global shear-slip relationships often used in literature. However, here

a local shear-slip relationship is adopted since such a relationship is more fundamental in nature.

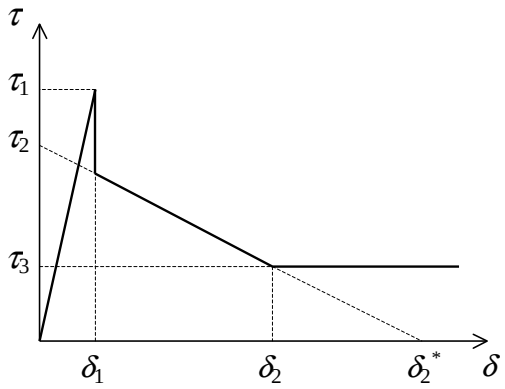

Figure 7.4 *Definition of bond-slip ($\tau - \delta$) relationship.*

Figure 7.4 shows the idealized bond-slip relation applied here. It is a trilinear curve allowing for a drop of friction at the end of the first linear part while it ends with a constant level of friction at a certain displacement discontinuity. This relationship is applied in the analytical model, as shown in the next section.

7.1.3 Tri-linear analytical model using shear-slip condition

Consider a cylindrical reinforcement bar with the diameter d_s embedded concentrically in a cylindrical concrete specimen with the diameter d_c. The length of the concrete cylinder is $2L$ and, in practice, the reinforcement bar extends beyond the concrete at both ends. Only half the specimen is modelled as shown in Figure 7.5, where the extending end of the bar is not shown. The results presented here are based on the work by Olesen (2002).

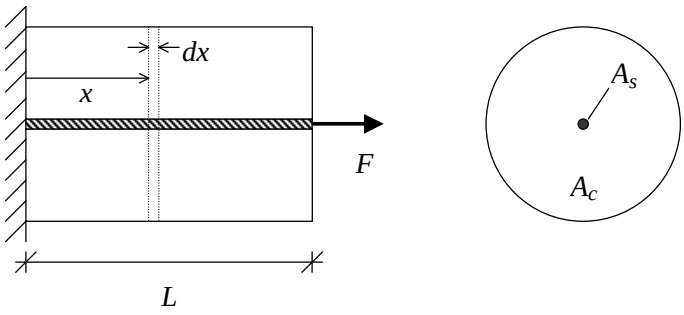

Figure 7.5 *Model of half the test specimen.*

In Figure 7.5 an x-axis is defined and an incremental slice of the specimen is also illustrated. Figure 7.6 shows this incremental part with an indication of the deformation functions $u_c(x)$ for the concrete and $u_s(x)$ for the reinforcement, respectively. The state of deformation is assumed to be plane in both materials, thus suppressing any shear deformation. Figure 7.6 also shows the stresses assumed to act on each incremental part of the compound specimen.

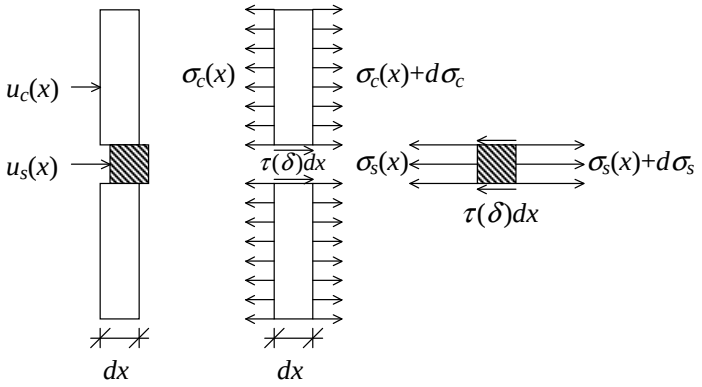

Figure 7.6 *Incremental slice of specimen. Definition of deformations (a), stresses on concrete part (b), stresses on reinforcement part (c).*

The interaction in terms of shear stresses τ between concrete and reinforcement bar is modelled as a bond-slip relationship, where the slip δ is defined as the difference between the reinforcement deformation and the concrete deformation:

$$\delta(x) = u_s(x) - u_c(x) \tag{7.4}$$

Figure 7.4 shows the idealized bond-slip relation applied here. It is a trilinear curve allowing for a drop of friction at the end of the first linear part; the definition is given by:

$$\tau(\delta) = \begin{cases} E_1\delta & 0 \le \delta \le \delta_1 = \dfrac{\tau_1}{E_1} \\ \tau_2 - E_2\delta & \delta_1 < \delta \le \delta_2 = \dfrac{\tau_2 - \tau_3}{E_2} \\ \tau_3 & \delta_2 < \delta \end{cases} \tag{7.5}$$

Note that E_1 and E_2 are positive constants giving the inclination of the sloping parts of the curve, and that the drop in τ at δ_1 is eliminated if $\tau_2 = \tau_1 + E_2\delta_1$.

The total equilibrium of the incremental slice shown in Figure 7.6 yields the condition

$$A_c\frac{d\sigma_c}{dx} + A_s\frac{d\sigma_s}{dx} = 0 \tag{7.6}$$

where A_c and A_s are the cross-sectional areas of the concrete and reinforcement, respectively, as shown in Figure 7.5, and σ_c and σ_s are the uniaxial stresses in the concrete and reinforcement, respectively, as shown in Figure 7.6. Equilibrium of the incremental part of the reinforcement bar is ensured by the condition

$$\frac{d\sigma_s}{dx} = \frac{4}{d_s}\tau(\delta(x)) \tag{7.7}$$

The slip between materials is defined in Equation 7.4. Taking the second derivative of δ and applying a linear strain definition together with the assumption of linear elastic bulk materials, we may derive the following relationship

$$\frac{d^2\delta}{dx^2} = \frac{1}{E_s}\frac{d\sigma_s}{dx} - \frac{1}{E_c}\frac{d\sigma_c}{dx} \tag{7.8}$$

Combining Equations 7.6, 7.7 and 7.8 we arrive at the following second order differential equation governing the variation of the slip

$$\frac{d^2\delta}{dx^2} - k\tau(\delta) = 0 \qquad \text{where} \qquad k = \frac{4(1+n\rho)}{E_s d_s} \tag{7.9}$$

Here we have introduced the stiffness ratio $n = E_s/E_c$ and the area ratio $\rho = A_s/A_c$.
As long as the load is so small that the slip does not exceed δ_1 at any point the behavior is governed by the initial elastic part of the $\tau - \delta$ relationship. We say that we are in Phase 1, and the differential equation takes the form

$$\frac{d^2\delta}{dx^2} - kE_1\delta = 0 \qquad \wedge \qquad 0 \le \delta \le \delta_1 \tag{7.10}$$

The boundary conditions are

$$\delta(0) = 0 \qquad \wedge \qquad \left.\frac{d\delta}{dx}\right|_{x=L} = \frac{F}{E_s A_s} \tag{7.11}$$

The solution to (7.10) and (7.11) may be written as

$$\frac{\delta(x)}{L} = \frac{F}{E_s A_s}\,\frac{\sinh(\lambda_1 x)}{\lambda_1 L\cosh(\lambda_1 L)} \tag{7.12}$$

where the parameter $\lambda_1 = \sqrt{kE_s}$ has been introduced. Phase 1 is limited by the condition $\delta(L) \leq \delta_1$, which is equivalent to the load limit condition

$$F \leq F_1 = E_s A_s \, \lambda_1 \delta_1 \coth(\lambda_1 L) \tag{7.13}$$

When the load exceeds F_1 the descending part of the $\tau - \delta$ relationship is invoked and we enter into what is called Phase 2. This phase is characterized by $\delta_1 < \delta(L) \leq \delta_2$. The slip behavior is now governed by two different differential equations, one for the left part ($0 \leq x < L_1$) of the specimen model and one for the right ($L_1 \leq x < L$). A new axis is introduced by $x_{\mathrm{II}} = x - L_1$ and the old axis is renamed such that $x_{\mathrm{I}} = x$. The slip in the two parts of the specimen are denoted $\delta_{\mathrm{I}}(x_{\mathrm{I}})$ and $\delta_{\mathrm{II}}(x_{\mathrm{II}})$, respectively. The differential equation governing δ_{I} is similar to Equation (7.10) and the general solution may be written as

$$\delta_{\mathrm{I}}(x_{\mathrm{I}}) = c_1 \sinh(\lambda_1 x_{\mathrm{I}}) + c_2 \cosh(\lambda_1 x_{\mathrm{I}}) \tag{7.14}$$

where c_1 and c_2 are constants to be determined from boundary and continuity conditions. Combining (7.5b) and (7.9) we derive the differential equation governing δ_{II}:

$$\frac{d^2 \delta_{\mathrm{II}}}{dx_{\mathrm{II}}^2} + kE_2 \delta_{\mathrm{II}} = k\tau_2 \qquad \wedge \qquad \delta_1 \leq \delta_{\mathrm{II}} \leq \delta_2 \tag{7.15}$$

The general solution to this equation may be written as

$$\delta_{\mathrm{II}}(x_{\mathrm{II}}) = c_3 \sin(\lambda_2 x_{\mathrm{II}}) + c_4 \cos(\lambda_2 x_{\mathrm{II}}) + \delta_2^* \tag{7.16}$$

where $\delta_2^* = \tau_2 / E_2$, and c_3 and c_4 are to be determined from boundary and continuity conditions. The boundary conditions are

$$\delta_{\mathrm{I}}(0) = 0 \qquad \wedge \qquad \left. \frac{d\delta_{\mathrm{II}}}{dx_{\mathrm{II}}} \right|_{x_{\mathrm{II}} = L_2} = \frac{F}{E_s A_s} \tag{7.17}$$

and the continuity conditions are

$$\delta_{\mathrm{I}}(L_1) = \delta_{\mathrm{II}}(0) = \delta_1 \qquad \wedge \qquad \left.\frac{d\delta_{\mathrm{I}}}{dx_{\mathrm{I}}}\right|_{x_{\mathrm{I}}=L_1} = \left.\frac{d\delta_{\mathrm{II}}}{dx_{\mathrm{II}}}\right|_{x_{\mathrm{II}}=0} \tag{7.18}$$

The solution to Phase 2, (7.14) and (7.16), may now be expressed in terms of the integration constants:

$$c_1 = \frac{\delta_1}{\sinh(\lambda_1 L_1)} \qquad c_2 = 0 \qquad c_3 = \delta_1 \frac{\lambda_1}{\lambda_2} \coth(\lambda_1 L_1) \qquad c_4 = -(\delta_2^* - \delta_1) \tag{7.19}$$

This solution assumes knowledge about the magnitude of L_1 and L_2, which are related through $L = L_1 + L_2$. In principle L_1 or L_2 is established by (7.17b), which reads

$$F = E_s A_s \left[\delta_1 \lambda_1 \coth(\lambda_1 L_1) \cos(\lambda_2 L_2) + (\delta_2^* - \delta_1)\lambda_2 \sin(\lambda_2 L_2)\right] \tag{7.20}$$

However, since our aim is to establish a relationship between the load F and the slip at the end of the specimen $\delta(L)$ it is not necessary to solve (7.20). Instead we choose L_2 as the independent variable and calculate $L_1 = L - L_2$ and $F(L_2)$ from (7.20) and $\delta(L)$ from

$$\delta(L) = \delta_{\mathrm{II}}(L_2) = \delta_1 \frac{\lambda_1}{\lambda_2} \coth(\lambda_1 L_1) \sin(\lambda_2 L_2) - (\delta_2^* - \delta_1) \cos(\lambda_2 L_2) \tag{7.21}$$

This Phase 2-solution is limited by $\delta_1 \leq \delta_{\mathrm{II}} \leq \delta_2$, and from the upper limit we may derive the following condition

$$\delta_1 \frac{\lambda_1}{\lambda_2} \coth(\lambda_1 L_1) \sin(\lambda_2 L_2) - (\delta_2^* - \delta_1) \cos(\lambda_2 L_2) + (\delta_2^* - \delta_2) = 0 \tag{7.22}$$

from which the upper limit on L_2 may be established by iteration. At the end of Phase 2 a new phase commences; in this Phase 3 $\delta(L) > \delta_2$ and the slip behavior is now governed by three different differential equations, one for small values of δ, Equation (7.10), one for medium values, Equation (7.15), and one for large values of δ:

$$\frac{d^2\delta_{\mathrm{III}}}{dx_{\mathrm{III}}^2} = k\tau_3 \qquad \wedge \qquad \delta_2 \leq \delta_{\mathrm{III}} \tag{7.23}$$

Here we have introduced a third axis by $x_{\mathrm{III}} = x - L_2$. The three parts of the model constitute the whole model, thus the first part is given by $0 \leq x_{\mathrm{I}} \leq L_1$, the second by $0 \leq x_{\mathrm{II}} \leq L_2$ and the third by $0 \leq x_{\mathrm{III}} \leq L_3$, and $L = L_1 + L_2 + L_3$. The general solutions (7.14) and (7.16) still apply, and from (7.23) the following general solution for δ_{III} is derived

$$\delta_{\mathrm{III}}(x_{\mathrm{III}}) = \frac{1}{2} k \tau_3 x_{\mathrm{III}}^2 + c_5 x_{\mathrm{III}} + c_6 \tag{7.24}$$

For Phase 3 the boundary conditions are

$$\delta_{\mathrm{I}}(0) = 0 \qquad \wedge \qquad \left.\frac{d\delta_{\mathrm{III}}}{dx_{\mathrm{III}}}\right|_{x_{\mathrm{III}}=L_3} = \frac{F}{E_s A_s} \tag{7.25}$$

and the continuity conditions are the ones given in (7.18) together with the following

$$\delta_{\mathrm{II}}(L_2) = \delta_{\mathrm{III}}(0) = \delta_2 \qquad \wedge \qquad \left.\frac{d\delta_{\mathrm{II}}}{dx_{\mathrm{II}}}\right|_{x_{\mathrm{II}}=L_2} = \left.\frac{d\delta_{\mathrm{III}}}{dx_{\mathrm{III}}}\right|_{x_{\mathrm{III}}=0} \tag{7.26}$$

The solution to Phase 3, (7.14), (7.16) and (7.24), in terms of the integration constants is given by (7.19) together with

$$c_5 = \frac{F}{E_s A_s} - k \tau_3 L_3 \qquad c_6 = \delta_2 \tag{7.27}$$

Now we choose L_3 as the independent variable and may determine L_1 or L_2 from the condition $\delta_{\mathrm{II}}(L_2) = \delta_2$, which may be written in either of the following two forms

$$L_2 = \frac{1}{\lambda_2} \arctan\left((\delta_2^* - \delta_1) \left[\delta_1 \frac{\lambda_1}{\lambda_2} \coth(\lambda_1 L_1) + \frac{\delta_2^* - \delta_2}{\sin(\lambda_2 L_2)} \right]^{-1} \right) \tag{7.28}$$

$$L_1 = \frac{1}{\lambda_1} \tanh^{-1}\left(\delta_1 \frac{\lambda_1}{\lambda_2} \left[(\delta_2^* - \delta_1) \cot(\lambda_2 L_2) - \frac{\delta_2^* - \delta_2}{\sin(\lambda_2 L_2)} \right]^{-1} \right) \tag{7.29}$$

Either of these equations may be solved iteratively, however, for small values of L_3 (7.28) should be applied for determining L_2, whereas (7.29) should be applied for determining

L_1 for larger values of L_3. The solution strategy for Phase 3 is to increase L_3 in steps from zero, then at each step determine L_2 (or L_1) by iteration ensuring that $L = L_1 + L_2 + L_3$. The iteration may be performed by calculating a new estimate for L_2 or L_1 by evaluating the right hand side of (7.28) or (7.29), respectively, based on the previous estimate.
We may now express the solution to Phase 3 as a function of (L_3) in terms of the load F and the slip at the end of the specimen $\delta(L)$:

$$F = E_s A_s \left[k\tau_3 L_3 + \delta_1 \lambda_1 \coth(\lambda_1 L_1)\cos(\lambda_2 L_2) + (\delta_2^* - \delta_1)\lambda_2 \sin(\lambda_2 L_2)\right] \tag{7.30}$$

$$\delta(L) = \delta_{\mathrm{III}}(L_3) = \frac{F}{E_s A_s} L_3 - \tfrac{1}{2} k\tau_3 L_3^2 + \delta_2 \tag{7.31}$$

For large values of L_3 the solution will approach the straight line asymptote given by

$$F = E_s A_s \frac{\delta}{L} + \tfrac{1}{2}\tau\pi d_s L(n\rho + 1) \tag{7.32}$$

which is parallel to the load-elongation curve for the reinforcement bar by itself.

The model has been implemented in MatLab. Figure 7.7 shows the results from a parameter variation where the shear-slip relationship has been varied. It was found convenient to vary τ_1', τ_2' and τ_3', which are the y-axis coordinates for the shear-slip relationship and E_1' and E_2', which are the first and second slope respectively, such that the parameters shown in Figure 7.4 are given by:

$$\begin{aligned} &\tau_1 = \tau_1' \qquad \tau_2 = \tau_2' + \tau_1' \frac{E_2'}{E_1'} \qquad \tau_3 = \tau_3' \\ &\delta_1 = \frac{\tau_1'}{E_1'} \qquad \delta_2 = \frac{\tau_1'}{E_1'} + \frac{\tau_2' - \tau_3'}{E_2'} \end{aligned} \tag{7.33}$$

The variation has been conducted using the following values for the fixed parameters:

$$\begin{aligned} \tau_1' &= 2 \\ \tau_2' &= 2 \\ \tau_3' &= 0.4 \\ E_1' &= 2000 \\ E_2' &= 250 \end{aligned} \tag{7.34}$$

Figure 7.7 clearly shows how changes in τ_1', τ_2' and τ_3' change the stiffening response. The first parameter, τ_1', controls the level for which phase I ends, however, the overall importance of the parameter is weak. The second parameter, τ_2', controls the level for which phase II ends, and phase II may vanish if the parameter is small or equal to τ_3'. The latter shear parameter τ_3' is seen to be very important since it controls the final level of shear transfer between the concrete and reinforcement. This parameter will equal zero if splitting occurs. However, if the concrete cover is well confined, then this parameter may attain high values which is attractive.

The first and second slopes of the shear-slip relationship are seen to have very different influence on the tension stiffening response, see Figure 7.7d-e. The first parameter is insignificant on the shape of the curve, while the second one increases the intermediate load level and prolongs phase II.

It is noteworthy that it seems almost impossible to distinguish between τ_2' and E_2'. This means that different combinations of these parameters may fit an experimental result with equal quality. Finally, it is noted that the influence of the parameters on the global load-end slip curves seem logical and confirms the model.

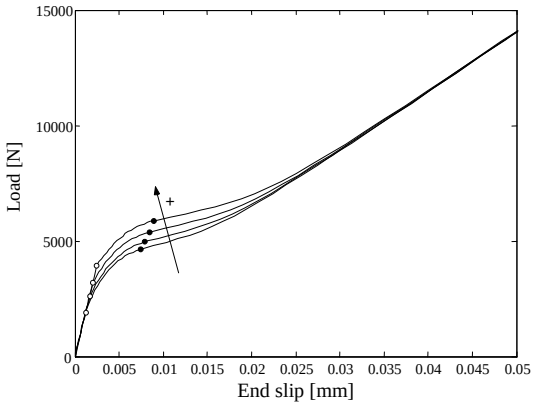

(a) τ_1' (2, 3, 4, 5)

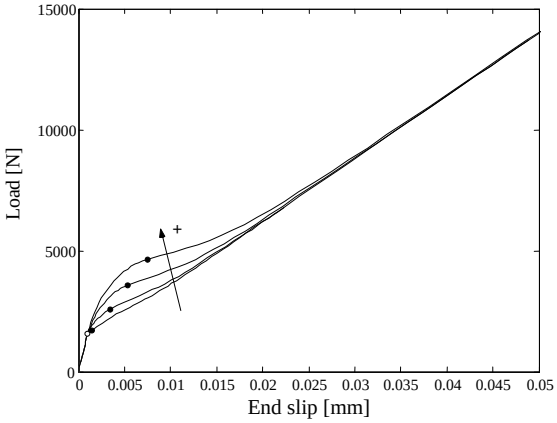

(b) τ_2' (0.5, 1.0, 1.5, 2.0)

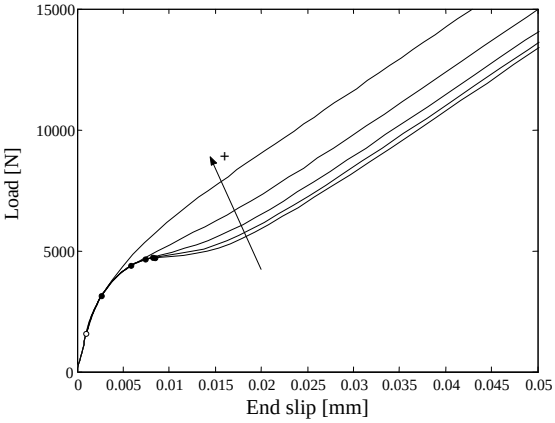

(c) τ_3' (0.1, 0.2, 0.4, 0.8, 1.6)

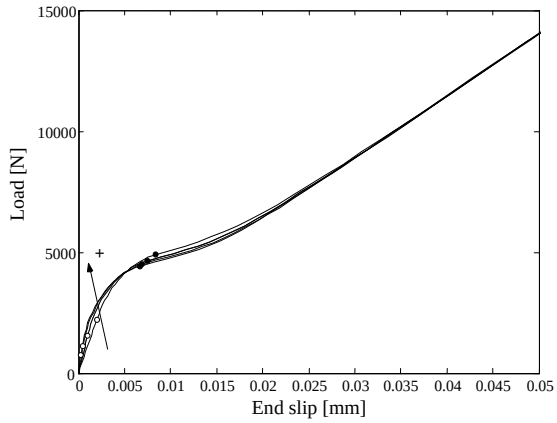

(d) E_1' (1000, 2000, 4000, 8000)

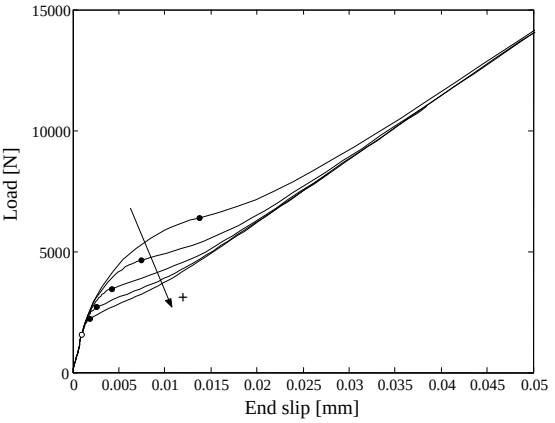

(e) E_2' (125, 250, 500, 1000, 2000)

Figure 7.7 *Shear-slip relationship: Parameter variation using the listed values. The hollow dots mark change from phase 1 to phase 2, while the filled dots mark the change to phase 3.*

7.2 Numerical Modelling

The bond between reinforcement and concrete has been investigated in a finite element model. Figure 7.8 shows the mesh used in the analysis. One quarter of the specimen is modelled and the axisymmetry is exploited. The reinforcement bar is modelled as linear elastic material with a modulus of elasticity of $E = 210$ GPa. The concrete is modelled as a linear elastic material before cracking. Concrete cracking is described using the smeared crack approach allowing for cracks to initiate in all directions (including the ring direction) depending on the maximum principal stress direction. The interface between the concrete and reinforcement is described by the modified Mohr-Coulomb failure criterion discussed earlier.

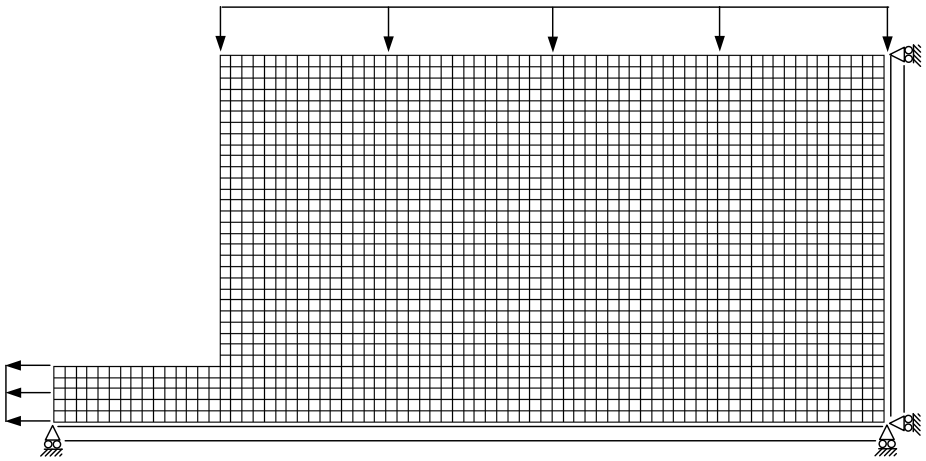

Figure 7.8 *The mesh used in the numerical analysis shown together with the boundary conditions. One quarter of the specimen is modelled.*

The confinement pressure is imposed on the outer boundary of the concrete as shown in the figure. The analysis is carried out by incrementally stepping the load imposed on the end of the reinforcement bar, see Figure 7.8. The stepping is delicate since several cracking mechanisms are interacting. Besides the interface crack which, depending on the material properties, may propagate along the reinforcement bar, also the different crack systems discussed in Figure 7.1 may develop. This results in frequent and necessary restart of the analysis in which the chosen step length and control procedures are changed. The model has been implemented in the DIANA finite element software package.

Figure 7.9 exemplifies the complexity of the problem analyzed.

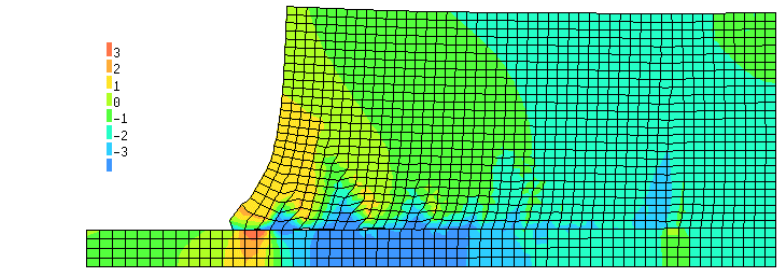

(a) λ=29.5

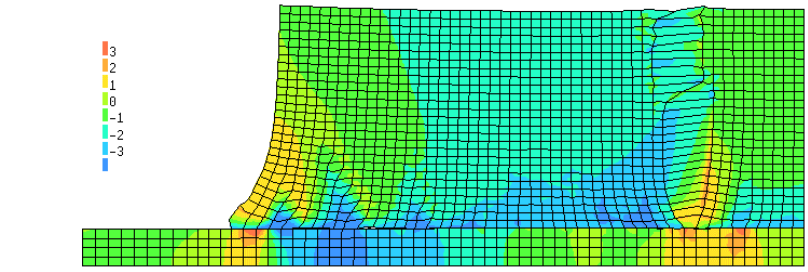

(b) λ=31.8

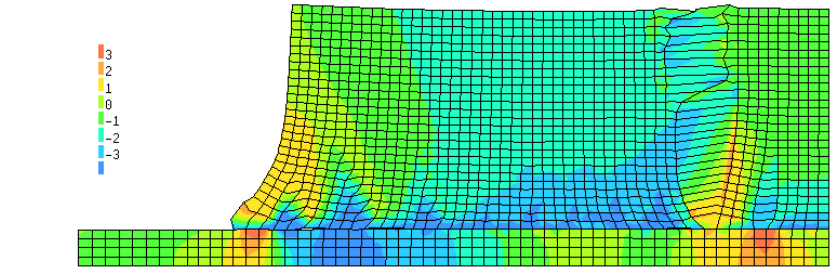

(c) λ=38.2

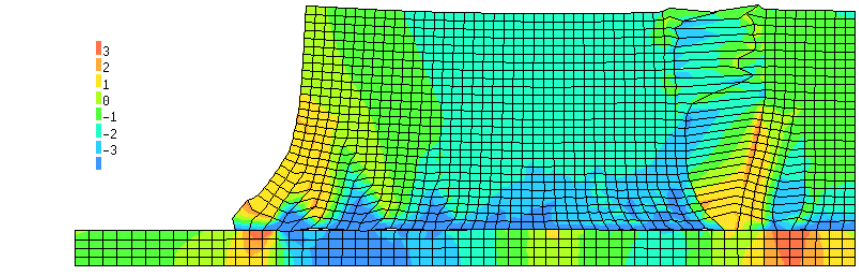

(d) λ=46.5

Figure 7.9 *Examples of deformation and stress plots at varying steps of analysis. Deformations are magnified 500 times. Stresses in the ring direction are shown (σ_{zz})*

The figure shows how the cracking in the concrete localizes. Note also the characteristic conical cracking which occurs around the reinforcement at the loaded end. This pattern is interesting since it is also observed in real experiments, see e.g. Goto (2001). It is also observed in the finite element model by Rots (1990). It thus seems like the model is able to capture the effects associated with pull-out of reinforcement in concrete.

Analysis of the influence of the constitutive parameters has been carried out. Figure 7.10 shows the results. The importance of description of the tensile strength of the interface is investigated in Figure 7.10a. The problem at hand is of course dominated by the sliding failure, but at the very end of the specimen, tensile failure occurs, and the depth of this depends on the interface tensile strength. However, it is seen from Figure 7.10a that this phenomenon is without any importance for the global load-end slip behavior and thus, the modelling may be simplified by using a Mohr-Coulomb failure envelope without tension cut-off.

The dependencies of the cohesion, c, and the confinement pressure, σ_{rr} are investigated in Figures 7.10c and 7.10e. It is seen that an increase in either of these parameters increases the load-end slip curves. This must obviously be so since an increase in the cohesion translates the sliding failure condition away from origin, while the confinement pressure increases compressive normal stress on the surface.

A number of other parameters influences the behavior of the interface region. The two most important ones are the friction angle, φ, and the dilatation angle, ψ. An increase of the friction angle will in general result in a raise of the load-end slip curve after sliding failure occurs. The dilation angle controls the dilation of the interfaces and has thus also influence on the magnitude of the normal stresses on the interface. Thus, if the concrete is well confined, this parameter controls the level of the tail of the load-end slip curves.

The shape of the local shear-slip curves which are shown in Figures 7.10b, d and f is of course a result of the input made with regard to the constitutive parameters of the modified Mohr-Coulomb failure condition. However, it is interesting to see the exact shape of the output since it gives information about the validity of the shear-slip type modelling. This is particularly interesting with regard to the confinement pressure and the dilation. As the figures show, the proposed modelling is capturing the main features of the relationship. The final level of the shear-slip relationship will be controlled by the degree of confinement, which must be assessed if the full modelling is not conducted. The increase in the relationship after the intermediate minimum is caused by the high degree of dilation included in the finite element modelling ($\psi = \varphi = 37°$). This will be much smaller for smooth reinforcement, and a final constant value of the shear-slip relationship will be achieved.

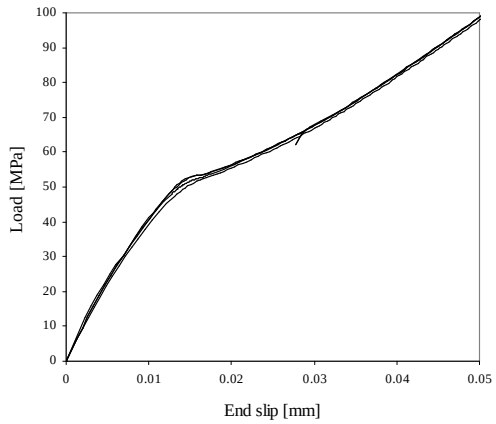

(a) f_t = 0.5, 1, 1.5, 2

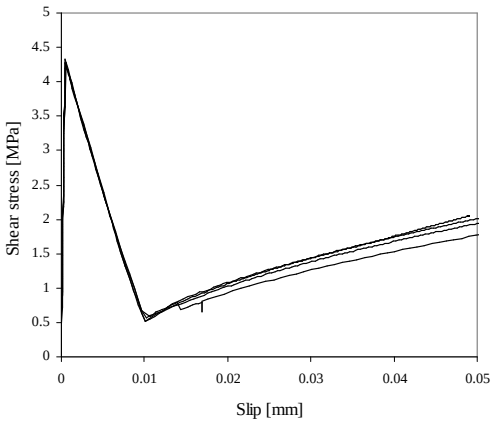

(b) f_t = 0.5, 1, 1.5, 2

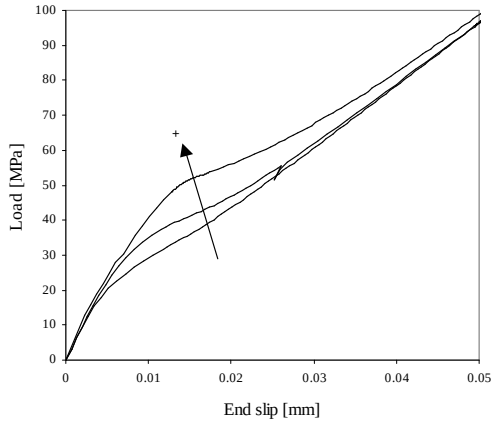

(c) c = 1, 2, 4

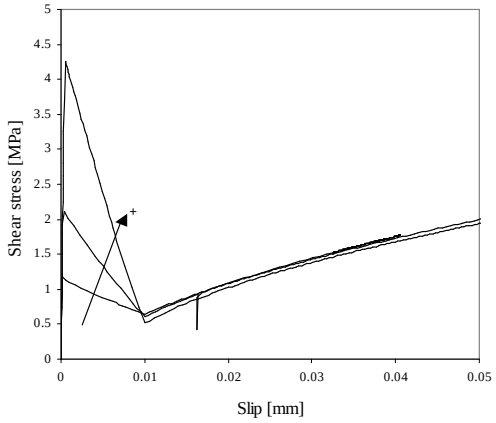

(d) c = 1, 2, 4

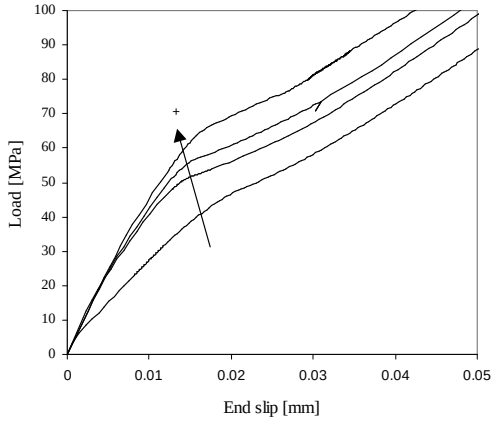

(e) σ_{rr} = 0, 1, 2, 4

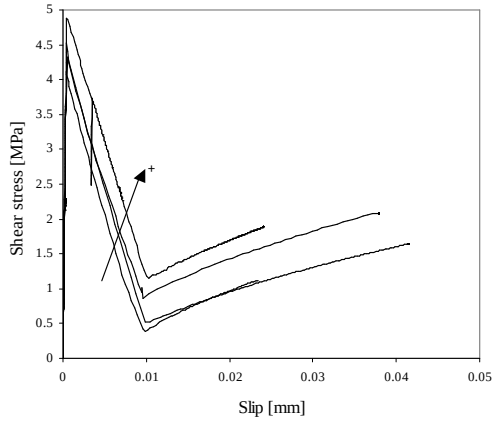

(f) σ_{rr} = 0, 1, 2, 4

Figure 7.10 *Variation of tensile strength of the interface, f_t, cohesion, c and confinement pressure, σ_{rr}, respectively. The figures are paired such that those on the left show the load-end slip curves while those on the right show the local shear-slip relationships*

7.3 Inverse Analysis

An inverse analysis algorithm similar to the one proposed for the wedge splitting test has been written. The code is included in Appendix C. Similar to the WST inverse method also in the bond case a subdivision of the optimization process is made and the then repeated until the parameters determined are not varying.

The first parameter to be optimized for is the initial slope of the stress-crack opening relationship, E_1', which is the only parameter, besides the elastic parameters for the reinforcement and the concrete, governing the behavior of the load-end slip curve. This is thus a one-dimensional optimization problem. Then, it was observed in the preliminary investigation of the problem that all other parameters included in the shear-slip relationship could be optimized for simultaneously without any problems with regard to the finding of local minimums.

The investigation of the presence of any local minimums was conducted employing a model curve generated by the program it self.

Further analysis is recommended with regard to the performance of the algorithm since it has not been possible to verify it on experimental data.

7.4 Development of Experimental Setup

An experimental method for determination of the bond properties between reinforcement and early age concrete was proposed in a recent Master's thesis, Henriksen (2002). The idea is to make an tension stiffening experiment which produces results that are suitable for determination of the bond properties using the proposed model. The experiment should furthermore be able, in general, to produce load-end slip diagrams capturing the minute properties of the bond in early age. Thus, any influence of the self-weight must be eliminated and furthermore, a sensitive measuring system must be established.

Another important issue is the confinement pressure. In traditional pull-out experiments on mature concrete this is established by an external steel ring or by spiral reinforcement. However, such passive confinement starts to function only when the deformations has reached a certain level. This is inadequate for early age concrete where the deformations are anticipated to be small. Thus, as an additional design criterion, active confinement must be applied such that it is active already from the very start of the experiment. Active confinement may be applied by an external pressure. The use of active confinement is very realistic since the young concrete will exert a hydrostatic pressure on the reinforcement. Furthermore, at later ages, gravity and reactions forces will also result in an active confinement.

7.4.1 Application of Confinement Pressure

The confinement pressure is established by an aluminium shell, see Figure 7.11. This aluminium shell is made of four parts which each covers a quarter of the circumference of the specimen. A 10 mm rubber layer is placed between the concrete and the aluminium shell such that an approximately hydrostatic pressure is exerted on the concrete specimen. The validity of the hydrostatic assumption was investigated and confirmed in Henriksen (2002).

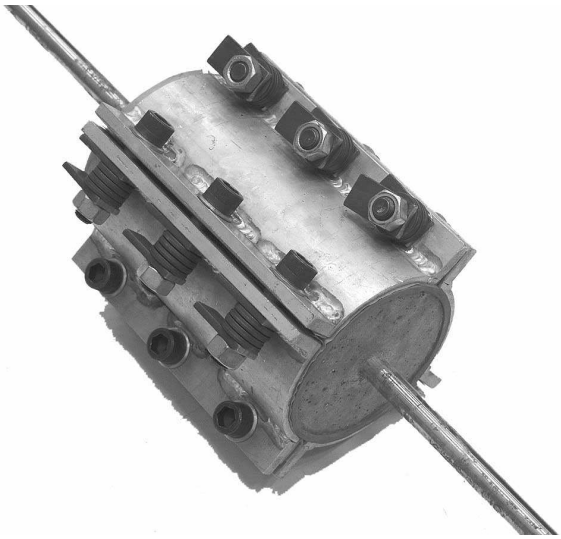

Figure 7.11 *The confinement is established by mounting and prestressing an aluminium shell around the concrete specimen. A 10 mm rubber membrane between the concrete and the aluminium shell ensures that the pressure is approximately hydrostatic*

The active confinement is established by very stiff platen springs which are seen in the figure. It is possible, by calibration, to prestress these springs such that a certain hydrostatic pressure is obtained in the rubber. This hydrostatic pressure will be constant during the experiment.

The system was designed to allow a maximum hydrostatic pressure of 1 MPa. A higher pressure may be obtained by adding more platen springs. However, for the early age configuration, the available maximum pressure was found to be acceptable.

7.4.2 Handling of Self-Weight

Different strategies are available for the handling of the self-weight. It is clear the a simple mounting of the reinforcement bar in the testing machine would require a significant load capacity of the bond, which is not necessarily present in an early-age sample. This can be overcome by making a horizontal testing arrangement, but this solution has other problems, i.e. most testing machines are vertical.

Figure 7.12 *The self-weight is eliminated by springs which support the concrete and reinforcement self-weight. The springs are so soft that their reaction imposed on the specimen does not change during experiment.*

These considerations have led to the system shown in Figure 7.12. The principle is to let the aluminium shell, which is mounted around the concrete specimen, rest on the spring loaded bars seen in the figure. The self-weight of the concrete is thereby not loading the bond. However, it is not possible to eliminate the self-weight loading entirely since in the proposed system the reinforcement bar will impose a load on the bond. But this load is much smaller that the weight of the concrete, and is, within the concrete ages of interest, insignificant.

The springs are so soft that the small elongation of the reinforcement bar during an experiment does not change the spring load and thus, the self-weight is compensated for during the entire experiment. This was shown in Henriksen (2002).

7.4.3 The Setup and Measurement Rig

The specimen enclosed in the aluminium shell is placed on the springs which are mounted on the testing machine. This is shown in Figure 7.13 which shows the entire setup inside the testing machine. The grips are activated when the specimen and the aluminium shell rest on the springs, thereby preventing any self-weight and redundant forces to be present in the system.

Figure 7.13 also shows the rig from which the measurements are made. On each side of the concrete specimen, a steel platen is mounted on the reinforcement. These steel platens are mounted with pins such that a rigid connection is made. Six LVDT's are mounted on the upper platen at two different radii. The radius of the inner three LVDT's is so small that they rest on the concrete specimens upper side. Thereby, the end slip between the reinforcement and the concrete is measured. The radius of the outer three LVDT's is

larger than the concrete specimen and they thereby measure the elongation of the entire reinforcement bar plus concrete specimen by the contact with the opposite measurement platen. Thus, these LVDT's gives a global elongation measurement.

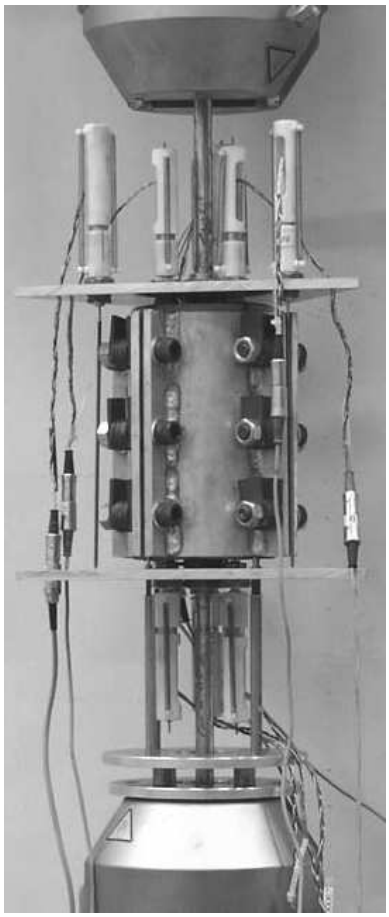

Figure 7.13 *The entire setup inserted in the testing machine. The measurement rig is mounted on the reinforcement bar and measures both the local slip and the global slip*

The applicability of the testing method for early age concrete was investigated in a set of pilot tests. It was found that concrete as early as 15-20 hours could be tested. It was not possible to test concrete at earlier ages due to the specimen dimensions and the necessary handling of the specimen, despite the measures taken to make the setup suitable for early age concrete. Note, as reported by Sule & van Breugel (2001), that no measurable bond strength had developed at 8 hours, whereas significant bond strength had developed at 24 hours. Thus, it seems like the proposed method will be able to measure from almost the start of the development of the bond.

7.5 Experimental Results

Experiments have been carried out and some are described here. More experimental results may be found in Henriksen (2002). The Figures 7.14 and 7.15 show experimental results together with the best fits obtained by application of the analytical model.

Figure 7.14 shows the influence of age of concrete on the shape of the load versus local end slip curve. These experiments are obtained applying smooth reinforcement with a diameter of 20 mm. Results from two different ages are shown. It is seen that the ageing raises the curve which is believed to be due to the development of the bond strength and stiffness. If no bond strength at all was present, the curve would be straight and correspond to the elongation of the reinforcement bar.

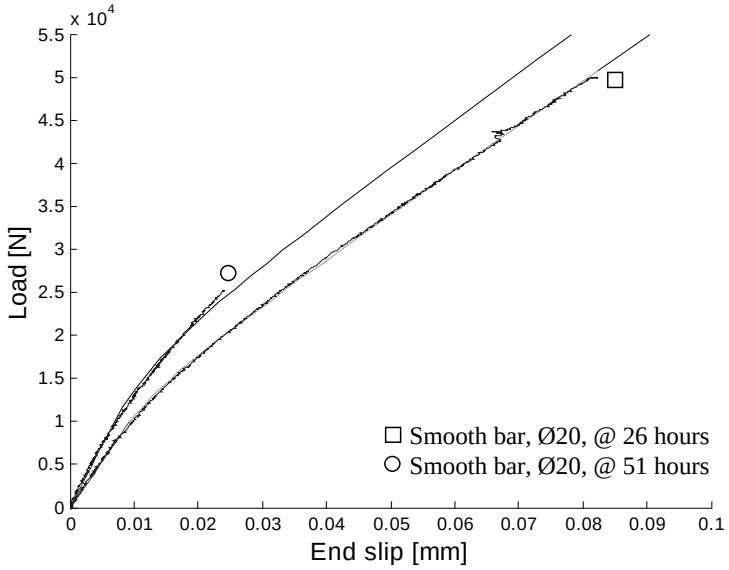

Figure 7.14 *The influence of age of concrete on the load-end slip curve. Experimental results shown together with results from the analytical model*

Figure 7.15 shows the influence of the type of reinforcement and age of concrete. These results are obtained using both smooth and deformed reinforcement bars with a diameter of 10 mm at two different ages. This figure shows the same trend as Figure 7.14 with regard to the ageing, i.e. that the ageing raises the curves, which means that the bond properties in terms of strength and stiffness are developing. The figure also shows that the type of reinforcement, as expected, is important for the bond properties. If reinforcement with ribs are used, then the curves are shifted upwards, which is due to a better bond between the reinforcement and the concrete. This is of course not due to a change in the material properties, but simply an artefact arising from the better geometrically induced interaction between the two materials.

The results clearly show that the setup is able to capture the bond properties in early age concrete, though more experiments are necessary in order to get a firm knowledge of these properties.

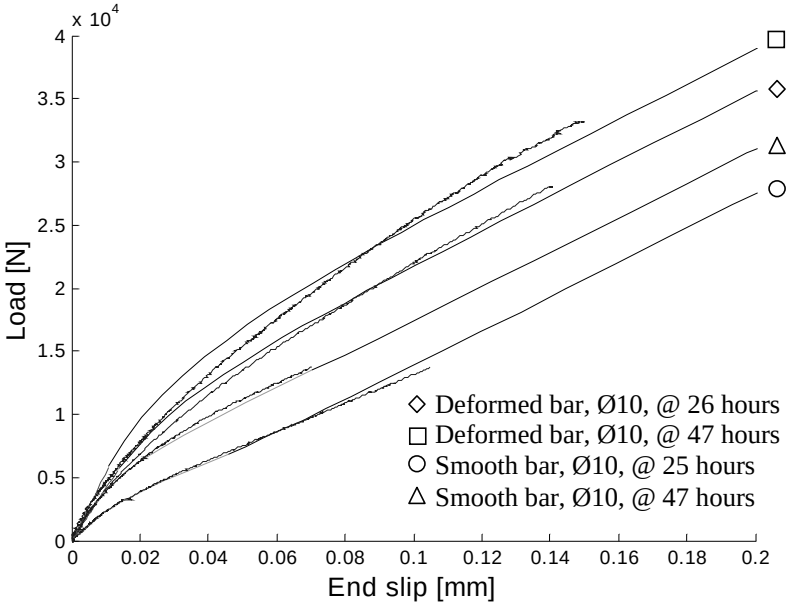

Figure 7.15 *The influence of age of concrete and type of reinforcement on the bond properties.*

The figures also show that the model is able to represent the experimental results. The fitting was done using a program which minimizes the difference between the experimental and the model curve. This finding is supportive for the proposed constitutive model. The parameters used for the fitting are given by:

Table 7.1 *Parameters used to fit the experimental results*

	τ_1' $[MPa]$	τ_2' $[MPa]$	τ_3' $[MPa]$	E_1' $[MPa/mm]$	E_2' $[MPa/mm]$
Smooth Ø20, 26 hrs	2.0	1.7	0.9	208	11
Smooth Ø20, 51 hrs	2.9	2.9	2.8	442	12
Deformed Ø10, 26 hrs	4.1	4.1	4.1	302	2.2
Deformed Ø10, 47 hrs	5.9	5.9	5.9	542	6.2
Smooth Ø10, 25 hrs	0.7	0.7	0	87	18
Smooth Ø10, 47 hrs	2.2	2.2	1.8	312	6.5

Chapter 8

Recommendations for Future Work

The outcome of the present research project has contributed to the understanding of concrete at early ages. However, major contributions are still needed.

The methods for interpretation of the different testing methods have been validated experimentally for plain concrete by the specimen type comparative study at 6 months. However, this assumption should be tried at other ages, as well as under different curing conditions. It is very challenging to conduct the uniaxial tension test at early ages and modifications of the experiment must be considered. However, this test method still stands as the only one, which is able to yield the stress-crack opening relationship directly. Also the three-point bending test is challenging to conduct at early ages, but it may be done. Conducting the specimen comparative study at early ages will give conclusive answers with regard to applicability of the test methods, the interpretation schemes and the experimental data generated in this work.

The inverse analysis described here is based on the cracked hinge model. The output of the method is calibrated employing the finite element method and also by conducting experiments. However, some questions are still to be answered. Experiments are needed with regard to application of the method for fiber reinforced concrete. This has only been tried in the comparison of the model with the finite element method. Adaption of the method such that it may be used for FRC would be useful. If this is impossible, then a new program could be written, which should be based directly on the finite element method. Such approaches do already exist in the literature, but they have only been tried on plain concrete.

The need of more experiments aiming at determining the fracture mechanical properties of concrete in early age is also pointed out. The results presented here do only give a sense of the importance of these properties. It would be interesting to investigate the influence of extremely low water-cement ratios, the behavior of mortars and pure cement pastes, high temperature curing, curing conditions and the effect of addition of fibres. The latter is interesting since it would be very interesting to see how well the fibers increase the toughness of the concrete in early age since they are often partly added to prevent cracking in early age.

The use of the results regarding the development of the stress-crack opening relationship for early age concrete requires development of the commercial finite element codes. Analysis capable of initially calculating a temperature and maturity profile of a structure and subsequently to use the results to calculate the stress-development exists. However, it not possible to couple the analysis with the development of the stress-crack opening relationship in e.g. the smeared crack formulation. Thus, it is not possible to conduct time analysis of the initiation and development of cracks, which may arise in the structure during hardening.

More experiments are needed with regard to the determination of the influence of time-dependent, or rate-dependent, effects in the crack under a sustained deformation or load. This work has not revealed a dependency but no firm conclusions may be drawn since the experimental evidence is scarce.

The investigations of the development of the bond properties between reinforcement and concrete is also a subject, which could benefit greatly from further development. This is due to the lack of knowledge on how the reinforcement interacts with arising crack patterns in early age concrete. The effort should initially be focused on the experimental side. However, more experiments are needed to determine what these properties are and how reliable the method for inverse analysis is.

Chapter 9

Conclusion

This thesis presents the results of the analysis of a number of types of specimens whose applicability with early age concrete has been investigated.

The uniaxial tension test (UTT) is recognized as the most direct method for determination of the stress-crack opening relationship. However, the experiment is very delicate to conduct and it is not suitable for early age concrete. The delicacy of the test method arises from the problems in achieving boundary conditions for the crack planes such that the actual stress-crack opening relationship is obtained. This is only the case if the specimen is small and compact and if the rotational stiffness of the testing machine is very high. It has been shown in the thesis that no rotational stiffness inevitably leads to an erroneous determination of the stress-crack opening relationship. This study showed that the rotational stiffness of the testing machine utilizing the RILEM UTT specimen must be in the range of 250 kNm/rad in order to conduct a test on a concrete with a tensile strength of 2 MPa. The stiffness must be higher for higher tensile strengths.

The unsuitability for early age concrete has also other reasons than the above mentioned. The correct conduction of the experiment requires that steel end platens are glued onto the ends of the specimen. This is almost impossible for concrete at early ages. Furthermore, it is also difficult to mount the deformation measurement rig onto the specimen at early ages.

Due to the problems concerning the uniaxial tension test, other methods are often applied. These are all indirect in nature, i.e. they do not directly determine the stress-crack opening relationship. Instead, a closed-loop experiment yields a global load-deformation curve from which proper analysis may yield the stress-crack opening relationship.

One such indirect method is the three point bending test (TPBT). This method may be used to obtain the stress-crack opening relationship if the finite element method is applied for interpretation. However, as shown in this thesis, also the crack hinge model may be applied. This will often be preferable since such semi-analytical methods almost always are easier to conduct, faster and more accessible to e.g. practitioners. The method presented in this thesis can conduct an inverse analysis on the TPBT test within a few minutes, depending on the computer hardware.

The interpretation and inverse analysis has been shown in this thesis to yield - as output - the constitutive parameters used as input within an error of few percents. Only FRC materials with a b_2 value above 0.7 results in problems for the algorithm. This, however, is attributed to the fact that the first part of the bilinear stress-crack opening relationship becomes unimportant for the global curve shape in the FRC-cases.

However, not only the ease of the interpretation is important for early age concrete. With regard to the handling of the specimen, this test method does have intrinsic problems. These problems are due to the large self-weight, which may cause failure of the specimen in early age if no compensating arrangement is made. The adverse influence of the self-weight will only gradually disappear. Compensating arrangements are complicated to construct, though it is possible. Another problem with the test method is the need of mounting a clip gage at the notch in order to achieve the closed-loop control. This is also problematic in early age.

Due to the problems with the most well-known test methods, UTT and TPBT, a proposal for another method is necessary. The solution is the wedge splitting test. This test method is very suitable with early age concrete since there are almost no problems with self-weight and since the small self-weight, which is present easily may be compensated for. Using this test method, concrete as early as right after final set may be tested, thus enabling the precise determination of the tensile strength from almost age zero. It is further more advantageous that the specimen is small and compact, thus minimizing the problems of temperature gradients etc. The only problem using this test method has been the uncertainty of method of interpretation. However, as proven in this thesis, the cracked hinge model represents a basis on which a inverse analysis method may be formulated, thus enabling the precise determination of not only the stress-crack opening relationship, but also the tensile strength.

The validation of the interpretation and method for inverse analysis was conducted employing the finite element method. It was conclusively found that a inverse analysis method without local minimums may be formulated. The outcome of the inverse analysis always converged at the global minimum. This minimum was furthermore equal to the input parameters within errors in the order of few percents. However, the method was once again found to be uncertain for FRC-materials with high b_2 values. The reason has been explained above.

It has been questioned whether the indirect methods are able to determine the tensile strength. Therefore, often, an apparent direct method is applied in this regard, namely the split cylinder test (SCT). However, it has been shown in this thesis that the test method should only be trusted if traditional materials are tested. The peak load is influenced by e.g. the slope of the initial part of the stress-crack opening relationship. This means that if materials with a initial slope significantly differing from the slope of traditional materials are tested, then erroneous results are produced. This may be the case with ultra high strength concrete. Also the addition of fibers may cause errors since the b_2 starts to influence the peak load when it is larger than 0.35. This is usually the case for

FRC. In this case, the peak load is no longer associated with the tensile strength using the traditional linear elastic interpretation. Instead, the peak load is a result of the addition of fibers.

Furthermore, as shown in this thesis, this method is very poor when applied to early age concrete since the failure mode changes significantly. In fact, in very early age the failure mode may occur in compression. It is therefore not a test method, which can be recommended for an independent determination of the tensile strength in early age concrete. In fact, experimental results from the SCT and the WST tests have been compared with regard to the tensile strength. It is observed that the SCT does not give meaningful results until at least 24 hours of age (normal hardening concrete, and even longer for slow hardening cements (48 hours).

Besides the analysis of test methods also a number of experimental observations have been made during the course of the study.

The ability of the indirect methods to determine the stress-crack opening relationship has been investigated experimentally in a specimen type comparative study. This study has shown that the inverse analysis methods based on the cracked hinge model is able to produce the stress-crack opening relationship, which may be obtained from the uniaxial tension test. However, it was necessary to calibrate the bandwidth parameter for the indirect methods. The bandwidth parameters determined from the finite element calibration were found to produce tensile strengths, which are up to 30% wrong. A second calibration was conducted using the experimental results. The goal for the calibration was to equalize the tensile strengths obtained from the indirect experiments with the one obtained from the uniaxial tension test. This was achieved when the bandwidth parameter for the WST was changed from 0.84 to 0.25 and likewise for the TPBT from 0.50 to 0.95. This probably accounts for the different microcracking patterns known to occur in the different test methods. Despite this calibration, it is very promising that it has been experimentally demonstrated that it is not always necessary to conduct the uniaxial tension test in order to arrive at the correct stress-crack opening relationship.

Having proved that the wedge splitting test can be employed for the determination of the stress-crack opening relationship, this method was applied in a series of tests with the aim to determine the development of the stress-crack opening relationship. This was successfully done. It is interesting that periods of small characteristic lengths occur during hardening. This may indicate periods of higher sensibility of cracking. The tensile strength was found to increase monotonically during hardening. This was also discovered for the modulus of elasticity and the fracture energy. The second slope of the stress-crack opening relationship, a_2, and the normalized cutoff parameter, b_2, were found to be independent of the ageing of the concrete. The initial slope, a_1, however, was found to decrease with age, indicating increased brittleness of the initial part of the stress-crack opening relationship.

Also a study of the creep of bulk concrete at early age was conducted. These studies formed the basis for the study of time-dependent effects of the stress-crack opening relationship in early ages. However, despite the fact that a significant number of long-term experiments were carried out, it was not possible to distinguish any time-dependency of the stress-crack opening relationship. This may be due to insensibility of the test setup. However, another explanation may be that the ageing of the concrete leads to a departure of the stress-crack opening relationship from the achieved stress state. If this departure is fast enough, then the crack ceases to grow, and in this situation only the bulk creep will be measured.

A study of the bond between concrete and reinforcement has also been conducted. This study has included an analytical model for which a new approach utilizing a local shear-slip relationship has been applied. The validity has been shown through comparison with a finite element model for which a modified Mohr-Coulomb failure criterion has been adopted. The section on bond does also introduce a new test setup, which is able to determine the bond properties in early age. Also a few experimental observations are reported.

Bibliography

ACI (1991), Fracture mechanics of concrete: Concepts, models & determination of material properties, Report 446.1R.91, American Concrete Institute.

Al-Khaiat, H. & Haque, M. N. (1998), 'Effect of initial curing on early strength and physical properties of a lightweight concrete', *Cement and Concrete Research* **28**(6), 859–866.

Alexanderson, J. (1972), Strength losses on heat cured concrete, Handl. No. 43, Swedish Cement and Concrete Research Institute. 135 pp.

Altoubat, S. A. (2000), Early age stresses and creep-shrinkage interaction of restrained concrete, PhD thesis, University of Illinois at Urbana-Champaign, Civil and Environmental Engineering, Urbana, Illinois, USA.

Auperin, M. (1989), Shrinkage and creep in certain high performance concrete for use in site, Technical report, Bouygues Research Department.

Avrami, M. (1939), 'Kinetics of phase change. I.', *Journal of Chemical Physics* **7**, 1103–1112.

Barenblatt, G. I. (1962), 'The mathematical theory of equilibrium cracks in brittle fracture', *Advances in Applied Mechanics* **7**, 55–129. Originally published in Russian, 1957, see e.g. (Karihaloo 1995).

Baroghel-Bouny, V. & Aïtcin, P.-C., eds (2000), *Proceedings of the International RILEM workshop, Shrinkage of Concrete, Shrinkage 2000*, 1 edn, Rilem Publications S.A.R.L.

Baroghel-Bouny, V. & Kheirbek, A. (2000), Effect of mix-parameters on autogenous deformations of cement pastes - microstructural interpretations, *in* 'Proceedings of the International RILEM workshop, Shrinkage of Concrete, Shrinkage 2000', Rilem Publications S.A.R.L. Draft print.

Baudeau, P. (1995), 'Comportement rhéologique du béton frais sous différents chemins de sollicitation', *Materials and Structures* **28**(183), 545–549.

Bažant, Z. P. & Chern, J. C. (1985), 'Triple power law for concrete creep', *Journal of Engineering Mechanics* **111**(1), 63–83.

Bažant, Z. P. & Li, Y.-N. (1997), 'Cohesive crack with rate-dependent opening and viscoelasticity: I. mathematical model and scaling', *International Journal of Fracture* **86**(3), 247–265.

Bažant, Z. P. & Oh, B. H. (1983), 'Crack band theory for fracture of concrete', *Materials and Structures* **16**, 155–157.

Bažant, Z. P. & Prasannan, S. (1989*a*), 'Solidification theory for concrete creep. I: Formulation', *Journal of Engineering Mechanics* **115**(8), 1691–1703.

Bažant, Z. P. & Prasannan, S. (1989*b*), 'Solidification theory for concrete creep. II: Verification and application', *Journal of Engineering Mechanics* **115**(8), 1704–1725.

Bažant, Z. P., ed. (1988), *Mathematical Modeling of Creep and Shrinkage of Concrete*, 1 edn, John Wiley and Sons Ltd.

Bažant, Z. P., Hauggaard, A. B. & Baweja, S. (1997), 'Microprestress-solidification theory for concrete creep. II: Algorithm and verification', *Journal of Engineering Mechanics* **123**(11), 1195–1201.

Bažant, Z. P., Hauggaard, A. B., Baweja, S. & Ulm, F.-J. (1997), 'Microprestress-solidification theory for concrete creep. i: Aging and drying effects', *Journal of Engineering Mechanics* **123**(11), 1188–1194.

Bentur, A. (2000), Early age skrinkage and cracking in cementitious systems, *in* 'Proceedings of the International RILEM workshop, Shrinkage of Concrete, Shrinkage 2000', Rilem Publications S.A.R.L. Draft print.

Bentur, A. & Kovler, K., eds (2001), *RILEM International Conference on Early-Age Cracking in Cementitous Systems (EAC'01), March 12-14, Haifa Israel*, Rilem Publications S.A.R.L.

Bentz, D. P. & Snyder, K. A. (1999), 'Protected paste volume in concrete - extension to internal curing using saturated lightweight fine aggregate', *Cement and Concrete Research* **29**(11), 1863–1867.

Bjøntegaard, Ø. & Sellevold, E. J. (1998), Thermal dilation-autogenous shrinkage: How to separate?, *in* 'AUTOSHRINK'98, Proceedings of the International Workshop on Autogenous Shrinkage of Concrete', Japan Concrete Institute, Japan.

Bjøntegaard, Ø. & Sellevold, E. J. (2001), 'Scientific reports - interaction between thermal dilation and autogenous deformation in high performance concrete', *Materials and Structures* **34**(239), 266–272.

Bonavetti, V., Donza, H., Rahhal, V. & Irassar, E. (2000), 'Influence of initial curing on the properties of concrete containing limestone blended cement', *Cement and Concrete Research* **30**, 703–708.

Bouguerra, A. (1999), 'Temperature and moisture dependence on the thermal conductivity of wood-cement-based composite: experimental and theoretical analysis', *J. Phys. D: Appl. Phys* **32**, 2797–2803.

Boumiz, A., Vernet, C. & Tenoudji, F. C. (1996), 'Mechanical properties of cement pastes and mortars at early ages', *Advanced Cement Based Materials* **3**(3–4), 94–106.

Brameshuber, W. (1988), Bruchmechanische Eigenschaften von jungem Beton, PhD thesis, Schriftenreihe des Instituts für Massivbau und Baustofftechnologie, J. Eibl & H. K. Hilsdorf.

Brameshuber, W. (1989), Selecting a suitable model law for very young concrete in tension, *in* 'Fracture of Concrete and Rock: Recent Developments', Elsevier Applied Science, pp. 566–576.

Brameshuber, W. & Hilsdorf, H. K. (1987), Development of strength and deformability of very young concrete, *in* 'Fracture of Concrete and Rock', Springer Verlag, pp. 409–421.

Brincker, R. & Dahl, H. (1989), 'Fictitious crack model of concrete fracture', *Magazine of Concrete Research* **41**(147), 79–86.

Brühwiler, E. & Wittmann, F. H. (1990), 'The wedge splitting test, a new method of performing stable fracture mechanics tests', *Engineering Fracture Mechanics* **35**(1/2/3), 117–125.

Byfors, J. (1980), Plain concrete at early ages, Technical report, CBI Research, Swedish Council for Building Research.

Carneiro, F. L. & Barcellos, A. (1949), 'Résistance a la traction des bétons', *RILEM Bulletin* **13**, 98–125.

CEB-FIP (2000), *Bond of reinforcement in concrete, State-of-art report prepared by Task Group Bond Models, CEB-FIP*, International Federation for Structural Concrete, Lausanne, Switzerland.

Chen, W. F. & Drucker, D. C. (1969), 'Bearing capacity of concrete blocks or rock', *Journal of Engineering Mechanics Div., ASCE* **95**(EM4), 955–978.

Cornelissen, H. A. W., Hordijk, D. A. & Reinhardt, H. W. (1986), 'Experimental determination of crack softening characteristics of normal and lightweight concrete', *HERON* **31**, 45–56.

Danish Standard, DS 411 (1982), DS 411, Ds 411, The Steering Committee of DIF's Codes of Practice Organization, Teknisk Forlag, Skelbækgade 4, DK-1717, Copenhagen V.

Davis, H. E. (1940), 'Autogenous volume changes of concrete', *43th. A.S.T.M Annual Meeting* **40**, 1103–1110. Atlantic City, N.J, June 24-28.

Dela, B. F. (2000), Eigenstresses in Hardening Concrete, Series r, no. 64, Department of Structural Engineering and Materials, Technical University of Denmark, Building 118, Brovej, Kgs. Lyngby.

DIANA (2000), *DIANA Manual*, 8.0 edn, TNO Building and Construction Research, P.O. Box 49, 2600 AA Delft, The Netherlands.

Double, D. D., Hellawell, A. & Perry, S. J. (1978), 'The hydration of portland cement', *Proceedings of the Royal Society of London, Series A, Mathematical and Physical Sciences* **359**(1699), 435–451.

Dugdale, D. S. (1960), 'Yielding of steel sheets containing slits', *Journal of the Mechanics and Physics of Solids* **8**, 100–104.

Eberhardt, M., Lokhorst, S. J. & van Breugel, K. (1995), On the reliability of temperature differentials as a criterion for the risk of early-age thermal cracking, *in* 'Thermal Cracking in Concrete at Early Ages, Proceedings of the International RILEM Symposium', E & FN Spon, London, pp. 353–360.

Eligehausen, R., Popov, E. P. & Bertero, V. V. (1982), Local bond stress-slip relationships of deformed bars under generalized excitations, UCB/EERC 83-23, University of California, Berkeley, California, U.S.A.

Emborg, M. (1989), Thermal stresses in concrete structures at early ages, 1989:73 d, Division of Structural Engineering, Luleå University of Technology, Luleå.

Emborg, M. & Bernander, S. (1995), Thermal stresses computed by a method for manual calculations, *in* 'Thermal Cracking in Concrete at Early Ages, Proceedings of the International RILEM Symposium', E & FN Spon, London, pp. 321–328.

Espinosa-Paredes, G., Garca, A., Santoyo, E., Contreras, E. & Morales, J. M. (2002), 'Thermal property measurement of mexican geothermal cementing systems using an experimental technique based on the jaeger method', *Applied Thermal Engineering* **22**, 279–294.

Flügge, W. (1975), *Viscoelasticity*, second revised edition edn, Springer Verlag, Berlin/Heidelberg.

Fu, X. & Chung, D. D. L. (1997), 'Effects of silica fume, latex, methylcellulose, and carbon fibers on the thermal conductivity and specific heat of cement paste', *Cement and Concrete Research* **27**(12), 1799–1804.

Gettu, R., Garcia-Álvarez, V. O. & Aguado, A. (1998), 'Effect of aging on the fracture characteristics and brittleness of a high-strength concrete', *Cement and Concrete Research* **28**(3), 349–355.

Gibbon, G. J. & Ballim, Y. (1998), 'Determination of the thermal conductivity of concrete during the early stages of hydration', *Magazine of Concrete Research* **50**(3), 229–236.

Goto, Y. (2001), 'Cracks formed in concrete around deformed tensions bars', *Journal of ACI* **31**(12), 244–251.

Griffith, A. A. (1920), 'The phenomena of rupture and flow in solids', *Philosophical transactions of the Royal Society of London, Series A, Physical sciences and engineering* **221**, 163–198.

Günzler, J. (1970), 'Mechanische eigenschaften von jungem beton im gleitbau', *Bauplanung Beutechnik* **24**(8), 372–375.

Hansen, E. A. (1990), A visco-elastic fictitious crack model, *in* 'Micromechanics of Failure of Quasi-Brittle Materials', Elsevier Applied Science, pp. 156–165.

Hansen, P. F. & Pedersen, E. J. (1977), 'Måleinstrument til kontrol af betons hærdning', *Nordisk Betong* **1**, 21–25.

Hansen, P. F. & Pedersen, E. J. (1982), Vinterstøbning af beton, SBI-anvisning 125, Statens Byggeforskningsinstitut.

Hansen, P. F., Hansen, J. H., Kjær, V. & Pedersen, E. J. (1982), Thermal properties of hardening cementpaste, *in* 'International Conference on Concrete at Early Ages', Vol. 1, Paris, Ecole Nationale des Ponts et Chausses.

Hansen, T. C. (1986), 'Physical structure of hardened cement paste. a classical approach', *Materials and Structures* **19**(114), 423–436.

Hariri, K. (2000), *Bruchmechanisches Verhalten jungen Betons. Laser-Speckle-Interferometrie und Modellierung der Rißprozeßzone*, number 509 *in* 'Deutscher Ausschuß für Stahlbeton', Beuth Verlag GmbH, Berlin.

Hauggaard, A. B., Damkilde, L. & Hansen, P. F. (1999), 'Transitional thermal creep of early age concrete', *Journal of Engineering Mechanics* **125**(4), 458–465.

Hauggaard, A. B., Damkilde, L., Hansen, P. F., Hansen, J. H., Christensen, S. L. & Nielsen, A. (1997), *HETEK, Control of Early Age Cracking in Concrete, Phase 3: Creep in Concrete*, The Danish Road Directorate.

Hauggaard-Nielsen, A. B. (1997), Mathematical Modelling and Experimental Analysis of Early Age Concrete, PhD thesis, Department of Structural Engineering and Materials, Technical University of Denmark, Kgs. Lyngby, Denmark.

Hawkins, N. M. (1985), The role of fracture mechanics in conventional reinforced concrete design, *in* 'Application of Fracture Mechanics to Cementitious Composites (NATO Advanced Research Workshop, Evanston, USA 1984', Martinus Nijhoff, Dordrecht, pp. 639–666.

Henriksen, T. N. (2002), Vedhæftning mellem armering og beton i tidlig alder, Master's thesis, Department of Civil Engineering, Technical University of Denmark, Brovej, Building 118.

Herholdt, A. D., Justesen, C. F. P., Nepper-Christensen, P. & Nielsen, A. (1985), *Beton-Bogen*, 2 edn, Aalborg Portland.

Hillerborg, A. (1989), Stability problems in fracture mechanics testing, *in* 'Fracture of Concrete and Rock: Recent Developments', Elsevier Applied Science, pp. 369–378.

Hillerborg, A., Modéer, M. & Petersson, P. E. (1976), 'Analysis of crack formation and crack growth in concrete by means of fracture mechanics and finite elements', *Cement Concrete Research* **6**, 773–782.

Holt, E. E. & Leivo, M. T. (2000), Methods of reducing early-age shrinkage, *in* 'Proceedings of the International RILEM workshop, Shrinkage of Concrete, Shrinkage 2000', Rilem Publications S.A.R.L. Draft print.

Hordjik, D. A. (1991), Local Approach to Fatigue of Concrete, PhD thesis, Delft University of Technology, The Netherlands.

Høyer, O. (1990), Betons egenskaber ved tidlig alder (state of the art), Det materialeteknologiske Udviklingsprogram, Højkvalitetsbetoner i 90'erne. 3.1, AEC Rådgivende Ingeniører A/S, Holte Midtpunkt 23-3, 2840 Holte. Reg. Nr. 63.062.

Ichinose, T. & Hayashi, T. (1998), Fundamental analysis of RC lap splices, *in* 'Bond and Development of Reinforcement: a tribute to Dr. Peter Gergely', ACI-International SP-180, pp. 431–457.

Irwin, G. R. (1957), 'Analysis of stresses and strains near the end of a crack traversing a plate', *Journal of Applied Mechanics* **24**, 361–364.

Izbicki, R. J. (1972), 'General yield condition: I. plane deformation', *Bull. Acad. Pol. Sci. Ser. Sci. Tech.* **20**(7-8), 255–262.

Jensen, O. M. & Hansen, P. F. (1995), 'A dilatometer for measuring autogenous deformation on hardening portland cement paste', *Materials and Structures* **28**(181), 406–409.

Jensen, O. M. & Hansen, P. F. (1996), 'Autogenous deformation and change of the relative humidity in silica fume modified cement paste', *ACI Materials Journal* **93**(6), 539–543.

Jensen, O. M. & Hansen, P. F. (1999), 'Influence of temperature on autogenous deformation and relative humidity change in hardening cement paste', *Cement and Concrete Research* **29**, 567–575.

Jensen, O. M. & Hansen, P. F. (2001*a*), 'Autogenous shrinkage and RH-change in perspective', *Cement and Concrete Research* **31**(12), 1859–1865.

Jensen, O. M. & Hansen, P. F. (2001*b*), 'Water-entrained cement-based materials - I-principle and theoretical background', *Cement and Concrete Research* **31**(4), 647–654.

Jensen, O. M., Hansen, P. F. & Østergaard, T. (2001), 'Water-entrained cement-based materials according to Power's model', Department of Building Research and Structural Engineering. Colour slide used in the Ph.D.-course Behavior and Performance of Early Age Concrete, Technical University of Denmark, Lyngby, June 17.-23. 2001.

Kada, H., Lachemi, M., Petrov, N., Bonneau, O. & Aïtchin, P.-C. (2002), 'Determination of the coefficient of thermal expansion of high performance concrete form initial setting', *Materials and Structures* **35**(245), 35–41.

Kaplan, M. F. (1961), 'Crack propagation and the fracture of concrete', *Journal of the American Concrete Institute* **58**, 591–610.

Karihaloo, B. L. (1995), *Fracture Mechanics & Structural Concrete*, Concrete Design and Construction Series, Longman Scientific & Technical, Essex, England.

Karihaloo, B. L. & Nallathambi, P. (1991), Notched beam test: Mode I fracture toughness, *in* S. Shah & A. Carpinteri, eds, 'Fracture Mechanics Test Methods for Concrete', Chapmann & Hall, chapter 1, pp. 1–86.

Karihaloo, B. L. & Santhikumar, S. (1999), 'Application of a visco-elastic tension-softening constitutive model to cracked and ageing concrete', *Construction and Building Materials* **13**, 15–21.

Kasai, Y. (1971), 'Tensile properties of early-age concrete', Proceedings of the 1971 International Conference on Mechanical Behavior of Materials. Vol. IV, pp. 288-299.

Khan, A. A., Cook, W. D. & Denis, M. (1998), 'Thermal properties and transient thermal analysis of structural members during hydration', *ACI Material Journal* **95**(3), 293–303.

Khan, M. I. (2002), 'Factors affecting the thermal properties of concrete and applicability of its prediction models', *Building and Environment* **37**, 607–614.

Kitsutaka, Y. (1997), 'Fracture parameters by polylinear tension-softening analysis', *Journal of Engineering Mechanics* **123**(5), 444–450.

Kovler, K. (1994), 'Testing system for determining the mechanical behavior of early age concrete under restrained and free uniaxial shrinkage', *Materials and Structures* **27**(170), 324–330.

Laplante, P. & Boulay, C. (1994), 'Evolution du coefficient de dilatation thermique du beton en fonction de sa maturite aux tout premiers ages', *Materials and Structures* **27**(174), 596–605.

Lemaitre, J. & Chaboche, J.-L. (1994), *Mechanics of Solid Materials*, Cambridge University Press.

Li, Y.-N. & Bažant, Z. P. (1997), 'Cohesive crack model with rate-dependent opening and viscoelasticity. II. numerical algorithm, behavior and size effect', *International Journal of Fracture* **86**(3), 267–288.

Linsbauer, H. N. & Tschegg, E. K. (1986), 'Fracture energy determination of concrete with cube shaped specimens (in german)', *Zement und Beton* **31**, 38–40.

Löfkvist, B. (1946), Temperatureffekter i härdnande betong, Teknisk meddelande 22, Kungl. Vattenfallsstyrelsen. Stockholm, 195 pp.

Magnusson, J. (1997), Bond and anchorage of deformed bars in high-strength concrete, Technical Report 97/1, Chalmers University of Technology.

Mangold, M. & Springenschmid, R. (1995), Why are temperature-related criteria so unreliable for predicting thermal cracking at early ages, *in* 'Thermal Cracking in Concrete at Early Ages, Proceedings of the International RILEM Symposium', E & FN Spon, London, pp. 361–368.

Mihashi, H. & Wittmann, F. H., eds (2002), *Control of Cracking in Early Age Concrete - Proceedings of an International Workshop, Sendai, Japan, 23-24 August 2000*, A. A. Balkema Publishers.

Nagy, A. (1997), 'Determination of E-modulus of young concrete with nondestructive method', *Journal of Materials In Civil Engineering* **9**(1), 15–20.

Nanakorn, P. & Horii, H. (1996), 'Back analysis of tensioning-softening relationship of concrete', *J. Materials, Conc. Struct., Pavements* **32**(544), 265–275.

Nemati, K. M., Monteiro, P. J. M. & Scrivener, K. L. (1998), 'Analysis of compressive stress-induced cracks in concrete', *American Concrete Institute Materials Journal* **95**(5), 617–631.

Neville, A. M. (1995), *Properties of Concrete*, fourth and final edition edn, Longman Group Limited.

Neville, A. M. & Brooks, J. J. (1990), *Concrete Technology*, updated edn, Longman Scientific & Technical.

Neville, A. M., Dilger, W. & Brooks, J. J. (1983), *Creep of Plain and Structural Concrete*, Construction Group, Longman Group Limited, London. 361 pp.

Nielsen, L. F. (1999*a*), Time-dependent behavior of concrete - a basic algorithm for FEM analysis, Bygningsstatiske Meddelelser 3, Dansk Selskab for Bygningsstatik, Copenhagen, Denmark. Årgang LXX.

Nielsen, M. P. (1999*b*), *Limit Analysis and Concrete Plasticity*, 2 edn, CRC Press, London.

Noghabai, K. (1995), Splitting of Concrete in the Anchoring Zone of Deformed Bars, PhD thesis, Luleå University of Technology, Division of Structural Engineering, Luleå (Sweden).

Ohgishi, S., Ono, H., Takatsu, M. & Tanahashi, I. (1986), Influence of test conditions on fracture toughness of cement paste and mortar, *in* 'Fracture Toughness and Fracture Energy of Concrete', Elsevier Science Publishers B.V., Amsterdam, pp. 299–306.

Olesen, J. F. (2001*a*), 'Fictitious crack propagation in fiber-reinforced concrete beams', *Journal of Engineering Mechanics* **127**(3), 272–280.

Olesen, J. F. (2001*b*), Measuring the moment stiffness of an Instron 8502 testing machine, Test and Design Methods for Steel Fiber Reinforced Concrete BRPR-CT98-813, Department of Structural Engineering and Materials, Technical University of Denmark, Lyngby, Denmark.

Olesen, J. F. (2002), Concrete-reinforcement bond-slip behavior, Technical report, Department of Civil Engineering, Technical University of Denmark.

Olesen, J. F., Østergaard, L. & Stang, H. (2003), 'Nonlinear fracture mechanics and plasticity of the split cylinder test', *Journal of Eng. Mech.* To be submitted.

Oluokun, F. A., Burdette, E. G. & Deatherage, J. H. (1991), 'Elastic modulus, Poisson's ratio, and compressive strength relationships at early ages', *ACI Materials Journal* **88**(1), 3–10.

Østergaard, L. & Stang, H. (2002), Finite element modelling of the uniaxial tension test, *in* '4th International Ph.D.-symposium in Civil Engineering', Vol. 2, Springer VDI Verlag, Düsseldorf, pp. 100–106.

Østergaard, L., Lange, D. A. & Stang, H. (2002), 'Early age stress-crack opening relationships for high performance concrete', *Submitted for publishing to Cement and Concrete Composites*.

Østergaard, L., Lange, D. A., Altoubat, S. A. & Stang, H. (2001), 'Tensile basic creep of early-age concrete under constant load', *Cement and Concrete Research* **31**(12), 1895–1899.

Østergaard, L., Olesen, J. F. & Stang, H. (2001), Modelling simultaneous tensile and compressive failure modes of the split cylinder test, *in* 'Proceedings of the 14th. Nordic Seminar on Computational Mechanics', KFS, Lund, Sweden, pp. 193–196.

Østergaard, L., Olesen, J. F., Stang, H. & Lange, D. A. (2002), 'Interpretation and inverse analysis of the wedge splitting test', *Submitted to Journal of Engineering Mechanics*.

Østergaard, L., Stang, H. & Olesen, J. F. (2002*a*), Interpretation and inverse analysis of the wedge splitting test, *in* 'Fracture Mechanics Beyond 2000', Vol. II, EMAS Publications, Sheffield, UK., pp. 593–600.

Østergaard, L., Stang, H. & Olesen, J. F. (2002*b*), Time-dependent fracture of early age concrete, *in* 'Non-Traditional Cement & Concrete', Brno University of Technology, pp. 394–408.

Pedersen, C. (1996), New production processes, materials, and calculation techniques for fiber-reinforced concrete pipes, PhD thesis, Department of Structural Engineering and Materials, Technical University of Denmark, Lyngby, Denmark.

Petersson, P. E. (1980), 'Fracture energy of concrete: Practical performance and experimental results', *Cement and Concrete Research* **10**, 91–101.

Pickett, G. (1942), 'The effect of change in mousture-content of the creep of concrete under a sustained load', *Proceedings for the American Concrete Institute* **38**(4), 333–355.

Plank, A. (1971), 'Über das Verformungsverhalden jungen zementmörtels bei Druckbeanspruchung', *Betonstein-Zeitung* **37**(12), 741–751.

Powers, T. C. & Brownyards, T. L. (1948), Studies of the physical properties of hardened cement paste, Bulletin 22, Research Laboratories of the Portland Cement Association, Chicago.

Quillin, K., Osborne, G., Majumdar, A. & Singh, B. (2001), 'Effects of w/c ratio and curing conditions on strength development in BRECEM concretes', *Cement and Concrete Research* **31**, 627–632.

Rehm, G. (1965), On the fundamentals of steel-concrete bond (in german), Technical Report 138, Deutscher Ansschuss für Stahlbeton.

RILEM (1981), 'Properties of set concrete at early ages - state of the art report', *Materials and Structures* **14**(84), 399–450.

RILEM (1985), 'Determination of the fracture energy of mortar and concrete by means of three-point bend tests on notched beams', *Materials and Structures* **18**(106), 99–101. Prepared by TC50-FMC.

RILEM (2000), 'Test and design methods for steel fiber reinforced concrete. recommendations for the three point bending test', *Materials and Structures* **33**, 3–5. Prepared by RILEM-Committee-TDF-162, Chairlady L. Vandewalle.

RILEM (2001), 'Test and design methods for steel fiber reinforced concrete. recommendations for uniaxial tension test', *Materials and Structures*. Prepared by RILEM-Committee-TDF-162, Chairlady L. Vandewalle.

Rocco, C., Guinea, G. V., Planas, J. & Elices, M. (1999), 'Size effect and boundary conditions in the brazilian test: theoretical analysis', *Materials and Structures* **32**, 437–444.

Roelfstra, P. E. & Wittmann, F. H. (1986), Numerical method to link strain softening with failure of concrete, *in* 'Fracture Toughness and Fracture Energy of Concrete', Elsevier, pp. 163–175.

Rossi, P., Brühwiler, E., Chhuy, S., Jenq, Y.-S. & Shah, S. P. (1991), Fracture properties of concrete as determined by means of wedge splitting tests and tapered double cantilever beam tests, *in* S. Shah & A. Carpinteri, eds, 'Fracture Mechanics Test Methods for Concrete', Chapmann & Hall, chapter 2, pp. 87–128.

Rots, J. G. (1990), Simulation of bond and anchorage: usefulness of softening fracture mechanics, *in* 'Applications of Fracture Mechanics to Reinforced Concrete', Elsevier Applied Science, pp. 285–306.

Santhikumar, S. (1998), Fracture of Visco-Elastic Ageing Materials with Tension Softening, PhD thesis, Department of Civil Engineering, The University of Sydney, Australia.

Santhikumar, S. & Karihaloo, B. L. (1996), 'Time-dependent tension softening', *Mechanics of Cohesive-Frictional Materials* **1**, 295–304.

Santhikumar, S., Karihaloo, B. L. & Reid, S. G. (1998), 'A model for ageing visco-elastic tension softening materials', *Mechanics of Cohesive-Frictional Materials* **3**, 27–39.

Schutter, G. D. & Taerwe, L. (1995), 'Specific heat and thermal diffusivity of hardening concrete', *Magazine of Concrete Research* **47**(172), 203–208.

Schutter, G. D. & Taerwe, L. (1997), 'Fracture energy of concrete at early ages', *Materials and Structures* **30**, 67–71.

Seigneur, V., Bonneau, O. & Aïtcin, P. C. (2000), Influence of the curing regine and of a shrinkage reducing admixture on shrinkage, *in* 'Proceedings of the International RILEM workshop, Shrinkage of Concrete, Shrinkage 2000', Rilem Publications S.A.R.L. Draft print.

Springenschmid, R., ed. (1994), *Thermal Cracking in Concrete at Early Ages*, E & FN Spon, 2-6 Boundary Row, London SE1 8HN, UK.

Stang, H. (1984), En Kompositmaterialeteori og dens Anvendelse til Beskrivelse af Trækpåvirkede Cementkompositter, Serie r no. 193, Department of Structural Engineering, Technical University of Denmark, Lyngby, Denmark.

Stang, H. (1992), Evaluation of prroperties of cementitious fiber composite materials, *in* 'High Performance Fiber Reinforced Cement Composites', Vol. I, E & FN Spon, London, pp. 388–406.

Stang, H. (1996), 'Significance of shrinkage induced clamping pressure in fiber-matrix bonding in cementitious composite materials', *Advanced Cement Based Materials* **4**, 106–115.

Stang, H. (2000), Analysis of 3 point bending test, Technical Report EU Contract - BRPR - CT98 - 813, Report from Test and Design Methods for Steel Fibre Reinforced Concrete. 7p.

Stang, H. & Olesen, J. F. (1998), On the interpretation of bending tests on FRC materials, *in* 'Proc., FRAMCOS-3, Fracture Mechanics of Concrete Structures', Vol. I, Aedificatio Publishers, Freiburg, Germany, pp. 511–520.

Stang, H. & Olesen, J. F. (2000), A fracture mechanics-based design approach to FRC, *in* 'Proc., 5th RILEM Symp. on Fiber-Reinforced Concretes (FRCs)', BEFIB 2000.

Sule, M. & van Breugel, K. (2001), 'Cracking behavior of reinforced concrete subjected to early-age shrinkage', *Materials and Structures* **34**, 284–292.

Tada, H., Paris, P. & Irwin, G. (1985), *The Stress Analysis of Cracks Handbook*, Paris Productions Incorporated, 226 Woodbourne Dr., St. Louis, Missouri, USA.

Tang, T. (1994), 'Effects of load-distributed width on split tension of unnotched and notched cylindrical specimens', *Journal of Testing and Evaluation* **22**(5), 401–409.

Tazawa, E., Sato, R., Sakai, E. & Miyazawa, S. (2000), Work of JCI committee on autogenous shrinkage, *in* 'Proceedings of the International RILEM workshop, Shrinkage of Concrete, Shrinkage 2000', Rilem Publications S.A.R.L. Draft print.

Tepfers, R. (1973), A Theory of Bond Applied to Overlapped Tensile Reinforcement Splices for Deformed Bars, PhD thesis, Chalmers University of Technology, Göteborg.

Tepfers, R. (1979), 'Cracking of concrete cover along anchored deformed reinforcing bars', *Magazine of Concrete Research* **31**(106), 3–12.

Tepfers, R. & Olsson, P. A. (1992), Ring test for evaluation of bond properties of reinforcing bars, *in* 'Proceedings of the International Conference, Bond in Concrete: from research to practics', CEB-RTU (Riga Technical University), Riga (Latvia), pp. 1.89–1.99.

Tian, M., Huang, S. & Liu, E. (1986), Fracture toughness of concrete, *in* 'Fracture Toughness and Fracture Energy of Concrete', Elsevier Science Publishers B.V., Amsterdam, pp. 299–306.

Timoshenko, S. P. & Goodier, J. (1970), *Theory of Elasticity*, 3rd edn, McGraw-Hill.

Ulfkjær, J., Krenk, S. & Brincker, R. (1995), 'Analytical model for fictitious crack propagation in concrete beams', *Journal of Engineering Mechanics* **121**(1), 7–15.

Ulfkjær, J. P. & Brincker, R. (1993), Indirect determination of the σ-w relation of HSC through three-point bending, *in* 'Fracture and Damage of Concrete and Rock - FCDR-2', E & FN Spon, pp. 135–144.

van Breugel, K. (2000), Numerical modelling of volume changes at early ages - potential pitfalls and challenges, *in* 'Proceedings of the International RILEM workshop, Shrinkage of Concrete, Shrinkage 2000', Rilem Publications S.A.R.L. Draft print.

van Mier, J. G. M. (1986), 'Fracture of concrete under complex stress', *HERON*.

van Mier, J. G. M. (1997), *Fracture Processes of Concrete*, CRC Press, Boca Raton.

van Mier, J. G. M. & Shi, C. (2002), 'Stability issues in uniaxial tensile tests on brittle disordered materials', *International Journal of Solids and Structures* **39**, 3359–3372.

van Mier, J. G. M. & van Vliet, M. R. A. (2002), 'Uniaxial tension test for the determination of fracture parameters of concrete: State of the art', *Engineering Fracture Mechanics* **69**, 235–247.

van Mier, J. G. M., Schlangen, E. & Vervuurt, A. (1995), Lattice type fracture models for concrete, *in* H.-B. Mühlhaus, ed., 'Continuum Models for Materials with Microstructure', E & FN Spon, chapter 10.

Vodák, F., Černý, R., Drchalová, J., Š Hošková, Kapičková, O., Michalko, O., Semerák, P. & Toman, J. (1997), 'Thermophysical properties of concrete for nuclear safety related structures', *Cement and Concrete Research* **27**(3), 415–426.

Westman, G. (1995), Basic creep and relaxation of young concrete, *in* 'Thermal Cracking in Concrete at Early Ages, Proceedings of the International RILEM Symposium', E & FN Spon, London, pp. 87–94.

Wittmann, F. H., Roelfstra, P. E., Mihashi, H., Huang, Y.-Y. & Zhang, X.-H. (1987), 'Influence of age of loading, water-cement ratio and rate of loading on fracture energy of concrete', *Materials and Structures* **20**, 103–110.

Wong, W. & Miller, R. A. (1990), Mixed mode fracture at early ages, *in* 'Micromechanics of Failure of Quasi-Brittle Materials', Elsevier Applied Science, pp. 166–175.

Wu, Z. S. & Bažant, Z. P. (1993), Finite element modeling of rate effect in concrete fracture with influence of creep, *in* 'Creep and Shrinkage of Concrete', E. & F. N. Spon, London, pp. 427–432.

Yao, B. & Murray, W. (1995), 'Study of concrete cracking and bond using a distributed discrete crack finite element model', *ACI Materials Journal* **92**(1), 93–104.

Yonekura, A., Kusaka, M. & Tanaka, S. (1988), 'Tensile creep of early age concrete with compressive stress history', *Cement Association of Japan Review* pp. 158–161.

Young, J. F. (1997), *Chemically bonded Ceramics*, revised edn, Department of Materials Science and Engineering, University of Illinois at Urbana-Champaign. Class notes for MATSE/CERE 330.

Young, J. F., Mindess, S. & Darwin, D. (2002), *Concrete*, 2 edn, Prentice Hall. 644 pp.

Zhou, F. P. (1988), Some aspects of tensile fracture behaviour and structural response of cementitious materials, Report TVBM 1008, Lund Institute of Technology, Lund, Sweden.

Zhou, F. P. (1992), Time-Dependent Crack Growth and Fracture in Concrete, PhD thesis, Lund University, Lund, Sweden.

Zijl, G. P. A. G., de Borst, R. & Rots, J. G. (2000), 'Time-dependent fracture of cementitious materials', *Heron* **45**(4), 255–273.

Zollinger, D. G., Tang, T. & Yoo, R. H. (1993), 'Fracture toughness of concrete at early ages', *ACI Materials Journal* **90**(5), 463–471.

Appendix A

Cracked hinge model

The cracked hinge model may be applied to model the cracking in structural elements subject to pure bending or bending in combination with axial load. It is assumed that the material is quasi-brittle and that it may be described by the fictitious crack model. Applications of the hinge model for three point bending beams and beams on elastic foundation have been investigated by Olesen (2001*a*). The idea of a cracked hinge was originally presented by Ulfkjær et al. (1995) and further developed by Pedersen (1996) and Stang & Olesen (1998), Stang & Olesen (2000). The advantage of the hinge model is that it yields closed-form analytical solutions for the entire load-crack opening curve. This feature allows for development of simple programs that can replace time consuming FEM-modelling and may be applied for fast analysis of experimental results.

The concept of the hinge is to view the crack as a local change in the overall stress and strain fields. This change is assumed to vanish outside a certain band width, s. Within this band, modelling of the crack takes place, and outside, the structural element is modelled employing the appropriate elastic theory. The hinge itself is modelled by incremental layers of independent springs, attached to the boundaries of the element. The constitutive relationship for each spring is assumed to be linear elastic in the pre-crack state, while the cracked state is approximated by a bilinear softening curve, see Equation (A.1) and Figure A.1.

$$\sigma = \begin{cases} E\varepsilon & \text{pre-crack state} \\ \sigma_w(w) = g(w) f_t & \text{cracked state} \end{cases} \tag{A.1}$$

where E = elastic modulus; ε = elastic strain; $\sigma_w(w)$ denotes the stress-crack opening relationship with w = crack opening; and f_t = uniaxial tensile strength. The function $g(w)$ is defined as:

$$g(w) = b_i - a_i w = \begin{cases} b_1 - a_1 w & 0 \leqq w < w_1 \\ b_2 - a_2 w & w_1 \leqq w \leqq w_2 \end{cases} \tag{A.2}$$

where $b_1 \equiv 1$; and where the limits w_1 and w_2 are given by the intersection of the two line segments, and the intersection of the second line segment and the abscissa, respectively:

$$w_1 = \frac{1 - b_2}{a_1 - a_2}; \qquad w_2 = \frac{b_2}{a_2} \tag{A.3}$$

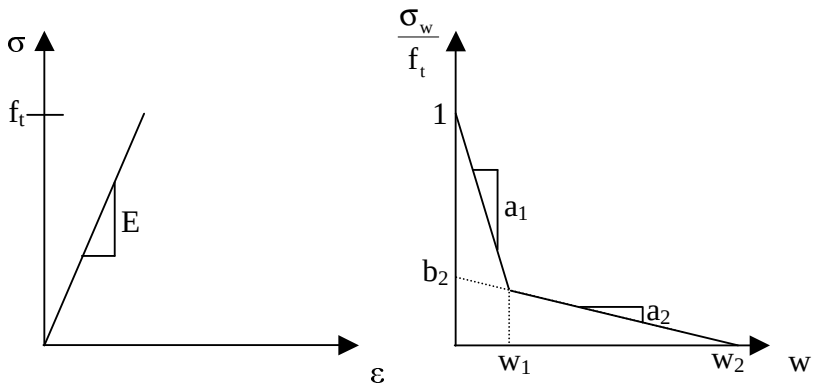

Figure A.1 *Stress-strain relationship (a) and stress-crack opening relationship (b)*

The boundaries of the hinge are assumed to be rigid and may rotate and translate. In this way, the hinge may be utilized in e.g. three point bending beams. Figure A.2 shows the geometry, loading and deformation of the hinge element.

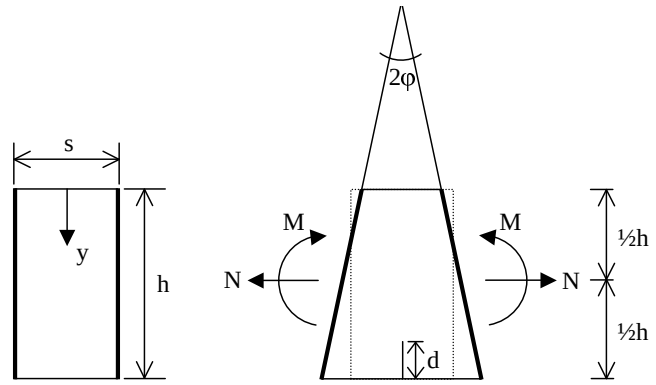

Figure A.2 *Geometry, loading and deformation of the hinge element*

Analysis of the hinge element makes it possible to determine the external normal force N and bending moment M for any given value of the angular hinge deformation φ. The

problem is solved in four phases, one for each state of crack propagation. Phase 0 represents the elastic state, where no crack has formed, while phases I, II and III represent different stages of propagation (linear, bilinear and bilinear with stress-free tail). The solution is presented in terms of normalized properties, where the following normalizations are used:

$$\beta_1 = \frac{f_t a_1 s}{E}, \qquad \beta_2 = \frac{f_t a_2 s}{E}, \qquad c = \frac{(1-b_2)(1-\beta_1)}{\beta_2 - \beta_1} \tag{A.4}$$

$$\mu = \frac{6M}{f_t h^2 t}, \qquad \rho = \frac{N}{f_t h t}, \qquad \theta = \frac{hE\varphi}{s f_t}, \qquad \alpha = \frac{d}{h} \tag{A.5}$$

The hinge solution is expressed in terms of the normalized crack depth α and the normalized moment μ as functions of the normalized hinge deformation θ and the normalized normal force ρ:

Elastic phase: $0 \leq \theta \leq 1 - \rho$

$$\alpha = 0 \tag{A.6}$$
$$\mu = \theta \tag{A.7}$$

Phase I: $1 - \rho < \theta \leq \theta_{\text{I-II}}$:

$$\alpha = 1 - \beta_1 - \sqrt{(1-\beta_1)\left(\frac{1-\rho}{\theta} - \beta_1\right)} \tag{A.8}$$
$$\mu = 4\left(1 - 3\alpha + 3\alpha^2 - \frac{\alpha^3}{1-\beta_1}\right)\theta + (6\alpha - 3)(1-\rho) \tag{A.9}$$

Phase II: $\theta_{\text{I-II}} < \theta \leq \theta_{\text{II-III}}$:

$$\alpha = 1 - \beta_2 - \frac{1-b_2}{2\theta} - \sqrt{(1-\beta_2)\left(\frac{(1-b_2)^2}{4\theta^2(\beta_1-\beta_2)} - \beta_2 + \frac{b_2-\rho}{\theta}\right)} \tag{A.10}$$
$$\mu = 4\left(1 - 3\alpha + 3\alpha^2 - \frac{\alpha^3}{1-\beta_2}\right)\theta + (6\alpha - 3)(1-\rho) - \frac{(1-b_2)\left(3\alpha^2 - \left(\frac{c}{2\theta}\right)^2\right)}{1-\beta_2} \tag{A.11}$$

Phase III: $\theta_{\text{II-III}} < \theta$:

$$\alpha = 1 - \frac{1}{2\theta}\left(1 + \sqrt{\frac{(1-b_2)^2}{\beta_1 - \beta_2} + \frac{b_2^2}{\beta_2} - 4\rho\theta}\right) \tag{A.12}$$

$$\begin{aligned}\mu &= 4\left(1 - 3\alpha + 3\alpha^2 - \alpha^3\right)\theta + (6\alpha - 3)(1-\rho) - 3\alpha^2 \\ &\quad + \frac{1}{4\theta^2}\left(1 - \frac{b_2}{\beta_2}\right)\left(1 - \frac{b_2}{\beta_2} + c\right)\left(1 + \frac{\beta_1 c}{1-\beta_1}\right) + \left(\frac{c}{2\theta}\right)^2\end{aligned} \tag{A.13}$$

The crack mouth opening displacement CMOD is given by:

$$\text{CMOD} = \frac{s f_t}{E}\frac{1 - b_i + 2\alpha\theta}{1 - \beta_i} \tag{A.14}$$

where:

$$(b_i, \beta_i) = \begin{cases} (1, \beta_1) & \text{in Phase I} \\ (b_2, \beta_2) & \text{in Phase II} \\ (0, 0) & \text{in Phase III} \end{cases} \tag{A.15}$$

Appendix B

MatLab-code, WST and TPBT short-term

The following subfunctions are listed in the following:

datared.m = Data reduction algorithm
dispmsg.m = Message displayer
E1.m = Object function, phase I
E2.m = Object function, phase II
E3.m = Object function, phase III
initialize.m = Initialization script
resplot.m = Result plotter
stimate.m = Estimation of bandwidth parameter
swcheck.m = Validity check of stress-crack opening relationship
tpbt_forward.m = TPBT, forward analysis
tpbt_inverse.m = TPBT, inverse analysis
tpbtmain.m = TPBT, main program
warn.m = Warnings displayer
wst.m = WST, program for unknown observations
wst_forward.m = WST, forward analysis
wst_inverse.m = WST, inverse analysis
wstmain.m = WST, main program

```
function [X,Y] = datared(X_full,Y_full,cs_s)
j=1;
row=2;
X = 0;
Y = 0;
peak=find(Y_full==max(Y_full));
m=peak(1);
max_Y=max(Y_full(:,1));
max_X=max(X_full(:,1));
X_full_int=X_full(:)./max_X;
Y_full_int=Y_full(:)./max_Y;
for i=2:m
    if (Y_full_int(i)>Y_full_int(j)) & ((X_full_int(i)>X_full_int(j)))
        X(row,1)=X_full(i);
        Y(row,1)=Y_full(i);
        row=row+1;
        j=i;
    end
end
for i=m+1:size(Y_full,1)
    if (Y_full_int(i)<Y_full_int(j)) & ((X_full_int(i)>X_full_int(j)))
        X(row,1)=X_full(i);
        Y(row,1)=Y_full(i);
        row=row+1;
        j=i;
    end
end
j=1;
row=2;
X_full = X;
Y_full = Y;
X = 0;
Y = 0;
peak=find(Y_full==max(Y_full));
m=peak(1);
max_Y=max(Y_full(:,1));
max_X=max(X_full(:,1));
X_full_int=X_full(:)./max_X;
Y_full_int=Y_full(:)./max_Y;
for i=2:m
    if X_full_int(i)>X_full_int(j)
        cs=((Y_full_int(i)-Y_full_int(j))^2+(X_full_int(i)...
           -X_full_int(j))^2)^0.5;
        if cs >= cs_s
            if cs <= 1.5*cs_s
```

```
                X(row,1)=X_full(i);
                Y(row,1)=Y_full(i);
                row=row+1;
                j=i;
            else
                a=(Y_full_int(i)-Y_full_int(j))/(X_full_int(i)-X_full_int(j));
                dx=sign(X_full_int(i)-X_full_int(j))*1/(1+a^2)^0.5*cs_s;
                dy=a*dx;
                k=1;
                while cs > 1.5*cs_s
                    X(row,1)=X_full(j)+k*dx*max_X;
                    Y(row,1)=Y_full(j)+k*dy*max_Y;
                    cs=((Y_full_int(i)-Y(row,1)/max_Y)^2+...
                       (X_full_int(i)-X(row,1)/max_X)^2)^0.5;
                    row=row+1;
                    k=k+1;
                end
                X(row,1)=X_full(i);
                Y(row,1)=Y_full(i);
                row=row+1;
                j=i;
            end
        end
    end
end
X(row,1)=X_full(m);
Y(row,1)=Y_full(m);
row=row+1;
i=m;
while i<=size(X_full,1)
    if X_full_int(i)>X_full_int(j)
        cs=((Y_full_int(i)-Y_full_int(j))^2+(X_full_int(i)...
           -X_full_int(j))^2)^0.5;
        if cs >= cs_s
            if cs < 1.5*cs_s
                X(row,1)=X_full(i);
                Y(row,1)=Y_full(i);
                row=row+1;
                j=i;
            else
                a=(Y_full_int(i)-Y_full_int(j))/(X_full_int(i)-X_full_int(j));
                dx=sign(X_full_int(i)-X_full_int(j))*1/(1+a^2)^0.5*cs_s;
                dy=a*dx;
                k=1;
                while cs > 1.5*cs_s
```

```
                    X(row,1)=X_full(j)+k*dx*max_X;
                    Y(row,1)=Y_full(j)+k*dy*max_Y;
                    cs=((Y_full_int(i)-Y(row,1)/max_Y)^2+...
                       (X_full_int(i)-X(row,1)/max_X)^2)^0.5;
                    row=row+1;
                    k=k+1;
                end
                X(row,1)=X_full(i);
                Y(row,1)=Y_full(i);
                row=row+1;
                j=i;
            end
        end
        i=i+1;
   else
        avg_index=find(Y_full(i:size(Y_full(:,1),1))...
                       ==max(Y_full(i:size(Y_full(:,1),1))));
        if (i+avg_index <= size(X_full,1)) & (Y_full(i)<Y_full(j))
            X(row,1)=X_full(i+avg_index);
            Y(row,1)=Y_full(i+avg_index);
            row=row+1;
            i=i+avg_index;
            j=j+avg_index;
        else
            i=i+1;
        end
    end
end
X(row,1)=X_full(size(X_full,1));
Y(row,1)=Y_full(size(X_full,1));
```

```
function disp(geometry,input,initial,output,rep,X)
disp(blanks(1)')
disp(['Geometry data from: ' blanks(1) geometry])
disp(['Exp. data from:     ' blanks(1) input])
disp(['Initial values from:' blanks(1) initial])
disp(['Output to:          ' blanks(1) output])
disp(blanks(1)')
disp(['No. of repetitions =' blanks(1) num2str(rep)])
disp(['No. of datapoints  =' blanks(1) num2str(size(X,1))])
disp(blanks(1)')
```

```
function E1 = E1(est,X,Y,geo,fix,lb,ub,type,warnings,i,rep,obstype)
inp=[fix(1);fix(2);fix(3);fix(4);est(1)];
if (est(1)<lb(5))|(est(1)>ub(5))|(swcheck(inp,stimate(inp,geo,type),0)==0)
    E1=1e12;
    warn(warnings,1,stimate(inp,geo,type),inp,lb,ub,i,rep,1);
else
    switch 1
    case strcmp(type,'wst')
        out = wstmain(geo,inp,X,0);
    case strcmp(type,'tpbt')
        out = tpbtmain(geo,inp,X,obstype,0);
    end
    E1 = sum((real(Y(1:size(out,1))-out(:,1))).^2)/size(out,1);
end
```

```
function E2 = E2(est,X,Y,geo,fix,lb,ub,type,warnings,i,rep,obstype)
inp=[est(1);est(2);fix(3);fix(4);fix(5)];
if (est(1)<lb(1))|(est(2)<lb(2))|(est(1)>ub(1))|(est(2)>ub(2))|...
        (swcheck(inp,stimate(inp,geo,type),0)==0)
    E2=1e12;
    warn(warnings,1,stimate(inp,geo,type),inp,lb,ub,i,rep,2);
else
    switch 1
    case strcmp(type,'wst')
        out = wstmain(geo,inp,X,1);
    case strcmp(type,'tpbt')
        out = tpbtmain(geo,inp,X,obstype,1);
    end
    E2 = sum((real(Y(1:size(out,1))-out(:,1))).^2)/size(out,1);
end
```

```
function E3 = E3(est,X,Y,geo,fix,lb,ub,type,warnings,i,rep,obstype)
inp=[fix(1);fix(2);est(1);est(2);fix(5)];
if (est(1)<lb(3))|(est(2)<lb(4))|(est(1)>ub(3))|(est(2)>ub(4))...
        |(swcheck(inp,stimate(inp,geo,type),0)==0)
    E3=1e12;
    warn(warnings,1,stimate(inp,geo,type),inp,lb,ub,i,rep,3);
else
    switch 1
    case strcmp(type,'wst')
        out = wstmain(geo,inp,X,1);
    case strcmp(type,'tpbt')
        out = tpbtmain(geo,inp,X,obstype,1);
    end
    E3 = sum((real(Y(1:size(out,1))-out(:,1))).^2)/size(out,1);
end
```

```
function ini = initialize(geo,X,Y,type,output,obstype)
options = optimset('Display','off','MaxFunEvals',5000,...
          'MaxIter',5000,'TolFun',1e-13);
switch 1
case strcmp(type,'wst')
    [X,Y] = datared(X,Y,0.09);
    m = geo(1); a0 = geo(2); am = geo(3); b = geo(4); bm = geo(5);
    d1 = geo(6); d2 = geo(7); h = geo(8); L = geo(9); t = geo(10);
    mu = geo(11); alpha_w = geo(12);
    if size(geo,1)==12
        y = (b-h)/b;
        v2 = y/(1-y)^2*(38.2-55.4*y+33.0*y^2);
    else
        v2 = geo(13);
    end
    A_1 = bm*(L-h-a0); A_2 = (L/2-am/2)*a0; A_3 = L/2*h;
    A = A_1 + A_2 + A_3;
    e = (L/2-bm/2)*A_1/A + (L/4+am/2)*A_2/A + L/4*A_3/A;
    kmu = (2*tan(alpha_w/180*pi)+2*mu)/(1-mu*tan(alpha_w/180*pi));
    ini(1,1) = 0.5*(max(Y)*(6*d2+3*d1*kmu-2*h)+6*(m/2)*9.82*e)/h^2/t;
    ini(4,1) = 0.5;
    ini(5,1) = X(1:ceil(find(Y==max(Y))/4))\Y(1:ceil(find(Y==max(Y))/4))/t*v2;
    a1 = [5;20;80;160];
    a2 = [0.05;0.20;0.80;1.60;3.20];
    for i=1:size(a1(:,1))
        for j=1:size(a2(:,1))
            b(i,j) = fzero(@fun,0.5,options,[ini(1,1);a1(i);a2(j);ini(4,1);...
                     ini(5,1)],X,Y,h,t);
            if (b(i,j) > 0) & (b(i,j) < 1) & (swcheck([ini(1,1); a1(i,1);...
                        a2(j,1); b(i,j); ini(5,1)],stimate([ini(1,1);...
                        a1(i,1); a2(j,1); b(i,j); ini(5,1)],geo,'wst'),0)==1)
                out = wstmain(geo,[ini(1,1);a1(i);a2(j);b(i,j);ini(5,1)],X,1);
                E(i,j) = sum((real(Y(1:size(out,1))-out(:,1))).^2)/size(out,1);
            else
                E(i,j)=Inf;
            end
        end
    end
    if (sum(sum(E(:,:)<Inf)) > 0)
        [i,j]=find(E==min(min(E)));
        ini(2,1) = a1(i,1);
        ini(3,1) = a2(j,1);
        ini(4,1) = b(i,j);
        if swcheck(ini,stimate(ini,geo,'wst'),0)==0
            errormsg(output)
```

```
        end
    else
        errormsg(output)
    end
case strcmp(type,'tpbt')
    [X,Y] = datared(X,Y,0.01);
    a0 = geo(1); H = geo(2); L = geo(3); t = geo(4);
    m = geo(5); d0 = geo(6); h = H-a0;
    if size(geo,1)==6
        y = a0/H;
        y1 = (a0+d0)/(H+d0);
        v1_stang = (a0+d0)/(a0)*(0.76-2.28*y+3.87*y^2-2.04*y^3+0.66/(1-y)^2);
                   %See ref. [11]
        v1_karihaloo = 0.76-2.28*y1+3.87*y1^2-2.04*y1^3+0.66/(1-y1)^2;
                   % See ref. [10]
        v1 = (v1_stang+v1_karihaloo)/2;
                   %This latter relation corresponds very well
                   %with FEM conducted on the Rilem beam
        v2 = (y/(1-y))^2*(5.58-19.57*y+36.82*y^2-34.94*y^3+12.77*y^4);
    else
        v1=geo(7);
        v2=geo(8);
    end
    ini(1,1) = 0.5*3/2*max(Y)*L/t/h^2;
    ini(4,1) = 0.5;
    if strcmp(obstype,'cmod')==1
        ini(5,1) = X(2:ceil(find(Y==max(Y))/4))\Y(2:ceil(find(Y==max(Y))/4))...
                   *6*v1*L*a0/t/H^2;
    elseif strcmp(obstype,'u')==1
        ini(5,1) = X(2:ceil(find(Y==max(Y))/4))\Y(2:ceil(find(Y==max(Y))/4))...
                   /4/h^2/t*(h/H)^2*L^2*(L/H+6*v2);
    end
    a1 = [5;20;80;160];
    a2 = [0.05;0.20;0.80;1.60;3.20];
    for i=1:size(a1(:,1))
        for j=1:size(a2(:,1))
            b(i,j) = fzero(@fun,0.5,options,[ini(1,1);a1(i);a2(j);ini(4,1)...
                     ;ini(5,1)],X,Y,h,t);
            if (b(i,j) > 0) & (b(i,j) < 1) & ((swcheck([ini(1,1); a1(i,1);...
                        a2(j,1); b(i,j); ini(5,1)],stimate([ini(1,1);...
                        a1(i,1); a2(j,1); b(i,j); ini(5,1)],geo,'tpbt'),0)==1))
                out = tpbtmain(geo,[ini(1,1);a1(i);a2(j);b(i,j);ini(5,1)],...
                      X,obstype,1);
                E(i,j) = sum((real(Y(1:size(out,1))-out(:,1))).^2)/size(out,1);
            else
```

```
                E(i,j)=Inf;
            end
        end
    end
    if (sum(sum(E(:,:)<Inf)) > 0)
        [i,j]=find(E==min(min(E)));
        ini(2,1) = a1(i,1);
        ini(3,1) = a2(j,1);
        ini(4,1) = b(i,j);
        if swcheck(ini,stimate(ini,geo,'tpbt'),0)==0
            errormsg(output)
        end
    else
        errormsg(output)
    end
end
function fun = fun(b2,ini,X,Y,h,t)
fun=1/2*ini(1)*(b2/ini(3)+(1-b2)/(ini(2)-ini(3))*(ini(3)-ini(2)*b2)/ini(3))...
    -trapz(X,Y)/h/t;
function errormsg(output)
disp('Initialization algorithm  has failed due to the below mentioned reason.')
disp('Please conduct a manual initialization. The best estimate on the'...
     'constitutive')
disp(['parameters obtained by the algorithm is stored in ' output '.'...
      'Only ft and E'])
disp('will be meaningful in this file.')
disp(blanks(1)')
```

```
function resplot(X,Y,out,datafile,name_X)
hold off
plot(X(:),Y(:),'-o','MarkerSize',6);
hold on
plot(X(:),out(:,1),'-x','MarkerSize',6);
title(datafile,'FontSize',14,'interpreter','none')
xlabel(name_X,'FontSize',14)
ylabel('P             ','Rotation',0,'FontSize',14)
axis([0 1.1*max(X) 0 1.1*max([max(Y);max(out(:,1))])])
saveas(gcf,[strtok(datafile,'.') '.fig'])
```

```
function s = stimate(inp,geo,type)
switch 1
case strcmp(type,'wst')
%    s=0.20*geo(8); %This value fits experimental results [8]
    s=0.84*geo(8); %This value fits FEM calculations [6]
case strcmp(type,'tpbt')
%    s=0.70*geo(2);%This value fits experimental results [8]
    s=0.50*geo(2); %This value fits FEM calculations [8], [2]
end
```

```
function swcheck = swcheck(inp,s,output)
beta1 = inp(1)*inp(2)*s/inp(5);
beta2 = inp(1)*inp(3)*s/inp(5);
w1=(1-inp(4))/(inp(2)-inp(3));
s1=inp(4)-inp(3)*w1;
switch 1
case output == 0
    if (beta1 >= 1)|(beta1 == 0)|(isinf(beta1) == 1)|(beta2 <= 0)...
            |(beta2 >= 1)|(beta2 == beta1)|(w1 <= 0)|(s1 <= 0)|...
            (isnan(inp(1))==1)|(isnan(inp(2))==1)|(isnan(inp(3))==1)...
            |(isnan(inp(4))==1)|(isnan(inp(5))==1)
        swcheck=0;
    else
        swcheck=1;
    end
case output == 1
    switch 1
    case (beta1 >= 1), disp('Invalid s-w curve. beta1>=1')
        swcheck=0;
    case (beta1 == 0), disp('Invalid s-w curve. beta1=0')
        swcheck=0;
    case (isinf(beta1) == 1), disp('Invalid s-w curve. beta1=inf')
        swcheck=0;
    case (beta2 <= 0), disp('Invalid s-w curve. beta2<=0')
        swcheck=0;
    case (beta2 >= 1), disp('Invalid s-w curve. beta2>=1')
        swcheck=0;
    case (beta2 == beta1), disp('Invalid s-w curve. beta1=beta2')
        swcheck=0;
    case (w1 <= 0), disp('Invalid s-w curve. w1<=0')
        swcheck=0;
    case (s1 <= 0), disp('Invalid s-w curve. s1<=0')
        swcheck=0;
    case (isnan(inp(1))==1),disp('Invalid tensile strength. ft = NaN')
        swcheck=0;
    case (isnan(inp(2))==1),disp('Invalid first slope. a1 = NaN')
        swcheck=0;
    case (isnan(inp(3))==1),disp('Invalid second slope. a2 = NaN')
        swcheck=0;
    case (isnan(inp(4))==1),disp('Invalid cut-off. b2 = NaN')
        swcheck=0;
    case (isnan(inp(5))==1),disp('Invalid Youngs modulus. E = NaN')
        swcheck=0;
    otherwise
        swcheck=1;
```

```
    end
end
```

```
function tpbt_forward(input,output,estimates,obstype,geometry,red)
tic
if (nargin==0)|(nargin==1)|(nargin==2)|(nargin>6)
    disp('Input not correctly specified')
else
    if nargin <= 5
        red = 0.02;
    end
    if nargin == 4
        geometry = 'tpbtgeometry.dat';
    end
    geo=textread(geometry);
    data=textread(input);
    est=textread(estimates);
    if (swcheck(est,stimate(est,geo,'tpbt'),1) == 1)&((strcmp(obstype,...
            'cmod')&geo(1)>0)|(strcmp(obstype,'u')))
        [X,Y]=datared(data(:,1),data(:,2),red);
        out=tpbtmain(geo,est,X,obstype,1);
        resplot(X(1:size(out,1)),Y(1:size(out,1)),out,input,obstype)
        dlmwrite(output,[X(1:size(out,1)) out],'\t')
        disp(['Time =' blanks(1) num2str(toc,3) blanks(1) 'sec'])
    elseif (strcmp(obstype,'cmod'))&(geo(1)==0)
        disp('CMOD as input is not supported for unnotched beams')
    end
end
```

```
function tpbt_inverse(input,obstype,geometry,output,initial,red,rep,tol)
% Inverse Analysis of the Three Point Bending Test (TPBT)
% Version 050303
%
% Written and copyrighted (2003) by
% M.Sc. Ph.D.-student Lennart Østergaard
% Department of Civil Engineering
% Technical University of Denmark
% Brovej, Building 118
% DK-2800 Kgs. Lyngby
% Denmark
% Fax:   (+45) 45 88 32 82
% Email: los@byg.dtu.dk
%
% This program determines a bilinear estimate of the stress-crack opening
% relationship of the material under analysis based on experimental load-
% deflection or load-crack mouth opening displacement (CMOD) results.
%
% The program is freeware. The author takes no responsibility for any use of
% the program and the user is encouraged to validate the results by other
% means.
%
% The methods used in the program are described in the papers referred in
% the Readme-file. Published results obtained by the program should refer
% the program and paper nos. [4] and [5].
%
tic
if (nargin==0)|(nargin==6)|(nargin==7)|(nargin>8)
    disp('Input not correctly specified')
else
    data = textread(input);
    if nargin <= 2
        geometry = 'tpbtgeometry.dat';
        if nargin == 1
            obstype = 'u';
    end,end
    if nargin <= 5
        red = 0.009;
        rep = 20;
        tol = 0.01;
        if nargin <= 4
            initial = [strtok(input,'.') '-ini' '.dat'];
            dlmwrite(initial,initialize(textread(geometry),data(:,1),...
                data(:,2),'tpbt',initial,obstype),'\t')
            if nargin <= 3
```

```
            output = [strtok(input,'.') '.out'];
end,end,end
fix = textread(initial);
geo = textread(geometry);
warnings = [strtok(input,'.') '_WARNINGS.dat'];
warn(warnings,0)
if (swcheck(fix,stimate(fix,geo,'tpbt'),1) == 1)&((strcmp(obstype,...
        'cmod')&geo(1)>0)|(strcmp(obstype,'u')))
    [X,Y]=datared(data(:,1),data(:,2),red);
    [lb ub]=textread('boundaries.dat','%f %f');
    options=optimset('TolX',0.01,'TolFun',0.01);
    dispmsg(geometry,input,initial,output,rep,X)
    i=1;err=1;
    while (i <= rep) & (err > tol)
        fix(5)=fminsearch('E1',fix(5),options,X,Y,geo,fix,lb,ub,...
            'tpbt',warnings,i,rep,obstype);
        disp(['Fit session no.' blanks(1) num2str(i) blanks(1)...
                'for E completed'])
        fix(1:2)=fminsearch('E2',[fix(1);fix(2)],options,X,Y,geo,...
            fix,lb,ub,'tpbt',warnings,i,rep,obstype);
        disp(['Fit session no.' blanks(1) num2str(i) blanks(1)...
                'for ft and a1 completed'])
        fix(3:4)=fminsearch('E3',[fix(3);fix(4)],options,X,Y,geo,...
            fix,lb,ub,'tpbt',warnings,i,rep,obstype);
        disp(['Fit session no.' blanks(1) num2str(i) blanks(1)...
                'for a2 and b2 completed'])
        out=tpbtmain(geo,fix,X,obstype,1);
        results(1:5,i)=fix;
        results(6,i)=1/2*fix(1)*(fix(4)/fix(3)+(1-fix(4))/(fix(2)...
            -fix(3))*(fix(3)-fix(2)*fix(4))/fix(3));
        results(7,i)=results(6,i)*fix(5)/fix(1)^2;
        results(8,i)=sqrt(sum((real(Y(:)-out(:,1))).^2)/size(out,1))...
            /max(Y)*100;
        if i > 1
            err = max(abs((results(1:7,i-1)-results(1:7,i))./...
                results(1:7,i)));
        end
        i=i+1;
        dlmwrite(output,results','\t')
    end
    if err > tol
        disp(['Max number of iterations reached. Relative error: ' ...
                num2str(100*err) ' %'])
    else
        disp(['Convergence achieved after ' num2str(i-1) ' iterations.'])
```

```
        end
        resplot(X,Y,out,input,obstype)
        disp(blanks(1)'), disp(['Time =' blanks(1) num2str(toc/60,3)...
                blanks(1) 'min'])
    elseif (strcmp(obstype,'cmod'))&(geo(1)==0)
        disp('CMOD as input is not supported for unnotched beams')
    end
end
```

```
function pre = tpbtmain(geo,est,obs,obstype,p)
a0 = geo(1); H = geo(2); L = geo(3); t = geo(4); m=geo(5); d0=geo(6); h=H-a0;
s=stimate(est,geo,'tpbt'); g=9.82;
ft=est(1); a1=est(2); a2=est(3); b2=est(4); E=est(5);
beta1 = ft*a1*s/E; beta2 = ft*a2*s/E;
if size(geo,1)==6
    y = a0/H;
    y1 = (a0+d0)/(H+d0);
    v1_stang = (a0+d0)/(a0)*(0.76-2.28*y+3.87*y^2-2.04*y^3+0.66/(1-y)^2);
               %See ref. [11]
    v1_karihaloo = 0.76-2.28*y1+3.87*y1^2-2.04*y1^3+0.66/(1-y1)^2;
               % See ref. [10]
    v1 = (v1_stang+v1_karihaloo)/2;
               %This latter relation corresponds very well
               %with FEM conducted on the Rilem beam [8]
    v2 = (y/(1-y))^2*(5.58-19.57*y+36.82*y^2-34.94*y^3+12.77*y^4);
else
    v1=geo(7);
    v2=geo(8);
end
c = (1-b2)*(1-beta1)/(beta2-beta1);
theta_1_2 = 1/2*(1-c+sqrt((1-c)^2+c^2/(beta1-1)));
theta_2_3 = 1/2*(b2/beta2+sqrt((1-b2)^2/(beta1-beta2)+b2^2/beta2));
cmod_0 = 4*a0*ft/E*(h/H)^2*v1-3*m*g*L/t/H^2/E*a0*v1;
u_0 = ft*L/h/E*(h/H)^2*(L/6*(h/H)+h*v2)-m*g/E/t*(3/4*(L/h)^2*v2+1/8*(L/H)^3);
row = 1; theta = 1;
options = optimset('Display','off','MaxFunEvals',50000,'MaxIter',50000,...
    'TolFun',1e-13);
if strcmp(obstype,'cmod')==1
    while obs(row) <= cmod_0
        pre(row,1)=1/6*E*t*H^2/a0/L/v1*obs(row);
        row=row+1;
    end
elseif strcmp(obstype,'u')==1
    while obs(row) <= u_0
        pre(row,1)=4*h^2*t*E*obs(row)*(H/h)^2/L^2/(L/H+6*v2);
        row=row+1;
    end
end
if p > 0
    for row=row:size(obs,1)
        theta = fzero(@fun,theta,options,theta_1_2,theta_2_3,beta1,beta2,...
            b2,c,a0,d0,ft,E,h,H,v1,v2,s,L,obstype,obs(row));
        pre(row,1)=2/3*ft*h^2*t/L*mu(theta,theta_1_2,theta_2_3,beta1,beta2,...
            b2,c)-1/2*m*g;
```

```
    end
end
function f = fun(theta,theta_1_2,theta_2_3,beta1,beta2,b2,c,a0,d0,ft,E,h,...
    H,v1,v2,s,L,obstype,obs)
if strcmp(obstype,'cmod')==1
    switch 1
    case theta <= theta_1_2
        alpha = 1-beta1-sqrt((1-beta1)*(1/theta-beta1));
        bi = 1; betai=beta1;
    case theta <= theta_2_3
        alpha = 1-beta2-(1-b2)/2/theta-sqrt((1-beta2)*((1-b2)^2/4/theta^2/...
            (beta1-beta2)-beta2+b2/theta));
        bi = b2; betai=beta2;
    case theta > theta_2_3
        alpha = 1-1/2/theta*(1+sqrt((1-b2)^2/(beta1-beta2)+b2^2/beta2));
        bi = 0; betai=0;
    end
    f = s*ft/E*(1-bi+2*alpha*theta)/(1-betai)+4*a0*ft/E*mu(theta,theta_1_2,...
        theta_2_3,beta1,beta2,b2,c)*(h/H)^2*v1+2*(a0+d0)*s*ft/h/E*(theta-1)...
        -obs;
elseif strcmp(obstype,'u')==1
    f = theta+(L/3/s*(h/H)^3+2*h/s/(H/h)^2*v2-1)*mu(theta,theta_1_2,...
        theta_2_3,beta1,beta2,b2,c)-obs*2*h*E/s/ft/L;
end
function mu = mu(theta,theta_1_2,theta_2_3,beta1,beta2,b2,c)
switch 1
case theta <= theta_1_2
    alpha = 1-beta1-sqrt((1-beta1)*(1/theta-beta1));
    mu = 4*(1-3*alpha+3*alpha^2-alpha^3/(1-beta1))*theta+(6*alpha-3);
case theta <= theta_2_3
    alpha = 1-beta2-(1-b2)/2/theta-sqrt((1-beta2)*((1-b2)^2/4/theta^2/...
        (beta1-beta2)-beta2+b2/theta));
    mu = 4*(1-3*alpha+3*alpha^2-alpha^3/(1-beta2))*theta+(6*alpha-3)-...
        (1-b2)*(3*alpha^2-(c/2/theta)^2)/(1-beta2);
case theta > theta_2_3
    alpha = 1-1/2/theta*(1+sqrt((1-b2)^2/(beta1-beta2)+b2^2/beta2));
    mu = 4*theta*(1-3*alpha+3*alpha^2-alpha^3)+(6*alpha-3)-3*alpha^2+...
        1/4/theta^2*(1-b2/beta2)*(1-b2/beta2+c)*(1+beta1*c/(1-beta1))+...
        (c/2/theta)^2;
end
```

```
function warn(warnings,p,s,inp,lb,ub,i,rep,phase)
switch 1
case (p == 0)
    if which(warnings) | 0
        fid = fopen(warnings,'w+');
        fprintf(fid,'This file contains warnings generated during inverse'...
            'analysis. Pls. check your results if any warnings have been'...
            'generated\n\n');
        fclose(fid);
    end
case (p == 1)
    WT = WarningType(inp,s,lb,ub);
    if which(warnings) | 0
        fid = fopen(warnings,'a');
        fprintf(fid,'Warning: The optimization was limited by: %s. '...
            '\nValues of parameters: [%8.5e %8.5e %8.5e %8.5e %8.5e].'...
            ' Phase %1.0f. Repetition: %1.0f\n',WT,inp,phase,i);
        fclose(fid);
    else
        fid = fopen(warnings,'w+');
        fprintf(fid,'This file contains warnings generated during inverse'...
            'analysis. Pls. check your results if any warnings have been '...
            'generated\n\n');
        fprintf(fid,'Warning: The optimization was limited by: %s. '...
            '\nValues of parameters: [%8.5e %8.5e %8.5e %8.5e %8.5e]. '...
            'Phase %1.0f. Repetition: %1.0f\n',WT,inp,phase,i);
        fclose(fid);
    end
end
function WarningType = WarningType(inp,s,lb,ub)
beta1 = inp(1)*inp(2)*s/inp(5);
beta2 = inp(1)*inp(3)*s/inp(5);
w1=(1-inp(4))/(inp(2)-inp(3));
s1=inp(4)-inp(3)*w1;
switch 1
case (beta1 >= 1), WarningType = 'Invalid s-w curve. beta1>=1';
case (beta1 == 0), WarningType = 'Invalid s-w curve. beta1=0';
case (isinf(beta1) == 1), WarningType = 'Invalid s-w curve. beta1=inf';
case (beta2 <= 0), WarningType = 'Invalid s-w curve. beta2<=0';
case (beta2 >= 1), WarningType = 'Invalid s-w curve. beta2>=1';
case (beta2 == beta1), WarningType = 'Invalid s-w curve. beta1=beta2';
case (w1 <= 0), WarningType = 'Invalid s-w curve. w1<=0';
case (s1 <= 0), WarningType = 'Invalid s-w curve. s1<=0';
case (inp(1)<lb(1)), WarningType = 'ft < lb';
case (inp(2)<lb(2)), WarningType = 'a1 < lb';
```

```
case (inp(3)<lb(3)), WarningType = 'a2 < lb';
case (inp(4)<lb(4)), WarningType = 'b2 < lb';
case (inp(5)<lb(5)), WarningType = 'E < lb';
case (inp(1)>ub(1)), WarningType = 'ft > ub';
case (inp(2)>ub(2)), WarningType = 'a1 > ub';
case (inp(3)>ub(3)), WarningType = 'a2 > ub';
case (inp(4)>ub(4)), WarningType = 'b2 > ub';
case (inp(5)>ub(5)), WarningType = 'E > ub';
case (isnan(inp(1))==1),WarningType = 'Invalid tensile strength. ft = NaN';
case (isnan(inp(2))==1),WarningType = 'Invalid first slope. a1 = NaN';
case (isnan(inp(3))==1),WarningType = 'Invalid second slope. a2 = NaN';
case (isnan(inp(4))==1),WarningType = 'Invalid cut-off. b2 = NaN';
case (isnan(inp(5))==1),WarningType = 'Invalid Youngs modulus. E = NaN';
otherwise WarningType = 'Unknown';
end
```

```
function out=wst(estimates,output,geometry,step,min_load,actout,actplot)
if nargin <=6
    actplot = 1;
    if nargin <= 5;
        actout = 0;
        if nargin <= 4
            min_load = 1;
            if nargin <= 3
                step = 0.1;
                if nargin <= 2
                    geometry = 'wstgeometry.dat';
                    if nargin == 1
                        output = 'wst.out';
end,end,end,end,end,end
est=textread(estimates);
geo=textread(geometry);
m = geo(1); a0 = geo(2); am = geo(3); b = geo(4); bm = geo(5); d1 = geo(6);
d2 = geo(7); h = geo(8); L = geo(9); t = geo(10); mu = geo(11);
alpha_w = geo(12);
s=stimate(est,geo,'wst');
g = 9.82;
ft=est(1); a1=est(2); a2=est(3); b2=est(4); E=est(5);
m = m/2;
alpha_w = alpha_w/180*pi;
beta1 = ft*a1*s/E; beta2 = ft*a2*s/E;
A_1 = bm*(L-h-a0); A_2 = (L/2-am/2)*a0; A_3 = L/2*h;
A = A_1 + A_2 + A_3;
e = (L/2-bm/2)*A_1/A + (L/4+am/2)*A_2/A + L/4*A_3/A;
if size(geo,1)==12
    y = (b-h)/b;
    v2 = y/(1-y)^2*(38.2-55.4*y+33.0*y^2);
else
    v2 = geo(13);
end
kmu = (2*tan(alpha_w)+2*mu)/(1-mu*tan(alpha_w));
c = (1-b2)*(1-beta1)/(beta2-beta1);
p_0 = (ft*h^2*t-6*m*g*e)/(6*d2+3*d1*kmu-2*h);
theta_0_1 = 1 - 1/(ft*h*t)*p_0;
cmod_0 = p_0/E/t*v2;
row = 3;
res = [0      0   0 0 0;... %cmod P alpha theta phase
       cmod_0 p_0 0 1 0];
options = optimset('Display','off','MaxFunEvals',5000,'MaxIter',5000,...
    'TolFun',1e-13);
while res(row-1,2) >= min_load
```

```
    res(row,4) = res(row-1,4)+step*res(row-1,4);
    res(row,2) = fsolve(@fun,res(row-1,2),options,ft,h,t,c,beta1,beta2,...
        b2,d2,kmu,d1,m,g,e,s,E,b,res(row,4));
    [res(row,1), res(row,3), res(row,5)] = params(res(row,2),ft,h,t,c,...
        beta1,beta2,b2,d2,kmu,d1,m,g,e,s,E,b,theta_0_1,v2,res(row,4));
    row = row + 1;
end
if actout == 1
    out = res;
end
if actplot == 1
    hold off
    plot(res(:,1),res(:,2),'-o','MarkerSize',6);
    hold on
    title(['P-CMOD curve based on "' estimates '"'],'FontSize',12,...
        'interpreter','none')
    xlabel('CMOD','FontSize',14)
    ylabel('P             ','Rotation',0,'FontSize',14)
    axis([0 1.1*max(res(:,1)) 0 1.1*max(res(:,2))])
end
dlmwrite(output,res,'\t')
function F = fun(x,ft,h,t,c,beta1,beta2,b2,d2,kmu,d1,m,g,e,s,E,b,theta)
rho = 1/(ft*h*t)*x;
theta_1_2 = 1/2*(1-rho-c+sqrt((1-rho-c)^2+c^2/(beta1-1)));
theta_2_3 = 1/2*(rho*(beta2-1)+b2/beta2+sqrt(rho^2*(beta2-1)^2+2*rho...
    *(beta2-1)*b2/beta2+(1-b2)^2/(beta1-beta2)+b2^2/beta2));
switch 1
case theta <= theta_1_2
    alpha = 1-beta1-sqrt((1-beta1)*((1-rho)/theta-beta1));
    mu = 4*(1-3*alpha+3*alpha^2-alpha^3/(1-beta1))*theta+(6*alpha-3)*(1-rho);
case theta <= theta_2_3
    alpha = 1-beta2-(1-b2)/2/theta-sqrt((1-beta2)*((1-b2)^2/4/theta^2/...
        (beta1-beta2)-beta2+(b2-rho)/theta));
    mu = 4*(1-3*alpha+3*alpha^2-alpha^3/(1-beta2))*theta+(6*alpha-3)...
        *(1-rho)-(1-b2)*(3*alpha^2-(c/2/theta)^2)/(1-beta2);
case theta > theta_2_3
    alpha = 1-1/2/theta*(1+sqrt((1-b2)^2/(beta1-beta2)+b2^2/beta2-...
        4*rho*theta));
    mu = 4*theta*(1-3*alpha+3*alpha^2-alpha^3)+(6*alpha-3)*(1-rho)-...
        3*alpha^2+1/4/theta^2*(1-b2/beta2)*(1-b2/beta2+c)*(1+beta1...
        *c/(1-beta1))+(c/2/theta)^2;
end
F = mu-6/(ft*h^2*t)*(x*(d2-h/2)+1/2*kmu*x*d1+m*g*e);
function [cmod, alpha, phase] = params(x,ft,h,t,c,beta1,beta2,b2,...
    d2,kmu,d1,m,g,e,s,E,b,theta_0_1,v2,theta)
```

```
rho = 1/(ft*h*t)*x;
theta_1_2 = 1/2*(1-rho-c+sqrt((1-rho-c)^2+c^2/(beta1-1)));
theta_2_3 = 1/2*(rho*(beta2-1)+b2/beta2+sqrt(rho^2*(beta2-1)^2+2*...
    rho*(beta2-1)*b2/beta2+(1-b2)^2/(beta1-beta2)+b2^2/beta2));
switch 1
case theta <= theta_1_2
    alpha = 1-beta1-sqrt((1-beta1)*((1-rho)/theta-beta1));
    bi = 1; betai=beta1;
    phase = 1;
case theta <= theta_2_3
    alpha = 1-beta2-(1-b2)/2/theta-sqrt((1-beta2)*((1-b2)^2/4/...
        theta^2/(beta1-beta2)-beta2+(b2-rho)/theta));
    bi = b2; betai=beta2;
    phase = 2;
case theta > theta_2_3
    alpha = 1-1/2/theta*(1+sqrt((1-b2)^2/(beta1-beta2)+b2^2/...
        beta2-4*rho*theta));
    bi = 0; betai=0;
    phase = 3;
end
cmod = s*ft/E*(1-bi+2*alpha*theta)/(1-betai)+2*(b-h)*((s*ft/...
    E*(1-bi+2*alpha*theta)/(1-betai))/2/alpha/h-s*ft/h/E*theta_0_1/...
    (1-beta1))+x/E/t*v2;
```

```
function wst_forward(input,output,estimates,geometry,red)
tic
if (nargin==0)|(nargin==1)|(nargin==2)|(nargin>5)
    disp('Input not correctly specified')
else
    if nargin <= 4
        red = 0.009;
    end
    if nargin == 3
        geometry = 'wstgeometry.dat';
    end
    geo=textread(geometry);
    data=textread(input);
    est=textread(estimates);
    if swcheck(est,stimate(est,geo,'wst'),1) == 1
        [X,Y]=datared(data(:,1),data(:,2),red);
        out=wstmain(geo,est,X,1);
        resplot(X,Y,out,input,'cmod')
        dlmwrite(output,[X out],'\t')
        disp(['Time =' blanks(1) num2str(toc,3) blanks(1) 'sec'])
    end
end
```

```
function wst_inverse(input,geometry,output,initial,red,rep,tol)
% Inverse Analysis of the Wedge Splitting Test (WST)
% Version 050303
%
% Written and copyrighted (2003) by
% M.Sc. Ph.D.-student Lennart Østergaard
% Department of Civil Engineering
% Technical University of Denmark
% Brovej, Building 118
% DK-2800 Kgs. Lyngby
% Denmark
% Fax:   (+45) 45 88 32 82
% Email: los@byg.dtu.dk
%
% This program determines a bilinear estimate of the stress-crack opening
% relationship of the material under analysis based on experimental load-
% crack mouth opening displacement (CMOD) results.
%
% The program is freeware. The author takes no responsibility for any use
% of the program and the user is encouraged to validate the results by other
% means.
%
% The methods used in the program are described in the papers referred in
% the Readme-file. Published results obtained by the program should refer
% the program and paper nos. [5] and [6].
%
tic
if (nargin==0)|(nargin==5)|(nargin==6)|(nargin>7)
    disp('Input not correctly specified')
else
    data = textread(input);
    if nargin == 1
        geometry = 'wstgeometry.dat';
    end
    if nargin <= 4
        red = 0.009;
        rep = 20;
        tol = 0.01;
        if nargin <= 3
            initial = [strtok(input,'.') '-ini' '.dat'];
            dlmwrite(initial,initialize(textread(geometry),data(:,1)...
                ,data(:,2),'wst',initial,'cmod'),'\t')
            if nargin <= 2
                output = [strtok(input,'.') '.out'];
    end,end,end
```

```
fix = textread(initial);
geo = textread(geometry);
warnings = [strtok(input,'.') '_WARNINGS.dat'];
warn(warnings,0)
if swcheck(fix,stimate(fix,geo,'wst'),1) == 1
    [X,Y]=datared(data(:,1),data(:,2),red);
    [lb ub]=textread('boundaries.dat','%f %f');
    options=optimset('TolX',0.01,'TolFun',0.01);
    dispmsg(geometry,input,initial,output,rep,X)
    i=1;err=1;
    while (i <= rep) & (err > tol)
        fix(5)=fminsearch('E1',fix(5),options,X,Y,geo,fix...
            ,lb,ub,'wst',warnings,i,rep);
        disp(['Fit session no.' blanks(1) num2str(i) blanks(1)...
                'for E completed'])
        fix(1:2)=fminsearch('E2',[fix(1);fix(2)],options,X,Y,geo,...
            fix,lb,ub,'wst',warnings,i,rep);
        disp(['Fit session no.' blanks(1) num2str(i) blanks(1)...
                'for ft and a1 completed'])
        fix(3:4)=fminsearch('E3',[fix(3);fix(4)],options,X,Y,geo,...
            fix,lb,ub,'wst',warnings,i,rep);
        disp(['Fit session no.' blanks(1) num2str(i) blanks(1)...
                'for a2 and b2 completed'])
        out=wstmain(geo,fix,X,1);
        results(1:5,i)=fix;
        results(6,i)=1/2*fix(1)*(fix(4)/fix(3)+(1-fix(4))/(fix(2)...
            -fix(3))*(fix(3)-fix(2)*fix(4))/fix(3));
        results(7,i)=results(6,i)*fix(5)/fix(1)^2;
        results(8,i)=sqrt(sum((real(Y(:)-out(:,1))).^2)/size(out,1))...
            /max(Y)*100;
        if i > 1
            err = max(abs((results(1:7,i-1)-results(1:7,i))./...
                results(1:7,i)));
        end
        i=i+1;
        dlmwrite(output,results','\t')
    end
    if err > tol
        disp(['Max number of iterations reached. Max. relative error: '...
                num2str(100*err) ' %'])
    else
        disp(['Convergence achieved after ' num2str(i-1) ' iterations.'])
    end
    resplot(X,Y,out,input,'cmod')
    disp(blanks(1)'), disp(['Time elapsed =' blanks(1) num2str(toc/60,4)...
```

```
                blanks(1) 'min'])
    end
end
```

```
function pre = wstmain(geo,est,obs,p)
m = geo(1); a0 = geo(2); am = geo(3); b = geo(4); bm = geo(5); d1 = geo(6);
d2 = geo(7); h = geo(8); L = geo(9); t = geo(10); mu = geo(11);
alpha_w = geo(12);
s=stimate(est,geo,'wst'); g = 9.82;
ft=est(1); a1=est(2); a2=est(3); b2=est(4); E=est(5);
m = m/2;
alpha_w = alpha_w/180*pi;
beta1 = ft*a1*s/E; beta2 = ft*a2*s/E;
A_1 = bm*(L-h-a0); A_2 = (L/2-am/2)*a0; A_3 = L/2*h;
A = A_1 + A_2 + A_3;
e = (L/2-bm/2)*A_1/A + (L/4+am/2)*A_2/A + L/4*A_3/A;
if size(geo,1)==12
    y = (b-h)/b;
    v2 = y/(1-y)^2*(38.2-55.4*y+33.0*y^2);
else
    v2 = geo(13);
end
kmu = (2*tan(alpha_w)+2*mu)/(1-mu*tan(alpha_w));
c = (1-b2)*(1-beta1)/(beta2-beta1);
p_0 = (ft*h^2*t-6*m*g*e)/(6*d2+3*d1*kmu-2*h);
theta_0_1 = 1 - 1/(ft*h*t)*p_0;
cmod_0 = p_0/E/t*v2;
row = 1;
options = optimset('Display','off','MaxFunEvals',50000,'MaxIter',50000,...
    'TolFun',1e-13);
x = [1.01*theta_0_1 ; 1.01*p_0];
while obs(row) <= cmod_0
    pre(row,1)=obs(row)*E*t/v2;
    row=row+1;
end
if p > 0
    for row=row:size(obs,1)
        x = fsolve(@fun,x,options,ft,h,t,c,beta1,beta2,b2,d2,kmu,d1,m,g,e,...
            s,E,b,theta_0_1,v2,obs(row));
        pre(row,1)=x(2);
    end
end
function F = fun(x,ft,h,t,c,beta1,beta2,b2,d2,kmu,d1,m,g,e,s,E,b,theta_0_1,...
    v2,cmod)
rho = 1/(ft*h*t)*x(2);
theta_1_2 = 1/2*(1-rho-c+sqrt((1-rho-c)^2+c^2/(beta1-1)));
theta_2_3 = 1/2*(rho*(beta2-1)+b2/beta2+sqrt(rho^2*(beta2-1)^2+2*rho*(beta2...
    -1)*b2/beta2+(1-b2)^2/(beta1-beta2)+b2^2/beta2));
switch 1
```

```
case x(1) <= theta_1_2
    alpha = 1-beta1-sqrt((1-beta1)*((1-rho)/x(1)-beta1));
    mu = 4*(1-3*alpha+3*alpha^2-alpha^3/(1-beta1))*x(1)+(6*alpha-3)*(1-rho);
    bi = 1; betai=beta1;
case x(1) <= theta_2_3
    alpha = 1-beta2-(1-b2)/2/x(1)-sqrt((1-beta2)*((1-b2)^2/4/x(1)^2/(beta1...
        -beta2)-beta2+(b2-rho)/x(1)));
    mu = 4*(1-3*alpha+3*alpha^2-alpha^3/(1-beta2))*x(1)+(6*alpha-3)*(1-rho)...
        -(1-b2)*(3*alpha^2-(c/2/x(1))^2)/(1-beta2);
    bi = b2; betai=beta2;
case x(1) > theta_2_3
    alpha = 1-1/2/x(1)*(1+sqrt((1-b2)^2/(beta1-beta2)+b2^2/beta2-4*rho*x(1)));
    mu = 4*x(1)*(1-3*alpha+3*alpha^2-alpha^3)+(6*alpha-3)*(1-rho)-3*alpha^2+...
        1/4/x(1)^2*(1-b2/beta2)*(1-b2/beta2+c)*(1+beta1*c/(1-beta1))...
        +(c/2/x(1))^2;
    bi = 0; betai=0;
end
F(1) = mu-6/(ft*h^2*t)*(x(2)*(d2-h/2)+1/2*kmu*x(2)*d1+m*g*e);
F(2) = s*ft/E*(1-bi+2*alpha*x(1))/(1-betai)+2*(b-h)*((s*ft/E*(1-bi+...
    2*alpha*x(1))/(1-betai))/2/alpha/h-s*ft/h/E*theta_0_1/(1-beta1))+...
    x(2)/E/t*v2-cmod;
```

Appendix C

MatLab-code, Reinforcement-Concrete Bond

The following subfunctions are needed by the program, but listed in Appendix B:

datared.m = Data reduction algorithm
dispmsg.m = Message displayer
resplot.m = Result plotter

The following subfunctions are listed in the following:

r_E1.m = Object function, phase I
r_E2.m = Object function, phase II
r_initialize.m = Initialization script
r_forward.m = Bond analysis, forward
r_inverse.m = Bond analysis, inverse
r_itdisp.m = Displays details about the iteration process
r_main.m = Bond analysis, main program
r_warn.m = Warnings displayer
tscheck.m = Validity check of shear-slip relationship

```
function E1 = E1(est,X,Y,geo,fix,lb,ub,warnings,i,rep)
disp_each_iteration=1;
inp=[fix(1) fix(2) fix(3) est(1) fix(5) fix(6) fix(7)];
tau1star=inp(1); tau2star=inp(2); tau3star=inp(3);
E1star=inp(4); E2star=inp(5); Es=inp(6); Ec=inp(7);
tau1=tau1star; tau2=tau2star+tau1star*E2star/E1star;
tau3=tau3star; delta1=tau1star/E1star;
delta2=tau1star/E1star+(tau2star-tau3star)/E2star; out=0;
if (inp(4)<lb(4))|(inp(4)>ub(4))|(tscheck(inp,0)==0)
    E1=1e498; negL=0; negP=0;
else
    [out,negL]=r_main(inp,X,geo,0);
    if textread('NobsI.dat')==0
        dlmwrite('NobsI.dat',sum((out(:,2).*(out(:,2)-2).*(out(:,2)-3)))/2)
    end
    NobsI=textread('NobsI.dat');
    if NobsI > size(out,1)
        NobsI=size(out,1);
    end
    E1 = sum((real(Y(1:NobsI,1)-out(1:NobsI,1))).^2)/NobsI;
end
if min(sign(out(:,1))) < 0
    negP=1;
else
    negP=0;
end
if (inp(4)<lb(4))|(inp(4)>ub(4))|(tscheck(inp,0)==0)|(negL>0)|(negP>0)
    r_warn(warnings,1,inp,lb,ub,i,rep,1,negL,negP)
end
if (negL>0)|(negP>0)
    E1=E1*1e498;
end
if disp_each_iteration==1
    r_itdisp(i,inp,E1,negL,negP,1)
end
```

```
function E2 = E2(est,X,Y,geo,fix,lb,ub,warnings,i,rep)
disp_each_iteration=1;
inp=[est(1) est(2) est(3) fix(4) est(4) fix(6) fix(7)];
tau1star=inp(1); tau2star=inp(2); tau3star=inp(3); E1star=inp(4);
E2star=inp(5); Es=inp(6); Ec=inp(7); tau1=tau1star;
tau2=tau2star+tau1star*E2star/E1star; tau3=tau3star; delta1=tau1star/E1star;
delta2=tau1star/E1star+(tau2star-tau3star)/E2star; out=0;
if (inp(1)<lb(1))|(inp(1)>ub(1))|(inp(2)<lb(2))|(inp(2)>ub(2))|...
   (inp(3)<lb(3))|(inp(3)>ub(3))|(inp(5)<lb(5))|(inp(5)>ub(5))|...
   (tscheck(inp,0)==0)
    E2=1e499; negL=0;negP=0;
else
    [out,negL]=r_main(inp,X,geo,2);
    E2 = sum((real(Y(1:size(out,1))-out(:,1))).^2)/size(out,1);
end
if min(sign(out(:,1))) < 0
    negP=1;
else
    negP=0;
end
if (inp(1)<lb(1))|(inp(1)>ub(1))|(inp(2)<lb(2))|(inp(2)>ub(2))|...
   (inp(3)<lb(3))|(inp(3)>ub(3))|(inp(5)<lb(5))|(inp(5)>ub(5))|...
   (tscheck(inp,0)==0)|(negL>0)|(negP>0)
    r_warn(warnings,1,inp,lb,ub,i,rep,3,negL,negP)
end
if (negL>0)|(negP>0)
    E2=E2*1e6;
end
if disp_each_iteration==1
    r_itdisp(i,inp,E2,negL,negP,3)
end
```

```
function ini=r_initialize()
%ini=[10    9   8   514.661 24.8124 210000  30000];
ini=[3 3 1.5 350 5 210000 40000];
```

```
function r_forward(est,geo,output,Nstepi,etamax,type,param_var,exp_file)
tic
tau1star=est(1); tau2star=est(2); tau3star=est(3); E1star=est(4);
E2star=est(5); Es=est(6); Ec=est(7);
tau1=tau1star; tau2=tau2star+tau1star*E2star/E1star; tau3=tau3star;
delta1=tau1star/E1star; delta2=tau1star/E1star+(tau2star-tau3star)/E2star;
if (E1star<=0)|(E2star==0)|(tau1star<=0)|(tau2star<=0)|...
   (tau3star<=0)|(delta1>=delta2)|(delta1<=0)|(delta2<=0)|...
   (tau1<=0)|(tau2<=0)|(tau3<=0)
    disp('Bad t-d')
else
    L=geo(1);
    ds=geo(2);
    dc=geo(3);
    n=Es/Ec; As=pi/4*ds^2; Ac=pi/4*dc^2; rho=As/Ac; E1=tau1/delta1;
    E2=(tau2-tau3)/delta2; delta2star=tau2/E2; k=4*(1+n*rho)/Es/ds;
    lambda1=(k*E1)^0.5; lambda2=(k*E2)^0.5;
    out=[0 0 0];
    %calculation of phase 1
    for i=1:Nstepi(1,1)
        out(i+1,1)=i/Nstepi(1,1)*delta1;
        out(i+1,2)=out(i+1,1)/L*Es*As*lambda1*L*cosh(lambda1*L)...
                    /sinh(lambda1*L);
        out(i+1,3)=out(i+1,2)-out(i+1,1)/L*Es*As;
    end
    % calculation of phase 2
    options = optimset('Display','off','MaxFunEvals',5000,...
                       'MaxIter',5000,'TolFun',1e-13);
    L2limit = fzero(@FL,0,options,delta1,lambda1,lambda2,delta2star,...
                    delta2,L,0);
    for i=1:Nstepi(1,2)
        L2=i/Nstepi(1,2)*L2limit;
        L1=L-L2;
        out(i+1+Nstepi(1,1),1)=delta1*lambda1/lambda2*coth(lambda1*L1)...
            *sin(lambda2*L2)-(delta2star-delta1)*cos(lambda2*L2)...
            +delta2star;
        out(i+1+Nstepi(1,1),2)=Es*As*(delta1*lambda1*coth(lambda1*L1)...
            *cos(lambda2*L2)+(delta2star-delta1)*lambda2*sin(lambda2*L2));
        out(i+1+Nstepi(1,1),3)=out(i+1+Nstepi(1,1),2)-out(i+1+...
                                   Nstepi(1,1),1)/L*Es*As;
    end
    %calculation of phase 3
    for i=1:Nstepi(1,3)
        L3=L*etamax*(1-40^(-i/Nstepi(1,3)))/(1-40^(-1));
        L2=fzero(@FL,L2,options,delta1,lambda1,lambda2,delta2star,...
```

```
                delta2,L,L3);
        L1=L-L2-L3;
        out(i+1+Nstepi(1,1)+Nstepi(1,2),2)=Es*As*(k*tau3*L3...
            +delta1*lambda1*coth(lambda1*L1)*cos(lambda2*L2)...
            +(delta2star-delta1)*lambda2*sin(lambda2*L2));
        out(i+1+Nstepi(1,1)+Nstepi(1,2),1)=out(i+1+Nstepi(1,1)...
            +Nstepi(1,2),2)/Es/As*L3-1/2*k*tau3*L3^2+delta2;
        out(i+1+Nstepi(1,1)+Nstepi(1,2),3)=out(i+1+Nstepi(1,1)...
            +Nstepi(1,2),2)-out(i+1+Nstepi(1,1)+Nstepi(1,2),1)/L*Es*As;
    end
    hold on
    if type == 1
        td=[0 0];
        td(2,:)=[delta1 tau1star];
        td(3,:)=[delta1 tau2star];
        td(4,:)=[delta2 tau3star];
        td(5,:)=[2*delta2 tau3star];
        plot(td(:,1),td(:,2))
    else
        out(:,3)=out(:,3)./(L*pi*ds);
        plot(out(1:Nstepi(1,1)+1,1),out(1:Nstepi(1,1)+1,type),'r')
        plot(out(Nstepi(1,1)+1:Nstepi(1,1)+Nstepi(1,2)+1,1),...
             out(Nstepi(1,1)+1:Nstepi(1,1)+Nstepi(1,2)+1,type),'g')
        plot(out(Nstepi(1,1)+Nstepi(1,2)+1:Nstepi(1,1)+Nstepi(1,2)...
             +Nstepi(1,3)+1,1),out(Nstepi(1,1)+Nstepi(1,2)...
             +1:Nstepi(1,1)+Nstepi(1,2)+Nstepi(1,3)+1,type),'k')
        title(param_var,'FontSize',14,'interpreter','none')
        xlabel('End slip [mm]','FontSize',14)
        ylabel('Load [kN]','Rotation',90,'FontSize',14)
    end
    dlmwrite(output,out,'\t')
    disp(['Time: ' num2str(toc) ' sec.'])
end hold on xy=textread(exp_file); plot(xy(:,1),xy(:,2))
basic_params=[tau1;tau2;tau3;delta1;delta2;Es;Ec];
function F = FL(L2,delta1,lambda1,lambda2,delta2star,delta2,L,L3)
F = delta1*lambda1*sin(lambda2*L2)-(delta2star-delta1)*lambda2...
    *tanh(lambda1*(L-L2-L3))*cos(lambda2*L2)-(delta2-delta2star)...
    *lambda2*tanh(lambda1*(L-L2-L3));
```

```
function r_inverse(input,output,initial,geometry,red,rep,tol)
tic
if (nargin==0)|(nargin==5)|(nargin==6)|(nargin>7)
    disp('Input not correctly specified')
else
    data=textread(input);
    dlmwrite('number.dat',1);
    dlmwrite('NobsI.dat',0);
    if nargin <= 4
        red = 0.009;
        rep = 20;
        tol = 0.01;
        if nargin <= 3
            geometry = 'r_geometry.dat';
            if nargin <= 2
                initial = [strtok(input,'.') '-ini' '.dat'];
                dlmwrite(initial,r_initialize,'\t')
                if nargin == 1
                    output = [strtok(input,'.') '.out'];
    end,end,end,end
    fix = textread(initial);
    geo = textread(geometry);
    warnings = [strtok(input,'.') '_WARNINGS.dat'];
    r_warn(warnings,0)
    if tscheck(fix,1) == 1
        [X,Y]=datared(data(:,1),data(:,2),red);
        [lb ub]=textread('r_boundaries.dat','%f %f');
        options=optimset('TolX',0.01,'TolFun',0.01);
        dispmsg(geometry,input,initial,output,rep,X)
        i=1;err=1;
        while (i <= rep) & (err > tol)
            fix(4)=fminsearch('r_E1',fix(4),options,X,Y,geo,fix,lb,ub,...
                   warnings,i,rep);
            disp(['Fit session no.' blanks(1) num2str(i) blanks(1) ...
                 'for E1 completed'])
            par=fminsearch('r_E2',[fix(1) fix(2) fix(3) fix(5)],options,...
                X,Y,geo,fix,lb,ub,warnings,i,rep);
            fix(1:3)=par(1:3);
            fix(5)=par(4);
            disp(['Fit session no.' blanks(1) num2str(i) blanks(1) ...
                 'for tau1, tau2, tau3 and E2 completed'])
            [out,negL]=r_main(fix,X,geo,2);
            results(1:7,i)=fix';
            results(8,i)=sqrt(sum((real(Y(:)-out(:,1))).^2)...
                         /size(out,1))/max(Y)*100;
```

```
            if i > 1
                err = max(abs((results(1:7,i-1)-results(1:7,i))./...
                      results(1:7,i)));
            end
            i=i+1;
            dlmwrite(output,results',',\t')
        end
        if err > tol
            disp(['Max number of iterations reached.'...
                 ' Max. relative error: ' num2str(100*err) ' %'])
        else
          disp(['Convergence achieved after ' num2str(i-1) ' iterations.'])
        end
        resplot(X,Y,out,input,'cmod')
        disp(blanks(1)'), disp(['Time elapsed =' blanks(1) ...
             num2str(toc/60,4) blanks(1) 'min'])
    end
end
```

```
function r_itdisp = r_itdisp(counter,inp,E,negL,negP,phase)
tau1star=inp(1); tau2star=inp(2); tau3star=inp(3); E1star=inp(4);
E2star=inp(5); Es=inp(6); Ec=inp(7);
tau1=tau1star; tau2=tau2star+tau1star*E2star/E1star; tau3=tau3star;
delta1=tau1star/E1star;
delta2=tau1star/E1star+(tau2star-tau3star)/E2star; out=0;
i=textread('number.dat');
disp('************************************')
disp(['Repetition no. ' num2str(counter)])
disp(['Iteration no. ' num2str(i)])
disp(['Phase no. ' num2str(phase)])
dlmwrite('number.dat',i+1)
disp('Values of input parameters')
disp(num2str(inp(1)))
disp(num2str(inp(2)))
disp(num2str(inp(3)))
disp(num2str(inp(4)))
disp(num2str(inp(5)))
disp(num2str(inp(6)))
disp(num2str(inp(7)))
disp(['Error norm = ' num2str(E)])
if negL==1
    disp('Negative values of L1, L2 or L3 in phase III')
end
if negP==1
    disp('Solution has resulted in negative pull in the reinforcement')
end
if (E1star<=0)|(E2star<=0)|(tau1star<=0)|(tau2star<=0)|(tau3star<=0)|...
   (delta1>=delta2)|(delta1<=0)|(delta2<=0)|(tau1<=0)|(tau2<=0)|...
   (tau3<=0)|(tau2star>tau1star)
    disp('Invalid tau-slip relation was used')
end
```

```
function [pre,negL]=r_main(est,X,geo,p)
tau1star=est(1); tau2star=est(2); tau3star=est(3); E1star=est(4);
E2star=est(5); Es=est(6); Ec=est(7);
tau1=tau1star; tau2=tau2star+tau1star*E2star/E1star; tau3=tau3star;
delta1=tau1star/E1star;
delta2=tau1star/E1star+(tau2star-tau3star)/E2star;
L=geo(1); ds=geo(2); dc=geo(3);
n=Es/Ec; As=pi/4*ds^2; Ac=pi/4*dc^2; rho=As/Ac; E1=tau1/delta1;
E2=(tau2-tau3)/delta2;
delta2star=tau2/E2; k=4*(1+n*rho)/Es/ds; lambda1=(k*E1)^0.5;
lambda2=(k*E2)^0.5;
options = optimset('Display','on','MaxFunEvals',50000,'MaxIter',...
          50000,'TolFun',1e-16);
i=1;L3=0;L2=0;negL=0;
while X(i,1)<=delta1
    pre(i,1)=X(i,1)/L*Es*As*lambda1*L*cosh(lambda1*L)/sinh(lambda1*L);
    pre(i,2)=1;
    i=i+1;
end
if p > 1
    while (X(i,1)<delta2) & (i<size(X,1))
        L2=fzero(@phase2,0,options,delta1,lambda1,lambda2,delta2star,...
           delta2,L,X(i,1));
        L1=L-L2;
        pre(i,1)=Es*As*(delta1*lambda1*coth(lambda1*L1)*cos(lambda2*...
                 L2)+(delta2star-delta1)*lambda2*sin(lambda2*L2));
        pre(i,2)=2;
        i=i+1;
    end
    for i=i:size(X,1)
        L3=fzero(@deltadelta,L3,options,delta1,lambda1,lambda2,...
           delta2star,delta2,L,k,tau3,Es,As,L2,X(i,1));
        L2=fzero(@FL,L2,options,delta1,lambda1,lambda2,delta2star,...
           delta2,L,L3);
        L1=L-L2-L3;
        pre(i,1)=Es*As*(k*tau3*L3+delta1*lambda1*coth(lambda1*L1)*...
                 cos(lambda2*L2)+(delta2star-delta1)*lambda2*...
                 sin(lambda2*L2));
        pre(i,2)=3;
        if ((L1<0)|(L2<0)|(L3<0))&(negL==0)
            negL=1;
        end
    end
end
function F = FL(L2,delta1,lambda1,lambda2,delta2star,delta2,L,L3)
```

```
F(1) = delta1*lambda1*sin(lambda2*L2)-(delta2star-delta1)*lambda2*...
       tanh(lambda1*(L-L2-L3))*cos(lambda2*L2)-(delta2-delta2star)*...
       lambda2*tanh(lambda1*(L-L2-L3));
function F = phase2(L2,delta1,lambda1,lambda2,delta2star,delta2,L,obs)
F=delta1*lambda1*sin(lambda2*L2)-(delta2star-delta1)*lambda2*...
  tanh(lambda1*(L-L2))*cos(lambda2*L2)-(obs-delta2star)*lambda2*...
  tanh(lambda1*(L-L2));
function deltaL3 = deltaL3(delta1,lambda1,lambda2,delta2star,delta2,...
                  L,L3,k,tau3,Es,As,L2)
options = optimset('Display','on','MaxFunEvals',50000,'MaxIter'...
          ,50000,'TolFun',1e-16);
L2=fzero(@FL,L2,options,delta1,lambda1,lambda2,delta2star,delta2,L,L3);
L1=L-L2-L3;
F=Es*As*(k*tau3*L3+delta1*lambda1*coth(lambda1*L1)*cos(lambda2*L2)+...
  (delta2star-delta1)*lambda2*sin(lambda2*L2));
deltaL3=F/Es/As*L3-1/2*k*tau3*L3^2+delta2;
function F = deltadelta(L3,delta1,lambda1,lambda2,delta2star,delta2,...
             L,k,tau3,Es,As,L2,obs)
F=obs-deltaL3(delta1,lambda1,lambda2,delta2star,delta2,L,L3,k,tau3,...
  Es,As,L2);
```

```
function warn(warnings,p,inp,lb,ub,i,rep,phase,negL,negP)
switch 1
case (p == 0)
    if which(warnings) | 0
        fid = fopen(warnings,'w+');
        fprintf(fid,'This file contains warnings generated during'...
                ' inverse analysis. Pls. check your results if any'...
                ' warnings have been generated\n\n');
        fclose(fid);
    end
case (p == 1)
    WT = WarningType(inp,lb,ub,negL,negP);
    if which(warnings) | 0
        fid = fopen(warnings,'a');
        fprintf(fid,'Warning: The optimization was limited by:'...
                ' %s. \nValues of parameters: [%8.5e %8.5e %8.5e'...
                ' %8.5e %8.5e %8.5e %8.5e]. Phase %1.0f. Repetition:'...
                ' %1.0f\n',WT,inp,phase,i);
        fclose(fid);
    else
        fid = fopen(warnings,'w+');
        fprintf(fid,'This file contains warnings generated during'...
                ' inverse analysis. Pls. check your results if any'...
                ' warnings have been generated\n\n');
        fprintf(fid,'Warning: The optimization was limited by: %s.'...
                ' \nValues of parameters: [%8.5e %8.5e %8.5e %8.5e'...
                ' %8.5e %8.5e %8.5e]. Phase %1.0f. Repetition:'...
                ' %1.0f\n',WT,inp,phase,i);
        fclose(fid);
    end
end
function WarningType = WarningType(inp,lb,ub,negL,negP)
tau1star=inp(1); tau2star=inp(2); tau3star=inp(3); E1star=inp(4);
E2star=inp(5); Es=inp(6); Ec=inp(7);
tau1=tau1star; tau2=tau2star+tau1star*E2star/E1star; tau3=tau3star;
delta1=tau1star/E1star;
delta2=tau1star/E1star+(tau2star-tau3star)/E2star;
switch 1
case (E1star<=0), WarningType = 'Invalid tau-slip relation. E1<=0';
case (E2star<=0), WarningType = 'Invalid tau-slip relation. E2<=0';
case (tau1star<=0), WarningType = 'Invalid tau-slip relation. tau1<=0';
case (tau2star<=0), WarningType = 'Invalid tau-slip relation. tau2<=0';
case (tau3star<=0), WarningType = 'Invalid tau-slip relation. tau3<=0';
case (delta1>=delta2), WarningType = 'Invalid tau-slip relation.'...
                                     ' delta1>=delta2 (calculated)';
```

```
case (delta1<=0), WarningType = 'Invalid tau-slip relation. delta1<=0'...
                                ' (calculated)';
case (delta2<=0), WarningType = 'Invalid tau-slip relation. delta2<=0'...
                                ' (calculated)';
case (inp(1)<lb(1)), WarningType = 'tau1 < lb';
case (inp(2)<lb(2)), WarningType = 'tau2 < lb';
case (inp(3)<lb(3)), WarningType = 'tau3 < lb';
case (inp(4)<lb(4)), WarningType = 'E1 < lb';
case (inp(5)<lb(5)), WarningType = 'E2 < lb';
case (inp(1)>ub(1)), WarningType = 'tau1 > ub';
case (inp(2)>ub(2)), WarningType = 'tau2 > ub';
case (inp(3)>ub(3)), WarningType = 'tau3 > ub';
case (inp(4)>ub(4)), WarningType = 'E1 > ub';
case (inp(5)>ub(5)), WarningType = 'E2 > ub';
case (tau1<=0),WarningType = 'Invalid tau-slip relation. tau1<=0'...
                             ' (calculated)';
case (tau2<=0),WarningType = 'Invalid tau-slip relation. tau2<=0'...
                             ' (calculated)';
case (tau3<=0),WarningType = 'Invalid tau-slip relation. tau3<=0'...
                             ' (calculated)';
case (tau2star>tau1star),WarningType = 'Invalid tau-slip relation.'...
                                       ' tau2>tau1. Hardening not allowed';
case (tau3star>tau2star),WarningType = 'Invalid tau-slip relation. '...
                                       'tau3>tau2. Hardening not allowed';
case (negL==1),WarningType = 'Solution resulted in negative values'...
                             ' of L1, L2 or L3';
case (negP==1),WarningType = 'Solution resulted in negative pull'...
                             ' in reinforcement';
otherwise WarningType = 'Unknown';
end
```

```
function tscheck=tscheck(inp,output)
tau1star=inp(1); tau2star=inp(2); tau3star=inp(3); E1star=inp(4);
E2star=inp(5); Es=inp(6); Ec=inp(7);
tau1=tau1star; tau2=tau2star+tau1star*E2star/E1star; tau3=tau3star;
delta1=tau1star/E1star;
delta2=tau1star/E1star+(tau2star-tau3star)/E2star;
switch 1
case output == 0
    if (E1star<=0)|(E2star<=0)|(tau1star<=0)|(tau2star<=0)|(tau3star<=0)...
       |(delta1>=delta2)|(delta1<=0)|(delta2<=0)|(tau1<=0)|(tau2<=0)...
       |(tau3<=0)|(tau2star>tau1star)|(tau3star>tau2star)
        tscheck=0;
    else
        tscheck=1;
    end
case output == 1
    switch 1
    case (E1star<=0), disp('Invalid tau-slip relation. E1<=0')
        tscheck=0;
    case (E2star<=0), disp('Invalid tau-slip relation. E2<=0')
        tscheck=0;
    case (tau1star<=0), disp('Invalid tau-slip relation. tau1<=0')
        tscheck=0;
    case (tau2star<=0), disp('Invalid tau-slip relation. tau2<=0')
        tscheck=0;
    case (tau3star<=0), disp('Invalid tau-slip relation. tau3<=0')
        tscheck=0;
    case (delta1>=delta2), disp('Invalid tau-slip relation.'...
                               ' delta1>=delta2 (calculated)')
        tscheck=0;
    case (delta1<=0), disp('Invalid tau-slip relation. delta1<=0'...
                          ' (calculated)')
        tscheck=0;
    case (delta2<=0), disp('Invalid tau-slip relation. delta2<=0 '...
                          '(calculated)')
        tscheck=0;
    case (tau1<=0), disp('Invalid tau-slip relation. tau1<=0 '...
                        '(calculated)')
        tscheck=0;
    case (tau2<=0), disp('Invalid tau-slip relation. tau2<=0 '...
                        '(calculated)')
        tscheck=0;
    case (tau3<=0), disp('Invalid tau-slip relation. tau3<=0 (calculated)')
        tscheck=0;
    case (tau2star>tau1star), disp('Invalid tau-slip relation. '...
```

```
                                    'tau2>tau1. Hardening not allowed')
        tscheck=1;
    case (tau3star>tau2star), disp('Invalid tau-slip relation. '...
                                    'tau3>tau2. Hardening not allowed')
        tscheck=1;
    otherwise
        tscheck=1;
    end
end
```

List of Symbols

Abbreviations

C	Cement
CA	Coarse Aggregates
CH	Calcium Hydroxide
CMOD	Crack Mouth Opening Displacement
COD	Crack Opening Displacement
CSH	Calcium Silica Hydrate
C_2S	Clinker mineral, $(CaO)_2SiO_2$
C_3S	Clinker mineral, $(CaO)_3SiO_2$
C_3A	Clinker mineral, $(CaO)_3Al_2O_3$
C_4AF	Clinker mineral, $(CaO)_4Al_2O_3Fe_2O_3$
F	Fly ash
FA	Fly Ash
FA	Fine Aggregates
FEM	Finite Element Method
FPZ	Fracture Process Zone
FRC	Fiber Reinforced Concrete
HPC	High Performance Concrete
HSC	High Strength Concrete
ITZ	Interfacial Transition Zone
LEFM	Linear Elastic Fracture Mechanics
MS	Microsilica
NLFM	Non-Linear Fracture Mechanics
NSC	Normal Strength Concrete
P	Powder
RVE	Representative Volume Element
SAP	Super Absorbent Polymers
SCT	Split Cylinder Test
SEM	Scanning Electron Microscopy
SF	Silica Fume
SRA	Shrinkage Reducing Admixture
TPBT	Three Point Bending Test
UTT	Uniaxial Tension Test
WST	Wedge Splitting Test
w/c	Water/Cement-ratio

Latin Letters

a	half of width of loading strip
a	notch length, crack length
a	slope of the stress-crack opening relationship
A	material constant
A	Area
b	distance
b	intersection of the stress-crack opening relationship with y-axis
c	integration constant
c	cohesion
c	specific heat capacity
C	material constant
d	thickness of measurement bricks
d	diameter
d	coordinates
d	depth of crack
D	diameter
e	eccentricity
E	modulus of elasticity
f	frequency
f	function
F	Force
F	function
F	material constant
f_c	compressive strength
f_t	tensile strength
g	function
g	gravitational acceleration
G_c	critical energy release rate
G_f	fracture energy
h	length, height
H	function
H	height
I	moment of inertia
J	compliance
k	ratio
k	stiffness
k	spring stiffness, constant
K	stiffness
K	stress intensity factor
L	length
L_{ch}	characteristic length
m	mass
m	exponent

M	maturity
M	Sectional moment
n	exponent
n	stiffness ratio
N	number of observations
N	Sectional normal force
p	material constant
p	material parameter
P	Load
q	material constant
Q	function
Q	total heat release
r	radius
R	gas constant
R	relaxation
s	distance, band width
t	width, thickness
t	time
t'	time at loading
T	temperature
u	displacement
U	potential of bond forces
v	displacement
V	volume
w	crack opening
W	work
W	characteristic dimension
x	variable
x,y	coordinates
z	distance

Greek Letters

α	normalized crack depth
α	thermal dilation coefficient
β	normalized fracture property
β	angle
δ	slip
δ	contribution to CMOD
ε	strain
ζ	normalized fracture property
η	viscosity
θ	angle
θ	temperature
θ	normalized rotation

κ	parameter, depending on stress state (plane stress or strain)
λ	parameter
λ	material constant
μ	normalized moment
μ	friction coefficient
ν	Poisson's ratio
ρ	normalized normal force
ρ	area ratio
σ	normal stress
τ	shear stress
τ	retardation time
φ	friction angle
φ	creep coefficient
ψ	dilatation angle
ψ	function
ω	angle

Subscripts

0	constant, neutral
1, 2, 3,.., n	numbering of constants etc.
0, I, II, III	phases
avg	average
b	balance
c	concrete
c	coefficient
c	critical, compressive
C	Celcius
ch	characteristic
COD	Crack Opening Displacement
cr	crack
e	elastic
el	elastic
ext	external
E	elastic
f	fracture
h	hinge
i	indices
I	mode I fracture
II	mode II fracture
III	mode III fracture
int	internal
K	Kelvin
m	machine
max	maximum

p	process zone
r	rotational
r	reference
s	steel (reinforcement)
sp	split
t	tensile
u	deflection
v	vertical
w	crack, crack opening
w	wedge

Superscripts

obs	observation
max	maximum
0	initial
$*$	position of tip of crack
$'$	modified

List of Figures

List of Tables